QUANTITATIVE PREDICTION OF NON-LOCAL MATERIAL AND TRANSPORT PROPERTIES THROUGH QUANTUM SCATTERING MODELS

A Dissertation

Submitted to the Faculty

of

Purdue University

by

Prasad Sarangapani

In Partial Fulfillment of the

Requirements for the Degree

of

Doctor of Philosophy

December 2018

Purdue University

West Lafayette, Indiana

THE PURDUE UNIVERSITY GRADUATE SCHOOL
STATEMENT OF DISSERTATION APPROVAL

Dr. Gerhard Klimeck, Co-Chair

School of Electrical and Computer Engineering

Dr. Tillmann Kubis, Co-Chair

School of Electrical and Computer Engineering

Dr. Joerg Appenzeller, Committee Member

School of Electrical and Computer Engineering

Dr. Supriyo Datta, Committee Member

School of Electrical and Computer Engineering

Approved by:

Dr. Pedro Irazoqui

Thesis Form Head

ACKNOWLEDGMENTS

I would like to express my sincere thanks and appreciation to my advisors, Dr. Tillmann Kubis and Prof. Gerhard Klimeck for providing academic and financial support during my PhD. I would like to express my sincere gratitude to Dr. Tillmann Kubis, who has mentored me for the last five years. His ability to constantly motivate me, guide me during the difficult phases of my research and support me both on technical and non-technical aspects of research have helped me shape as a mature researcher. I particularly enjoyed his lectures on fundamentals of NEGF and those interactions have definitely helped me get a good grasp over quantum transport modeling approaches. I would like to thank Prof. Gerhard Klimeck for providing insightful discussions on my research and career development. I would like to express my gratitude to Prof. Supriyo Datta and Prof. Joerg Appenzeller for agreeing to be on my committee. Their valuable comments have definitely helped me improve the quality of my research work. I am glad to be part of the NEMO5 team and happy to have shared my lab space with them. I would like to thank theNEMO5 teammembers James Charles, Yuanchen Chu, Kuang Chung Wang, Daniel Lemus, Chinyi Chen, Rifat Ferdous, Harshad Sahasrabuddhe, Tarek Ameen, Daniel Valencia, Mehdi Salmani and Daniel Mejia for making my stay in the group and Purdue an enjoyable and memorable experience.

I owe my deepest gratitude to Amma and Appa who have made this possible for me. Their support, sacrifice and constant motivation has pushed me to strive hard in my pursuit of excellence. I would like to thank my sister Nitya, my brother-in-law Rajan and my nephew Anirudh who ensured that my transition to/from graduate school and my stay at Purdue was as comfortable as possible. Times spent during the holidays in Kansas were a big stress buster from my hectic research. I would be the first doctorate in my extended family and words cannot express how much joy this brings to my family.

My time at Purdue would be incomplete without my friends. I would like to thank Vignesh for pulling me out of my shell and for the constant inquiries about my research

and well-being. I would like to thank Bharath for being a wonderful roommate and my partner partner in crime for the past five years. I would like to thank Aravind, Sudharshan, Swetha, Saranya, Kaushik, Adarsh for being an extended family, a strong support system and for the countless memories. I would like to thank Adithya Sarathy for his inputs on research, job applications and for his support during the final phase of my PhD.

Music has had a strong presence during my stay at Purdue and the music is incomplete without the musical group. I would like to thank Rohith, Suchitra, Ajita, Hrishikesh, Chandnee, Sukshitha, Shraddha, Shreya, Bhavana, Gani and Aditya for the musical interaction and for making my ICMAP experience memorable. What began as a music group has now grown into a close-knit friend circle. I would also like to thank Tatvam members Sai, Anamika, Sarath, Ranjani, Rithesh, Parul, Janav and Anan for the countless performances and jam sessions.

I would like to specifically thank Prof. Vijay Raghunathan for being my musical mentor and for his hospitality and warmth. His timely advice and opinions in matters of research and career development have been immensely helpful to me.

Last, but not the least, I would like to thank Purnima for being a constant pillar of support and motivation. She has been a great source of strength during the difficult phases of my research. Her grit, determination and ability to see light at the end of the tunnel has been a major source of inspiration for my research and life in general.

TABLE OF CONTENTS

Page

Page

LIST OF TABLES

LIST OF FIGURES

Figure Page

Figure Page

Figure Page

Figure Page

Figure Page

Figure Page

ABBREVIATIONS

ITRS	International Techonology Roadmap for Semiconductors
MOSFET	Metal-oxide semiconductor field effect transistor
finFET	fin shaped field effect transistor
NEGF	Non-equilibrium Green's function
SS	Sub-threshold slope
TFET	Tunneling field effect transistor
III-V	Semiconductor materials belonging to the III-V group of the Periodic table
UTB	Ultra-thin body device
NW	Nanowire
TMD	Transition metal dichalcogenides
POP	Polar optical phonons
SCBA	Self-consistent Born approximation
LO	Longitudinal optical phonons
DOS	Density of states
LO	Longitudinal optical
RGF	Recursive Green's function

ABSTRACT

Sarangapani, Prasad Ph.D., Purdue University, December 2018. Quantitative Prediction of Non-Local Material and Transport Properties Through Quantum Scattering Models. Major Professors: Gerhard Klimeck, Tillmann Kubis.

Challenges in the semiconductor industry have resulted in the discovery of a plethora of promising materials and devices such as the III-Vs (InGaAs, GaSb, GaN/InGaN) and 2D materials (Transition-metal dichalcogenides [TMDs]) with wide-ranging applications from logic devices, optoelectronics to biomedical devices. Performance of these devices suffer significantly from scattering processes such as polar-optical phonons (POP), charged impurities and remote phonon scattering. These scattering mechanisms are long-ranged, and a quantitative description of such devices require non-local scattering calculations that are computationally expensive. Though there have been extensive studies on coherent transport in these materials, simulations are scarce with scattering and virtually non-existent with non-local scattering.

In this work, these scattering mechanisms with full non-locality are treated rigorously within the Non-Equilibrium Green's function (NEGF) formalism. Impact of non-locality on charge transport is assessed for GaSb/InAs nanowire TFETs highlighting the underestimation of scattering with local approximations. Phonon, impurity scattering, and structural disorders lead to exponentially decaying density of states known as Urbach tails/band tails. Impact of such scattering mechanisms on the band tail is studied in detail for several bulk and confined III-V devices (GaAs, InAs, GaSb and GaN) showing good agreement with existing experimental data. A systematic study of the dependence of Urbach tails with dielectric environment (oxides, charged impurities) is performed for single and multilayered 2D TMDs (MoS2, WS2 and WSe2) providing guideline values for researchers.

Often, empirical local approximations (ELA) are used in the literature to capture these non-local scattering processes. A comparison against ELA highlight the need for non-local scattering. A physics-based local approximation model is developed that captures the essential physics and is computationally feasible.

1. INTRODUCTION

This decade has been one of the exciting and challenging ones for the semiconductor industry. Transistor field has moved from the planar Metal-semiconductor field-effect transistors (MOSFETs), workhorse of microprocessors for the past 40 years to three-dimensional finFETs and has been able to push the boundaries of Moore's law predictions [1].

The Economist recently came up with an opinion and review article on the transistor count and power consumption trend for the past 45 years [2]. While the semiconductor industry has reaped benefits from Moore's law for over 5 decades, power consumption and clock speed have tanked in the past 10 years. The economics of producing a transistor is increasing as well resulting in delay of next generation ICs into the market. Despite the trend, Moore's law has not hit a brick wall. Chipmakers are spending billions on new designs and materials that may make transistors amenable to a bit more shrinkage and allow another few turns of the exponential crank. This has led to the discovery of a plethora of promising materials and devices such as the nanowires [3], [4], III-V MOSFETs and tunnel FETs [5], [6], two dimensional materials such as the transition metal dichalcogenides (MoS2, WSe2) [7].

In the context of FET scaling, metal-semiconductor contact resistance poses a critical challenge for continued MOSFET scaling. With shrinking device area, the parasitic source/drain resistance increases unless the metal-semiconductor contact resistivity, ρ_c is designed to decrease proportionately [8]. The International Technology Roadmap for Semiconductor (ITRS) has set a target on achievable values for ρ_c by 2023 to meet both scaling and performance requirements for logic devices and with each additional node, this has become an uphill. Unless possible mitigation schemes are proposed, power consumption of a transistor will be dominated by the contact resistance and interconnects.

Another possible way to reduce the power consumption is to reduce voltage to achieve the same current levels as current FETs. Conventional FETs are limited by the thermal

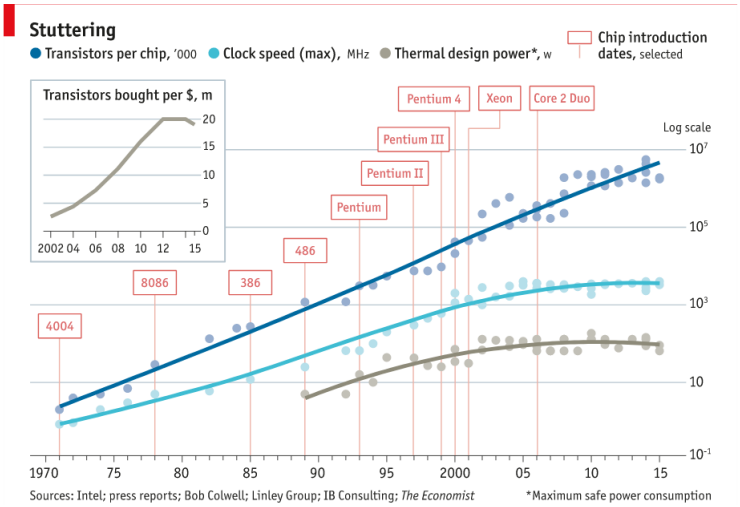

Fig. 1.1.: Over the past few years, power consumption and clock speed of transistors have tanked due to the limitations imposed by scaling of transistors. Source: Economist [2]

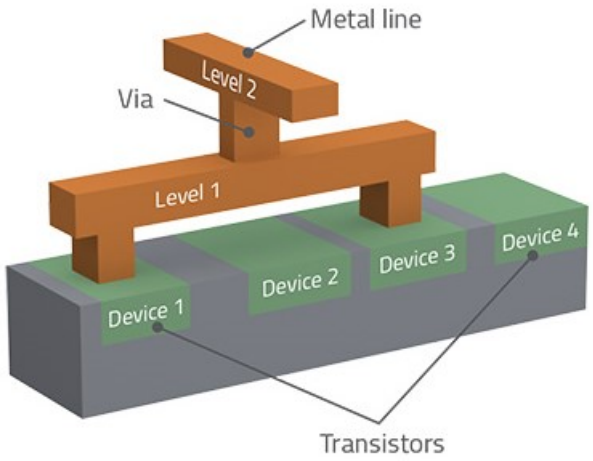

Fig. 1.2.: With aggressive scaling of transistors, contact resistance is a major source of bottleneck in transistor performance. Source: Lam Research [9]

Boltzmann limit of 60mV/decade. Also, known as subthreshold slope, it is amount of voltage required to bring about a decade increase in current. TFETs overcome this barrier by harnessing quantum mechanical tunneling to generate electric current. They offer a possible solution to sustain the Moore's law scaling. Their ability to provide sub-60 mV/dec subthreshold slope offers possibilities to operate transistors at low voltages and perform low-power computation. A plethora of materials such as InGaAs, GaSb and InAs are considered as potential candidates as TFETs due to their direct band gap and lower effective masses which is important in the context of tunneling [10–14]. Tunneling transistors provide sub-thermal switching by filtering out the high energy states in the Fermi distribution and by clever band engineering. Steep switching is achieved by a sudden onset of density of states through band alignment. Despite the ongoing research in TFETs, only a handful devices have managed to achieve sub-60 mV/dec SS [10, 15–17]. This is mainly due to imperfections in the device contributing to higher OFF current and SS. These imperfections include phonon scattering, alloy disorder, roughness, heavy doping induced band tail states and interface trap states which prevent sub-60 mV/dec SS performance. On the other hand, simulation results have shown extremely positive results for several TFETs. Since these materials are in the nanoscale regime, atomistic modeling approaches are needed to capture the essential physics and a quantum mechanical transport is definitely needed to capture the complex scattering processes that the electrons undergoes with the surrounding.

Among the scattering mechanisms present in tunneling junctions, polar optical phonons, impurities play an important role in determining the performance of these devices. They not only result in scattering of electronic states but also result in broadening and shift of energy levels affecting tunneling considerably. Tailing of band edge states (known as Urbach tails) and band gap narrowing can alter the behaviour of such device. Switching behaviour of TFET is drastically affected by such tailing states [19, 20]. Such band tail and narrowing phenomenon is not only restricted to tunnel junctions such as TFETs and Esaki diodes but is also of significant importance in optical devices such as GaN/InGaN light-emitting diodes [21–23] and high-performance solar cells [24–26]. Currently, there are analytical descriptions of these phenomenons and even the simulations that exist cor-

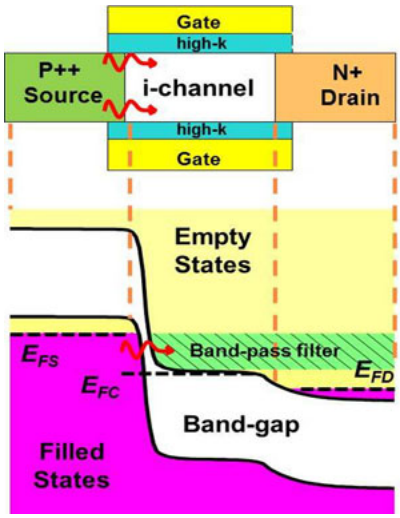

Fig. 1.3.: Illustration of tunneling transistor. TFET provides sub-60 mV/dec subthrehsold slope by creating a band pass filter excluding high energy electron/hole contribution. Source: Penn State [18]

respond to the bulk regime. It is not clear how these scattering parameters scale down to ultra-scaled devices such as thin films and nanowires. This requires a rigorous treatment of scattering mechanisms in the quantum transport regime to provide a physical intuition and a guideline. One of the interesting features of these scattering mechanisms is that they are non-local in nature. By non-local, we mean that the electron scattering is not restricted to just a single atomic or impurity site but is smeared out over a characteristic distance dependent on the electrostatic screening of the system. This adds additional complexity in solving such scattering interactions.

2D FETs provide an avenue to push the scaling to the ultimate limit where the devices are only few atomic layers thick. Two dimensional materials have attracted considerable attention recently due to their unique electronic, optical and mechanical properties [27]. Unlike graphene, transition metal dichalcogenide (TMDs) have a finite band gap which provides for applications in electronics as a replacement for Si transistors [28], in opto-electronics as possible materials in light emitting diodes [29], [30] and solar cells [31] applications. TMD layers have weak van der Waals coupling which enables low cost fabrication (through mechanical cleavage) and have electronic/optical properties that show strong dependence as a function of layers. Ability to stack multiple TMD materials on top of another significantly widens the design space available resulting in a plethora of devices such as $MoS_2 - WSe_2$ p-n junctions [32], $MoS_2 - Ge$ based tunnel field-effect transistor (TFET). 2D layered semiconductors have the ability to alleviate several of the scattering problems mention earlier due to their pristine surface and weak inter layer coupling. However, being an atomically thin material, their behaviour is highly dependent on the nature of the dielectric environment such as nature of oxide layer on which it is exfoliated, on the number of layers as dielectric constant of TMD materials varies sharply with layers and is anisotropic [33]. Charge scattering and mobility is shown to depend heavily on the interplay between impurity concentration and native oxides due to dielectric screening [34, 35]. This requires a rigorous treatment of both the material and associated dielectric environment to get a good understanding on the behaviour of Urbach parameters for TMD materials.

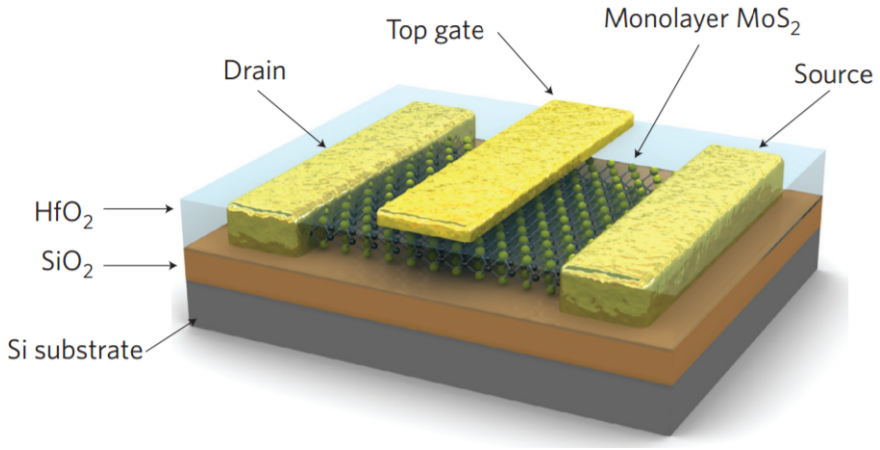

Fig. 1.4.: Successful synthesis of several 2D materials has led to demonstration of single and multilayer FETs. Source: Nature Nanotechnology [7]

This work has been split into 8 different chapters. Chapter 2 tries to address the problem of scaling of contacts and investigates contact resistance in pMOS Schottky contacts for Si and SiGe systems. This chapter specifically tries to answer the question of achievable contact resistances in pMOS devices through quantum transport approach. At the end of this chapter, guideline values for contact resistances are provided for several material and device parameters. Chapter 3 introduces modeling methodology for non-local scattering mechanisms, specifically focusing on three different scattering mechanisms - polar optical phonons, charged impurities and remote oxide phonons. Self-consistent Born approach to treat scattering is introduced with self-energy expressions being rigorously derived for bulk and confined devices. These scattering models are compared to analytical Fermi's golden rule which serves as a benchmark. This chapter sets the tone for discussions for other subsequent chapters. Chapter 4 is an extension of Chapter 3 and provides a numerical scheme to estimate non-locality in a system and ease the computational burden of such non-local scattering calculations. Chapter 5 tries to investigate the current-voltage characteristics of III-V GaSb/InAs nanowire TFET in the presence of such scattering mechanisms. Clear deviation from ideal simulation is observed and the observations are explained with high resolution results which resolve several degrees of freedom in the system such as energy, momentum, position and scattering orders. Chapter 6 provides a detailed discussion on one of the artifacts of non-local scattering - band tails and band gap narrowing. Both these parameters significantly affect performance of tunneling and optical devices. Several candidate materials are chosen and band tail/band gap narrowing parameters are extracted from rigorous non-local scattering calculations. For several simulation cases, results are compared against experimental data and are shown to be in good agreement. Finally, a parameter list based on a fitting function is generated to provide guideline values to researchers. Chapter 7 describes modeling band tails in 2D TMD materials and investigates the role of dielectric environment on band tail enhancement. 2D TMDs being atomically thin, have their performance affected significantly by several environmental effects such as oxides, phonons and impurities. This chapter tries to look into 3 candidate TMD materials

and the impact of band tails on these external parameters such as nature of oxide material, number of layers, doping and temperature dependence.

2. ATOMISTIC TIGHT-BINDING STUDY OF CONTACT RESISTIVITY IN SI/SIGE PMOS SCHOTTKY CONTACTS

2.1 Summary

The metal-semiconductor contact resistivity has started to play a critical role for the overall device performance as Si is reaching 10nm size ranges. The ITRS target predicts a requirement of $10^{-9}\Omega.cm^2$ by 2023 which has been a challenging target to achieve. This work explores the impact of doping concentration, Schottky barrier height, strain and SiGe mole fraction on the resistivity of Si/SiGe PMOS contacts with 20-band atomistic tight binding quantum transport simulations. Commonly used simple effective mass approximation models are shown to overestimate the resistivity values. The predicted model results are compared with experimental data and the device parameters needed to achieve $10^{-9}\Omega.cm^2$ are identified.

2.2 Motivation

The metal-semiconductor contact resistance poses a critical challenge for continued MOSFET scaling. With shrinking device area, the parasitic source/drain resistance increases unless the metal-semiconductor contact resistivity, ρ_{c} is designed to decrease proportionately [8]. The ITRS has set a target for ρ_{c} as $10^{-9}\ \Omega.cm^2$ to meet both the scaling and performance requirements for logic devices by 2023 [36]. To meet that scaling requirement, it is imperative to evaluate the effect of different device parameters such as doping concentration ($\mathrm{N_d}$), Schottky barrier height (ϕ_{B}), semiconductor material and strain on ρ_{c}. This problem of metal-semiconductor interfaces is typically studied using the Wentzel-Kramers-Brillouin (WKB) approximation which is fundamentally only valid for barrier potentials that vary slowly compared to the electron wavelength [37]. As device scales

approach a few nanometers, material and electronic properties vary on an atomistic level rather than a mesoscopic length-scale. Hence, this work employs a quantum transport approach to investigate metal-semiconductor junctions.

There have been studies based on quantum transport and mode counting approaches. For instance, in Ref. [38] an intrinsic lower limit of the contact resistivity was found using full band tight binding (TB) and density functional theory (DFT) calculations. Transport studies using the non-equilibrium Green's function (NEGF) method have been performed by [39] with an effective mass (EM) model. Refs. [40] and [41] use NEGF along with DFT on realistic silicide-silicon contacts and show an increase in contact resistance due to valley filtering in metals. The published results available so far discuss electron transport across a metal-semiconductor interface but have, to our best knowledge, not considered a rigorous treatment of hole transport.

Since the CMOS process depends both on electron and hole transport, it is critical but very challenging to study the hole transport as well. The hole bandstructure is non-parabolic and highly anisotropic such that EM approaches are even less applicable in general. A 20-band tight binding approach is taken here to represent the hole bandstructure accurately. SiGe/Ge based finfets and nanowires have been demonstrated and considered to be possible options for continued scaling of transistors (see refs. [42], [3] and [43]). Hence, the focus of this work is to identify with atomistic tight binding simulations for Si/SiGe PMOS metal-semiconductor contacts device parameters that can either meet or even supersede the ITRS requirements.

This work is composed of 3 sections. Section II describes the simulation approach used to model these metal-semiconductor junctions. Section III describes the simulation results as a function of different device parameters and Section III provides a summary and conclusion.

2.3 Simulation Approach

Ballistic quantum transport across Schottky contacts is modeled with the Quantum Transmitting Boundary Method (QTBM) of the nanoelectronic modeling tool, NEMO5 [44]. A 20 band sp3d5s* empirical tight binding basis (TB) with spin-orbit coupling is chosen to represent the hole bandstructure [45]. Figure 2.1 shows the bandstructure of Si plotted along high symmetry points. The metal is modeled by extrapolating the semiconductor structure into the leads and by shifting the valence bands up by a potential offset to mimic the density of states (DoS) of the corresponding metal around the Fermi level [46]. NiSi is chosen as the corresponding metal and the potential offset of 0.5eV is applied to the semiconductor by matching the DoS of NiSi at Fermi level obtained from [47]. Figure 2.2 illustrates a schematic of the typical device valence bandedge profiles along with the atomic structure of the device considered in this work. The device is periodic in y and z directions and is treated with open boundary conditions in the x direction. ϕ_{SBH} corresponds to the Schottky barrier height set in the simulation and ϕ_{offset} corresponds to the valence band offset of 0.5eV mentioned above. This approach does not capture valley filtering effects due to the metal-semiconductor contacts but does provide us with a best estimate of resistivity values [41]. Convergence with respect to the momentum resolution was achieved with a 20×20 momentum-grid in the two periodic directions. For charge self-consistency, the QTBM equations are solved iteratively with the Poisson equation until convergence is achieved. The $Si_{1-x}Ge_x$ alloy is modeled within the Virtual Crystal Approximation (VCA) [48]. Strain effects in TB are captured with the model of [49]. The resistivity is computed by simulating transport at low bias ($10\mathrm{mV}$) and extracting it from Landauer's expression [50]

$$\frac{1}{\rho_c} = \frac{2q^2}{h} \int_{-\infty}^{\infty} T(E) \left(-\frac{\partial f}{\partial E} \right) dE \tag{2.1}$$

For the parameter space assessments, first a center parameter point that represents a conventional p-type Si Schottky contact is chosen. Then, the respective parameter is varied around that center point. Table I shows these parameter centers and the respective variation

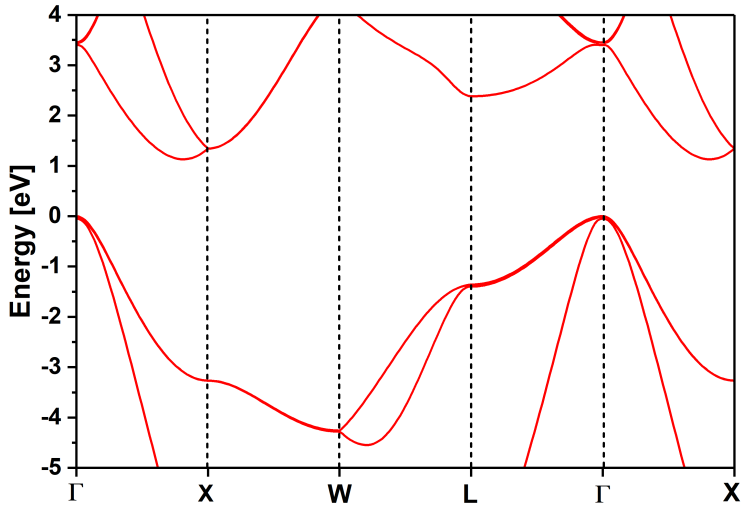

Fig. 2.1.: Plot of Si bandstructure along high symmetry points obtained from 20 band sp3d5s* tight- binding approach with spin-orbit coupling.

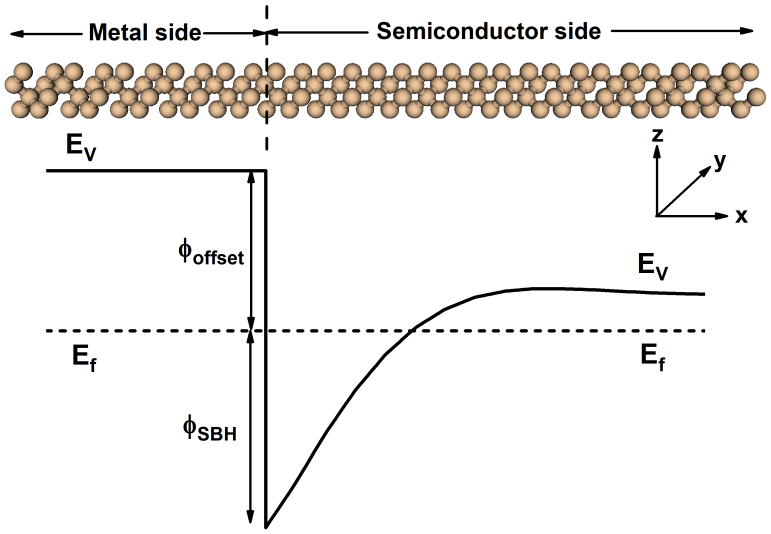

Fig. 2.2.: Schematic of a atomic structure of device with typical valence band edge profile. ϕ_{SBH} corresponds to the Schottky barrier height at the metal-semiconductor interface and ϕ_{offset} represents the valence band offset that is added to mimic the metal density of states around the Fermi level.

Parameter	Center Point Value	Parameter Variation
N_D	$2 \times 10^{20} cm^{-3}$	$0.5 - 4 \times 10^{20} cm^{-3}$
ϕ_{SBH}	0.35 eV	0.2 eV - 0.8 eV
Crystal direction	[100]	[110] and [111]
$Si_{(1-x)}Ge_x$	$x = 0$	$x = 0$ to $x = 0.5$
Strain	No strain	-1.5% to 1.5%

Table 2.1.: Considered device parameters along with their center point values and variation ranges.

ranges. For the Ge mole fraction calculations, barrier heights are correspondingly lowered with increasing Ge mole fraction values according to [51]. The comparison against effective mass simulations are done by simulating multi-valley effective mass tunneling model as prescribed by [52]. Transport is in the X direction with Y and Z being transverse periodic directions. Table 2.1 shows the center case parameters and the range over which each one of them is varied.

2.4 Simulation Results

2.4.1 Variation with Schottky barrier height and doping concentration

Figures 2.3 and 2.4 show the valence band edge variation and hole density as a function of transport direction. For Schottky barrier height variations, doping is kept constant at $2 \times 10^{20} cm^{-3}$ and for doping concentration variations, barrier height is kept fixed at 0.35eV. Since the doping concentations are above $10^{20} cm^{-3}$ for most of the simulations, hole transport happens in the degenerate situation (about 0.1eV below the band edge) and deep valence states start contributing to the transport process. To benchmark the simu-

lations, contact resistivities are plotted against barrier heights and doping concentrations as shown in Fig. 2.5 and compared against experimental data obtained from [53]. The comparison against two sets of experimental curves for NiSi-Si and PtSi-Si contacts shows excellent agreement with the expected resistivity values over a wide doping range providing confidence in the approach. Variations with barrier height and doping suggest that barrier heights lower than 0.2eV and doping values higher than $3 \times 10^{20} cm^{-3}$ are required to achieve the ITRS target of $10^{-9} \Omega.cm^2$ limit.

A similar comparison is performed with an effective mass approximation model. The tunneling current and resistivity are calculated following [52] with a multi-band effective mass model. For effective mass calculations, the tunneling and transverse effective masses of $0.22 m_o$ are used in the calculations [54]. As shown in Fig. 2.6, contact resistivity values predicted with the effective mass model are consistently higher than those resulting from tight binding simulations. This is expected since the effective mass approach is based on the parabolic approximation and neglects non-parabolic effects inherently present in valence bands. This leads to underestimation of conducting modes across the interface and a higher resistivity. The difference is particularly evident for higher doping concentrations where deep lying valence states with significant non-parabolicity start contributing to tunneling through the barrier.

2.4.2 Variation with crystal orientation

Transport along the crystal directions [100], [110] and [111] are the experimentally most relevant situations. Note that tight binding based simulations automatically capture changes in the hole effective masses with direction variation. Figure 2.7 shows the contact resistivity values for these 3 different directions as a function of the doping concentration. Transport along [111] and [110] consistently shows lower contact resistivity compared to transport in [100] direction.

In effective mass approximation, tunneling current is given by the expression

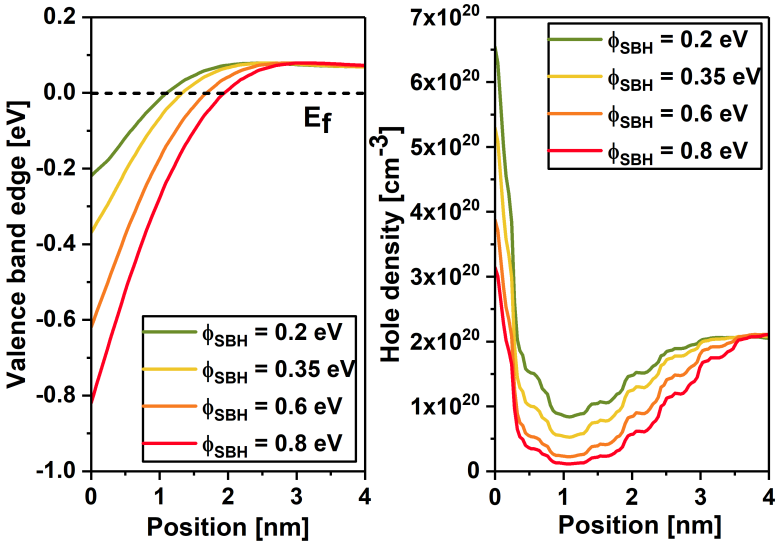

Fig. 2.3.: Position resolved valence band edges (left) and hole densities (right) as a function of the Schottky barrier height.

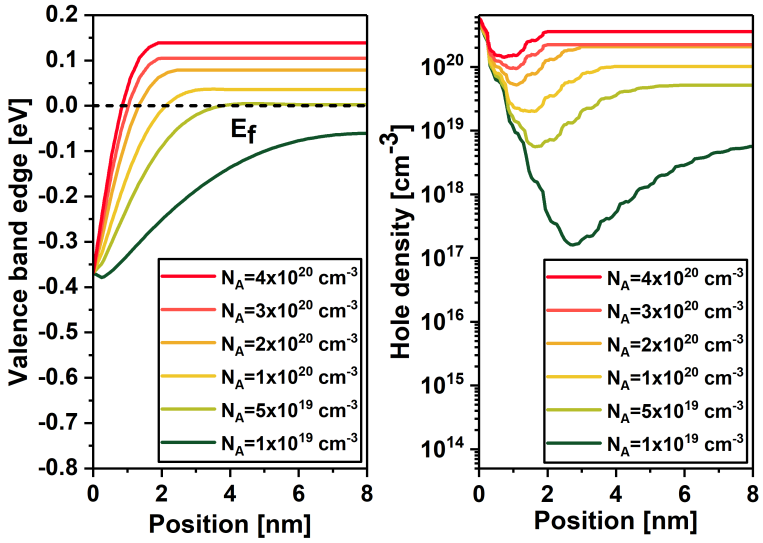

Fig. 2.4.: Position resolved valence band edges (left) and hole densities (right) as a function of doping concentration.

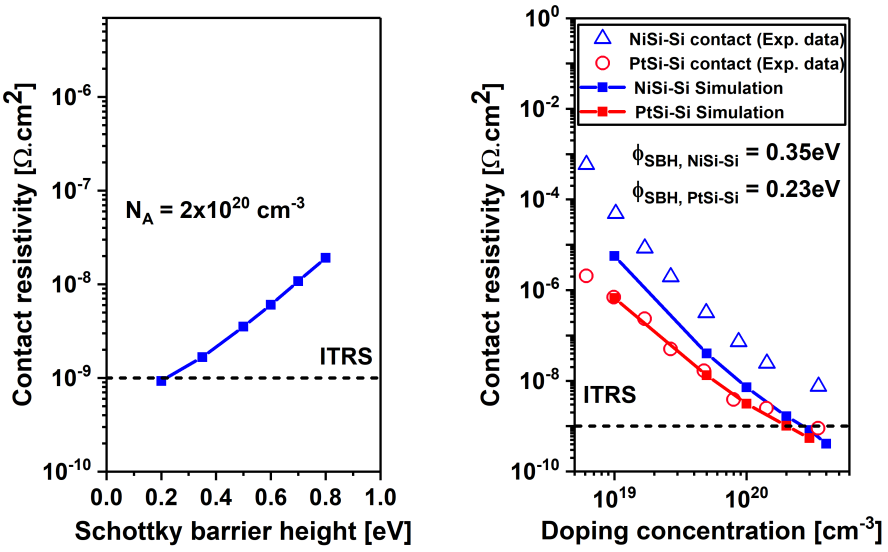

Fig. 2.5.: (a) Resistivity as a function of Schottky barrier height for a doping concentration of $2\times10^{20}cm^{-3}$. The ITRS limit (dashed line) is attained for barrier heights less than 0.2eV. (b) Resistivity as a function of doping concentration for ϕ_{SBH} = 0.35eV (NiSi-Si) and ϕ_{SBH} = 0.23eV (PtSi-Si). The ITRS limit (dashed line) is attained for doping values higher than $3 \times 10^{20}cm^{-3}$. Tight binding simulation results are compared against experimental data (symbols) [53] for NiSi-Si and PtSi-Si contacts.

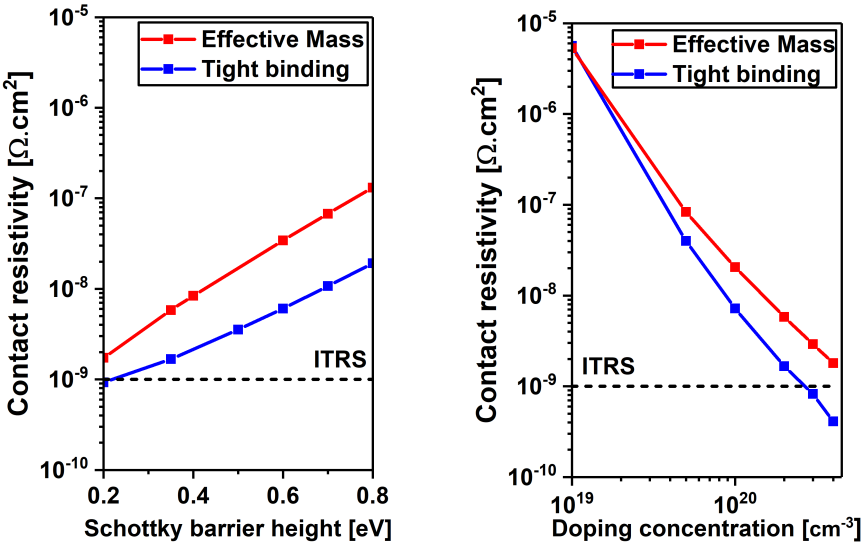

(a) (b)

Fig. 2.6.: (a) Comparison of contact resistivity predicted with effective mass and 10-band tight binding calculations for (a) a doping concentration of $2 \times 10^{20} cm^{-3}$ and (b) a barrier height of 0.35eV. The effective mass calculations overestimate the resistivity significantly. Deviations increase for higher doping values where the parabolic band assumption increasingly fails.

$$\rho_c \propto \frac{1}{\sqrt{m_y m_z}} exp\left(\frac{2\phi_{SBH}}{\hbar}\sqrt{\frac{\epsilon_s m_x^*}{N_D}}\right) \tag{2.2}$$

The smaller the transport effective mass and larger the transverse effective masses, the smaller will be the resistivity. However, hole transport cannot be analyzed with such a simplified model due to the non-parabolicity of the bands. Variation with crystal orientation can be better understood by looking at contour plots of velocities of heavy hole and light hole bands for each direction. Figure 2.8 shows the velocity contour plot for heavy and light hole bands in [001], [110] and [111] directions along the transverse momentum directions. These plots are obtained by taking a constant energy surface for the heavy/light hole band and finding set of transverse ky and kz points corresponding to that particular energy. For each of the transverse ky and kz points, velocity in the transport direction is obtained by evaluating

$$v_x = \frac{1}{\hbar}\frac{\partial E}{\partial k_x} \tag{2.3}$$

Contours plots of velocity are obtained over an energy range $E_f - 3k_BT$ to $E_f + 3k_BT$. These plots provide two-fold information - number of current carrying modes and velocity of each of those modes. The extent of spread of ky and kz points determine the number of current carrying modes at a particular energy and the contour determines the velocity at which the modes travel. The faster the velocity, the lower the effective mass and hence, higher the transmission.

In Fig. 2.8, [001] and [110] directions have most of the velocity contributions coming from light hole bands. Heavy hole bands have velocities which are twice as small as the light hole bands for all energies within the Fermi window. However, in the [111] case, velocities of heavy hole band are comparable to that of the light hole band and also contribute significant number of modes which results in smaller resistivity values compared to the other two directions.

Figure 2.9 shows the energy resolved current density as a function of energy. At the Fermi energy, [111] and [110] transport offer higher current densities than the [100] case.

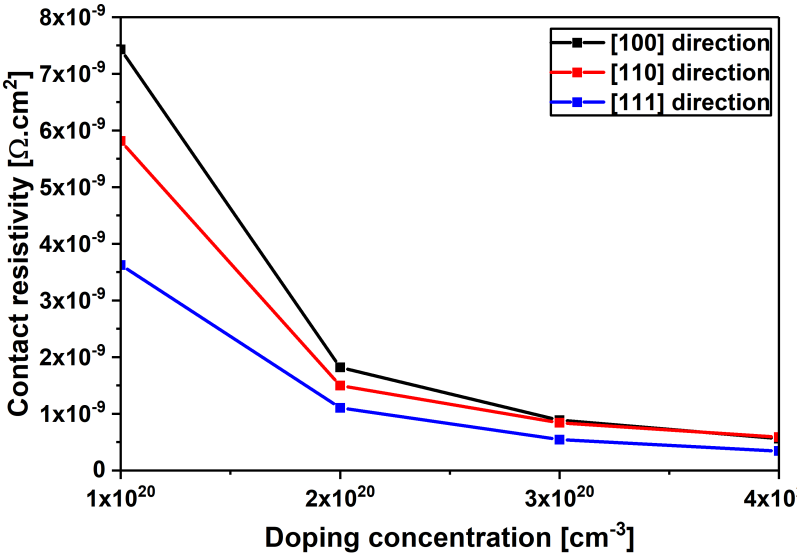

Fig. 2.7.: Contact resistivity as a function of doping for transport along [100], [110] and [111] crystal direction. Transport along [111] offers the lowest resistivity due to the smaller light hole effective mass and higher transverse density of states.

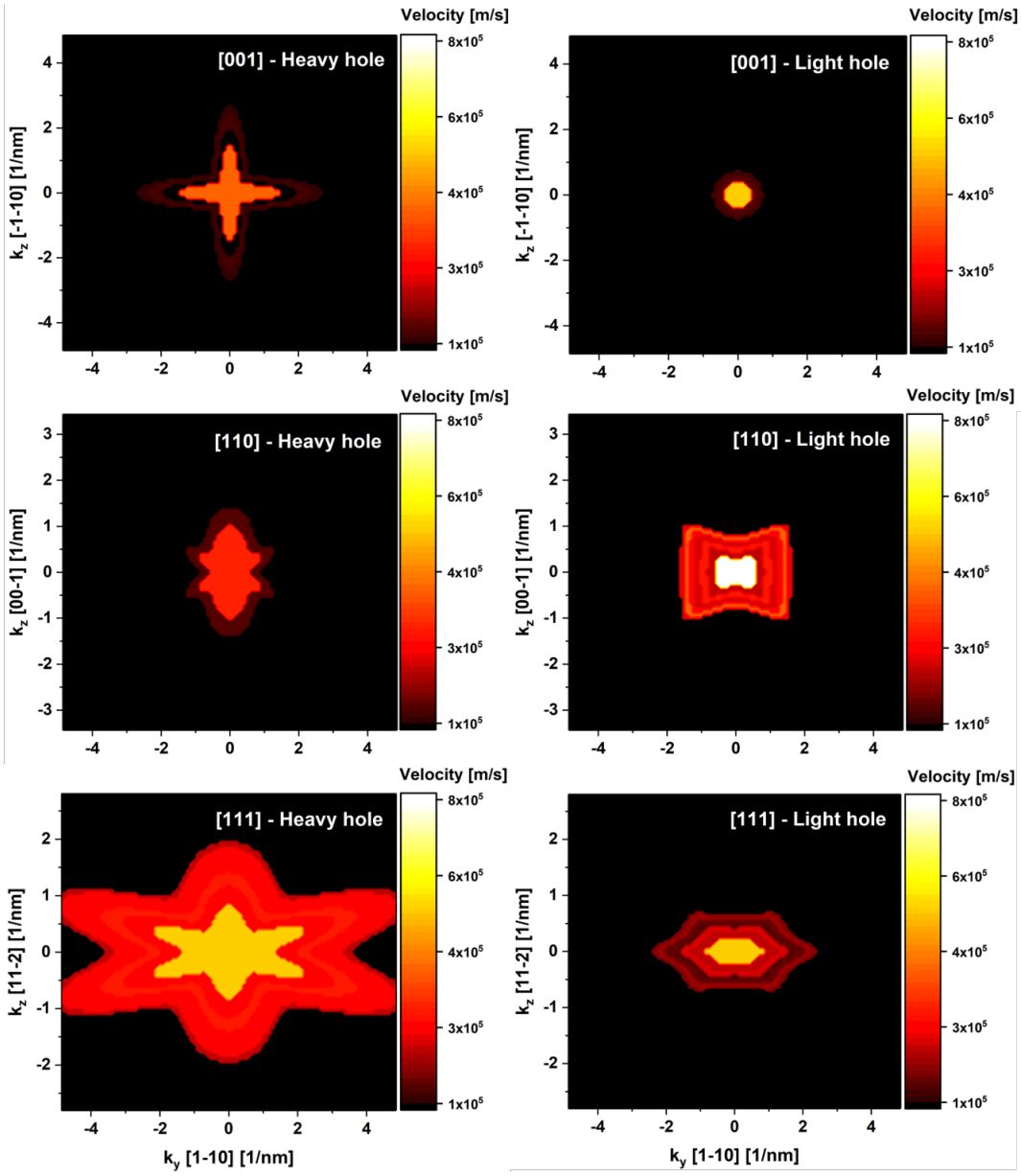

Fig. 2.8.: Contour plots of velocities of the heavy hole band and light hole band in the transport direction plotted as a function of transverse momentum points for [001], [110] and [111] transport directions over the energy range $[E_f - 3k_bT, E_f + 3k_bT]$

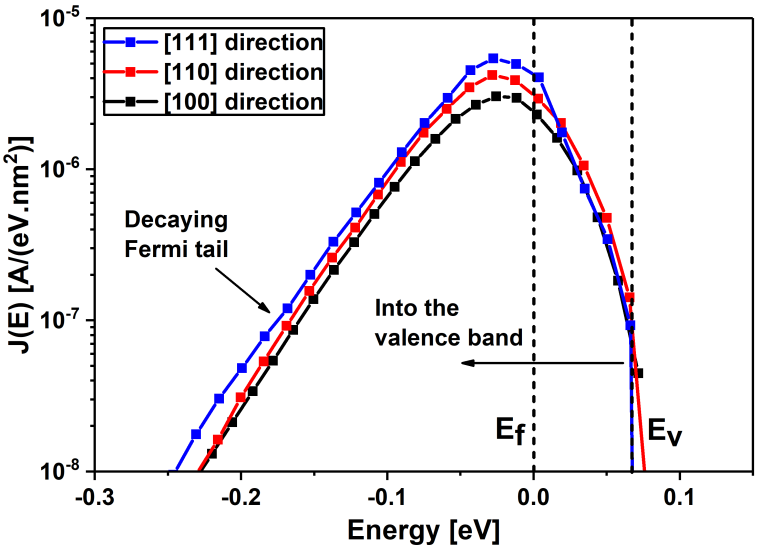

Fig. 2.9.: Energy resolved current density for transport along [100], [110] and [111] crystal direction. The [111] direction yields a larger current for the same applied bias voltage due to smaller light hole effective mass and larger spread of transmission across in-plane momentum space.

2.4.3 Variation with Ge mole fraction

The silicide contact technology based on NiSiGe/SiGe, PtSiGe/SiGe for SiGe devices have demonstrated lower contact resistivity compared to typical values for the Si technology [55], [56], [51]. Due to the decreasing band gap of $Si_{1-x}Ge_x$ alloys with increasing mole fraction, the barrier height reduces leading to a decrease in contact resistivity. Lower effective masses of $Si_{1-x}Ge_x$ lower the resistivity values further. To model $Si_{1-x}Ge_x$ devices, the virtual crystal approximation (VCA) is used where a virtual atom is constructed that carries properties of both Si and Ge weighed by the mole fraction. The Hamiltonian elements of $Si_{1-x}Ge_x$ read as follows

$$H_{Si_{(1-x)}Ge_x} = (1-x)H_{si} + xH_{Ge} \tag{2.4}$$

Based on this approach, $Si_{1-x}Ge_x$ is simulated with mole fractions varying from $x = 0$ to $x = 0.5$. Figure 2.10 shows the contact resistivity as a function of the Ge mole fraction for different doping concentrations. Due to the combined effect of lower barrier heights and tunneling effective masses, the contact resistivity is well below the $10^{-9}\Omega.cm^2$ limit even with nominal doping values $2 - 3 \times 10^{20} cm^{-3}$. These doping values are readily achievable in modern semiconductor processing [57], [58]. However, the above simulations neglect scattering processes such as alloy scattering and interface mismatch that can elevate the achievable resistivity values. The presented ballistic simulations yield the best possible resistivity values.

2.4.4 Variation with strain

The impact of tensile and compressive strain is considered by explicitly changing atom positions and by including the effect of strain into the electronic Hamiltonian following [49]. Conduction band effective masses (longitudinal and transverse) show a monotonic behaviour with compressive and tensile strain leading to an decrease in resistivity with compressive strain and increase with tensile strain [54]. In contrast, due to the inherent non-parabolicity of bands, behaviour of heavy, light and split-off bands are non-

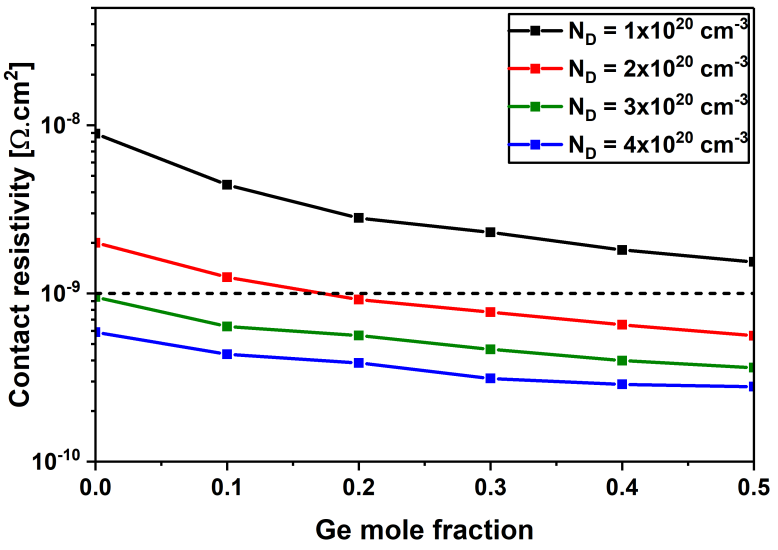

Fig. 2.10.: Contact resistivity as a function of Ge mole fraction for doping concentrations from $1 \times 10^{20} cm^{-3}$ to $4 \times 10^{20} cm^{-3}$

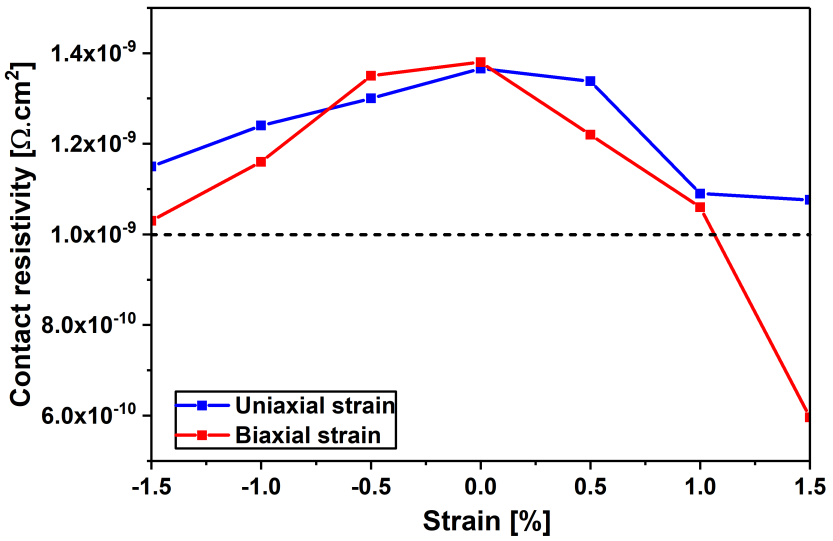

Fig. 2.11.: Contact resistivity as a function of uniaxial and biaxial strain.

monotonic with strain. Out-of-plane LH effective mass increases with compressive strain and decreases with tensile strain. SO effective mass, on the other hand, decreases with compressive strain and decreases with tensile strain. This results in a cumulative behavior where resistivity decreases in both compressive and tensile strain directions [54]. A similar effect of a non-monotonic behaviour is observed with contact resistivity that decreases both with compressive and tensile strain as shown in Fig. 2.11. Overall, the resistivity is minimal with tensile strain. The resistivity can decrease by a factor of 2 within the experimentally available strain range.

The simulation results can be summarized into a guideline for optimal barrier heights and doping concentrations to achieve particular resistivity targets. Figure 2.12 shows several constant resistivity contours as a function of barrier height and doping concentration. Resistivity contour plots are provided from $\rho = 1 \times 10^{-8} \Omega.cm^2$ to $\rho = 1 \times 10^{-10} \Omega.cm^2$.

2.5 Conclusion

In this work, the impact of Si/SiGe PMOS metal-semiconductor contact parameters on the contact resistivity is calculated within the atomistic tight binding quantum transport

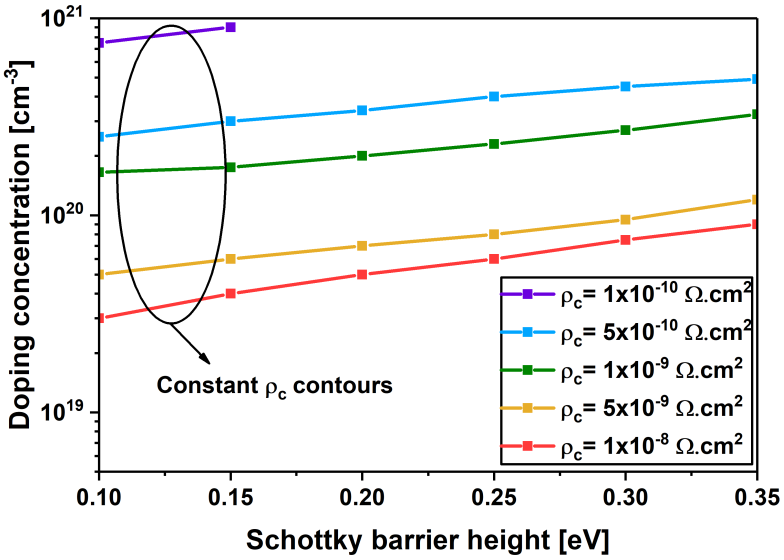

Fig. 2.12.: Constant resistivity contour lines as a function of doping concentration and barrier height offer a guideline on optimal barrier heights and doping values for specific resistivity values.

model of NEMO5. Doping concentrations and barrier heights are identified as two key design parameters for the contact resistivity. Comparisons against multi-band effective mass approaches show that effective mass resistivities are higher than the tight binding counterparts due to the parabolic approximation. Effective mass approaches increasingly deviate from atomistic ones with higher doping concentrations. Transport along the [111] crystal direction offers lower resistivity in comparison to [100] and [110] directions. This is due to comparable velocities of heavy and light hole bands and larger number of current carrying modes in [111] direciton. SiGe contact resistivities are significantly lower than the Si counterpart and can sustain future resistivity scaling challenges. Tensile strain offers maximum benefit in resistivity reduction. Constant resistivity contours are extracted from the simulations. These are meant as design guidelines for optimal barrier heights and doping concentrations for specific target resistivity values.

3. MODELING NON-LOCAL SCATTERING MECHANISMS

3.1 Summary

In this chapter, modeling and simulation approaches for three non-local scattering mechanisms, namely - polar optical phonon scattering, charged impurity scattering and remote phonon scattering are discussed in detail. Important aspects of each scattering mechanism are highlighted and expressions for scattering self-energies derived within the Non-equilibrium Green's function (NEGF) and self-consistent Born approximation approach. Scattering self-energies are validated by comparing them either with scattering rates obtained through Fermi's golden rule approach or by comparing experimental mobility values. These scattering self-energies will later form an important part of discussion for subsequent chapters where they will applied to relevant problems.

3.2 Non-equilibrium Green's function and self-consistent Born approximation

Non-equilibrium Green's function (NEGF) approach is widely accepted as the most consistent approach to treat electronic, thermal and optoelectronic transport in nanoscale devices [59], [60], [61], [62], [63] and [64]. It has been widely applied in modeling transistors [65], [66], [67], resonant-tunneling devices [68], metal-semiconductor contacts [69], [41], phonon transport across interfaces [70], GaN
InGaN light-emitting diodes [21] with quantitative agreements with experimental data.

This is attributed to the ability of NEGF to consistently treat quantum mechanical effects such as confinement, tunneling, interference effects and incoherent scattering on an equal footing. NEGF approach involves solving the retarded and lesser Green's function that correspond to the density of states and density in the device respectively. Injection and extraction of carriers are modeled with self-energies which account for the open boundary

nature of the problem. One of the important aspects of NEGF is the clear distinction between the active device and the reservoirs. Both physical (source and drain regions) and conceptual (scattering mechanisms) reservoirs are modeled through self-energies.

The ballistic retarded and lesser Green's function are solved as follows.

$$\left(E - H - \Sigma^R_{source} - \Sigma^R_{drain}\right) G^R = I \tag{3.1}$$

$$G^< = G^R \left(\Sigma^<_{source} + \Sigma^<_{drain}\right) G^{R\dagger} \tag{3.2}$$

where E is the energy of the incoming particle, H is the device Hamiltonian, G^R and $G^<$ are the retarded and lesser Green's function, Σ^R and $\Sigma^<$ are retarded and lesser self-energies. Ballistic NEGF approach corresponds to the ideal transport situation where particles are transported from source to drain coherently. There is no energy or momentum relaxation during the transport process. In reality, particles encounter various scattering mechanisms during the transport process such as interaction with phonons, neutral and charged impurities, alloy disorder, surface roughness, remote phonons and photons and such scattering effects need to be captured consistently to provide a quantitative prediction of device/material properties.

There are several approaches to treat scattering in NEGF. The simplest approach involves adding a constant, energy independent dephasing/damping factor $i\eta$ to the Green's function. This approach assumes that there is a constant background scattering breaking the coherent mechanism. However, special care needs to be taken in calibrating the $i\eta$ value to the corresponding scattering mechanisms expected in the device and ensuring that the current throughout the device is conserved which is not guaranteed. Current conservation needs to be enforced by coupling NEGF to a semi-classical models such as drift-diffusion/recombination where experimentally known values for mobility/recombination rates are used. There have been several works in literature that employ this approach to treat scattering [67], [71], [21]. However, this approach cannot consistently include inelastic scattering mechanisms such as phonon scattering and as mentioned before needs careful calibration for each specific device under consideration.

Other approaches include Büttiker probes where artificial probes/scattering centers are setup in the device that act as reservoirs for energy and momentum relaxation [72]. Each reservoir is characterized by a $i\eta$ which provides dephasing to the incoming and outgoing electrons. Current throughout the device is conserved by ensuring that the sum of current entering/exiting a probe is always zero. This allows for different flavours of scattering where one can have momentum relaxation, energy relaxation or elastic scattering. It has been successfully applied to transistors and phonon transport problems [73], [74]. However, the constraint again is the fact that the $i\eta$ needs calibration against existing scattering rate values which are usually equilibrium values. For confined devices such as ultra-thin body and nanowires where scattering can be dimension dependent, an additional calibration might have to be undertaken for specific geometries.

This brings us to the Self-consistent Born approximation (SCBA) approach to study scattering that will form a major portion of subsequent discussions. SCBA approach is based on representing interactions/scattering through scattering self-energies which are expansions of the Green's function. Since the SCBA is inherently a Green's function approach, it allows one to easily take into account and calculate nonequilibrium distribution functions of electrons and the surrounding environment. Inelastic scattering, appropriate energy and momentum relaxation rates and dependence of scattering on confinement is automatically included. SCBA involves defining a scattering self-energy (representative of corresponding scattering mechanism) that can be represented, in the most general manner as

$$\Sigma^R_{scatt} = G^R D^R + G^R D^< + G^< D^R \tag{3.3}$$

$$\Sigma^<_{scatt} = G^< D^< \tag{3.4}$$

where D^R and $D^<$ correspond to the scattering propagators. For phonons, it corresponds to the phonon Green's function. The Green's function, on the other hand depend on the scattering self-energies through the expressions below

$$\left(E - H - \Sigma^R_{source} - \Sigma^R_{drain} - \Sigma^R_{scatt}\right) G^R = I \tag{3.5}$$

$$G^< = G^R \left(\Sigma^<_{source} + \Sigma^<_{drain} + \Sigma^<_{scatt}\right) G^{R\dagger} \tag{3.6}$$

Since the Green's function depends on the scattering self-energies and the self-energies on the Green's function, it requires a self-consistent loop that needs to be solved until the corresponding density, density of states and current converge upto the numerical tolerance criterion. Since it involves self-consistent iterations of matrices, there is an additional burden on compute time and memory.

Description of SCBA described above is for a fixed potential profile and once the SCBA approach has converged, the NEGF equations need to be coupled back to Poisson to solve charged density and electrostatic potential self-consistently. Fig.3.1 shows the flowchart of the simulation methodology. Physical quantities such as density of states, density, current density are extracted as follows.

$$DOS(r_i) = -\frac{i}{(2\pi)^N} \int dk_{||} \int \frac{dE}{2\pi} G^R_{r_i,r_i}(E, k_{||}) \tag{3.7}$$

$$n(r_i) = -\frac{i}{(2\pi)^N} \int dk_{||} \int \frac{dE}{2\pi} G^<_{r_i,r_i}(E, k_{||}) \tag{3.8}$$

$$J_{N\to N+1} = -\frac{e}{\hbar} \frac{1}{(2\pi)^N} \int dk_{||} \int \frac{dE}{2\pi} tr\left(t_{N+1,N} G^<_{N,N+1} - G^<_{N+1,N} t_{N,N+1}\right) \tag{3.9}$$

where $DOS(r_i)$ and $n(r_i)$ are the density of states and density at position r_i, $J_{N\to N+1}$ from one transporting semiconductor layer to another and $t_{N+1,N}$ is the interlayer coupling hamiltonian.

Next few sections will cover self-energy expressions and results for different scattering mechanisms.

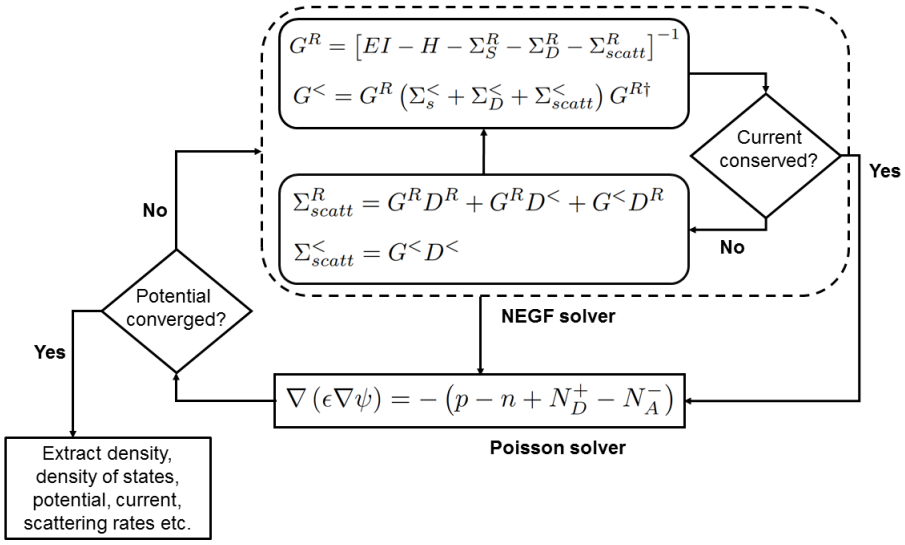

Fig. 3.1.: Flowchart showing the simulation procedure. NEGF equations are coupled with the Poisson solver and relevant physical quantities such as density, density of states, current, scattering rate are extracted when convergence is achieved.

3.3 Self-energies for scattering with polar optical phonons

In polar semiconductors, the electron-longitudinal optical (LO) phonon scattering is the dominant scattering mechanism [75], [76], [77]. This scattering is mediated by dipoles induced by optical vibration modes that interact with electrons. Due to the Coulombic nature of scattering, it is a long-ranged interaction. Starting from the general formula for the phonon scattering self-energy (assuming bulk equilibrium phonons)

$$\begin{aligned}\Sigma^{<}(\vec{x}_1,\vec{x}_2,E) = \frac{1}{(2\pi)^3}\int d\vec{q}\,|U_q|^2\, e^{i\vec{q}.(\vec{x_1}-\vec{x}_2)}[n_q G^{<}(\vec{x}_1,\vec{x}_2,E-\hbar\omega_q) \\ +(1+n_q)\,G^{<}(\vec{x}_1,\vec{x}_2,E+\hbar\omega_q)]\end{aligned} \tag{3.10}$$

The interaction potential for an electron that scatters optical phonon mediated dipoles is given by the ubiquitous Frohlich coupling

$$|U_q|^2 = e^2\frac{\hbar\omega_q}{2\epsilon_o}\left(\frac{1}{\epsilon_\infty}-\frac{1}{\epsilon_s}\right)\frac{q^2}{(q^2+\zeta^{-2})^2} \tag{3.11}$$

The static and dynamic dielectric constant are represented by ϵ_s and ϵ_∞ respectively. The phonon frequency and momentum are represented by $\hbar\omega_q$ and q respectively. Since maximal interaction is with longitudinal-optical (LO) phonons, the phonon frequency is assumed to be dispersionless and the frequency corresponds to the value at the Gamma point. Total screening is assumed to be the sum of screening from valence band electrons (ϵ_0), electronic (ζ) and phononic ($1/\epsilon_\infty - 1/\epsilon_s$). Electrostatic screening is calculated within the Lindhard formalism. Estimation of screening length will be discussed in detail at the end of this chapter.

Using Eqns.3.10 and 6.1, we can write the lesser self-energy as

$$\begin{aligned}\Sigma^{<}(\vec{x}_1,\vec{x}_2,E) = \frac{e^2}{(2\pi)^3}\left(\frac{1}{\epsilon_\infty}-\frac{1}{\epsilon_s}\right)\int d\vec{q}\frac{\hbar\omega_q}{2\epsilon_0}\frac{q^2 e^{i\vec{q}.(\vec{x}_1-\vec{x}_2)}}{\left(q^2+\zeta^{-2}\right)^2} \\ \times[n_q G^{<}(\vec{x}_1,\vec{x}_2,E-\hbar\omega_q)+(1+n_q)\,G^{<}(\vec{x}_1,\vec{x}_2,E+\hbar\omega_q)]\end{aligned} \tag{3.12}$$

Based on the above assumptions, scattering self-energies are derived specifically for each degree of confinement (bulk/quasi1D system (1D), ultra-thin body system (2D) and nanowire (3D) system). Principal value integrals presented in the equations below are

neglected as they are computationally intensive to calculate and their contribution towards scattering is negligible [78].

3.3.1 Self-energy expressions for bulk/quasi1D system

Deriving self-energy from above expressions requires splitting the scattering potential into momentum components that are parallel and perpendicular to the transport direction as follows

$$|U_q|^2 = e^2 \frac{\hbar\omega_q}{2\epsilon_o}\left(\frac{1}{\epsilon_\infty} - \frac{1}{\epsilon_s}\right)\frac{q_{||}^2 + q_z^2}{\left(q_{||}^2 + q_z^2 + \zeta^{-2}\right)^2} \tag{3.13}$$

Self-energy for bulk can be expressed as

$$\begin{aligned}\Sigma^{<}\left(z_1, z_2, \vec{k}_{||}, , E\right) = \frac{e^2}{(2\pi)^3}\frac{\hbar\omega_q}{2\epsilon_0}\left(\frac{1}{\epsilon_\infty} - \frac{1}{\epsilon_s}\right)\int dq_z \int d\vec{l}_{||}\frac{q_{||}^2 + q_z^2}{\left(q_{||}^2 + q_z^2 + \zeta^{-2}\right)^2}e^{iq_z\cdot(z_1 - z_2)} \\ \times\left[n_q G^{<}\left(z_1, z_2, \vec{l}_{||}, E - \hbar\omega_q\right) + (1 + n_q)\, G^{<}\left(z_1, z_2, \vec{l}_{||}, E + \hbar\omega_q\right)\right]\end{aligned} \tag{3.14}$$

where $k_{||}$ is the momentum for which scattering self-energy is calculated. $l_{||}$ is the set of all momentums that is integrated with respect to the scattering potential and Green's function and $q_{||} = \left|\vec{k}_{||} - \vec{l}_{||}\right| = \sqrt{k_{||}^2 + l_{||}^2 - 2k_{||}l_{||}cos\theta}$ is the transfered momentum.

The scattering integral can be solved separately by performing the integration over q_z. We should note that the actual integration range of q_z goes only from $-\pi/a$ to $-\pi/a$ which is extent of the electron's Brillouin zone. However, by extending the integration range from $-\infty$ to $+\infty$, the integral can be solved analytically and it simplifies much of the numerical complications. Furthermore, such an approximation is justified due to the fact that the scattering potential decays with larger q_z values. Scattering integral can be written as

$$I(q_{||}, z_1, z_2) = \int_{-\infty}^{\infty} dq_z \frac{q_{||}^2 + q_z^2}{\left(q_{||}^2 + q_z^2 + \zeta^{-2}\right)^2}e^{iq_z(z_1 - z_2)} \tag{3.15}$$

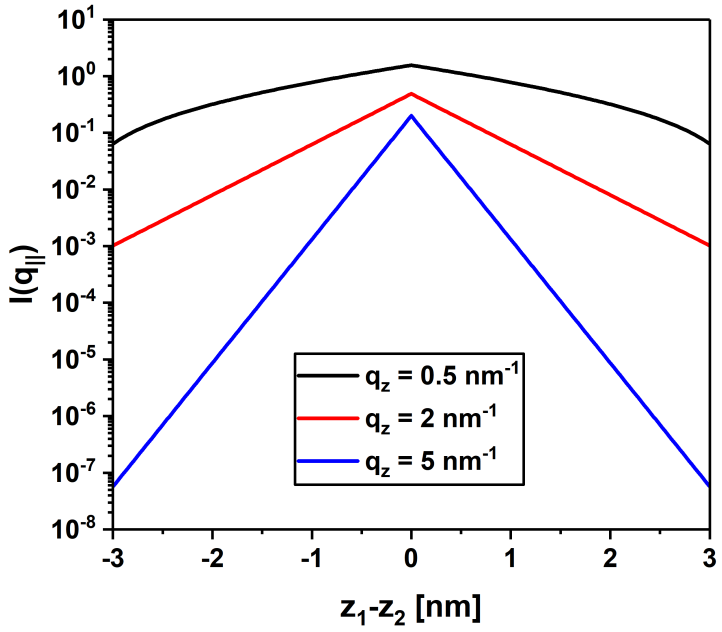

Fig. 3.2.: Contour plot of scattering kernel as a function of distance for different values of q_z. Value of scattering kernel decreases drastically with q_z justifying the integration $(0, \infty)$.

The above integral can be solved using complex contour technique (elaborated in Appendix) to get

$$I(q_{||}, z_1, z_2) = \frac{\pi exp\left(-\sqrt{q_{||}^2 + \zeta^{-2}}\,|z_1 - z_2|\right)}{\sqrt{q_{||}^2 + \zeta^{-2}}} \left(1 - \frac{\zeta^{-2}\,|z_1 - z_2|}{2\sqrt{q_{||}^2 + \zeta^{-2}}} - \frac{\zeta^{-2}}{2\left(q_{||}^2 + \zeta^{-2}\right)}\right) \tag{3.16}$$

Scattering kernel is plotted as a function of distance for different values of q_z as shown in Fig 3.2. Also, the integrated scattering kernel is plotted as a function of initial and final momentum values for local and non-local cases as shown in Figs 3.3 and 3.4. Both these figures highlight the anisotropic nature of scattering process where scattering is non-uniform across the momentum values unlike local scattering where it is equally distributed. Scattering strength is maximal at lower momentum values and decays with higher momentum values. With increasing non-locality, the strength of total scattering decreases as well.

This gives us following expressions for the lesser and retarded self-energies.

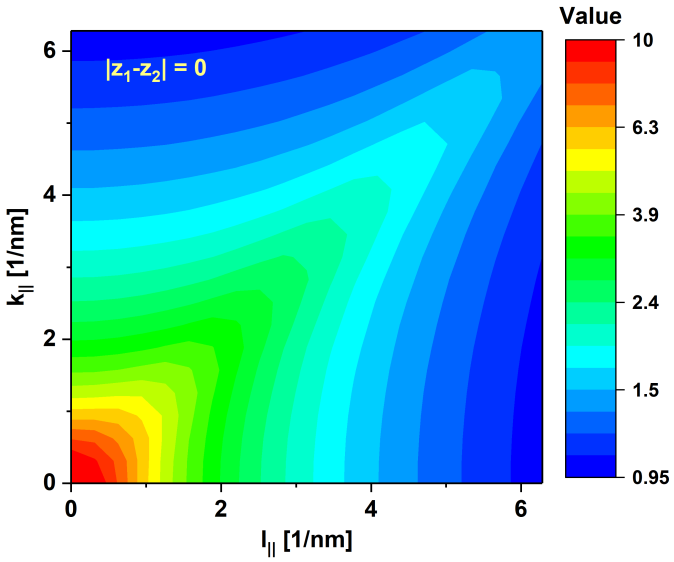

Fig. 3.3.: Contour plot of integrated scattering kernel as a function of momentum values $k_{||}$ and $l_{||}$ for screening length of 3 nm and non-local distance set to zero. Scattering is anisotropic and favours small momentum scattering.

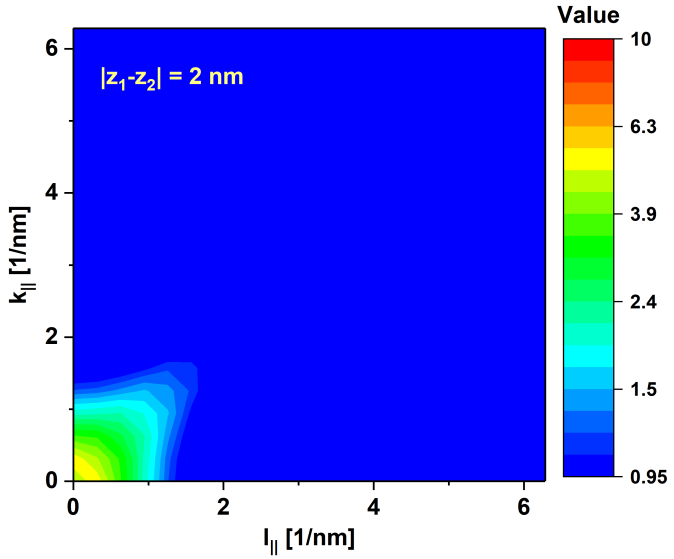

Fig. 3.4.: Contour plot of integrated scattering kernel as a function of momentum values $k_{||}$ and $l_{||}$ for screening length of 3 nm and non-local distance of 2 nm. Scattering in general decreases with increasing non-local distance.

$$\Sigma^{<}\left(z_1, z_2, k_{||}, E\right)$$
$$= \frac{e^2\pi}{(2\pi)^3}\left(\frac{1}{\epsilon_\infty}-\frac{1}{\epsilon_s}\right)\frac{\hbar\omega_o}{2\epsilon_o}\int d\vec{l_{||}}\frac{e^{-\sqrt{q_{||}^2+\zeta^{-2}}|z_1-z_2|}}{\sqrt{q_{||}^2+\zeta^{-2}}}\left(1-\frac{\zeta^{-2}\left|z_1-z_2\right|}{2\sqrt{q_{||}^2+\zeta^{-2}}}-\frac{\zeta^{-2}}{2\left(q^2+\zeta^{-2}\right)}\right)$$
$$\left[n_o G^{<}\left(z_1, z_2, l_{||}, E-E_o\right)+\left(n_o+1\right)G^{<}\left(z_1, z_2, l_{||}, E+E_o\right)\right] \tag{3.17}$$

$$\Sigma^{R}\left(z_1, z_2, k_{||}, E\right)$$
$$= \frac{e^2\pi}{(2\pi)^3}\left(\frac{1}{\epsilon_\infty}-\frac{1}{\epsilon_s}\right)\frac{\hbar\omega_o}{2\epsilon_o}\int d\vec{l_{||}}\frac{e^{-\sqrt{q_{||}^2+\zeta^{-2}}|z_1-z_2|}}{\sqrt{q_{||}^2+\zeta^{-2}}}\left(1-\frac{\zeta^{-2}\left|z_1-z_2\right|}{2\sqrt{q_{||}^2+\zeta^{-2}}}-\frac{\zeta^{-2}}{2\left(q^2+\zeta^{-2}\right)}\right)$$
$$\times\left[\left(n_o+1\right)G^{R}\left(z_1, z_2, l_{||}, E-E_o\right)+n_o G^{R}\left(z_1, z_2, l_{||}, E+E_o\right)+\frac{1}{2}G^{<}\left(z_1, z_2, l_{||}, E-E_o\right)\right.$$
$$\left.-\frac{1}{2}G^{<}\left(z_1, z_2, l_{||}, E-E_o\right)+i\int\frac{d\tilde{E}}{2\pi}G^{<}(z_1, z_2, l_{||}, \tilde{E})\left(Pr\frac{1}{E-\tilde{E}-E_o}-Pr\frac{1}{E-\tilde{E}+E_o}\right)\right] \tag{3.18}$$

3.3.2 Self-energy expressions for ultra-thin body system

We start the derivation with the general self-energy expression

$$\Sigma^{<}\left(\vec{x}_1, \vec{x}_2, E\right)=\frac{e^2}{\left(2\pi\right)^3}\left(\frac{1}{\epsilon_\infty}-\frac{1}{\epsilon_s}\right)\int d\vec{q}\frac{\hbar\omega_q}{2\epsilon_0}\frac{q^2 e^{i\vec{q}.(\vec{x}_1-\vec{x}_2)}}{\left(q^2+\zeta^{-2}\right)^2}$$
$$\times\left[n_q G^{<}\left(\vec{x}_1, \vec{x}_2, E-\hbar\omega_q\right)+\left(1+n_q\right)G^{<}\left(\vec{x}_1, \vec{x}_2, E+\hbar\omega_q\right)\right] \tag{3.19}$$

By transforming the self-energy and Green's function to a one-dimensional k-space, we get

$$\Sigma^{<}\left(\vec{x}_1, \vec{x}_2, k_{||}, E\right)=\frac{e^2}{(2\pi)^3}\left(\frac{1}{\epsilon_\infty}-\frac{1}{\epsilon_s}\right)\frac{\hbar\omega_q}{2\epsilon_o}\int d\vec{q}\int dl_{||}\frac{\left(q^2+l_{||}^2\right)e^{i\vec{q}.(\vec{x}_1-\vec{x}_2)}}{\left(q^2+l_{||}^2+\zeta^{-2}\right)^2}$$
$$\times\left[n_q G^{<}\left(\vec{x}_1, \vec{x}_2, k_{||}-l_{||}, E-\hbar\omega_q\right)+\left(1+n_q\right)G^{<}\left(\vec{x}_1, \vec{x}_2, k_{||}-l_{||}, E+\hbar\omega_q\right)\right] \tag{3.20}$$

where $k_{||}$ is the transverse momentum of self-energy term, $l_{||}$ is the set of all transverse momentum points of Green's function. Since the inner integral is a convolution of scattering

potential with Green's function, we can substitute $l_{||}$ with $k_{||} - l_{||}$ and convert the integral over $\vec{q}$ to cylindrical coordinates to give

$$\Sigma^{<}\left(\vec{x}_1, \vec{x}_2, k_{||}, E\right) = \frac{e^2}{(2\pi)^3}\left(\frac{1}{\epsilon_\infty} - \frac{1}{\epsilon_s}\right)\frac{\hbar\omega_q}{2\epsilon_o}\int_0^\infty dq \int_0^{2\pi} d\theta \int dl_{||} \frac{q\left(q^2 + (k_{||} - l_{||})^2\right) exp(iq\left|\vec{x}_1 - \vec{x}_2\right| cos\theta)}{\left(q^2 + (k-l)^2 + \zeta^{-2}\right)^2} \times \left[n_q G^{<}\left(\vec{x}_1, \vec{x}_2, l_{||}, E - \hbar\omega_q\right) + (1+n_q)\, G^{<}\left(\vec{x}_1, \vec{x}_2, l_{||}, E + \hbar\omega_q\right)\right] \tag{3.21}$$

The angular integral can be integrated to give

$$\int_0^{2\pi} d\theta exp(iq\left|\vec{x}_1 - \vec{x}_2\right| cos\theta) = 2\pi J_o\left(q\left|\vec{x}_1 - \vec{x}_2\right|\right) \tag{3.22}$$

where $J_o(x)$ is the J-Bessel function of 0th order. The momentum integral over q can now be written as

$$I(k_{||}, l_{||}, \vec{x}_1, \vec{x}_2) = \int_0^\infty dq \frac{q\left(q^2 + (k_{||} - l_{||})^2\right).2\pi J_o\left(q\left|\vec{x}_1 - \vec{x}_2\right|\right)}{\left(q^2 + (k_{||} - l_{||})^2 + \zeta^{-2}\right)^2}$$

The above integral can be solved analytically by using the following relation from Ref.

$$\int_0^\infty \frac{J_\nu(bx)x^{\nu+1}}{(x^2+a^2)^{\mu+1}} = \frac{a^{\nu-\mu}b^\mu}{2^\mu\Gamma(\mu+1)}K_{\nu-\mu}(ab)$$
$$for\ a > 0,\ b > 0,\ -1 < Re(\nu) < Re\left(2\mu + \frac{3}{2}\right)$$

where $K_{\nu-\mu}(x)$ is the K-Bessel function of order $\nu - \mu$. This gives us

$$I(k_{||}, l_{||}, \vec{x}_1, \vec{x}_2) = \begin{cases} \pi\left[\sqrt{\left(k_{||} - l_{||}\right)^2 + \zeta^{-2}}\left|\vec{x}_1 - \vec{x}_2\right| + \frac{\left(k_{||} - l_{||}\right)^2\left|\vec{x}_1 - \vec{x}_2\right|}{\sqrt{\left(k_{||} - l_{||}\right)^2 + \zeta^{-2}}}\right] K_1\left(\sqrt{\left(k_{||} - l_{||}\right)^2 + \zeta^{-2}}\left|\vec{x}_1 - \vec{x}_2\right|\right), \\ \qquad\qquad \left|\vec{x}_1 - \vec{x}_2\right| \neq 0 \\ \pi\left[1 + \frac{\left(k_{||} - l_{||}\right)^2}{\left(k_{||} - l_{||}\right)^2 + \zeta^{-2}}\right],\ \left|\vec{x}_1 - \vec{x}_2\right| = 0 \end{cases} \tag{3.23}$$

Scattering kernel is plotted as a function of distance for several momentum points as shown in Fig. 3.5. Scattering is quite non-local for small momentum points and becomes sharper and sharper as one moves to larger momentum points.

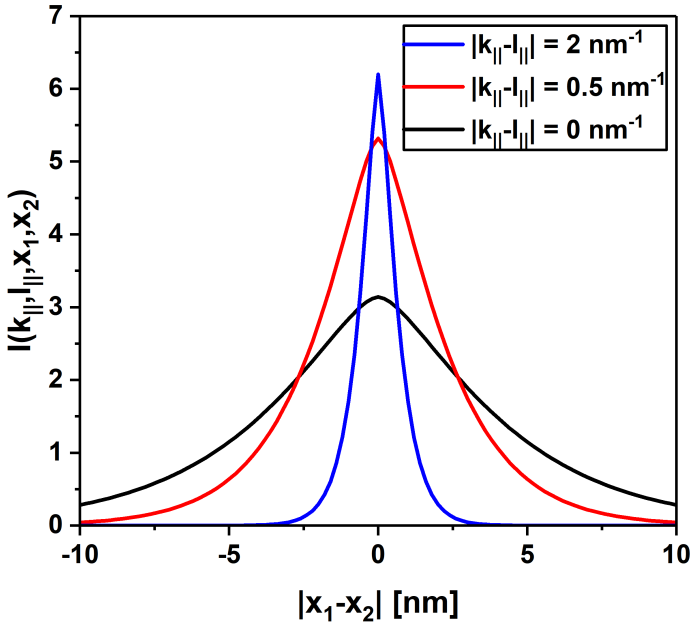

Fig. 3.5.: Plot of non-locality of scattering kernel for ultra-thin body polar optical phonon scattering for $q_z = 0nm^{-1},\ 0.5nm^{-1},\ 2nm^{-1}$ and screening length of 3nm. Scattering kernel becomes more and more local with increasing momentum values.

The lesser and retarded self-energy expressions for ultra-thin body polar optical phonon scattering can now be written as

$$\Sigma^{<}\left(\vec{x}_1,\vec{x}_2,k_{||},E\right)=\frac{e^2}{(2\pi)^3}\left(\frac{1}{\epsilon_\infty}-\frac{1}{\epsilon_s}\right)\frac{\hbar\omega_o}{2\epsilon_o}\int dl_{||}I(k_{||},l_{||},\vec{x}_1,\vec{x}_2) \times\left[n_oG^{<}\left(\vec{x}_1,\vec{x}_2,l_{||},E-E_o\right)+(1+n_q)\,G^{<}\left(\vec{x}_1,\vec{x}_2,l_{||},E+E_o\right)\right] \tag{3.24}$$

$$\Sigma^{R}\left(\vec{x}_1,\vec{x}_2,k_{||},E\right)=\frac{e^2}{(2\pi)^3}\left(\frac{1}{\epsilon_\infty}-\frac{1}{\epsilon_s}\right)\frac{\hbar\omega_o}{2\epsilon_o}\int dl_{||}I(k_{||},l_{||},\vec{x}_1,\vec{x}_2) \times\left[(1+n_o)G^{R}\left(\vec{x}_1,\vec{x}_2,l_{||},E-E_o\right)+n_oG^{R}\left(\vec{x}_1,\vec{x}_2,l_{||},E+E_o\right)+\frac{1}{2}G^{<}(\vec{x}_1,\vec{x}_2,l_{||},E-E_o) -\frac{1}{2}G^{<}(\vec{x}_1,\vec{x}_2,l_{||},E+E_o)+i\int\frac{d\tilde{E}}{2\pi}G^{<}\left(\vec{x}_1,\vec{x}_2,l_{||},\tilde{E}\right)\left(Pr\frac{1}{E-\tilde{E}-E_o}-Pr\frac{1}{E-\tilde{E}+E_o}\right)\right] \tag{3.25}$$

3.3.3 Self-energy expressions for nanowire system

Due to the lack of momentum space in a nanowire, the scattering potential needs to be integrated completely to get the scattering kernel. By transforming the scattering integral to spherical coordinates we get

$$\int d\vec{q}\frac{q^2e^{i\vec{q}.(\vec{x}_1-\vec{x}_2)}}{\left(q^2+\zeta^{-2}\right)^2}$$

$$=\int_0^{2\pi}d\phi\int_{-\pi/2}^{\pi/2}d\theta sin\theta\int_0^{\infty}dq\frac{q^4exp(iq\left|\vec{x}_1-\vec{x}_2\right|cos\theta)}{\left(q^2+\zeta^{-2}\right)^2}$$

$$=2\pi\int_0^{\infty}dq\int_{-1}^{1}dcos\theta\frac{q^4exp(iq\left|\vec{x}_1-\vec{x}_2\right|cos\theta)}{\left(q^2+\zeta^{-2}\right)^2}$$

$$=4\pi\int_0^{\infty}dq\frac{q^3}{\left(q^2+\zeta^{-2}\right)^2}\frac{sin\left(q\left|\vec{x}_1-\vec{x}_2\right|\right)}{\left|\vec{x}_1-\vec{x}_2\right|}$$

Now, we have two conditions for which we need to solve ($|\vec{x}_1-\vec{x}_2|=0$ and $|\vec{x}_1-\vec{x}_2|\neq 0$). Taking the case, $|\vec{x}_1-\vec{x}_2|=0$, we get

$$I(\vec{x}_1,\vec{x}_2)=4\pi\int_0^{\infty}dq\frac{q^4}{\left(q^2+\zeta^{-2}\right)^2}\lim_{|\vec{x}_1-\vec{x}_2|\to 0}\frac{sin\left(q\left|\vec{x}_1-\vec{x}_2\right|\right)}{q\left|\vec{x}_1-\vec{x}_2\right|}$$

$$= 4\pi \int_0^{\infty} dq \frac{q^4}{\left(q^2 + \zeta^{-2}\right)^2}$$

However, the integral from 0 to ∞ diverges and we are only interested in momentum values that are within the Brillouin zone. By changing the integration range to $(0, \pi/a)$ we get

$$\begin{aligned} I(\vec{x}_1, \vec{x}_2) &= 4\pi \int_0^{\pi/a} dq \frac{q^4}{\left(q^2 + \zeta^{-2}\right)^2} \\ &= \frac{4\pi^2}{a} \left[\frac{1}{2\left(\zeta^2 \left(\frac{\pi}{a}\right)^2 + 1\right)} - \frac{3a}{2\zeta\pi} tan^{-1}\left(\frac{\zeta\pi}{a}\right) + 1 \right] \end{aligned} \tag{3.26}$$

For $|\vec{x}_1 - \vec{x}_2| \neq 0$, we take the integration range upto ∞ since the integration can be solved analytically

$$\begin{aligned} I(\vec{x}_1, \vec{x}_2) &= 4\pi \int_0^{\infty} dq \frac{q^3}{\left(q^2 + \zeta^{-2}\right)^2} \frac{sin\left(q\left|\vec{x}_1 - \vec{x}_2\right|\right)}{\left|\vec{x}_1 - \vec{x}_2\right|} \\ = -\frac{\zeta^{-2}\pi^2}{\left|\vec{x}_1 - \vec{x}_2\right|} &\left[2\zeta \left(sinh\left(\left|\vec{x}_1 - \vec{x}_2\right|/\zeta\right) - cosh(\left|\vec{x}_1 - \vec{x}_2\right|/\zeta)\right)\right. \\ &\left. + \left|\vec{x}_1 - \vec{x}_2\right| \left(cosh(\left|\vec{x}_1 - \vec{x}_2\right|/\zeta) - sinh(\left|\vec{x}_1 - \vec{x}_2\right|/\zeta)\right)\right] \end{aligned} \tag{3.27}$$

The above integrals can be summarized as follows.

$$I(\vec{x}_1, \vec{x}_2) = \begin{cases} \dfrac{4\pi^2}{a} \left[\dfrac{1}{2\left(\zeta^2 \left(\frac{\pi}{a}\right)^2 + 1\right)} - \dfrac{3a}{2\zeta\pi} tan^{-1}\left(\dfrac{\zeta\pi}{a}\right) + 1 \right], & |\vec{x}_1 - \vec{x}_2| = 0 \\ \dfrac{\pi^2}{\zeta} \left(\dfrac{2\zeta}{|\vec{x}_1 - \vec{x}_2|} - 1\right) e^{-|\vec{x}_1 - \vec{x}_2|/\zeta} & |\vec{x}_1 - \vec{x}_2| \neq 0 \end{cases} \tag{3.28}$$

Scattering kernel is plotted as a function of distance for lattice constant of 0.5nm and different screening lengths as shown in Fig. 3.6. Non-locality of scattering increases with increasing screening length values. The kernel has a discontinuity at for local case due to the choice of different integration ranges for local and non-local cases.

The lesser and retarded self-energies expressions for nanowire polar optical phonon scattering can now be written as

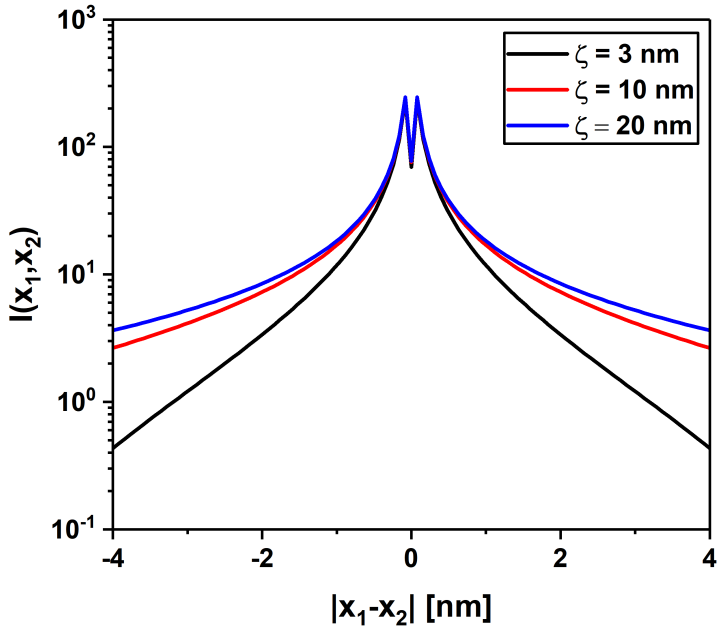

Fig. 3.6.: Plot of non-locality of scattering kernel for a wire as a function of distance for different values of screening lengths. Scattering becomes more and more local with decreasing values of screening length. Discontinuity at the origin is due to the choice of integration range.

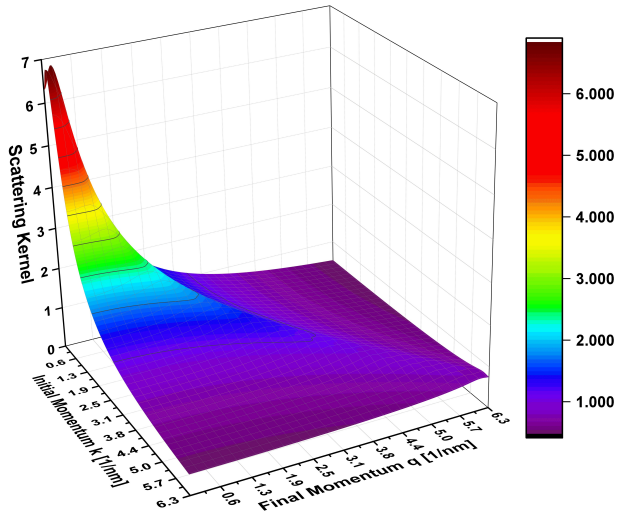

Fig. 3.7.: Scattering kernel of POP scattering for bulk GaAs. POP scattering favours small momentum changes and is anisotropic in nature.

$$\Sigma^{<}\left(\vec{x}_1,\vec{x}_2,E\right)=\frac{e^2}{(2\pi)^3}\left(\frac{1}{\epsilon_\infty}-\frac{1}{\epsilon_s}\right)\frac{\hbar\omega_o}{2\epsilon_o}I(\vec{x}_1,\vec{x}_2)$$
$$\times\left[n_oG^{<}\left(\vec{x}_1,\vec{x}_2,E-E_o\right)+\left(1+n_q\right)G^{<}\left(\vec{x}_1,\vec{x}_2,E+E_o\right)\right] \tag{3.29}$$

$$\Sigma^{R}\left(\vec{x}_1,\vec{x}_2,E\right)=\frac{e^2}{(2\pi)^3}\left(\frac{1}{\epsilon_\infty}-\frac{1}{\epsilon_s}\right)\frac{\hbar\omega_o}{2\epsilon_o}I(\vec{x}_1,\vec{x}_2)$$
$$\times\left[(1+n_o)G^{R}\left(\vec{x}_1,\vec{x}_2,E-E_o\right)+n_oG^{R}\left(\vec{x}_1,\vec{x}_2,E+E_o\right)+\frac{1}{2}G^{<}(\vec{x}_1,\vec{x}_2,E-E_o)\right.$$
$$\left.-\frac{1}{2}G^{<}(\vec{x}_1,\vec{x}_2,E+E_o)+i\int\frac{d\tilde{E}}{2\pi}G^{<}\left(\vec{x}_1,\vec{x}_2,\tilde{E}\right)\left(Pr\frac{1}{E-\tilde{E}-E_o}-Pr\frac{1}{E-\tilde{E}+E_o}\right)\right] \tag{3.30}$$

3.3.4 Important features of polar optical phonon scattering

Unlike, deformation potential acoustic and optical phonon scattering, POP scattering is anisotropic and favours small momentum scattering. Shown below is the scattering kernel for bulk GaAs against initial and final momentum values of electron for a screening length of $\zeta = 10nm$.

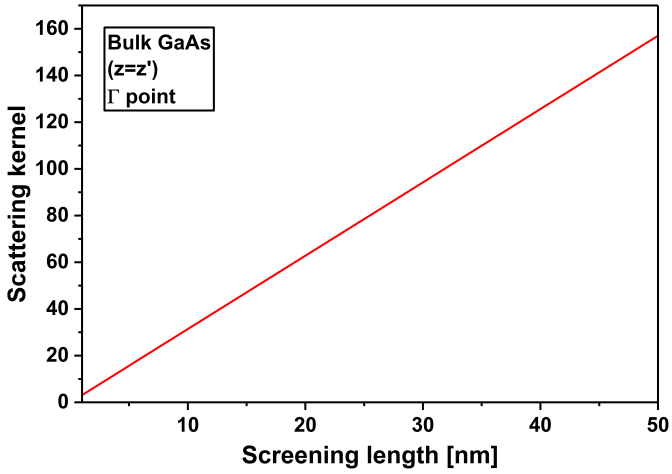

Fig. 3.8.: Scattering kernel versus screening length for bulk GaAs. Increasing screening length results in lesser shielding increasing the scattering strength.

Fig.3.8 shows the scattering kernel as a function of screening length for scattering at the gamma point. With increasing screening length, effective shielding for electrons against the optical-mode dipoles reduces increasing the scattering rate. This shows up as an increase in the scattering kernel with increasing screening length.

POP scattering is a non-local scattering process resulting in dense self-energy terms. The self-energy terms are strongest along the diagonal of the matrix and decay exponentially with increasing number of off-diagonal terms. The decay rate of the off-diagonal terms depends on the extent of screening. Fig.3.9 shows a contour plot of self-energy extracted from a nanowire calculation where the non-locality extends upto few nanometers. Fig.3.10 shows the anti-diagonal or the cross diagonal of self energy showing the decay rate for different values of screening lengths.

3.4 Self-energies for scattering with charged impurities

Semiconductors offer variations in resistivity in orders of magnitude which is one of the important reasons for their widespread application in electronics. This has been possible mainly due to the fact that they can be doped either N-type or P-type. Electrons and

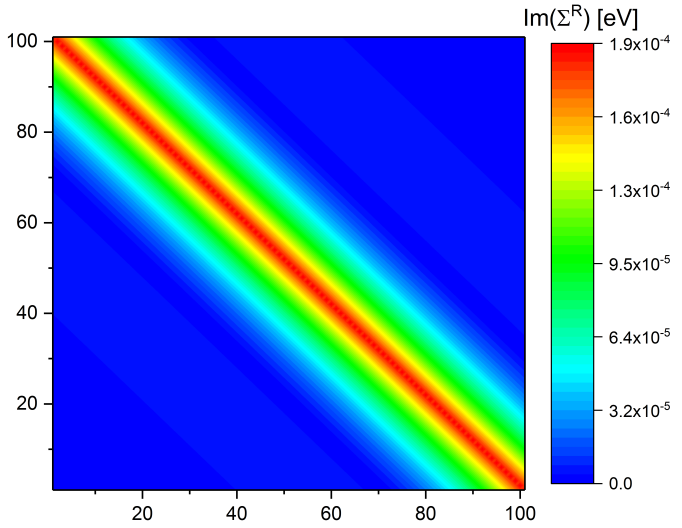

Fig. 3.9.: Contour plot of self energy from a GaAs nanowire simulation highlighting the extent of non-locality

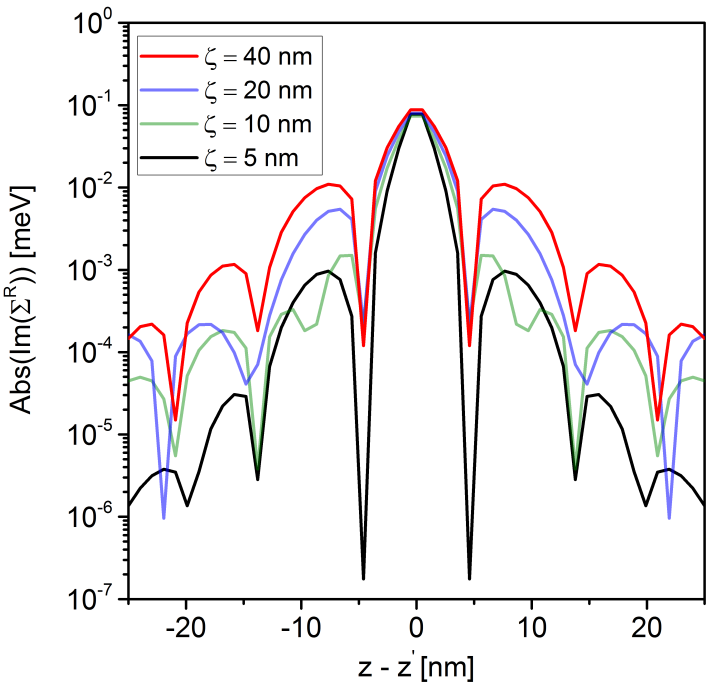

Fig. 3.10.: Anti-diagonal of POP self energy for different values of screening length. With decreasing screening length, non-local contribution decays faster.

holes carry current in the presence of a large background ionized dopant concentration (it is the ionization of dopants that gives rise to additional free carrier concentration). Thus, with each dopant there is an associated Coulomb potential and the incoming electrons/holes scatter with positively/negatively charged impurity atoms. This scattering process is dominant especially in heavily doped source/drain regions of any conventional electronic device such as transistors, LEDs, p-n diodes. This process is referred to as charged impurity scattering. Since it is a Coulombic interaction, it is inherently a non-local process as well.

There have been several approaches to model impurity scattering. Brooks-Herring (BH) [79] and Conwell-Weisskopf (CW) [80] are two well-known approaches with each one of them having their own validity range. A brief description of both the approaches is presented below.

The bare impurity potential is of the form

$$eV(r) = \frac{Ze^2}{4\pi\epsilon_o r}$$

where Z is the ionization of the impurity (usually $Z = 1$) and ϵ_o is the static dielectric constant of the material. The Fourier component can be represented as

$$eV(q) = \frac{Ze^2}{\epsilon_o q^2}$$

It is a long range potential interacting with electrons right from the origin to infinite distance and it diverges at small momentum values. Brooks-Herring model makes the assumption that potential is not long ranged but short-ranged due to electrostatic screening of impurity charge by electrons. The impurity potential is screened by the static-dielectric function with a screening wavevector ζ^{-2} to cast the bare impurity potential into

$$eV(q) = \frac{Ze^2}{\epsilon_o \left(q^2 + \zeta^{-2}\right)} \tag{3.31}$$

This assumes that not all electrons feel the Coulombic potential and electrons that are at a distance greater than the screening length do not scatter with the impurity atom.

However, there is an inconsistency in the way screening is handled in the Brooks-Herring model. All electrons are assumed to be pure plane waves and also equally par-

ticipate in the screening process. This leads to double-counting of electrons. Mahan [81] has done extensive calculations of actual electron wavefunctions in the presence of ionized impurities. It is observed at low impurity concentrations, electrons indeed pile up near the impurity atoms screening the potential but at high impurity concentrations electron density is pretty homogeneous across the device. This is mainly due to the fact that the inter-dopant distance is lesser than the electron wavelength.

Thus, at large densities, scattering is better represented by the model of Conwell and Weisskopf. In this model, the Coulomb potential is unscreened but the electrons interact only with their nearest impurity atoms or collisions are independent. The average dopant separation is defined by

$$n_D = \frac{1}{4\pi r_o^3/3} \implies r_o = \left(\frac{3}{4\pi n_D}\right)^{1/3} \tag{3.32}$$

Conwell-Weisskopf Coulomb potential can now be represented as

$$eV(q) = \frac{Ze^2}{\epsilon_o q^2}\left(1 - cos(qr_o)\right) \tag{3.33}$$

Fig 3.11 shows a comparison of impurity potential between Brooks-Herring and Conwell-Weisskopf model against the bare unscreened potential.

Ridley has developed an intermediate scattering model that provides a seamless shift from one model to another depending on the doping concentration [82]. According to this approach, the choice of model depends on the screening regime, which is determined by the dimensionless parameter η

$$\eta = \frac{16Z^2 N_{imp}^{2/3}}{q_{scr}^2}\frac{13.605 m_k^*}{\epsilon_k m_e \epsilon^2} \tag{3.34}$$

where m_k^* is the effective mass of electrons at wavevector **k** in the Brillouin zone [83]. Brooks-Herring is valid when $\eta < 1$ (screening dominated regime). Conwell-Weisskopf is valid when $\eta > 1$ (scattering center dominated regime). For all the materials and devices under consideration in this study, $\eta < 1$ and Brooks-Herring model will be used in further discussions.

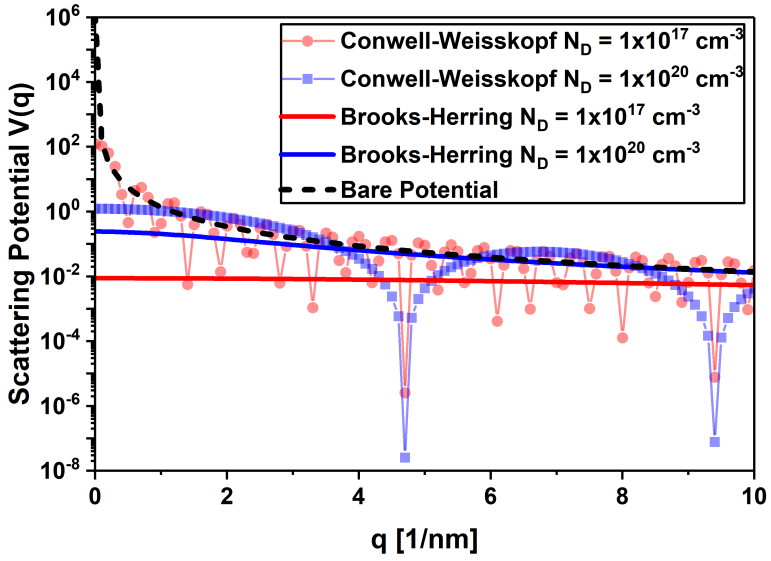

Fig. 3.11.: Comparison of scattering potential versus momentum between Brooks-Herring and Conwell-Weisskopf approaches along with bare unscreened potential for two doping concentrations for GaAs electrons.

For self-energy derivations, ionized impurities are assumed to be distributed homogeneously across the device. Hence, the derivation is not specific to any particular impurity configuration but is an ensemble average. Self-energy for scattering at homogeneously distributed ionized impurity is given by

$$\Sigma^{<,R}\left(\vec{x}_1,\vec{x}_2,E\right)=\frac{<N_D>_{x_1,x_2}}{(2\pi)^3}\int d\vec{q}\left|V_{imp}(q)\right|^2 e^{i\vec{q}.(\vec{x}_1-\vec{x}_2)}G^{<,R}\left(\vec{x}_1,\vec{x}_2,E\right) \tag{3.35}$$

where $<N_D>_{x1,x2}$ is the average doping concentration between two coordinates in the device. One important difference in comparison with phonon scattering is that impurity is an elastic scattering process. The impurity potential merely acts as a scattering center to mix different momentum components of electrons and as such the impurity does not absorb or emit energy into the electron bath. This simplifies both the formulation and numerical implementation as well.

3.4.1 Self-energy expressions for bulk/quasi1D system

Starting with the self-energy definition as mentioned above, we can express the self-energy for a bulk system with 2 transverse momentum components as

$$\Sigma^{<}\left(z_1,z_2,\vec{k}_{||},E\right)=\frac{N_D}{(2\pi)^3}\left(\frac{e^2}{\epsilon_o\epsilon_r}\right)^2\int dq_z\int d\vec{l}_{||}\frac{1}{\left(q_{||}^2+q_z^2+\zeta^{-2}\right)^2}e^{iq_z.(z_1-z_2)}G^{<}\left(z_1,z_2,\vec{l}_{||},E\right) \tag{3.36}$$

where $q_{||}=\left|\vec{k}_{||}-\vec{l}_{||}\right|=\sqrt{k_{||}^2+l_{||}^2-2k_{||}l_{||}cos\theta}$. The above expression can be simplified by integrating over q_z

$$I(q_{||},z_1,z_2)=\int dq_z\frac{e^{iqZ(z_1-z_2)}}{\left(q_{||}^2+q_z^2+\zeta^{-2}\right)^2}$$

The above integral can be solved on the complex contour (elaborated in the Appendix) to give

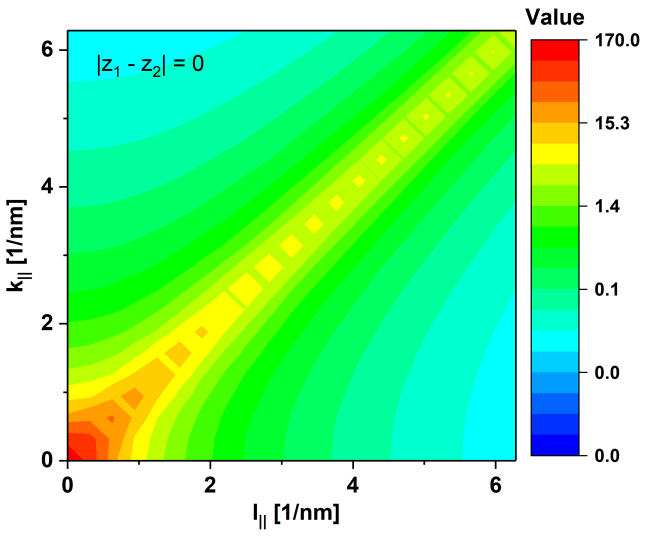

Fig. 3.12.: Contour plot of integrated scattering kernel as a function of momentum values $k_{||}$ and $l_{||}$ for screening length of 3 nm and non-local distance set to zero. Scattering is anisotropic and favours small momentum shifts.

$$I(q_{||}, z_1, z_2) = \frac{\pi}{2}\left[\frac{|z_1 - z_2| + 1/\sqrt{q_{||}^2 + \zeta^{-2}}}{q_{||}^2 + \zeta^{-2}} e^{-\sqrt{q_{||}^2+\zeta^{-2}}|z_1 - z_2|}\right] \tag{3.37}$$

where $I(q_{||}, z_1, z_2)$ is the scattering kernel. Figs 3.12 and 3.13 show a contour plot of the scattering kernel for different non-local range. Scattering kernel looks pretty much diagonal highlighting the fact that the impurity potential changes the electron momentum only slightly . Contour plot for different non-local range shows that the scattering decreases drastically with increasing non-local range.

This gives us the following expressions for lesser and retarded self-energies for bulk impurity scattering.

$$\Sigma^{<}\left(z_1, z_2, \vec{k}_{||}, E\right) = \frac{N_D}{4.\,(2\pi)^2}\left(\frac{e^2}{\epsilon_o \epsilon_r}\right)^2 \int d\vec{l}_{||} I\left(\vec{k}_{||}, \vec{l}_{||}, z_1, z_2\right) G^{<}\left(z_1, z_2, \vec{l}_{||}, E\right) \tag{3.38}$$

$$\Sigma^{R}\left(z_1, z_2, \vec{k}_{||}, E\right) = \frac{N_D}{4.\,(2\pi)^2}\left(\frac{e^2}{\epsilon_o \epsilon_r}\right)^2 \int d\vec{l}_{||} I\left(\vec{k}_{||}, \vec{l}_{||}, z_1, z_2\right) G^{R}\left(z_1, z_2, \vec{l}_{||}, E\right) \tag{3.39}$$

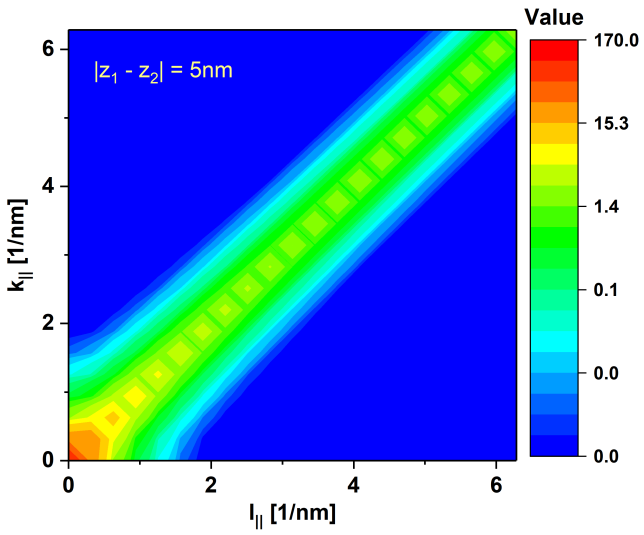

Fig. 3.13.: Contour plot of integrated scattering kernel as a function of momentum values $k_{||}$ and $l_{||}$ for screening length of 3 nm and non-local distance of 5 nm. Scattering in general decreases with increasing non-local distance.

3.4.2 Self-energy expressions for ultra-thin body system

Self-energy for an ultra-thin body system with a transverse momentum components can be written as

$$\Sigma^{<}\left(\vec{x}_1,\vec{x}_2,k_{||},E\right)=\frac{N_D}{(2\pi)^3}\left(\frac{e^2}{\epsilon_o\epsilon_r}\right)^2\int dq_{||}\int d\vec{q}\frac{1}{\left(q_{||}^2+q^2+\zeta^{-2}\right)^2}e^{i\vec{q}.(\vec{x}_1-\vec{x}_2)}G^{<}\left(\vec{x}_1,\vec{x}_2,l_{||},E\right) \tag{3.40}$$

where $q_{||}=k_{||}-l_{||}$. The inner integral over $d\vec{q}$ can be simplified by converting it to cylindrical coordinates as follows

$$\int d\vec{q}\frac{1}{\left(q_{||}^2+q^2+\zeta^{-2}\right)^2}e^{i\vec{q}.(\vec{x}_1-\vec{x}_2)}=\int qdq\int_0^{2\pi}d\theta\frac{e^{iq|\vec{x}_1-\vec{x}_2|cos\theta}}{\left(q_{||}^2+q^2+\zeta^{-2}\right)^2}$$

The angular integral can be integrated to give

$$\int_0^{2\pi}d\theta exp(iq\left|\vec{x}_1-\vec{x}_2\right|cos\theta)=2\pi J_o\left(q\left|\vec{x}_1-\vec{x}_2\right|\right) \tag{3.41}$$

where $J_o(x)$ is the J-Bessel function of 0th order. The momentum integral over q can now be written as

$$I(k_{||},l_{||},\vec{x}_1,\vec{x}_2)=\int_0^{\infty}dq\frac{q.2\pi J_o\left(q\left|\vec{x}_1-\vec{x}_2\right|\right)}{\left(q^2+(k_{||}-l_{||})^2+\zeta^{-2}\right)^2} \tag{3.42}$$

The above integral can be solved analytically by using the following relation from Ref.

$$\begin{gathered}\int_0^{\infty}\frac{J_\nu(bx)x^{\nu+1}}{(x^2+a^2)^{\mu+1}}=\frac{a^{\nu-\mu}b^\mu}{2^\mu\Gamma(\mu+1)}K_{\nu-\mu}(ab)\\ for\ a>0,\ b>0,\ -1<Re(\nu)<Re\left(2\mu+\frac{3}{2}\right)\end{gathered} \tag{3.43}$$

where $K_{\nu-\mu}(x)$ is the K-Bessel function of order $\nu-\mu$. This gives us

$$\begin{gathered}I(k_{||},l_{||},\vec{x}_1,\vec{x}_2)=\\ \begin{cases}\pi\left[\dfrac{|\vec{x}_1-\vec{x}_2|}{\left(k_{||}-l_{||}\right)^2+\zeta^{-2}}\right]K_1\left(\sqrt{\left(k_{||}-l_{||}\right)^2+\zeta^{-2}}\,|\vec{x}_1-\vec{x}_2|\right), & \\ \qquad |\vec{x}_1-\vec{x}_2|\neq 0 & \\ \pi\left[\dfrac{1}{\left(k_{||}-l_{||}\right)^2+\zeta^{-2}}\right],\ |\vec{x}_1-\vec{x}_2|=0 & \end{cases}\end{gathered} \tag{3.44}$$

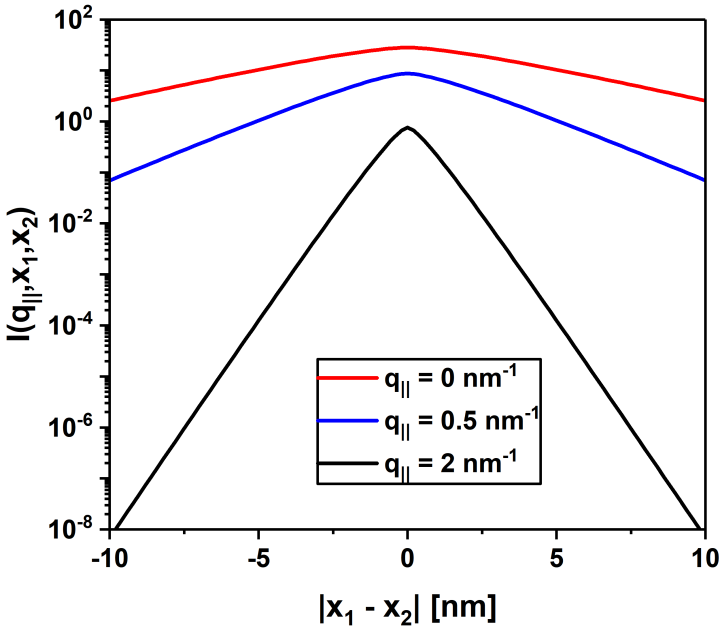

Fig. 3.14.: Plot of non-locality of scattering kernel for impurity scattering for $q_{||} = 0nm^{-1}$, $0.5nm^{-1}$, $2nm^{-1}$ and screening length of 3nm. Scattering kernel decreases exponentially with increasing momentum values implying that small momentum changes are preferred.

Scattering kernel is plotted as a function of distance for several momentum points as shown in Fig. 3.14. Scattering is quite non-local for small momentum points and decays sharply for larger momentum points.

The lesser and retarded self energies for ultra-thin body impurity scattering can now be written as

$$\Sigma^{<}\left(\vec{x}_1,\vec{x}_2,k_{||},E\right) = \frac{N_D}{(8\pi)^2}\left(\frac{e^2}{\epsilon_o\epsilon_r}\right)^2 \int dl_{||} I(k_{||},l_{||},\vec{x}_1,\vec{x}_2) G^{<}\left(\vec{x}_1,\vec{x}_2,l_{||},E\right) \tag{3.45}$$

$$\Sigma^{R}\left(\vec{x}_1,\vec{x}_2,k_{||},E\right) = \frac{N_D}{(8\pi)^2}\left(\frac{e^2}{\epsilon_o\epsilon_r}\right)^2 \int dl_{||} I(k_{||},l_{||},\vec{x}_1,\vec{x}_2) G^{R}\left(\vec{x}_1,\vec{x}_2,l_{||},E\right) \tag{3.46}$$

3.4.3 Self-energy expressions for nanowire system

Due to the lack of momentum space in a nanowire, the scattering potential needs to be integrated completely to get the scattering kernel. By transforming the scattering integral to spherical coordinates we get

$$\int d\vec{q} \frac{e^{i\vec{q}.(\vec{x}_1-\vec{x}_2)}}{\left(q^2+\zeta^{-2}\right)^2}$$

$$= \int_0^{2\pi} d\phi \int_{-\pi/2}^{\pi/2} d\theta sin\theta \int_0^{\infty} dq \frac{q^2 exp(iq\left|\vec{x}_1-\vec{x}_2\right| cos\theta)}{\left(q^2+\zeta^{-2}\right)^2}$$

$$= 2\pi \int_0^{\infty} dq \int_{-1}^{1} dcos\theta \frac{q^2 exp(iq\left|\vec{x}_1-\vec{x}_2\right| cos\theta)}{\left(q^2+\zeta^{-2}\right)^2}$$

$$= 4\pi \int_0^{\infty} dq \frac{q}{\left(q^2+\zeta^{-2}\right)^2} \frac{sin\left(q\left|\vec{x}_1-\vec{x}_2\right|\right)}{\left|\vec{x}_1-\vec{x}_2\right|}$$

Now, we have two conditions for which we need to solve ($|\vec{x}_1-\vec{x}_2|=0$ and $|\vec{x}_1-\vec{x}_2|\neq 0$). Taking the case, $|\vec{x}_1-\vec{x}_2|=0$, we get

$$I(\vec{x}_1,\vec{x}_2) = 4\pi \int_0^{\infty} dq \frac{q^2}{\left(q^2+\zeta^{-2}\right)^2} \lim_{|\vec{x}_1-\vec{x}_2|\to 0} \frac{sin\left(q\left|\vec{x}_1-\vec{x}_2\right|\right)}{q\left|\vec{x}_1-\vec{x}_2\right|} = 4\pi \int_0^{\infty} dq \frac{q^2}{\left(q^2+\zeta^{-2}\right)^2}$$

$$I(\vec{x}_1,\vec{x}_2) = \pi^2\zeta$$

For $|\vec{x}_1-\vec{x}_2|\neq 0$, we get

$$I(\vec{x}_1,\vec{x}_2) = \pi^2\zeta e^{-|\vec{x}_1-\vec{x}_2|/\zeta} \tag{3.47}$$

which holds good for the local case as well.

Scattering kernel is plotted as a function of distance and different screening lengths as shown in Fig. 3.15. Non-locality of scattering increases with increasing screening length values.

The lesser and retarded self-energies expressions for nanowire impurity scattering can now be written as

$$\Sigma^{<}(\vec{x}_1,\vec{x}_2,E) = \frac{N_D}{8\pi}\left(\frac{e^2}{\epsilon_o\epsilon_r}\right)^2 I(\vec{x}_1,\vec{x}_2)G^{<}(\vec{x}_1,\vec{x}_2,E) \tag{3.48}$$

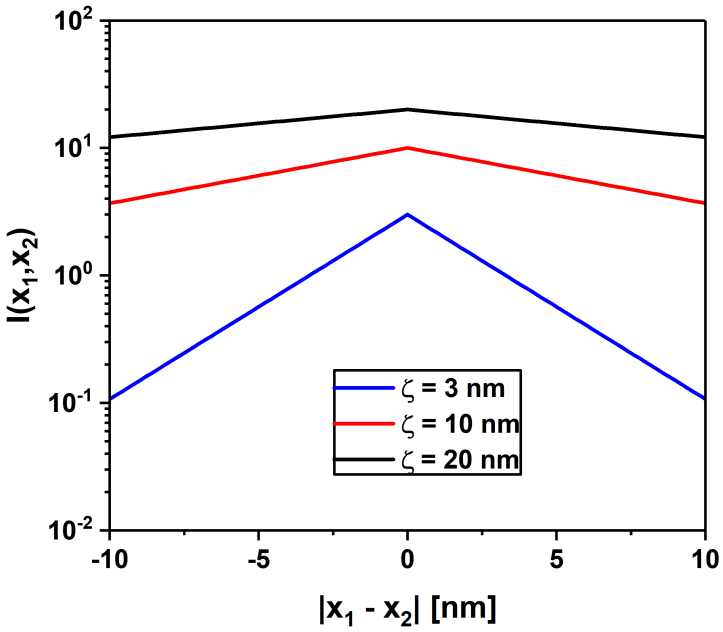

Fig. 3.15.: Plot of non-locality of scattering kernel for a wire as a function of distance for different values of screening lengths. Scattering becomes more and more local with decreasing values of screening length.

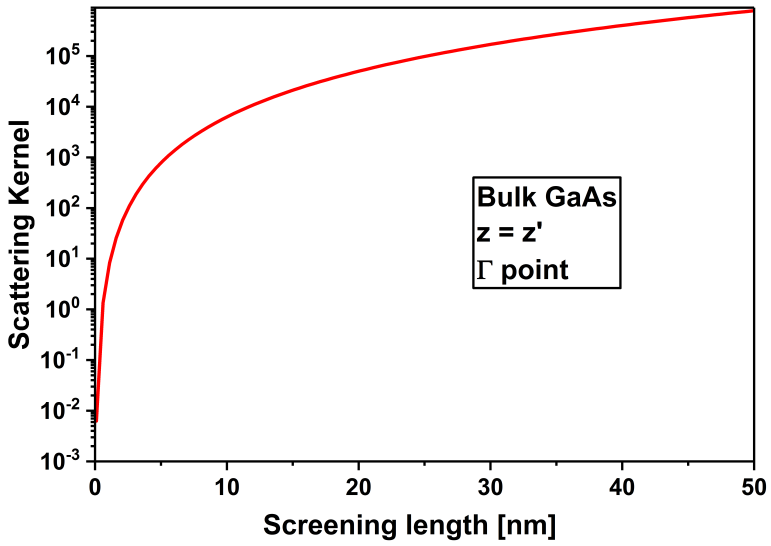

Fig. 3.16.: Impurity scattering kernel as a function of screening length

$$\Sigma^R(\vec{x}_1, \vec{x}_2, E) = \frac{N_D}{8\pi}\left(\frac{e^2}{\epsilon_o \epsilon_r}\right)^2 I(\vec{x}_1, \vec{x}_2) G^R(\vec{x}_1, \vec{x}_2, E) \tag{3.49}$$

3.4.4 Important features of impurity scattering

Similar to POP, Impurity is a non-local scattering process and favours small momentum scattering. One distinguishing feature between impurity and POP is that impurity is an elastic scattering process. Fig.3.16 illustrates the scattering kernel for impurity scattering.

3.5 Self-energies for scattering with remote oxide phonons

Remote oxide phonon/Remote-phonon scattering, as the name suggests, corresponds to scattering of electrons with phonons originating in the dielectric material of the active device. This is a dominant scattering mechanism in ultra-scaled transistors where High-κ dielectrics are used as gate oxide materials to provide good electrostatic control and suppress gate leakage. They are also an important scattering mechanism in most of the

2D materials such as graphene [84], transition-metal dichalcogenides such as MoS2 [85], WSe2 [86].

High-κ dielectrics owe their large dielectric constants to the large ionic polarization resulting from highly polarizable metal-oxygen bonds. It is the polarization of these soft bonds which screens the external electric field resulting in a large κ. Associated with these soft bonds are the low-energy optical phonons. Wang and Mahan [87] showed that electrons in the inversion layer can couple to the surface optical (SO) modes of the insulator resulting in electron-phonon scattering. Later, the effect of High-κ on mobility of transistors was first demonstrated by [88]. Since then, there have been extensive studies of High-κ on inversion layer of Si MOSFETs and graphene [89], [90].

Remote-phonon scattering potential has been derived in detail in seminal work by [88]. Electron-phonon coupling Hamiltonian is given by

$$H_{e-ph} = F_\nu \sum_q \frac{e^{-q_{||}z}}{\sqrt{q_{||}}} \left(a_q e^{i\mathbf{q}_{||}\cdot\mathbf{r}_{||}} + a_q^\dagger e^{-i\mathbf{q}_{||}\cdot\mathbf{r}_{||}} \right) \tag{3.50}$$

where q is the surface 2D phonon momentum, a_q and $a_q^\dagger$ are particle annihilation and creation operators and coupling constant F_ν is described as

$$F_\nu = \left[\frac{e^2 \hbar\omega_{SO}^\nu}{2\epsilon_o} \left(\frac{1}{\epsilon_{ox}^\infty + \epsilon_s^\infty} - \frac{1}{\epsilon_{ox}^o + \epsilon_s^\infty} \right) \right]^{1/2} \tag{3.51}$$

where $\hbar\omega_{SO}^\nu$ is νth oxide SO optical phonon frequency, ϵ_{ox}^o is static oxide dielectric constant,ϵ_{ox}^∞ is oxide high frequency dielectric constant and ϵ_s^∞ is semiconductor high frequency dielectric constant.

Using the electron-phonon coupling Hamiltonian, the generic self-energy expression can be written as

$$\begin{aligned} \Sigma^< (\vec{x}_1, \vec{x}_2, E) = \frac{e^2}{(2\pi)^2} \frac{\hbar\omega_{SO}^\nu}{2\epsilon_0} \left(\frac{1}{\epsilon_{ox}^\infty + \epsilon_s^\infty} - \frac{1}{\epsilon_{ox}^s + \epsilon_s^\infty} \right) \int d\vec{q}_{||} \frac{e^{i\vec{q}_{||}\cdot\left(\vec{x}_{1,||} - \vec{x}_{2,||}\right)}}{q_{||}} . e^{-q_{||}(z_1 + z_2 - 2t)} \\ \times \left[n_q G^< (\vec{x}_1, \vec{x}_2, E - E_o) + (1 + n_q) G^< (\vec{x}_1, \vec{x}_2, E + E_o) \right] \end{aligned} \tag{3.52}$$

where $z = t$ is the oxide-semiconductor interface.

3.5.1 Self-energy expressions for ultra-thin body system

Converting the above expression to an ultra-thin body case with a single transverse momentum, we get

$$\begin{aligned}\Sigma^{<}\left(\vec{x}_1,\vec{x}_2,k,E\right)=\frac{e^2}{\left(2\pi\right)^2}\frac{\hbar\omega_{SO}^{\nu}}{2\epsilon_0}\left(\frac{1}{\epsilon_{ox}^{\infty}+\epsilon_s^{\infty}}-\frac{1}{\epsilon_{ox}^{s}+\epsilon_s^{\infty}}\right)\\ \int dl\int dq\frac{e^{i\sqrt{q^2+(k-l)^2}.\left|\vec{x}_{1,||}-\vec{x}_{2,||}\right|cos\theta}}{\sqrt{q^2+(k-l)^2}}.e^{-\sqrt{q^2+(k-l)^2}(z_1+z_2-2t)}\\ \times\left[n_qG^{<}\left(\vec{x}_1,\vec{x}_2,l,E-E_o\right)+\left(1+n_q\right)G^{<}\left(\vec{x}_1,\vec{x}_2,l,E+E_o\right)\right]\end{aligned}\tag{3.53}$$

The above integral as such does not have a well-defined analytical expression. However, if we make the approximation that the magnitude of two dimensional momentum $q_{||}$ is equivalent to the momentum range of Green's function, then we can rewrite the self-energy as

$$\begin{aligned}\Sigma^{<}\left(\vec{x}_1,\vec{x}_2,k,E\right)=\frac{e^2}{\left(2\pi\right)^2}\frac{\hbar\omega_{SO}^{\nu}}{2\epsilon_0}\left(\frac{1}{\epsilon_{ox}^{\infty}+\epsilon_s^{\infty}}-\frac{1}{\epsilon_{ox}^{s}+\epsilon_s^{\infty}}\right)\\ \int dl\int_0^{2\pi}d\theta\frac{\left|k-l\right|e^{i|k-l|\left|\vec{x}_{1,||}-\vec{x}_{2,||}\right|cos\theta}}{|k-l|}.e^{-|k-l|(z_1+z_2-2t)}\\ \times\left[n_qG^{<}\left(\vec{x}_1,\vec{x}_2,l,E-E_o\right)+\left(1+n_q\right)G^{<}\left(\vec{x}_1,\vec{x}_2,l,E+E_o\right)\right]\end{aligned}\tag{3.54}$$

then the solution becomes tractable immediately. However, due to the approximation, the whole range of two-dimensional $q_{||}$ is not covered and it's magnitude is restricted only to the range of one-dimensional momentum and the whole scattering space is not covered. The scattering potential, however decays exponentially with $q_{||}$ and the contribution by the phase space left out by this approximation is only going to be minimal. The scattering integral can now be solved by integrating over θ to give

$$\begin{aligned}I(k,l,\vec{x}_1,\vec{x}_2,z_1,z_2)&=\int_0^{2\pi}d\theta e^{i|k-l|\left|\vec{x}_{1,||}-\vec{x}_{2,||}\right|cos\theta}.e^{-|k-l|(z_1+z_2-2t)}\\ &=2\pi J_o\left(|k-l|\left|\vec{x}_{1,||}-\vec{x}_{2,||}\right|\right)e^{-|k-l|(z_1+z_2-2t)}\end{aligned}\tag{3.55}$$

where $J_o(x)$ is the J-Bessel function of 0th order. Unlike the scattering kernels in polar optical phonon and impurity scattering, here it not only depends on the non-local distance but also on distance from the oxide-semiconductor interface. The scattering potential is maximal at the interface and decays exponentially as one moves away from the interface.

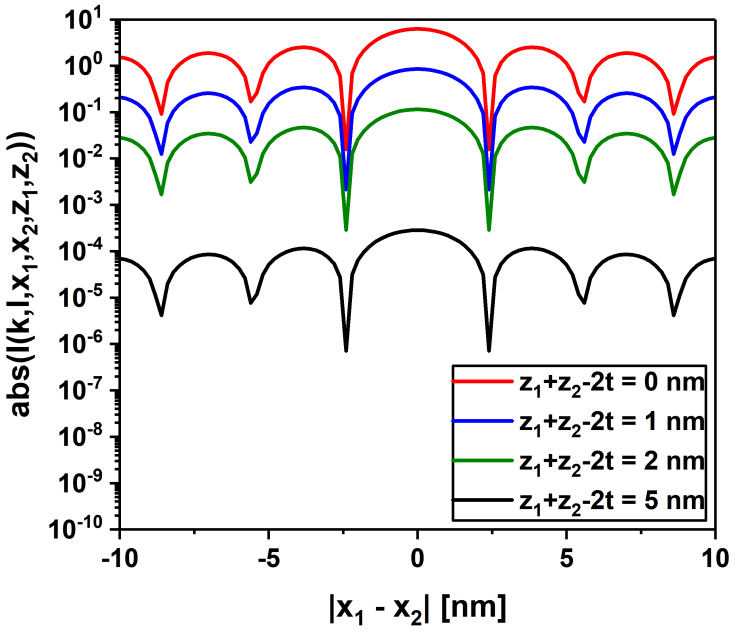

Fig. 3.17.: Plot of non-locality of scattering kernel for a ultra-thin body as a function of distance for different values of oxide-semiconductor interface distance. Scattering becomes more and more local as one moves away from the interface.

Scattering kernel is plotted as a function of non-local distance for different values of interface distance as shown in Fig. 3.17. Non-locality of the scattering process depends both on the momentum value and the distance from interface.

The lesser and retarded self energies for ultra-thin body remote phonon scattering can now be written as

$$\Sigma^{<}\left(\vec{x}_1,\vec{x}_2,k,E\right)=\frac{e^2}{(2\pi)}\frac{\hbar\omega_{SO}^{\nu}}{2\epsilon_0}\left(\frac{1}{\epsilon_{ox}^{\infty}+\epsilon_s^{\infty}}-\frac{1}{\epsilon_{ox}^{s}+\epsilon_s^{\infty}}\right)\int dlI(k,l,\vec{x}_1,\vec{x}_2,z_1,z_2)$$
$$\times\left[n_qG^{<}\left(\vec{x}_1,\vec{x}_2,l,E-E_o\right)+\left(1+n_q\right)G^{<}\left(\vec{x}_1,\vec{x}_2,l,E+E_o\right)\right] \tag{3.56}$$

$$\Sigma^R(\vec{x}_1,\vec{x}_2,k,E)=\frac{e^2}{(2\pi)}\frac{\hbar\omega_{SO}^{\nu}}{2\epsilon_0}\left(\frac{1}{\epsilon_{ox}^{\infty}+\epsilon_s^{\infty}}-\frac{1}{\epsilon_{ox}^{s}+\epsilon_s^{\infty}}\right)\int dlI(k,l,\vec{x}_1,\vec{x}_2,z_1,z_2)$$
$$\times\left[(1+n_o)G^R(\vec{x}_1,\vec{x}_2,l,E-E_o)+n_oG^R(\vec{x}_1,\vec{x}_2,l,E+E_o)+\frac{1}{2}G^<(\vec{x}_1,\vec{x}_2,l,E-E_o)\right.$$
$$\left.-\frac{1}{2}G^<(\vec{x}_1,\vec{x}_2,l,E+E_o)+i\int\frac{d\tilde{E}}{2\pi}G^<\left(\vec{x}_1,\vec{x}_2,l,\tilde{E}\right)\left(Pr\frac{1}{E-\tilde{E}-E_o}-Pr\frac{1}{E-\tilde{E}+E_o}\right)\right] \tag{3.57}$$

3.5.2 Important features of remote phonon scattering

3.6 Estimation of screening

Estimation of screening length is crucial to the determination of scattering rates. Commonly used approximations include the Thomas-Fermi and the Debye approximation. Figs. 3.18 and 3.19 show the comparison of these two approaches against the Lindhard formalism. For mild doping concentrations of $1\times10^{16}cm^{-3}$, Debye and Lindhard methods agree well with each other. However for higher doping concentrations, $1\times10^{19}cm^{-3}$, Debye underestimates the screening (thereby scattering). For both these cases, Thomas-Fermi approximation completely underestimates the screening and works well only if temperature is too low or if doping concentrations are well beyond $1\times10^{21}cm^{-3}$. For devices relevant to the discussion of this report, Lindhard formalism works well.

$$\zeta_{Lindhard}=\left(\frac{e^2}{\epsilon_o\epsilon_r}\frac{-2}{(2\pi)^3}\int d\vec{q}\,\frac{\partial f}{\partial\epsilon}\bigg|_{\epsilon(\vec{q})}\right)^{-1/2} \tag{3.58}$$

3.7 Conclusion

In summary, modeling and simulation procedure for several non-local scattering mechanisms within the NEGF formalism is discussed. Features of POP and impurity scattering are discussed in detail with self-energy expressions derived for 1D/2D and 3D systems. Self-energy calculations are verified by comparing them against Fermi's golden rule.

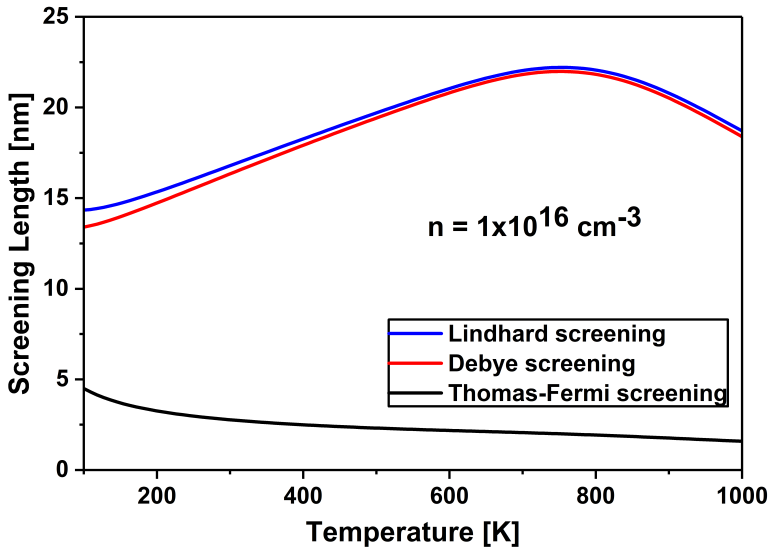

Fig. 3.18.: Comparison of screening length calculated from three different approaches: Lindhard, Debye and Thomas-Fermi model for bulk GaAs at a doping concentration of $1 \times 10^{16} cm^{-3}$

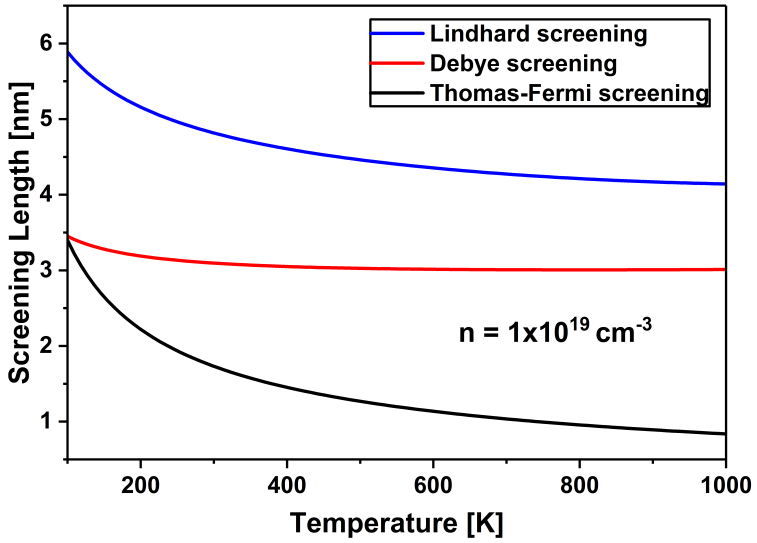

Fig. 3.19.: Comparison of screening length calculated from three different approaches: Lindhard, Debye and Thomas-Fermi model for bulk GaAs at a doping concentration of $1 \times 10^{19} cm^{-3}$

4. LOCAL SCATTERING APPROXIMATION MODEL FOR NON-LOCAL SCATTERING

4.1 Summary

In the previous chapter, different non-local scattering mechanisms were introduced and their respective self-energies were derived and compared with Fermi's golden rule. Despite the straightforward representation of the self-energies, it is computationally demanding to solve them for any realistic device. Computation of many off-diagonal blocks required for the self-energy calculation, makes the calculation atleast 10x more prohibitive both in terms of computation time and memory. It is common in literature to approximate it as a local/diagonal scattering approach. In this section, validity of this approximation will be discussed and a possible approach to treat the non-local scattering as an equivalent local scattering with a scaling factor will be presented.

4.2 Local scattering approximations

Recursive Green's function approach is among the widely used numerical technique to solve NEGF for realistic devices [60], [91]. This approach makes use of the fact that observables such as density, density of states depend only on the diagonal of the Green's function. This allows one to solve only required diagonal blocks (along with few off-diagonal blocks required for current density calculation) and is completely equivalent to computing the Green's function by inverting the matrix. However, this places a restriction on the nature of self-energies. They can only be diagonal/block diagonal as only diagonal entries of Green's function as calculated. Hence, there is limited study of non-local scattering with NEGF in the literature [65], [60], [64], [92]. Among the studies done with non-local scattering, either local approximations are made where non-local entries in self

energy are truncated or are simulated for the effective mass approach with full inversion, which restricts the types of devices that can be investigated. [93] have tried to use a diagonal approximation with a scaling factor to treat POP scattering. However, it turns out that the scaling factor used in the study needs to be fit to specific device geometries and bias condition which makes the scaling factor highly device specific.

Recently, a non-local recursive Green's function (NL-RGF) technique has been developed by [94] that extends the computation of Green's function to any number of off-diagonal elements. This approach can now be employed to study any long-ranged scattering process. However, as shown in Figs 4.1 and 4.2 it does take considerable time and memory even for small non-locality range of 2 nm. This definitely augments the capability to study non-local scattering and is better than a simple local approximation but numerical limitations limit us to study ony small non-locality ranges and a study of complete non-locality is not possible for a reasonable device in a multiband basis.

This brings us to the question of how good a local approximation is and whether an equivalent local approximation can be achieved with a compensating scaling factor. Impact of local approximations to scattering is analyzed by performing an exact scattering calculation (including all non-local elements) and comparing it with diagonal approximation where other off-diagonal terms are truncated. Scattering rates for bulk and nanowire GaAs is presented and behaviour of Urbach tails/band tails are calculated with both approaches to check the validity of local approximation.

It is evident from Figs.4.3 and 4.5 that local approximation underestimates both the scattering rate and also the Urbach parameter. It completely misses the temperature dependence of Urbach parameter. Upon closer look, the non-local/local prefactor is 1.5x and depends both on temperature and the energy of incoming electrons. The situation is worse for nanowire where the non-local case is almost 70x larger than the local counterpart. Similar to bulk, nanowire scaling factor has a strong energy dependence and the energy dependence is different from that of the bulk highlighting strong dimensional dependence on the scaling factor.

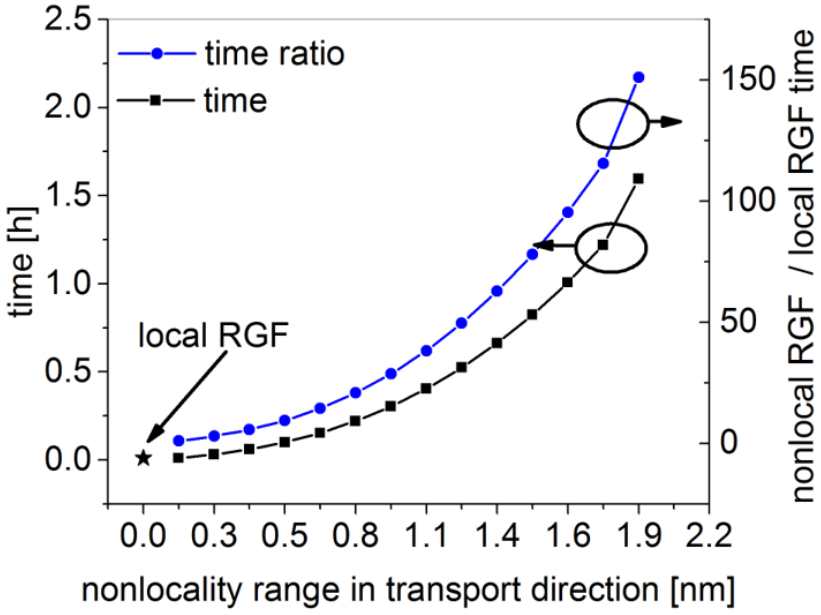

Fig. 4.1.: Ratio of time taken for computation with non-local RGF approach for different non-locality range for a 10-band sp3d5s* basis. Non-local RGF is 150x more computationally expensive in comparison with ballistic calculation. Plots provided by James Charles.

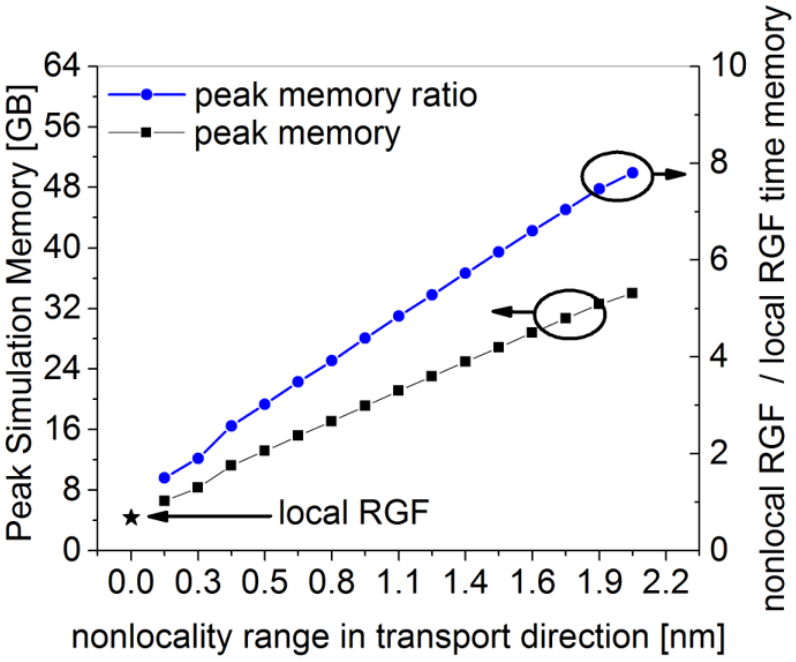

Fig. 4.2.: Ratio of time taken for memory with non-local RGF approach for different non-locality range for a 10-band sp3d5s* basis. Non-local RGF is 8x more memory expensive in comparison with ballistic calculation. Plots provided by James Charles.

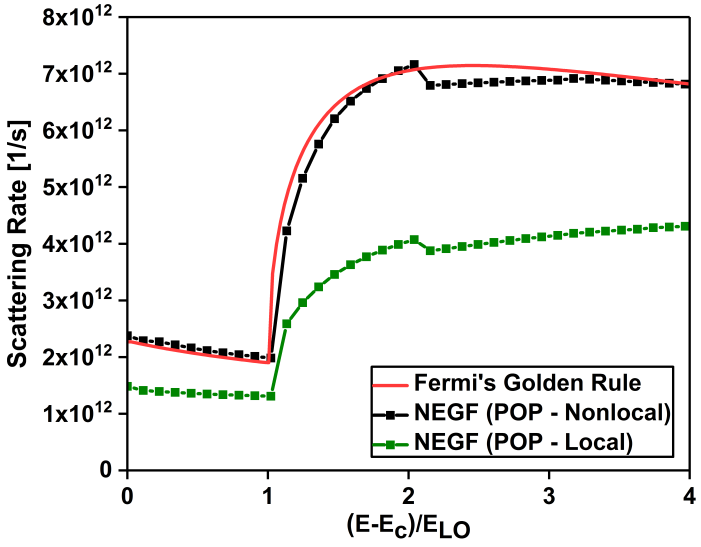

Fig. 4.3.: Comparison of scattering rate for bulk GaAs with and without the local approximation.

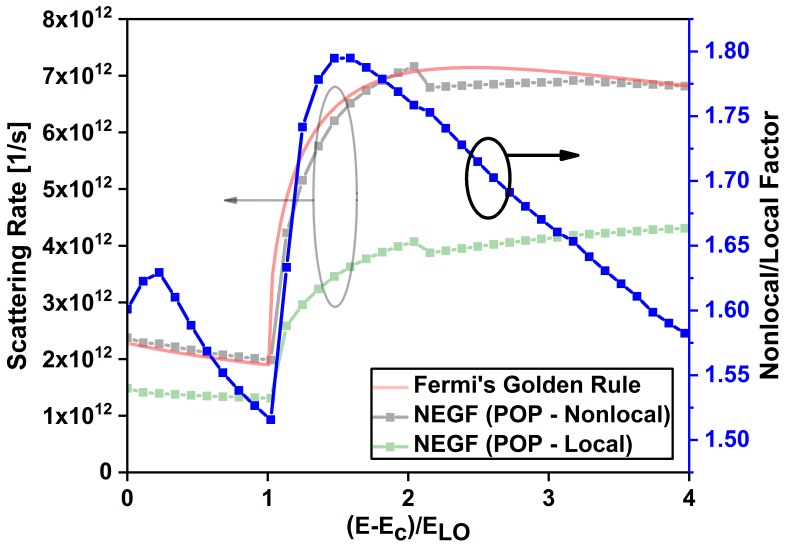

Fig. 4.4.: Nonlocal/local scattering prefactor plotted on top of both scattering rates. The prefactor is about 1.5x and is dependent on the incoming electron energy.

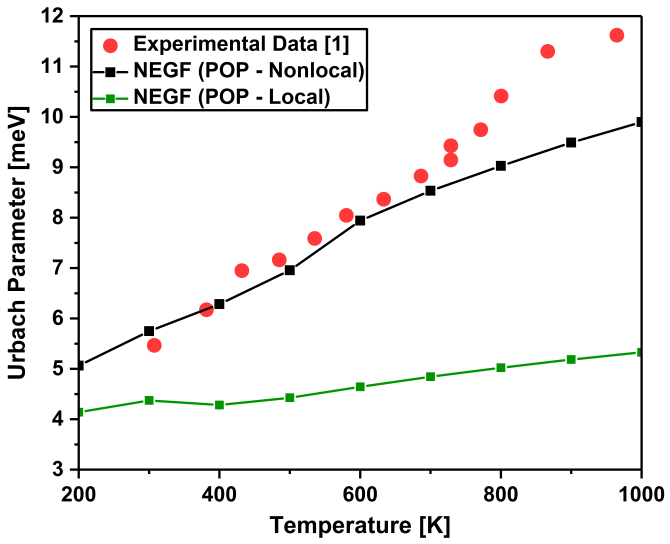

Fig. 4.5.: Comparison of Urbach parameter variation for bulk GaAs with and without the local approximation.

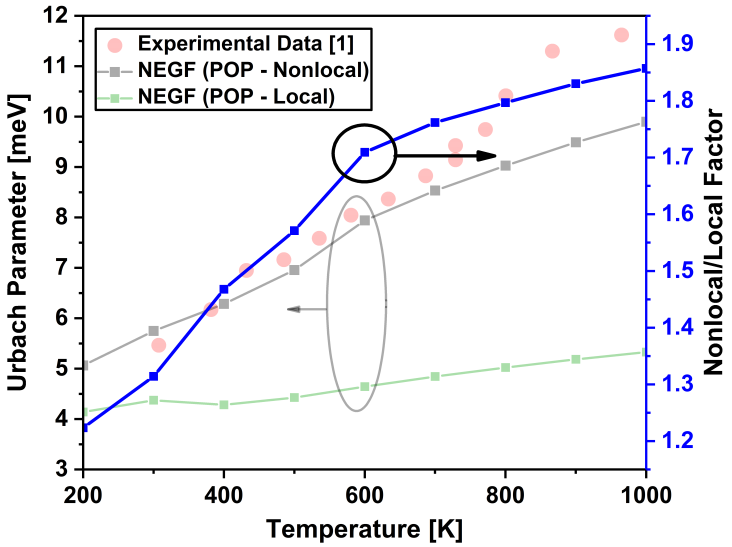

Fig. 4.6.: Nonlocal/local scattering prefactor plotted on top of both Urbach parameters. The prefactor is about 2x and is dependent on the temperature.

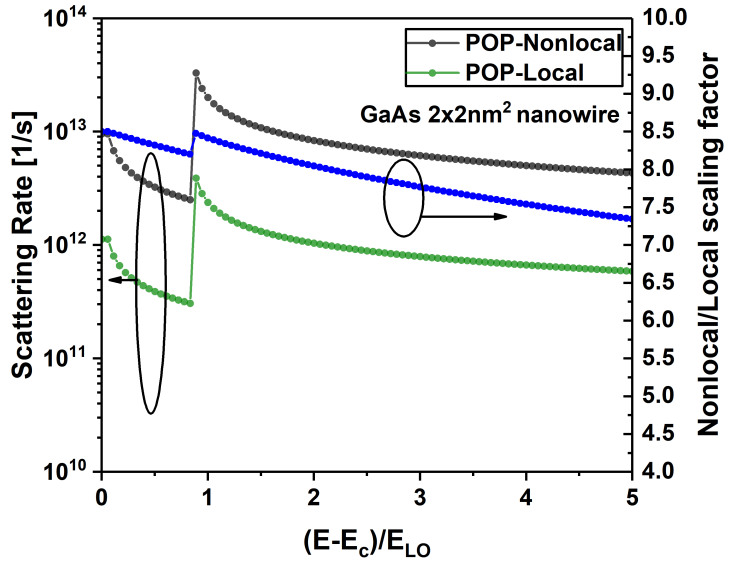

Fig. 4.7.: Comparison of scattering rate for GaAs nanowire with and without the local approximation. Non-local scattering is almost 70x larger than the local case and is highly energy dependent.

Based on the results above, a physics based local approximation is developed based on the Fermi's golden rule. The local approximation takes into account dimensionality of the device, size dependence, screening and energy dependence.

4.3 Local approximation model for non-local scattering

Local approximation model is based on the fact that the Fermi's golden rule for each scattering process has an associated form factor calculation which depends on the spatial scattering kernel. The current formalism is based on effective mass approach and assumes a parabolic dispersion but in principle, this approach can be applied to a general dispersion relation (which will be need for hole transport). Due to the dependence of scaling factor on spatial dependence, it has a well-defined expression only for the confined devices such as ultra-thin body and nanowire devices. Lack of a spatial dependence in bulk device prevents one from deriving such a similar expression within the Fermi's golden rule formalism. However, one can get the equivalent bulk result by having a large enough 2D device with requisite modes. This approach in it's strictest form is only applicable at equilibrium or near-equilibrium situation where Fermi's golden rule holds good. Deriving such a scaling factor for non-equilibrium cases, would involve solving the propagating modes in the device. However, even with the equilibrium approximation, agreement with non-equilibrium simulation cases are not that far off as it will be shown in the subsequent chapter.

Taking the case of polar optical scattering, Fermi's golden rule expression (absorption branch) for ultra-thin body for polar optical phonon scattering can be written as

$$\frac{1}{\tau_{ij,a}(E)} = \frac{4\pi e^2 m^* \hbar\omega_{LO}}{\hbar^3}\left(\frac{1}{\epsilon_\infty} - \frac{1}{\epsilon_s}\right)\left[N_{ph}\int_0^{2\pi} d\theta F_a(\left|\vec{k}_{||} - \vec{k}'_{||}\right|, \theta)\right] \tag{4.1}$$

where $F(q_{||}) = \int_0^{L_z}\int_0^{L_z} dz dz' \rho_{ij}(z)\rho_{ij}(z')I(q_{||}, z, z')$ and

$$|\tilde{\mathbf{k}}_{||} - \tilde{\mathbf{k}}'_{||}| = \left[2k^2 \pm \frac{2\left(\hbar\omega_{LO} \pm (E_i - E_j)\right)}{\hbar^2} - 2k\left[k^2 \pm \frac{2\left(\hbar\omega_{LO} \pm (E_i - E_j)\right)}{\hbar^2}\right]^{1/2} cos\theta\right]^{1/2} \tag{4.2}$$

$$I(q_{||},z,z') = \frac{e^{-\sqrt{q_{||}^2+\zeta^{-2}}|z-z'|}}{\sqrt{q_{||}^2+\zeta^{-2}}}\left[1-\frac{|z-z'|\,\zeta^{-2}}{2\sqrt{q_{||}^2+\zeta^{-2}}}-\frac{\zeta^{-2}}{2\left(q_{||}^2+\zeta^{-2}\right)}\right] \tag{4.3}$$

and $\rho_{ij}(z) = \psi_i^*(z)\psi_j(z)$

and for nanowires can be written as

$$\frac{1}{\tau_{ij,a}(E)} = \frac{e^2\hbar\omega_{LO}N_{ph}}{\hbar^2}\left(\frac{1}{\epsilon_\infty}-\frac{1}{\epsilon_s}\right).\frac{2}{(2\pi)^2}.\sqrt{2m^*}\left(\frac{F_a(k_x-k_x^{'})+F_a(k_x+k_x^{'})}{\sqrt{E-E_j+\hbar\omega_{LO}}}\right) \tag{4.4}$$

where $F(q_x) = \int_0^{L_y}\int_0^{L_z}\int_0^{L_y}\int_0^{L_z}\mathbf{dr}_{||}\mathbf{dr}_{||}^{'}\rho_{ij}^*(\mathbf{r}_{||})\rho_{ij}(\mathbf{r}_{||}^{'})I(q_x,\mathbf{r}_{||},\mathbf{r}_{||}^{'})$ and

$$I(q_x,\mathbf{r}_{||},\mathbf{r}_{||}^{'}) = \begin{cases} \left(\sqrt{q_x^2+\zeta^{-2}}\left|\mathbf{r}_{||}-\mathbf{r}_{||}^{'}\right| + \dfrac{q_x^2\left|\mathbf{r}_{||}-\mathbf{r}_{||}^{'}\right|}{\sqrt{q_x^2+\zeta^{-2}}}\right)\dfrac{K_1\left(\sqrt{q_x^2+\zeta^{-2}}\left|\mathbf{r}_{||}-\mathbf{r}_{||}^{'}\right|\right)}{2}, & \left|\mathbf{r}_{||}-\mathbf{r}_{||}^{'}\right|\neq 0 \\ \left(\dfrac{1}{2}+\dfrac{q_x^2}{2\left(q_x^2+\zeta^{-2}\right)}\right), & \left|\mathbf{r}_{||}-\mathbf{r}_{||}^{'}\right| = 0 \end{cases}$$

and $\rho_{ij}(\mathbf{r}_{||}) = \psi_i^*(\mathbf{r}_{||})\psi_j(\mathbf{r}_{||})$

From both the equations for ultra-thin body and nanowires, one can see that the scattering kernel is dependent on the non-local distance. The scattering kernel, in turn is integrated along with the squared of the wavefuctions to get the corresponding rate for a particular momentum and screening length. An equivalent expression for the local case would only correspond to truncating terms other than the diagonal in the scattering kernel. The local version of scattering kernels for ultra-thin body and nanowire can be written as follows

$$I_{Local}(q_{||},z,z') = \begin{cases} \dfrac{1}{\sqrt{q_{||}^2+\zeta^{-2}}}\left[1-\dfrac{\zeta^{-2}}{2\left(q_{||}^2+\zeta^{-2}\right)}\right], & |z-z'| = 0 \\ 0, & |z-z'|\neq 0 \end{cases} \tag{4.5}$$

$$I_{Local}(q_x,\mathbf{r}_{||},\mathbf{r}_{||}^{'}) = \begin{cases} \left(\dfrac{1}{2}+\dfrac{q_x^2}{2\left(q_x^2+\zeta^{-2}\right)}\right), & \left|\mathbf{r}_{||}-\mathbf{r}_{||}^{'}\right| = 0 \\ 0, & \left|\mathbf{r}_{||}-\mathbf{r}_{||}^{'}\right|\neq 0 \end{cases} \tag{4.6}$$

The scaling factor is now just a division of form factors for the local case with the non-local one. In effective mass basis, the factor as such does not have an explicit effective mass

dependence (implicitly through energy-momentum relation) and depends significantly on the spatial nature of modes, dimension of the device and screening length. The scaling factor for both these cases can be represented as

$$S_{UTB} = \frac{\int_0^{2\pi} d\theta \int_0^{L_z} \int_0^{L_z} dz dz' \rho_{ij}(z)\rho_{ij}(z') I(|\tilde{\mathrm{k}}_{||} - \tilde{\mathrm{k}}'_{||}|, z, z')}{\int_0^{2\pi} d\theta \int_0^{L_z} \int_0^{L_z} dz dz' \rho_{ij}(z)\rho_{ij}(z') I_{Local}(|\tilde{\mathrm{k}}_{||} - \tilde{\mathrm{k}}'_{||}|, z, z')} \tag{4.7}$$

$$S_{wire} = \frac{\int_0^{L_y} \int_0^{L_z} \int_0^{L_y} \int_0^{L_z} \mathbf{dr}_{||} \mathbf{dr}'_{||} \rho^*_{ij}(\mathbf{r}_{||})\rho_{ij}(\mathbf{r}'_{||}) I(q_x, \mathbf{r}_{||}, \mathbf{r}'_{||})}{\int_0^{L_y} \int_0^{L_z} \int_0^{L_y} \int_0^{L_z} \mathbf{dr}_{||} \mathbf{dr}'_{||} \rho^*_{ij}(\mathbf{r}_{||})\rho_{ij}(\mathbf{r}'_{||}) I_{Local}(q_x, \mathbf{r}_{||}, \mathbf{r}'_{||})} \tag{4.8}$$

Fig 4.8 shows the scaling factor variation with energy for different confinement thicknesses for GaAs ultra-thin body. Scaling factor is non-monotonic and shows a oscillatory behaviour with increasing confinement thickness. Multiple kinks present in the scaling factor are associated with higher modes contributing to the scattering rate. With increasing confinement thickness the scaling factor converges to a shape that is consistent with NEGF result from Fig. The average scaling factor for 100 nm confinement thickness is 2.2 which is close to the NEGF result of 1.5. Scaling factor trend with energy is captured correctly and the device becomes more and more bulk like.

Fig 4.9 shows the scaling trend for GaAs nanowires for dimensions ranging from $2x2nm^2$ upto $10x10nm^2$. Scaling factor in general is larger for wires in comparison with ultra-thin bodies and bulk devices. With increasing wire dimensions, the scaling factor decreases as expected. In literature, a scaling factor of 10x is often applied to account for the non-local nature of scattering. However, from this plot it is evident that the factor also varies sharply with dimensions.

4.4 Conclusion

In summary, diagonal approximations to non-local scattering simulations were discussed. It was shown that commonly employed crude local approximation underestimates both the scattering rates and other physical quantities such as the Urbach parameter by a

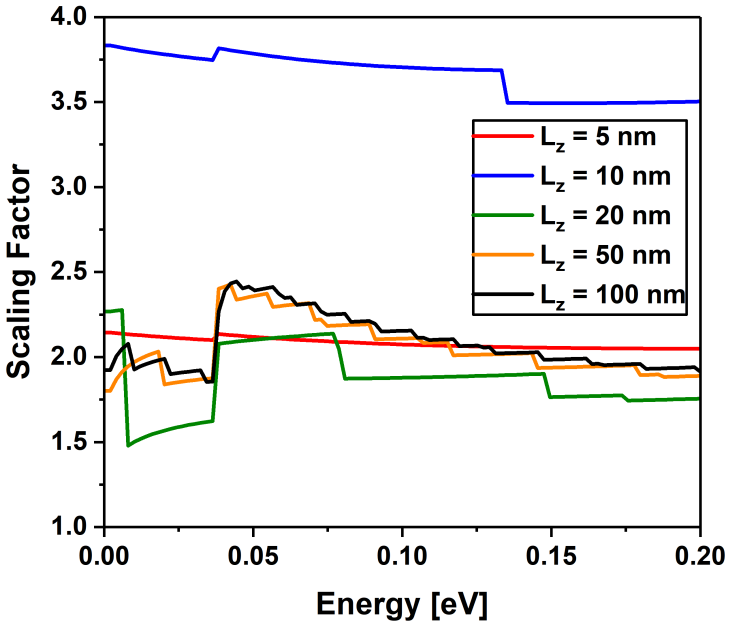

Fig. 4.8.: Variation of local scaling factor with energy for different confinement thicknesses for GaAs ultra-thin body. With increasing confinement thickness, scaling factor converges to a bulk like shape.

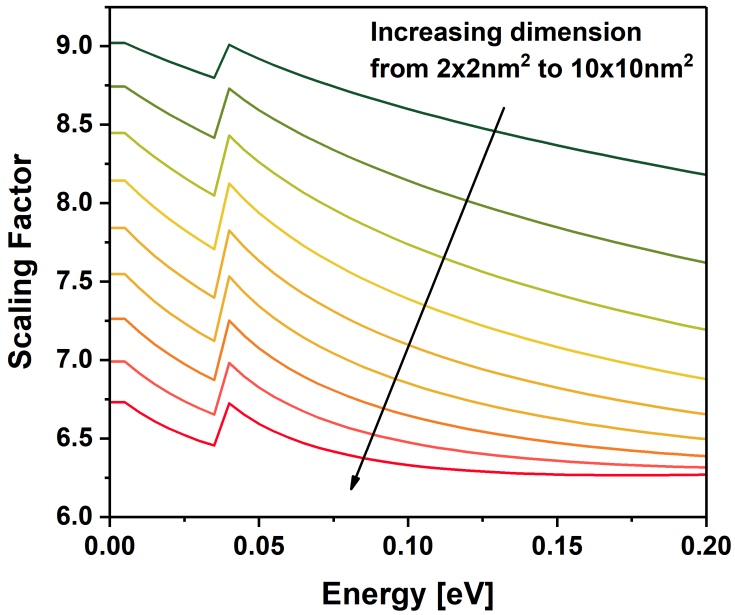

Fig. 4.9.: Variation of local scaling factor with energy for different nanowire dimensions. Scaling factor decreases with increasing dimension and in general has a higher value compared to bulk and ultra-thin body devices.

factor of $\sqrt{2}$ for bulk devices. It is shown that the local scaling rule as such is not a simple constant but depends on energy, temperature, material dimensions and screening. A physics based model using the Fermi's golden rule approach is employed to extract scaling factors for different devices. This approach is based on excluding/truncating terms within the scattering kernel to mimic local scattering and extract scaling factor from it. It is shown that the scaling factor is indeed energy dependent and bulk scaling factor resembling the NEGF result is achieved. Also, with increasing confinement the scaling factor increases highlighting the need for physics based local approximation model. In the next chapter, validity of this local approximation model in non-equilibrium regime will be studied by simulating InAs/GaSb TFET with non-local POP scattering.

5. ATOMISTIC SIMULATION OF III-V GASB/INAS NANOWIRE TFET WITH NON-LOCAL POLAR OPTICAL PHONON SCATTERING

5.1 Summary

In this chapter, impact of non-local polar optical phonon scattering (POP) is investigated through an atomistic simulation of III-V GaSb/InAs nanowire tunneling field effect transistor (TFET). Comparison of rigorous non-local scattering simulation against a simple local approximation and the newly developed physics-based scaling factor approach is performed. Impact of polar optical phonons on tunneling transport is investigated in detail.

5.2 Motivation

Tunnel field-effect transistors (TFETs) are promising candidates to sustain the Moore's law scaling. Their ability to provide sub-60 mV/dec subthreshold slope offers possibilities to operate transistors at low voltages and perform low-power computation. A plethora of materials such as InGaAs, GaSb and InAs are considered as potential candidates as TFETs due to their direct band gap and lower effective masses which is important in the context of tunneling [10–14]. Tunneling transistors provide sub-thermal switching by filtering out the high energy states in the Fermi distribution and by clever band engineering. Steep switching is achieved by a sudden onset of density of states through band alignment. Despite the ongoing research in TFETs, only a handful devices have managed to achieve sub-60 mV/dec SS [10, 15–17]. This is mainly due to imperfections in the device contributing to higher OFF current and SS. These imperfections include phonon scattering, alloy disorder, roughness, heavy doping induced band tail states and interface trap states which prevent sub-60 mV/dec SS performance.

On the other hand, simulation results have shown extremely positive results for several TFETs. Available ballistic NEGF approaches provide optimistic results with SS as low as 20mV/dec being reported [95–98]. Hence, there is a need to address this gap and provide quantitative and qualitative predictions that come close to experimental observations. Among the scattering mechanisms, polar optical phonon scattering (POP) is one of the dominant scattering mechanisms in the polar materials and is responsible for phonon assisted tunneling processes and formation of band tail states which are known to contribute to current [99]. However, simulating TFETs with polar optical phonons has been a major challenge due to the non-locality of the scattering process. This non-locality increases the computational burden and often non-local scattering terms techniques are truncated while simulating POP scattering [65, 100] or an empirical scaling factor is used to account for the underestimation of scattering [66].

In this work, a physically consistent model to treat POP scattering with non-locality through self-energies has been developed and applied to a GaSb/InAs nanowire TFET. This method has been implemented within the multipurpose device simulator, NEMO5 and is available in multiple electronic models (e.g. effective mass, tight binding, Wannier function representations) [44] Non-local scattering calculation is achieved through a recently developed non-local recursive Green's function approach [94] which enables calculation of off-diagonal Green's function elements which is necessary for calculating non-local scattering contributions. A physics based scaling factor approach is developed that provides appropriate scaling factors to use while truncating the self-energy to usual local approximations so that the total impact of non-local scattering is captured. Using this approach, nanowire I-V results are compared against a simple ballistic approach and physical explanation for the behaviour is provided through current density plots which capture essential phonon assisted and band assisted tunneling process consistently.

5.3 Simulation approach

Ultrascaled devices such as ultra-thin bodies and nanowires require atomistic resolution to capture essential physics. The device Hamiltonian is described in the empirical tight binding representation with a 10-band sp3d5s* tight binding model. Tight binding parameters for InAs are taken from [101] and for GaSb are taken from [102]. Device is simulated with NEGF using the non-local recursive Green's function approach (non-local RGF) [94]. In the usual recursive Green's function scheme [91], device is segmented into layers, and the diagonal blocks of the Green's functions, G^R and $G^<$ are solved recursively. However, now we need to evaluate off-diagonal elements of self-energy as well. Hence, the non-local recursive Green's function approach is employed. An adaptive energy mesh is employed to resolve the band edges and density with finer resolution as described in [103]. Modeling TFETs involves inclusion of both valence and conduction band electron densities. However, due to the large energy window of the valence band, electrons and holes are modeled instead. This ensures that the energy range is limited to few k_BT above and below the Fermi window. Wherever there is a tunneling from a valence band state to a conduction band state, there is a transition of particles from holes to electrons and vice-versa. This transition is modeled by linearly interpolating the change in particle type. The spatial dependence of the conduction valence band edge is used to decide whether a particle is considered an electron or hole. In the transition region near the tunneling gap, a linear interpolated factor is used to smoothly transition between electrons and hole.

The NEGF equations with scattering self-energies involved solving the retarded and lesser Green's function as follows

$$\left(E - H - \Sigma^R_{source} - \Sigma^R_{drain} - \Sigma^R_{scatt}\right) G^R = I \tag{5.1}$$

$$G^< = G^R \left(\Sigma^<_{source} + \Sigma^<_{drain} + \Sigma^<_{scatt}\right) G^{R\dagger} \tag{5.2}$$

Polar optical phonon scattering self-energies for nanowires are expressed as

$$\Sigma^{<}\left(\vec{x}_1,\vec{x}_2,E\right)=\frac{e^2}{(2\pi)^3}\left(\frac{1}{\epsilon_\infty}-\frac{1}{\epsilon_s}\right)\frac{\hbar\omega_o}{2\epsilon_o}I(\vec{x}_1,\vec{x}_2)$$
$$\times\left[n_oG^{<}\left(\vec{x}_1,\vec{x}_2,E-E_o\right)+\left(1+n_o\right)G^{<}\left(\vec{x}_1,\vec{x}_2,E+E_o\right)\right] \tag{5.3}$$

$$\Sigma^{R}\left(\vec{x}_1,\vec{x}_2,E\right)=\frac{e^2}{(2\pi)^3}\left(\frac{1}{\epsilon_\infty}-\frac{1}{\epsilon_s}\right)\frac{\hbar\omega_o}{2\epsilon_o}I(\vec{x}_1,\vec{x}_2)$$
$$\times\left[(1+n_o)G^{R}\left(\vec{x}_1,\vec{x}_2,E-E_o\right)+n_oG^{R}\left(\vec{x}_1,\vec{x}_2,E+E_o\right)+\frac{1}{2}G^{<}(\vec{x}_1,\vec{x}_2,E-E_o)\right.$$
$$\left.-\frac{1}{2}G^{<}(\vec{x}_1,\vec{x}_2,E+E_o)+i\int\frac{d\tilde{E}}{2\pi}G^{<}\left(\vec{x}_1,\vec{x}_2,\tilde{E}\right)\left(Pr\frac{1}{E-\tilde{E}-E_o}-Pr\frac{1}{E-\tilde{E}+E_o}\right)\right] \tag{5.4}$$

where

$$I(\vec{x}_1,\vec{x}_2)=\begin{cases}\dfrac{4\pi^2}{a}\left[\dfrac{1}{2\left(\zeta^2\left(\dfrac{\pi}{a}\right)^2+1\right)}-\dfrac{3a}{2\zeta\pi}tan^{-1}\left(\dfrac{\zeta\pi}{a}\right)+1\right], & |\vec{x}_1-\vec{x}_2|=0\\ \dfrac{\pi^2}{\zeta}\left(\dfrac{2\zeta}{|\vec{x}_1-\vec{x}_2|}-1\right)e^{-|\vec{x}_1-\vec{x}_2|/\zeta} & |\vec{x}_1-\vec{x}_2|\neq 0\end{cases} \tag{5.5}$$

$\hbar\omega_o$ is the LO phonon frequency, ϵ_s and ϵ_∞ correspond to the static and infinite frequency dielectric constants. n_o is the Bose-Einstein distribution and ζ is the screening length. Screening length is calculated within the Lindhard formalism [104] as follows

$$\zeta_{Lindhard}=\left(\frac{e^2}{\epsilon_o\epsilon_r}\frac{-2}{(2\pi)^3}\int d\vec{q}\,\frac{\partial f}{\partial\epsilon}\bigg|_{\epsilon(\vec{q})}\right)^{-1/2} \tag{5.6}$$

where f is the Fermi distribution.

Solving a complete self-consistent simulation between transport involving self-consistent Born iterations and Poisson is challenging for in a multi-band basis due to the enormous computational load. To alleviate the problem, self-consistent Born iterations now involve solving off-diagonal elements of scattering self-energy which increase the computational load several orders even with the non-local recursive Green's function approach. Hence, the device is solved charge self-consistently with Poisson's equation and ballistic NEGF. The converged potentials are now imported into the transport solver and solved with non-local

recursive Green's function with polar optical phonon scattering until current is uniform throughout the device. The potentials, in general vary with scattering but due to computational constraint the ballistic potential is assumed to represent the potential profile for scattering. Charge density and current are extracted as follows

$$\begin{aligned} n(\vec{x}) &= \int n(\vec{x}, E) dE \\ &= \frac{1}{2\pi} \int \Im \left(diag \left(tr \left(G^{<}(\vec{x}, \vec{x}, E) \right) \right) \right) dE \end{aligned} \tag{5.7}$$

$$J_{i \to i+1}(E) = \frac{q}{\hbar} \int \frac{dE}{2\pi} \times 2\Re \left(tr \left[H_{i,i+1}, G^{<}_{i+1,i}(E) \right] \right) \tag{5.8}$$

Despite the ability to simulate off-diagonal elements of self-energy with non-local recursive Green's function approach, only a couple of off-diagonal elements can be calculated for a reasonable device in multi-band basis due to the enormous computational load. A compensation/scaling factor for the self-energies will be extremely useful in this regard where we can multiply the local self-energies (which are computatiaonally cheap) with the appropriate scaling factor to account for the effect of non-locality. Major requirement of the scaling factor should be that it's physics based and dependent on the confinement potential, bandstructure and energy. In this regard, a physics based scaling factor approach is developed to capture the effect of non-locality. Scaling factors are calculated based off of the Fermi's golden rule for the corresponding device under interest and the respective factor is multiplied with diagonal self-energy so that it mimics the actual non-local self-energy which is numerically challenging to solve for a realistic device.

The scaling factor is based on effective mass approach and assumes a parabolic dispersion but in principle, this approach can be applied to a general dispersion relation (which will be need for hole transport). Fermi's golden rule expression (absorption branch) for nanowires for polar optical phonon scattering can be written as

$$\frac{1}{\tau_{ij,a}(E)} = \frac{e^2 \hbar \omega_{LO} N_{ph}}{\hbar^2} \left(\frac{1}{\epsilon_\infty} - \frac{1}{\epsilon_s} \right) \cdot \frac{2}{(2\pi)^2} \cdot \sqrt{2m^*} \left(\frac{F_a(k_x - k_x') + F_a(k_x + k_x')}{\sqrt{E - E_j + \hbar\omega_{LO}}} \right) \tag{5.9}$$

where $F(q_x) = \int_0^{L_y}\int_0^{L_z}\int_0^{L_y}\int_0^{L_z} \mathbf{dr}_{||}\mathbf{dr}_{||}^{'}\rho_{ij}^{*}(\mathbf{r}_{||})\rho_{ij}(\mathbf{r}_{||}^{'})I(q_x,\mathbf{r}_{||},\mathbf{r}_{||}^{'})$ and

$$I(q_x,\mathbf{r}_{||},\mathbf{r}_{||}^{'}) = \begin{cases} \left(\sqrt{q_x^2+\zeta^{-2}}\left|\mathbf{r}_{||}-\mathbf{r}_{||}^{'}\right| + \dfrac{q_x^2\left|\mathbf{r}_{||}-\mathbf{r}_{||}^{'}\right|}{\sqrt{q_x^2+\zeta^{-2}}}\right)\dfrac{K_1\left(\sqrt{q_x^2+\zeta^{-2}}\left|\mathbf{r}_{||}-\mathbf{r}_{||}^{'}\right|\right)}{2}, & \left|\mathbf{r}_{||}-\mathbf{r}_{||}^{'}\right| \neq 0 \\ \left(\dfrac{1}{2}+\dfrac{q_x^2}{2\left(q_x^2+\zeta^{-2}\right)}\right), & \left|\mathbf{r}_{||}-\mathbf{r}_{||}^{'}\right| = 0 \end{cases}$$

and $\rho_{ij}(\mathbf{r}_{||}) = \psi_i^{*}(\mathbf{r}_{||})\psi_j(\mathbf{r}_{||})$

From the equations above, one can observe that the scattering kernel is dependent on the non-local distance. The scattering kernel, in turn is integrated along with the squared of the wavefuctions to get the corresponding rate for a particular momentum and screening length. An equivalent expression for the local case would only correspond to truncating terms other than the diagonal in the scattering kernel. The local version of scattering kernels for nanowires can be written as follows

$$I_{Local}(q_x,\mathbf{r}_{||},\mathbf{r}_{||}^{'}) = \begin{cases} \left(\dfrac{1}{2}+\dfrac{q_x^2}{2\left(q_x^2+\zeta^{-2}\right)}\right), & \left|\mathbf{r}_{||}-\mathbf{r}_{||}^{'}\right| = 0 \\ 0, & \left|\mathbf{r}_{||}-\mathbf{r}_{||}^{'}\right| \neq 0 \end{cases} \tag{5.10}$$

The scaling factor is now just a division of form factors for the local case with the non-local one. In effective mass basis, the factor as such does not have an explicit effective mass dependence (implicitly through energy-momentum relation) and depends significantly on the spatial nature of modes, dimension of the device and screening length. The scaling factor can now be represented as

$$S_{wire} = \frac{\int_0^{L_y}\int_0^{L_z}\int_0^{L_y}\int_0^{L_z} \mathbf{dr}_{||}\mathbf{dr}_{||}^{'}\rho_{ij}^{*}(\mathbf{r}_{||})\rho_{ij}(\mathbf{r}_{||}^{'})I(q_x,\mathbf{r}_{||},\mathbf{r}_{||}^{'})}{\int_0^{L_y}\int_0^{L_z}\int_0^{L_y}\int_0^{L_z} \mathbf{dr}_{||}\mathbf{dr}_{||}^{'}\rho_{ij}^{*}(\mathbf{r}_{||})\rho_{ij}(\mathbf{r}_{||}^{'})I_{Local}(q_x,\mathbf{r}_{||},\mathbf{r}_{||}^{'})} \tag{5.11}$$

Fig. 5.1 shows the GaSb/InAs TFET considered in this study. Device considered is a $2 \times 2nm^2$ nanowire with a device length of 36 nm. Source region is 12nm long and is p-doped GaSb with a doping concentration of $5 \times 10^{19} cm^{-3}$. Channel region is 12nm long and is taken to be intrinsic InAs. Drain region is 12nm long as well and is n-doped InAs with a doping concentration of $2 \times 10^{19} cm^{-3}$. Intrinsic region is surrounded by gate

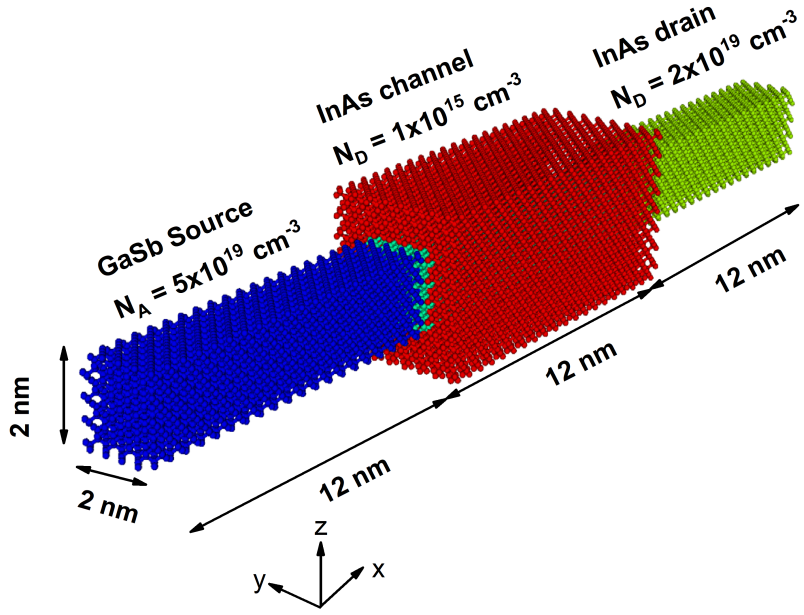

Fig. 5.1.: Schematic of the simulated TFET device. Nanowire dimensions are $2nm \times 2nm \times 36nm$. Source is p-doped GaSb, gate region is intrinsic InAs and drain is n-doped InAs region each 12nm in the transport direction. Oxide thickness is 1 nm.

oxide 1nm thick with a dielectric constant of 20. Oxide region is considered only in the Poisson's equation and is not part of transport. Phonon scattering parameters are averaged across InAs and GaSb parameters and remains constant throughout the device. LO phonon energy is taken to be 30 meV, static and infinite frequency dielectric constants are taken to be 15.42 and 13.35. These material parameters have been taken from [105]. Screening length is set to 3nm. POP scattering simulations are performed both with simple local approximation where the off-diagonal terms are truncated to zero and by actually including off-diagonal elements upto a non-local range of 0.3 nm (1st offdiagonal) to cover non-local scattering. Subsequently, the scaling factor procedure described above is used to multiply the local self-energy with an appropriate scaling factor for the given non-local range to account for the underestimation of scattering. Based on the calculations, the scaling factor is estimated to be 5 for a non-local range of 0.3 nm (energy averaged).

5.4 Results

Simulations results with nanowire TFET are discussed in this section. Fig. 5.2 shows the I-V characteristics of the GaSb/InAs TFET over the voltage range 0-0.35V. There are several important observations that one can make from this figure. Ballistic simulation of TFET provides a very good ON-OFF ratio ($\approx 10^3$) resulting in a steep switching of transistor. This happens in a voltage range of about 50 mV which corresponds to the transition point where the conduction band profile of the channel meets the valence band edge of the source. However, POP scattering with a simple local approximation where the off-diagonals are truncated to zero shows an immediate jump in OFF current. Also, the transition is not as steep as the ballistic case highlighting the impact of phonon scattering in tunneling process. Non-local POP scattering increases the OFF current floor further due to additional elements of the self-energy contributing to the scattering process. Local POP scattering with scaling factor of 5x increases the current as expected due to strong phonon scattering. It is interesting to note that the predicted scaling factor of 5x from Fermi's

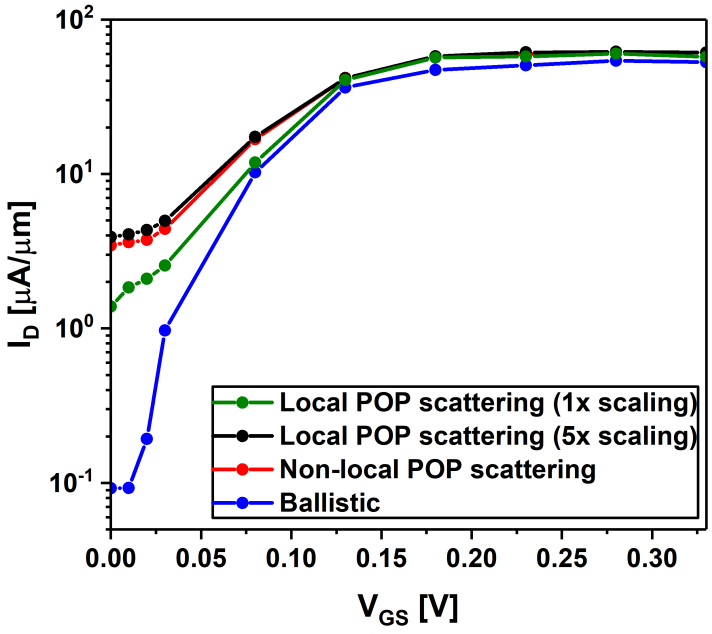

Fig. 5.2.: Current-voltage characteristics of the device. Ballistic simulation shows almost 3 orders of range in current with abrupt switching within 50 mV of V_{GS}. POP scattering with 1x scaling factor shows an order of magnitude increase in the OFF current and an increase in subthreshold slope (SS). Non-local POP scattering and local scattering with 5x scaling show good agreement with each other and raise the OFF current floor and SS further.

golden rule agrees quite well with the complete non-local simulation providing confidence in the scaling factor extraction approach.

Fig. 5.3 shows the subthreshold slope as a function of V_{GS} for all the simulation cases discussed above. Ballistic simulation shows an optimistic SS of 16 mV/dec due to a sharp transition between the ON-OFF state. However, with the addition of scattering, the SS is raised above the thermal limit and the device no longer offers subthreshold slope < 60 mV/dec. Increasing the non-locality of scattering further enhances the SS making it a poor switching device.

A detailed physical picture behind the transport process can be observed by looking at the energy resolved current density across the device as shown in Figs. 5.4 and 5.5 for the OFF state and Figs. 5.6 and 5.7 for the ON state of the device. OFF state ballistic profile

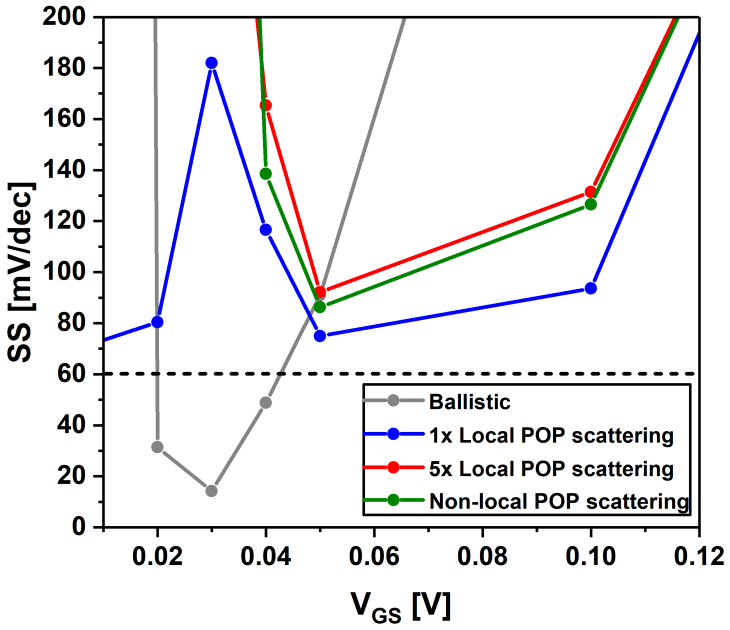

Fig. 5.3.: Comparison of subthreshold slope (SS) for ballistic and scattering cases. Ballistic case assumes the ideal switching scenario and achieves a low SS of 16 mV/dec. All scattering cases enhance the OFF current and the SS thereby raising it above the thermal limit. Increasing the scaling factor of POP scattering raises the minimum SS from 80 mV/dec to 90 mV/dec.

has a low current density due to the large tunneling distance and has a peak only in the transmission energy window. However, the moment scattering is turned on, the current density is no longer restricted to the ballistic energy profile and is smeared out throughout the Fermi window. There are several interesting features in the OFF state. Firstly, the current density in general is higher than the ballistic case due to phonon assisted tunneling processes. Secondly, there are several sharp density channels separated by LO phonon energies. At energy range [-0.2,0.0] eV on the source side, there are several peaks that correspond to phonon emission processes. There is significant tunneling in the channel region with electrons tunneling by absorbing LO phonons and propagating to the drain side. This increases both the OFF current and also results in a higher SS since the device no longer has a energy barrier window where transmission can be prevented. Transmission can now occur in this energy barrier window through phonon assisted tunneling processes.

The ON state, on the other hand, does have distinguishing features between the ballistic and scattered case but is not as dramatic as the OFF state. In the ON state, since the transmission in general is higher due to the smaller tunneling energy and distance, current density is high in both ballistic and scattered case. However, some additional channels are created with phonon abosrption process on the source side which provides tunneling windows that decays down rapidly with energy ([-0.4,-0.2] eV energy range). The rapid decay of the LO phonon echoes is due to vanishing Fermi distribution function which decays rapidly beyond the Fermi energy window. This results in current densities being similar in the ON state with the phonon scattering current slightly higher than the ballistic case.

Impact of phonon scattering and it's non-locality can be observed by taking cross section cuts of energy resolved current density J(E) at various points. Figs. 5.8 and 5.9 show the cross section cuts of the current density at x=5nm (p-doped GaSb region) and x=20nm (tunneling region). In the p-doped GaSb region, one can clearly observe the narrow region in which ballistic transmission occurs and the current density drops by 6 orders of magnitude in the region outside the window. However, with phonon scattering, energy values higher than the window are enhanced due to decreasing tunneling window and phonon as-

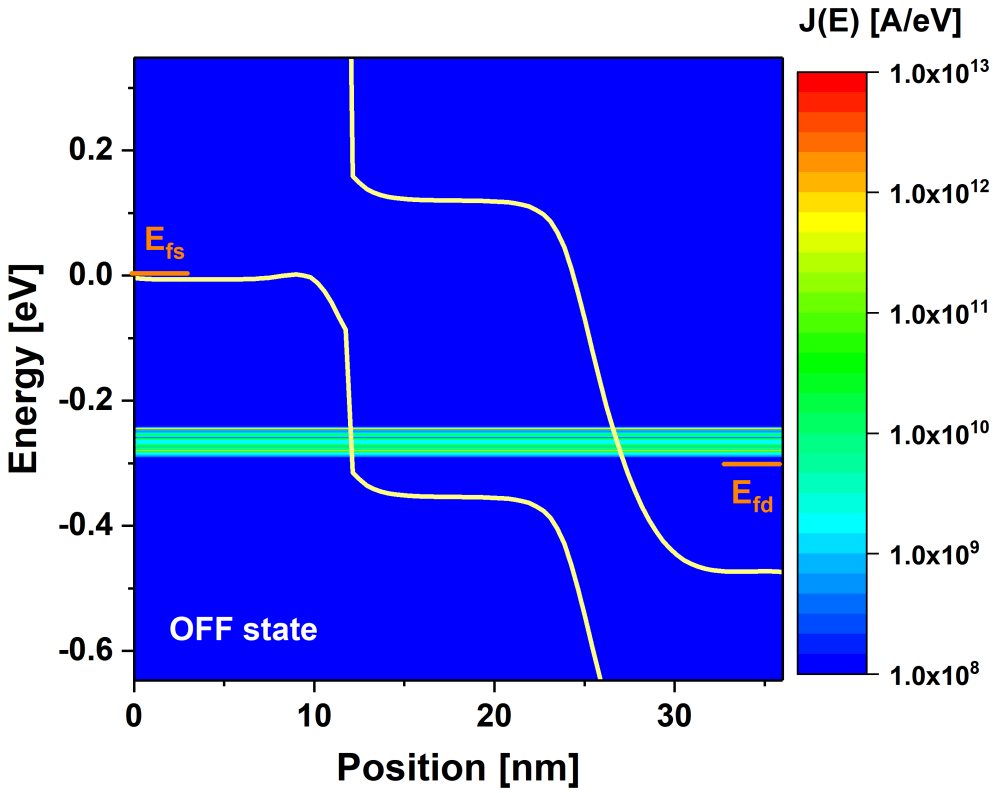

Fig. 5.4.: Ballistic energy resolved current density J(E) at OFF state along with the potential profile.

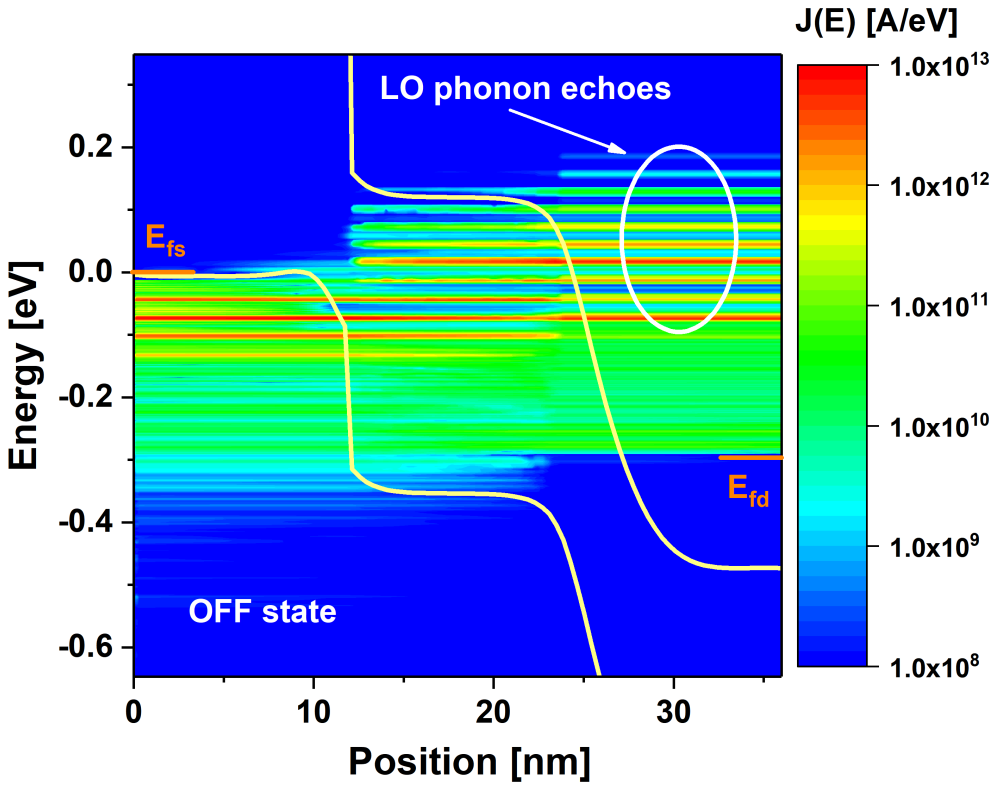

Fig. 5.5.: Energy resolved current density J(E) at OFF state along with the potential profile in the presence of non-local POP scattering. Phonons aid the tunneling process through band tail states and additional phonon echo peaks flooding the tunneling region with current thereby raising the OFF current. LO phonon echoes spaced at 30meV (LO phonon frequency of InAs) can be observed in the drain side.

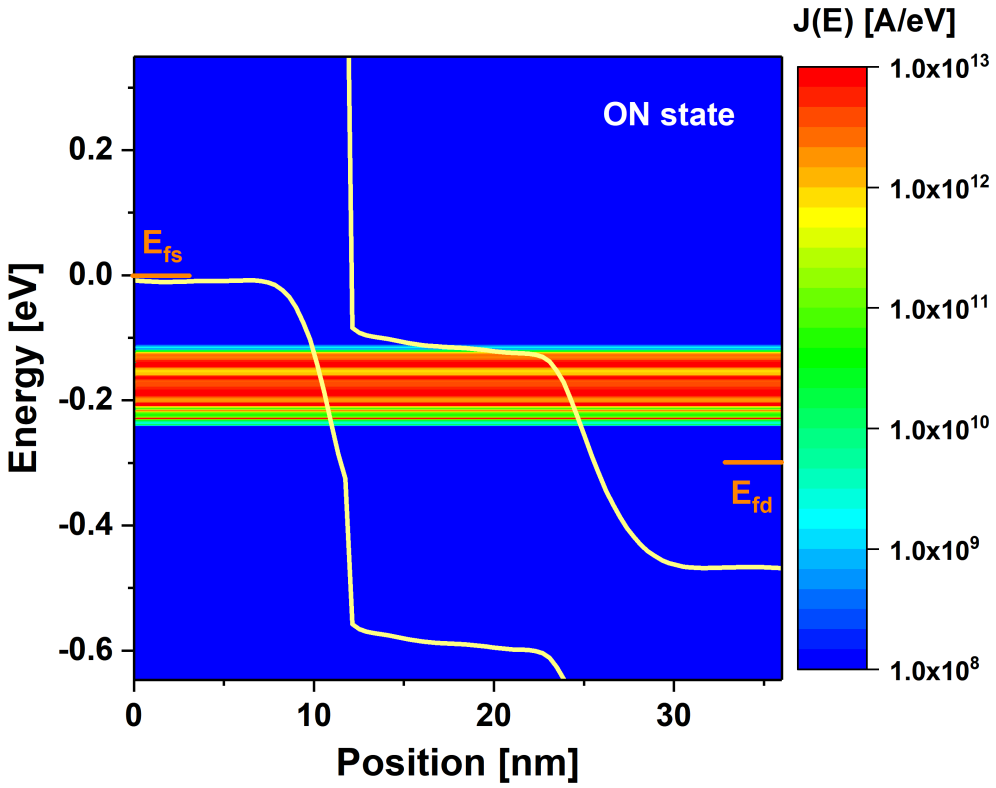

Fig. 5.6.: Ballistic energy resolved current density J(E) at ON state along with the potential profile.

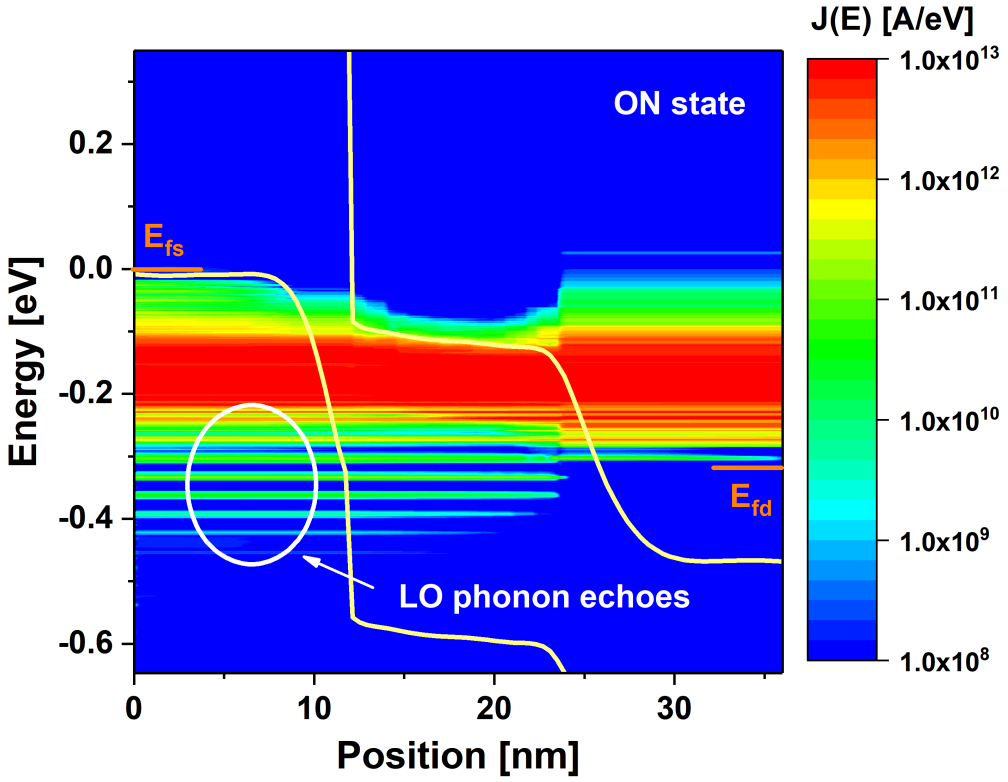

Fig. 5.7.: Energy resolved current density J(E) at ON state along with the potential profile in the presence of non-local POP scattering. Phonon scattering enhances not only the OFF state current but also the OFF state current by conduction from band tail states and phonon emission processes. LO phonon echoes spaced apart at 30 meV (LO phonon frequency of GaSb) can be observed in the source side aiding the tunneling process.

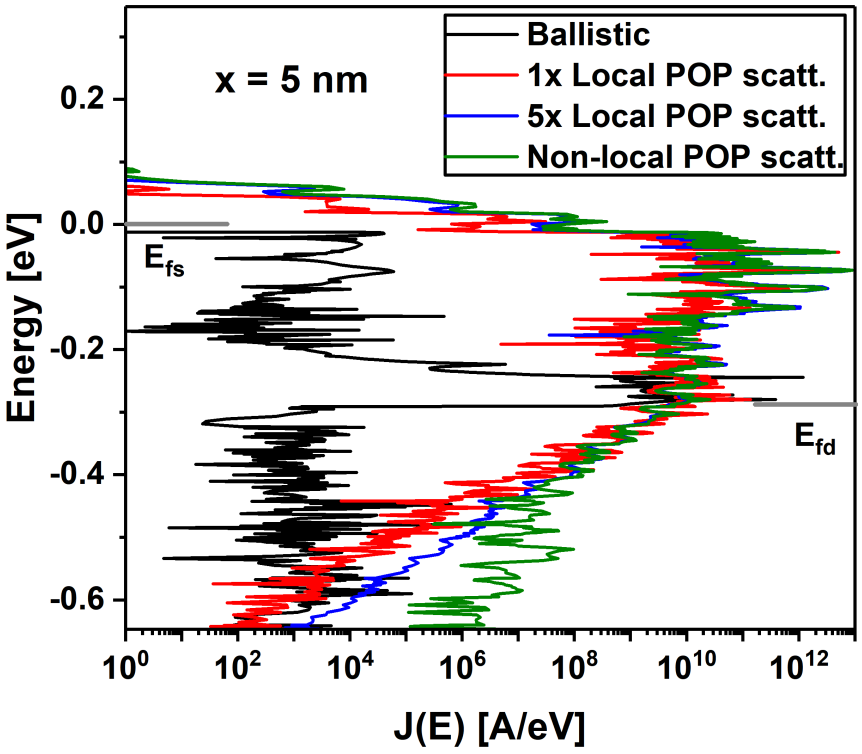

Fig. 5.8.: Cut section of energy resolved current density at x = 5nm (p-doped GaSb region). Scattering enhances the tunneling current by orders of magnitude through hole-phonon emission process. Exponentially decaying current density from band tail states can be observed above the valence bandedge.

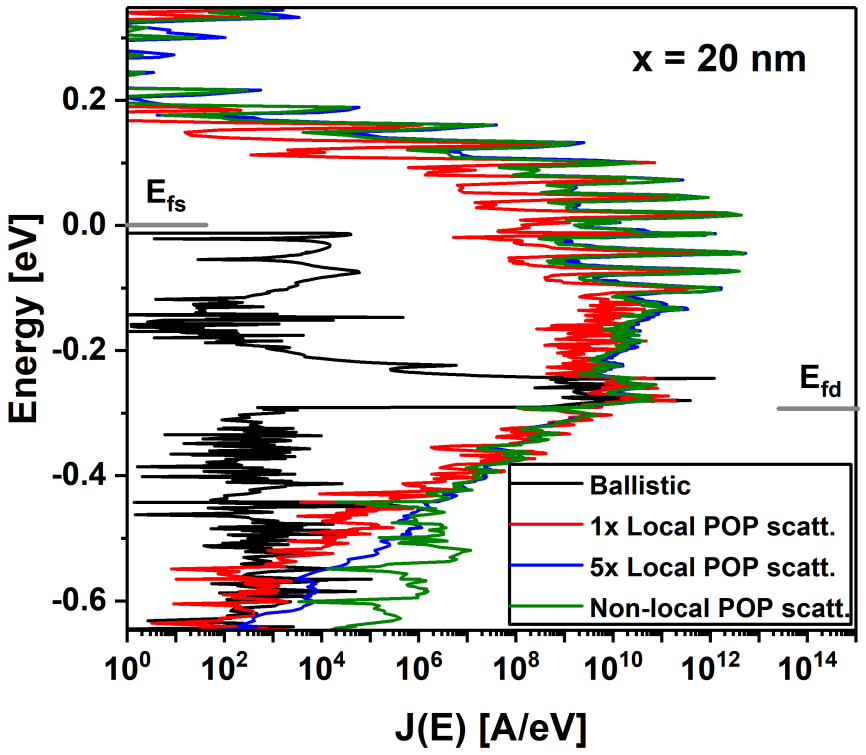

Fig. 5.9.: Cut section of energy resolved current density at x = 20nm (tunneling region). Scattering enhances the tunneling current by orders of magnitude through hole-phonon emission and band tail states conduction. Distinct conduction channels separated by LO phonon energy can be observed. Exponentially decaying current density from band tail states can be observed above the valence bandedge.

sisted tunneling process. Once the bandedge is reached, transport does not stop abruptly (as one would expect in a ballistic transport situation) but decreases exponentially with echoes separated apart by LO phonon energy. These echoes are generated by exponentially decaying band tail states present above the valence band edge. These band tail states are generated by inelastic multi-phonon emission processes that are automatically captured in the self-consistent Born picture in NEGF. Also, the scaling factor approach captures not only the non-local scattering current accurately but also the density profile as seen in Fig. 5.8. There is deviation at higher energies where the scaling rule fails but the important energies are captured accurately.

In the intrinsic region (Fig. 5.9), one can observe that the current density has very well defined peak states that are separated by LO phonon energies. This effect can only be captured by a true inelastic scattering process where these interesting features are exhibited. These channels of current density correspond to electrons tunneling across the junctions aided by a phonon emission/absorption process and similar to the current density in the p-doped region, they decay down gradually due to exponentially decaying band tail states. The simulation can capture both phonon assisted and band tail assisted tunneling quite well and provides an intuitive explanation behind the observed I-V profile with scattering.

5.5 Conclusion

An atomistic simulation of III-V GaSb/InAs nanowire TFET is performed with non-local polar optical phonon scattering and the impact of scattering is assessed. Device is simulated with NEGF approach with scattering included within the self-consistent Born iteration scheme. A scaling factor methodology is developed to provide physics based scaling factors for non-local scattering using Fermi's golden rule. Scattering self-energy is solved using 3 different scenarios - local approximation with truncation of non-local terms, local approximation with scaling factor and non-local scattering with a finite non-local range. I-V characteristics for all the cases are compared and scattering is shown to increase both OFF current floor and SS due to enhanced tunneling from phonon assisted

and band tail assisted tunneling. Detailed tunneling process is analyzed by looking at the energy resolved current density profile of the device. Scaling factor is shown to capture the actual non-local scattering quite accurately.

6. QUANTITATIVE PREDICTION OF URBACH TAILS AND BAND GAP NARROWING IN BULK AND CONFINED III-V DEVICES WITH NEGF APPROACH

6.1 Summary

In this chapter, band tails or Urbach tails and band gap narrowing will be discussed in detail. Physics of band tails/bandgap narrowing will be investigated through POP and impurity simulations. Extraction of band tail parameter / Urbach parameter and band gap narrowing parameter will be shown along with comparison with available experimental data.

6.2 Motivation

The need for ultra-low power applications, efficient lighting and renewable energy source have resulted in the quest for novel devices such as the tunnel field-effect transistor (TFET) [11, 106, 107], GaN/InGaN light-emitting diodes [21–23] and high-performance solar cells [24–26]. Carrier transport and sub-60 mV subthreshold slope (SS) performance in TFETs, optical recombination and generation is highly dependent on a good description of conduction/valence band edge properties. Tailing of band edge states (known as Urbach tails) and band gap narrowing can alter the behaviour of the device. Switching behaviour of TFET is drastically affected by such tailing states [19, 20]. Urbach tails (band tails) are exponentially decaying tailing of density-of-states below band edge and is known to place a fundamental limit on the lowest achievable SS in TFETs [10, 19]. On the other hand, Band gap narrowing alters the optical frequency at which recombination/generation occurs and shift the turn-on/threshold voltage of optical devices [21, 108] and tunneling current in TFETs. Band tailing and band gap narrowing effects are mainly attributed to the interac-

tion of electrons/holes with environmental defects such as phonons, randomly distributed dopant impurity atoms and native lattice disorders/defects. They exhibit a strong dependence on temperature and doping concentration. [109–112]. Though the effect has been studied for quite some time, actual values used for a given material are based either on simplified analytical expressions or parameters that are directly extracted from experimental results. [20, 109, 110, 112, 113]. This presents few challenges. Firstly, the applicability of the expressions are limited either to the doping range, assumptions in the band dispersion relation (e.g. parabolic E-k). Secondly, dependence for confined devices such as ultra-thin body and nanowire is tough to predict due to the lack of available experimental measurements. In this work, the above problem is addressed by calculating band-tailing and band gap narrowing through scattering self-energies using the non-equilibrium Green's function (NEGF) approach with only material dependent parameters. Non-equilibrium Green's function (NEGF) approach is widely accepted as the most consistent approach to treat electronic, thermal and optoelectronic transport in a variety of devices [59–64]. It has been widely applied in modeling transistors [65–67], resonant-tunneling devices [68], metal-semiconductor contacts [41,69], phonon transport across interfaces [70], GaN/InGaN light-emitting diodes [21] with quantitative agreements with experimental data. NEGF approach enables a consistent treatment of different scattering mechanisms through scattering self-energies. Scattering is modeled through self-energies within the self-consistent Born approximation (SCBA) [60]. Amongst the scattering mechanisms present in doped III-V semiconductor, polar optical phonons (POP) and charged impurity scattering mechanisms are the dominant mechanisms [75, 114]. Both these scattering mechanisms are considered with electrostatic screening. Scattering self-energies are derived for both scattering mechanisms for both bulk and confined devices (ultra-thin body and nanowires) and the scattering rates are verified by comparing them against Fermi's golden rule validating the approach. Urbach tails and band gap narrowing parameters are then directly extracted by examining the converged density of states (DoS) from NEGF simulation for a given material. 4 candidate III-V materials - GaAs, InAs, GaSb and GaN are taken up for detailed study. Bulk, ultra-thin body of confinement thickness 4nm and ultra-scaled nanowire of $2 \times 2nm^2$

dimensions are analyzed. Comparison against available experimental results from photoluminescence measurements are performed for bulk devices. Guideline values for Urbach tail and band gap narrowing are presented for ultra-thin body and nanowire devices.

6.3 Simulation approach

6.3.1 Modeling self-energies

Electron-phonon interaction modeled through the Fröhlich coupling [115]. Scattering potential is given as

$$|U_q|^2 = e^2 \frac{\hbar\omega_q}{2\epsilon_o} \left(\frac{1}{\epsilon_\infty} - \frac{1}{\epsilon_s} \right) \frac{q^2}{(q^2 + \zeta^{-2})^2} \tag{6.1}$$

The static and dynamic dielectric constant are represented by ϵ_s and ϵ_∞ respectively. The phonon frequency and momentum are represented by $\hbar\omega_q$ and q respectively. Since maximal interaction is with longitudinal-optical (LO) phonons, the phonon frequency is assumed to be dispersionless and the frequency corresponds to the value at the Gamma point. Total screening is assumed to be the sum of screening from valence band electrons (ϵ_0), electronic (ζ) and phononic ($1/\epsilon_\infty - 1/\epsilon_s$). Electrostatic screening is calculated within the Lindhard formalism [104]. Charged impurity scattering is modeled by assuming an ensemble average of homogeneous distribution of impurity atoms. In this work, Brooks-Herring impurity scattering approach [79] is employed due to it's validity in the doping range studied for III-V materials. Electrostatic screening is calculated within the Lindhard formalism. The scattering potential is given by

$$eV(q) = \frac{Ze^2}{\epsilon_s \left(q^2 + \zeta^{-2}\right)} \tag{6.2}$$

Bulk, ultra-thin body and nanowire devices all are modeled in atomic resolution with atoms in native lattice. GaSb, InAs and GaSb are treated in the conventional zincblende cystal structure and GaN is treated in the wurtzite structure. Both POP and impurity scattering mechanisms are long-ranged and the extent of non-locality is determined by the

screening length. Due to the non-local nature of scattering, self-energy expressions need to be derived separately for each degree of confinement (bulk, ultra-thin body and nanowires) for POP and impurity scattering. A 10-band sp3d5s* tight-binding Hamiltonian is used for both conduction and valence bands [116, 117]. Scattering self-energies are assumed to be atom block-diagonal. Self-energies are block-diagonal in orbital space and inter-orbital transitions exist only on the same atom position. Due to the diagonal treatment of non-local scattering self-energies, scattering will be underestimated. To compensate for this underestimation, a new scaling factor calculation is proposed where the factors are directly calculated from Fermi's golden rule rather than using an empirical scaling factor.

POP scattering bulk self-energies are represented as

$$\begin{aligned}&\Sigma^{<}\left(z_1,z_2,k_{||},E\right)\\&=\frac{e^2\pi}{(2\pi)^3}\left(\frac{1}{\epsilon_\infty}-\frac{1}{\epsilon_s}\right)\frac{\hbar\omega_o}{2\epsilon_o}\int d\vec{l_{||}}\frac{e^{-\sqrt{q_{||}^2+\zeta^{-2}}|z_1-z_2|}}{\sqrt{q_{||}^2+\zeta^{-2}}}\left(1-\frac{\zeta^{-2}\left|z_1-z_2\right|}{2\sqrt{q_{||}^2+\zeta^{-2}}}-\frac{\zeta^{-2}}{2\left(q^2+\zeta^{-2}\right)}\right)\\&\left[n_oG^{<}\left(z_1,z_2,l_{||},E-E_o\right)+\left(n_o+1\right)G^{<}\left(z_1,z_2,l_{||},E+E_o\right)\right]\end{aligned}\tag{6.3}$$

$$\begin{aligned}&\Sigma^{R}\left(z_1,z_2,k_{||},E\right)\\&=\frac{e^2\pi}{(2\pi)^3}\left(\frac{1}{\epsilon_\infty}-\frac{1}{\epsilon_s}\right)\frac{\hbar\omega_o}{2\epsilon_o}\int d\vec{l_{||}}\frac{e^{-\sqrt{q_{||}^2+\zeta^{-2}}|z_1-z_2|}}{\sqrt{q_{||}^2+\zeta^{-2}}}\left(1-\frac{\zeta^{-2}\left|z_1-z_2\right|}{2\sqrt{q_{||}^2+\zeta^{-2}}}-\frac{\zeta^{-2}}{2\left(q^2+\zeta^{-2}\right)}\right)\\&\times\left[\left(n_o+1\right)G^{R}\left(z_1,z_2,l_{||},E-E_o\right)+n_oG^{R}\left(z_1,z_2,l_{||},E+E_o\right)+\frac{1}{2}G^{<}\left(z_1,z_2,l_{||},E-E_o\right)\right.\\&\left.-\frac{1}{2}G^{<}\left(z_1,z_2,l_{||},E-E_o\right)+i\int\frac{d\tilde{E}}{2\pi}G^{<}(z_1,z_2,l_{||},\tilde{E})\left(Pr\frac{1}{E-\tilde{E}-E_o}-Pr\frac{1}{E-\tilde{E}+E_o}\right)\right]\end{aligned}\tag{6.4}$$

Similarly, the POP scattering UTB self-energies can be written as

$$\begin{aligned}&\Sigma^{<}\left(\vec{x}_1,\vec{x}_2,k_{||},E\right)=\frac{e^2}{(2\pi)^3}\left(\frac{1}{\epsilon_\infty}-\frac{1}{\epsilon_s}\right)\frac{\hbar\omega_o}{2\epsilon_o}\int dl_{||}I(k_{||},l_{||},\vec{x}_1,\vec{x}_2)\\&\times\left[n_oG^{<}\left(\vec{x}_1,\vec{x}_2,l_{||},E-E_o\right)+\left(1+n_q\right)G^{<}\left(\vec{x}_1,\vec{x}_2,l_{||},E+E_o\right)\right]\end{aligned}\tag{6.5}$$

$$\Sigma^R\left(\vec{x}_1,\vec{x}_2,k_{||},E\right)=\frac{e^2}{(2\pi)^3}\left(\frac{1}{\epsilon_\infty}-\frac{1}{\epsilon_s}\right)\frac{\hbar\omega_o}{2\epsilon_o}\int dl_{||}I(k_{||},l_{||},\vec{x}_1,\vec{x}_2)$$
$$\times\left[(1+n_o)G^R\left(\vec{x}_1,\vec{x}_2,l_{||},E-E_o\right)+n_oG^R\left(\vec{x}_1,\vec{x}_2,l_{||},E+E_o\right)+\frac{1}{2}G^<(\vec{x}_1,\vec{x}_2,l_{||},E-E_o)\right.$$
$$\left.-\frac{1}{2}G^<(\vec{x}_1,\vec{x}_2,l_{||},E+E_o)+i\int\frac{d\tilde{E}}{2\pi}G^<\left(\vec{x}_1,\vec{x}_2,l_{||},\tilde{E}\right)\left(Pr\frac{1}{E-\tilde{E}-E_o}-Pr\frac{1}{E-\tilde{E}+E_o}\right)\right] \tag{6.6}$$

where

$$I(k_{||},l_{||},\vec{x}_1,\vec{x}_2)=$$
$$\begin{cases}\pi\left[\sqrt{\left(k_{||}-l_{||}\right)^2+\zeta^{-2}}\,|\vec{x}_1-\vec{x}_2|+\dfrac{\left(k_{||}-l_{||}\right)^2|\vec{x}_1-\vec{x}_2|}{\sqrt{\left(k_{||}-l_{||}\right)^2+\zeta^{-2}}}\right]K_1\left(\sqrt{\left(k_{||}-l_{||}\right)^2+\zeta^{-2}}\,|\vec{x}_1-\vec{x}_2|\right), \\ \qquad |\vec{x}_1-\vec{x}_2|\neq 0 \\ \pi\left[1+\dfrac{\left(k_{||}-l_{||}\right)^2}{\left(k_{||}-l_{||}\right)^2+\zeta^{-2}}\right],\ |\vec{x}_1-\vec{x}_2|=0\end{cases} \tag{6.7}$$

Finally, the POP scattering wire self-energies are expressed as

$$\Sigma^<\left(\vec{x}_1,\vec{x}_2,E\right)=\frac{e^2}{(2\pi)^3}\left(\frac{1}{\epsilon_\infty}-\frac{1}{\epsilon_s}\right)\frac{\hbar\omega_o}{2\epsilon_o}I(\vec{x}_1,\vec{x}_2)$$
$$\times\left[n_oG^<\left(\vec{x}_1,\vec{x}_2,E-E_o\right)+\left(1+n_q\right)G^<\left(\vec{x}_1,\vec{x}_2,E+E_o\right)\right] \tag{6.8}$$

$$\Sigma^R\left(\vec{x}_1,\vec{x}_2,E\right)=\frac{e^2}{(2\pi)^3}\left(\frac{1}{\epsilon_\infty}-\frac{1}{\epsilon_s}\right)\frac{\hbar\omega_o}{2\epsilon_o}I(\vec{x}_1,\vec{x}_2)$$
$$\times\left[(1+n_o)G^R\left(\vec{x}_1,\vec{x}_2,E-E_o\right)+n_oG^R\left(\vec{x}_1,\vec{x}_2,E+E_o\right)+\frac{1}{2}G^<(\vec{x}_1,\vec{x}_2,E-E_o)\right.$$
$$\left.-\frac{1}{2}G^<(\vec{x}_1,\vec{x}_2,E+E_o)+i\int\frac{d\tilde{E}}{2\pi}G^<\left(\vec{x}_1,\vec{x}_2,\tilde{E}\right)\left(Pr\frac{1}{E-\tilde{E}-E_o}-Pr\frac{1}{E-\tilde{E}+E_o}\right)\right] \tag{6.9}$$

where

$$I(\vec{x}_1,\vec{x}_2)=\begin{cases}\dfrac{4\pi^2}{a}\left[\dfrac{1}{2\left(\zeta^2\left(\dfrac{\pi}{a}\right)^2+1\right)}-\dfrac{3a}{2\zeta\pi}tan^{-1}\left(\dfrac{\zeta\pi}{a}\right)+1\right],\ |\vec{x}_1-\vec{x}_2|=0\\ \dfrac{\pi^2}{\zeta}\left(\dfrac{2\zeta}{|\vec{x}_1-\vec{x}_2|}-1\right)e^{-|\vec{x}_1-\vec{x}_2|/\zeta}\ \ |\vec{x}_1-\vec{x}_2|\neq 0\end{cases} \tag{6.10}$$

Impurity scattering bulk, UTB and nanowire self-energies are expressed as

$$\Sigma^{<,R}\left(z_1,z_2,\vec{k}_{||},E\right)=\frac{N_D}{4.\left(2\pi\right)^2}\left(\frac{e^2}{\epsilon_o\epsilon_r}\right)^2\int d\vec{l}_{||}I\left(\vec{k}_{||},\vec{l}_{||},z_1,z_2\right)G^{<,R}\left(z_1,z_2,\vec{l}_{||},E\right) \tag{6.11}$$

$$\Sigma^{<,R}\left(\vec{x}_1,\vec{x}_2,k_{||},E\right)=\frac{N_D}{(8\pi)^2}\left(\frac{e^2}{\epsilon_o\epsilon_r}\right)^2\int dl_{||}I(k_{||},l_{||},\vec{x}_1,\vec{x}_2)G^{<,R}\left(\vec{x}_1,\vec{x}_2,l_{||},E\right) \tag{6.12}$$

where

$$I(k_{||},l_{||},\vec{x}_1,\vec{x}_2)=\begin{cases}\pi\left[\dfrac{|\vec{x}_1-\vec{x}_2|}{\left(k_{||}-l_{||}\right)^2+\zeta^{-2}}\right]K_1\left(\sqrt{\left(k_{||}-l_{||}\right)^2+\zeta^{-2}}\,|\vec{x}_1-\vec{x}_2|\right),\\ |\vec{x}_1-\vec{x}_2|\neq 0\\ \pi\left[\dfrac{1}{\left(k_{||}-l_{||}\right)^2+\zeta^{-2}}\right],\ |\vec{x}_1-\vec{x}_2|=0\end{cases} \tag{6.13}$$

$$\Sigma^{<,R}\left(\vec{x}_1,\vec{x}_2,E\right)=\frac{N_D}{8\pi}\left(\frac{e^2}{\epsilon_o\epsilon_r}\right)^2\zeta e^{-|\vec{x}_1-\vec{x}_2|/\zeta}G^{<,R}\left(\vec{x}_1,\vec{x}_2,E\right) \tag{6.14}$$

Note that a major distinction between the polar optical phonons and impurity scattering is the inelastic nature of scattering for phonons and elastic scattering for electrons with impurity potential. This is one of the important factors shaping the band tails as will be seen in subsequent section. For all further discussions, device is assumed to be in equilibrium with the density corresp onding to the doping concentration. Self-energies derived are solved consistently with the corresponding Green's function until particle conservation is

achieved throughout the device. Following are the corresponding NEGF equations solved to achieve converged density and density of states.

$$\begin{aligned} G^R &= \left(EI - H - \Sigma^R_{pop} - \Sigma^R_{imp} - \Sigma^R_{source} - \Sigma^R_{drain}\right) \\ G^< &= G^R \left(\Sigma^<_{pop} + \Sigma^<_{imp} + \Sigma^<_{source} + \Sigma^<_{drain}\right) G^{R\dagger} \end{aligned} \tag{6.15}$$

The real and imaginary part of the retarded self-energy are related through the Kramers-Krönig relation. The real part of scattering self-energy provides the energy shift and the imaginary part provides the broadening associated with the scattering mechanism. Band tail is extracted by taking slope of the exponentially decaying density of states below band edge and the band gap narrowing is determined by running two sets of simulation - one with real part of self-energy set to zero and other with real part present. The difference in shift is equivalent to the band gap narrowing. On-shell scattering rates from NEGF are computed by performing a Fourier transform of the self-energy with respect to the Wigner coordinate $(r - r')$ across the cross-diagonal of the matrix. This provides on-shell scattering rates in the full E-k space. In tight-binding basis, for a given E-k tuple, multiple k_x values can exist and hence they need to be summed up. For ultra-thin body and nanowires, the self-energy is first transformed into mode-space and then the Fourier transform is performed to get inter and intra-mode scattering rates.

For bulk,

$$\Gamma\left(k_{||}, k_x, E\right) = -\sum_{k_x} \frac{2}{\hbar a} \int_{-\infty}^{\infty} d(r - r') e^{ik_x(r-r')} \Sigma^R \left(k_{||}, r - r', \frac{r + r'}{2}\right)$$

For ultra-thin body,

$$\Gamma_{ij}\left(k, k_x, E\right) = -\sum_{k_x} \frac{2}{\hbar a} \int_{-\infty}^{\infty} d(r - r') e^{ik_x(r-r')} \tilde{\Sigma}^R \left(k, r - r', \frac{r + r'}{2}\right)$$

For nanowires,

$$\Gamma_{ij}\left(k_x, E\right) = -\sum_{k_x} \frac{2}{\hbar a} \int_{-\infty}^{\infty} d(r - r') e^{ik_x(r-r')} \tilde{\Sigma}^R \left(r - r', \frac{r + r'}{2}\right)$$

$$\tilde{\Sigma}^R = V \Sigma^R V^\dagger$$

where $\tilde{\Sigma}^R$ is the mode-space self-energy and V is the eigenmode transformation matrix.

6.3.2 Verification of scattering self-energies

Scattering self-energies are verified by comparing them against the corresponding Fermi's golden rule. Due to the non-local nature of scattering, Fermi's golden rule is separately derived for each degree of confinement based on the approach taken by [118]. Detailed derivations of Fermi's golden rule is provided in Appendix A. Envelope wave functions of the form

$$\psi(R) = \frac{e^{i\vec{k}.\vec{R}}}{\sqrt{V}}$$

for bulk,

$$\psi(R) = \frac{e^{i\vec{k}.\vec{r}}}{\sqrt{A}}\zeta_i(z)$$

for ultra-thin body, and

$$\psi(R) = \frac{e^{ikx}}{\sqrt{L}}\zeta_i(y,z)$$

for nanowires are assumed. Scattering rate is calculated by computing the transition matrix elements as follows

$$\frac{1}{\tau_{i,j}} = \frac{2\pi}{\hbar}\sum_q |k \pm q, jHk, i|^2 f_{initial}(1 - f_{final})\delta(E_{final} - E_{initial})$$

where i and j correspond to the initial and final modes (for ultra-thin bodies and nanowires), q is the phonon momentum/impurity potential wavevector, $f_{initial}$ and f_{final} are the occupancy functions for initial and final scattering states. Transition element $|k \pm q, jHk, i|^2$ for bulk, ultra thin body and nanowires can be expressed as

$$|k \pm qHk|^2 = U_q^2$$

$$|k \pm q, jHk, i|^2 = U_q^2 \int_{-\infty}^{\infty} dz \int_{-\infty}^{\infty} dz' \rho_{ij}(z) \rho_{ij}^*(z') e^{iq(z-z')}$$

$$\rho_{ij}(z) = \zeta_i^*(z) \zeta_j(z)$$

$$|k \pm q, jHk, i|^2 = U_q^2 \int_{-\infty}^{\infty} d\vec{r}_{||} \int_{-\infty}^{\infty} d\vec{r}'_{||} \rho_{ij}(\vec{r}_{||}) \rho_{ij}^*(\vec{r}'_{||}) e^{iq\vec{_{||}} \cdot (\vec{r}_{||} - \vec{r}'_{||})}$$

$$\rho_{ij}(\vec{r}_{||}) = \zeta_i^*(y, z) \zeta_j(y, z)$$

where U_q is the scattering potential.

Based on the definition of transition matrix elements and envelope wavefunctions, Fermi's golden rule for charged impurity for bulk can be expressed as

$$\frac{1}{\tau(E)} = \frac{2e^4 m^* N_D}{\pi \hbar^3 \epsilon_o^2} \frac{\sqrt{\frac{2m^* E}{\hbar^2}}}{\zeta^{-2} \left(\zeta^{-2} + \frac{8m^* E}{\hbar^2} \right)} \tag{6.16}$$

Fermi's golden rule for charged impurity for ultra-thin body takes the form

$$\frac{1}{\tau_{ij}(E)} = \frac{2e^4 N_D m^*}{\hbar^3 \epsilon^2 (2\pi)^3} \int_0^{2\pi} d\theta F(|\tilde{\mathbf{k}}_{||} - \tilde{\mathbf{k}}'_{||}|, \theta) \tag{6.17}$$

where

$$|\tilde{\mathbf{k}}_{||} - \tilde{\mathbf{k}}'_{||}| = \left[\frac{2m^*}{\hbar^2} (2E - E_i - E_j) - 2. \frac{2m^*}{\hbar^2} \sqrt{E - E_i}. \sqrt{E - E_j} cos\theta \right]^{1/2} \tag{6.18}$$

Form factor F is given by $F_{abs/emi}(q_{||}) = \int_0^{L_z} \int_0^{L_z} dz dz' \rho_{ij}(z) \rho_{ij}(z') I(q_{||}, z, z')$
where $\rho_{ij}(z) = \psi_i^*(z) \psi_j(z)$ (product of mode i and mode j) and

$$I(q_{||}, z, z') = \frac{\pi e^{-|z-z'| \sqrt{q_{||}^2 + \zeta^{-2}}}}{2 \left(q_{||}^2 + \zeta^{-2} \right)} \left[\frac{1}{\sqrt{q_{||}^2 + \zeta^{-2}}} + |z - z'| \right] \tag{6.19}$$

The above scattering rate is between two modes i and j. Multi-modal scattering rate can be calculated by summing up contributions from different inter-mode scattering

$$\Gamma(E) = \sum_j \Gamma_{ij}(E) = \sum_j \frac{1}{\tau_{ij}(E)} \tag{6.20}$$

Finally, Fermi's golden rule for charged impurity for nanowire can be expressed as

$$\frac{1}{\tau_{ij}(E)} = \frac{e^4 N_D \sqrt{2m^*}}{\hbar^2 \epsilon^2 (2\pi)^3} \left(\frac{F(k_x - k_x^{'}) + F(k_x + k_x^{'})}{\sqrt{E - E_i}} \right) \tag{6.21}$$

Form factor F is given by

$F(q_x) = \int_0^{L_y} \int_0^{L_z} \int_0^{L_y} \int_0^{L_z} \mathbf{dr}_{||} \mathbf{dr}_{||}^{'} \rho_{ij}^*(\mathbf{r}_{||}) \rho_{ij}(\mathbf{r}_{||}^{'}) I(q_x, \mathbf{r}_{||}, \mathbf{r}_{||}^{'})$

where $\rho_{ij}(\mathbf{r}_{||}) = \psi_i^*(\mathbf{r}_{||}) \psi_j(\mathbf{r}_{||})$ (product of mode i and mode j) and

$$I(q_x, \mathbf{r}_{||}, \mathbf{r}_{||}^{'}) = \begin{cases} \dfrac{\left| \mathbf{r}_{||} - \mathbf{r}_{||}^{'} \right|}{2\sqrt{q_x^2 + \zeta^{-2}}} K_1 \left(\sqrt{q_x^2 + \zeta^{-2}} \left| \mathbf{r}_{||} - \mathbf{r}_{||}^{'} \right| \right), & \left| \mathbf{r}_{||} - \mathbf{r}_{||}^{'} \right| \neq 0 \\ \dfrac{1}{2\left(q_x^2 + \zeta^{-2}\right)}, & \left| \mathbf{r}_{||} - \mathbf{r}_{||}^{'} \right| = 0 \end{cases} \tag{6.22}$$

The above scattering rate is between two modes i and j. Multi-modal scattering rate can be calculated by summing up contributions from different inter-mode scattering

$$\Gamma(E) = \sum_j \Gamma_{ij}(E) = \sum_j \frac{1}{\tau_{ij}(E)} \tag{6.23}$$

The corresponding Fermi's golden rule expressions are compared against self-energy calculations performed with NEGF approach. From Fig. 6.1 scattering rate obtained from NEGF shows good agreement with Fermi's golden rule for 4nm GaAs ultra-thin body. Rate follows the 2D density of states and at the same time decreases with increasing energy. This is characteristic of impurity scattering mechanism where the impurity scattering potential has a q^{-2} dependence on momentum. NEGF scattering rate exhibits spikes and steps due to the numerical resolution of transverse k-space. Obtaining a smooth scattering rate requires prohibitively large computational resources.

Similarly, electron scattering rate obtained from NEGF shows good agreement with Fermi's golden rule for $2 \times 2nm^2$ GaAs nanowire as observed in Fig 6.2. Scattering rate

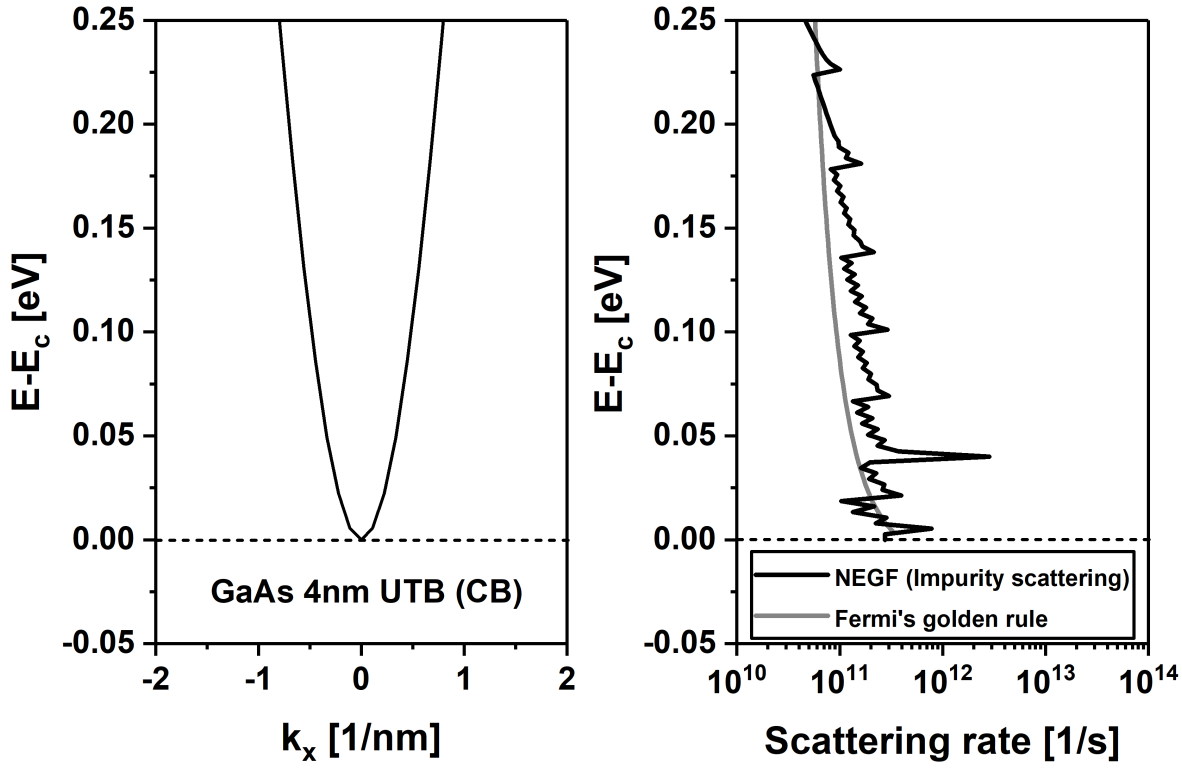

Fig. 6.1.: a) Conduction band profile of a 4nm GaAs ultra-thin body at Γ point. b) Comparison of conduction band scattering rates obtained from NEGF against Fermi's golden rule for charged impurity scattering for 4nm GaAs ultra-thin body in 10-band sp3d5s* tight binding basis for a doping concentration of $2 \times 10^{18} cm^{-3}$. Screening length is set at 3 nm. Good agreement is achieved between the NEGF scattering rate and Fermi's golden rule over a wide energy range. NEGF simulation has observable spikes in scattering rate due to limited resolution of periodic k-space.

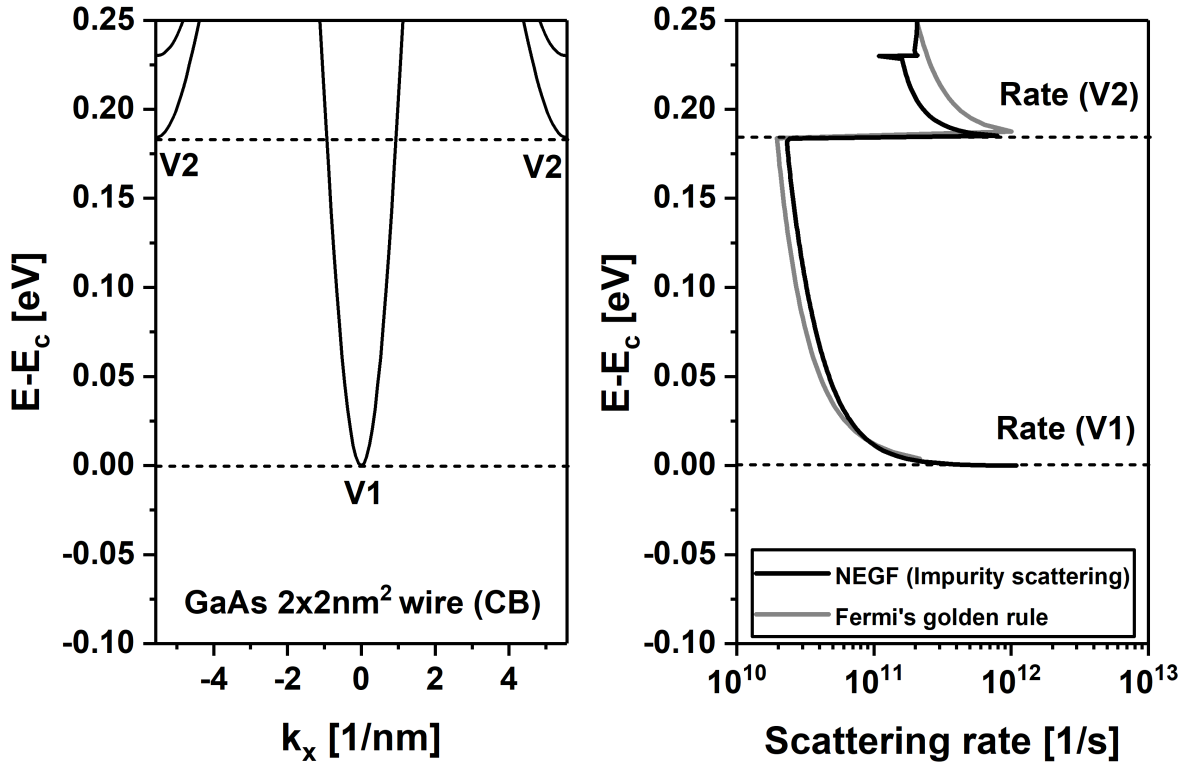

Fig. 6.2.: a) Conduction band profile of $2 \times 2nm^2$ GaAs nanowire. Valleys at Γ point and the zone boundary are labelled as V1 and V2. b) Comparison of conduction band scattering rates obtained from NEGF against Fermi's golden rule for charged impurity scattering for $2 \times 2nm^2$ GaAs nanowire in 10-band sp3d5s* tight binding basis for a doping concentration of $2 \times 10^{18} cm^{-3}$. Screening length is set at 3 nm. Fermi's golden rule shows good agreement with NEGF over a wide energy range. Distinct scattering rates can be observed for valleys V1 and V2.

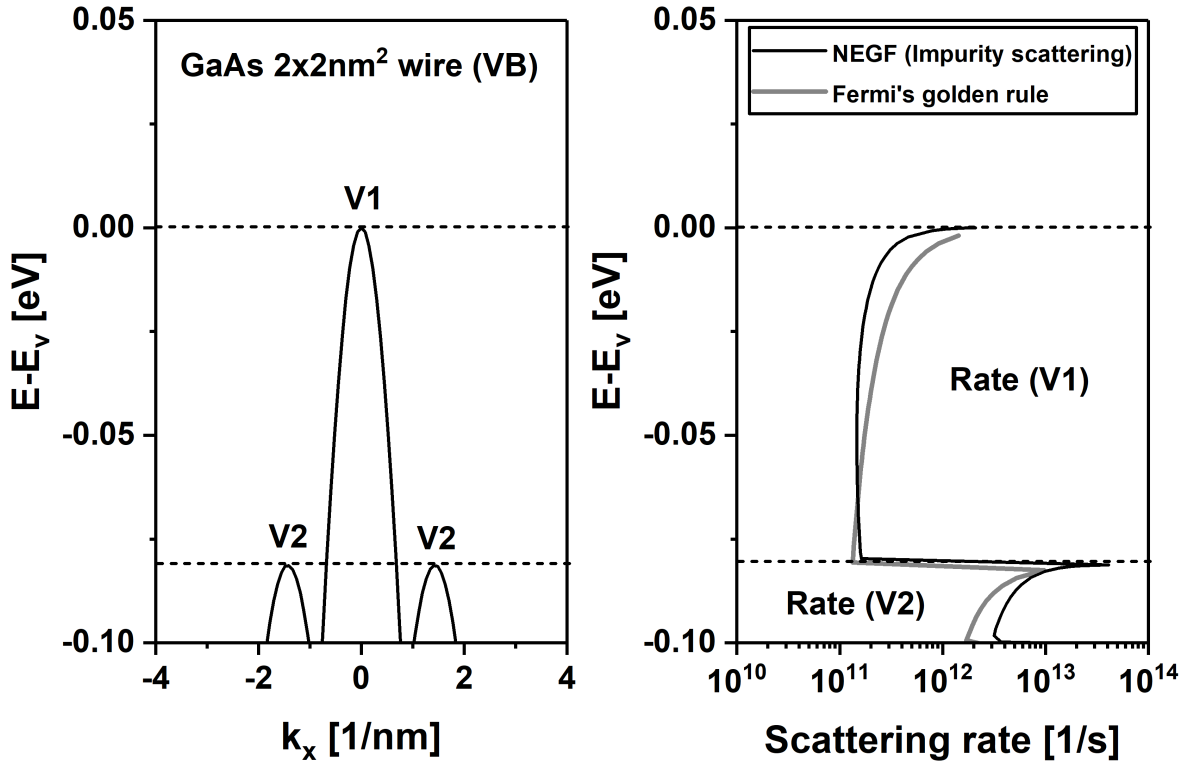

Fig. 6.3.: a) Valence band profile of $2\times 2nm^2$ GaAs nanowire. Valleys at Γ point and higher energies are labelled as V1 and V2 respectively. b) Comparison of valence band scattering rates obtained from NEGF against Fermi's golden rule for charged impurity scattering for $2\times 2nm^2$ GaAs nanowire in 10-band sp3d5s* tight binding basis for a doping concentration of $2 \times 10^{18} cm^{-3}$. Screening length is set at 3 nm. Fermi's golden rule shows reasonable agreement with NEGF over the available energy window. Non-parabolicity of valence bands results in observed deviations from Fermi's golden rule. Distinct scattering rates can be observed for valleys V1 and V2.

follows both 1D density of states profile along with characteristic decrease of rate with increasing energy for impurity scattering. Scattering rate has an abrupt jump at the onset of valley V2 due to larger effective mass of V2 in comparison with V1.

Comparison of hole scattering rate obtained from NEGF shows agreement with Fermi's golden rule for $2 \times 2nm^2$ GaAs nanowire evident from Fig 6.3. Hole bands are parabolic closer to the Γ point and non-parabolicity increases as one goes deeper into the valence

bands. Fermi's golden rule, on the other hand, employs parabolic E-k assumption and this results in observed deviations in the scattering rate. Scattering rate shows an abrupt jump at V2 due to a difference in effective masses between valleys V1 and V2.

A similar comparison is done between Fermi's golden rule obtained for polar optical phonon scattering with NEGF. Scattering rate results for bulk are expressed below with absorption and emission branches highlighted separately.

Absorption process

$$\frac{1}{\tau_{ab}(\mathbf{k})} = \frac{e^2 m^* \hbar \omega_{LO} N_{ph}}{4\pi\hbar^3 k}\left(\frac{1}{\epsilon_\infty} - \frac{1}{\epsilon_s}\right)\int_{q_-}^{q+} dq \frac{q^3}{\left(q^2+\zeta^{-2}\right)^2} \tag{6.24}$$

where the integration limits of q are

$$\left(\frac{2m^*}{\hbar^2}\right)^{1/2}\left[\sqrt{E+\hbar\omega_{LO}} - \sqrt{E}\right] \leq q \leq \left(\frac{2m^*}{\hbar^2}\right)^{1/2}\left[\sqrt{E+\hbar\omega_{LO}} + \sqrt{E}\right]$$

Emission process

$$\frac{1}{\tau_{em}(\mathbf{k})} = \theta\left(E-\hbar\omega_{LO}\right)\frac{e^2 m^* \hbar \omega_{LO}\left(1+N_{ph}\right)}{4\pi\hbar^3 k}\left(\frac{1}{\epsilon_\infty} - \frac{1}{\epsilon_s}\right)\int_{q_-}^{q+} dq \frac{q^3}{\left(q^2+\zeta^{-2}\right)^2} \tag{6.25}$$

where the integration limits of q are

$$\left(\frac{2m^*}{\hbar^2}\right)^{1/2}\left[\sqrt{E} - \sqrt{E-\hbar\omega_{LO}}\right] \leq q \leq \left(\frac{2m^*}{\hbar^2}\right)^{1/2}\left[\sqrt{E} + \sqrt{E-\hbar\omega_{LO}}\right]$$

Total scattering rate is the sum of emission and absorption processes and is given by

$$\frac{1}{\tau(\mathbf{k})} = \frac{1}{\tau_{em}(\mathbf{k})} + \frac{1}{\tau_{ab}(\mathbf{k})}$$

Fermi's golden rule for polar optical phonons for ultra-thin body can be expressed as

Absorption process

$$\frac{1}{\tau_{ij,abs}(E)} = \frac{4\pi e^2 m^* \hbar \omega_{LO}}{\hbar^3}\left(\frac{1}{\epsilon_\infty} - \frac{1}{\epsilon_s}\right) N_{ph}\int_0^{2\pi} d\theta F_{abs}(|\tilde{\mathbf{k}}_{||} - \tilde{\mathbf{k}}'_{||}|, \theta) \tag{6.26}$$

where

$$|\tilde{\mathbf{k}}_{||} - \tilde{\mathbf{k}}'_{||}| = \left[2k^2 + \frac{2\left(\hbar\omega_{LO} + (E_i - E_j)\right)}{\hbar^2} - 2k\left[k^2 + \frac{2\left(\hbar\omega_{LO} + (E_i - E_j)\right)}{\hbar^2}\right]^{1/2} cos\theta\right]^{1/2} \tag{6.27}$$

Emission process

$$\frac{1}{\tau_{ij,emi}(E)} = \frac{4\pi e^2 m^* \hbar\omega_{LO}}{\hbar^3}\left(\frac{1}{\epsilon_\infty} - \frac{1}{\epsilon_s}\right)(N_{ph}+1)\int_0^{2\pi} d\theta F_{emi}(|\tilde{\mathbf{k}}_{||} - \tilde{\mathbf{k}}'_{||}|, \theta) \quad (6.28)$$

where

$$|\tilde{\mathbf{k}}_{||} - \tilde{\mathbf{k}}'_{||}| = \left[2k^2 - \frac{2\left(\hbar\omega_{LO} - (E_i - E_j)\right)}{\hbar^2} - 2k\left[k^2 - \frac{2\left(\hbar\omega_{LO} - (E_i - E_j)\right)}{\hbar^2}\right]^{1/2} cos\theta\right]^{1/2} \quad (6.29)$$

Form factor $F_{abs/emi}$ is given by $F_{abs/emi}(q_{||}) = \int_0^{L_z}\int_0^{L_z} dz dz' \rho_{ij}(z)\rho_{ij}(z') I(q_{||}, z, z')$ where $\rho_{ij}(z) = \psi_i^*(z)\psi_j(z)$ (product of mode i and mode j) and

$$I(q_{||}, z, z') = \frac{e^{-\sqrt{q_{||}^2+\zeta^{-2}}|z-z'|}}{\sqrt{q_{||}^2+\zeta^{-2}}}\left[1 - \frac{|z-z'|\,\zeta^{-2}}{2\sqrt{q_{||}^2+\zeta^{-2}}} - \frac{\zeta^{-2}}{2\left(q_{||}^2+\zeta^{-2}\right)}\right]$$

Total scattering is the sum of absorption and emission processes and is given by

$$\frac{1}{\tau_{ij}(E)} = \frac{1}{\tau_{ij,emi}(E)} + \frac{1}{\tau_{ij,abs}(E)}$$

The above scattering rate is between two modes i and j. Multi-modal scattering rate can be calculated by summing up contributions from different inter-mode scattering

$$\Gamma(E) = \sum_j \Gamma_{ij}(E) = \sum_j \frac{1}{\tau_{ij}(E)}$$

Finally, Fermi's golden rule for polar optical phonons for nanowire are expressed as

Absorption process

$$\frac{1}{\tau_{ij,abs}(E)} = \frac{e^2\hbar\omega_{LO}N_{ph}}{\hbar^2}\left(\frac{1}{\epsilon_\infty} - \frac{1}{\epsilon_s}\right)\cdot\frac{2}{(2\pi)^2}\cdot\sqrt{2m^*}\left(\frac{F(k_x - k_x') + F(k_x + k_x')}{\sqrt{E - E_j + \hbar\omega_{LO}}}\right) \quad (6.30)$$

$$k_x = \sqrt{\frac{2m^*\left(E - E_i\right)}{\hbar^2}} \quad k_x' = \sqrt{\frac{2m^*\left(E - E_j + \hbar\omega_{LO}\right)}{\hbar^2}}$$

Emission process

$$\frac{1}{\tau_{ij,emi}(E)} = \frac{e^2\hbar\omega_{LO}\left(N_{ph}+1\right)}{\hbar^2}\left(\frac{1}{\epsilon_\infty}-\frac{1}{\epsilon_s}\right)\cdot\frac{2}{(2\pi)^2}\cdot\sqrt{2m^*}\left(\frac{F(k_x-k_x^{'})+F(k_x+k_x^{'})}{\sqrt{E-E_j-\hbar\omega_{LO}}}\right) \tag{6.31}$$

$$k_x = \sqrt{\frac{2m^*\left(E-E_i\right)}{\hbar^2}} \quad k_x^{'} = \sqrt{\frac{2m^*\left(E-E_j-\hbar\omega_{LO}\right)}{\hbar^2}}$$

Form factor F is given by

$F(q_x) = \int_0^{L_y}\int_0^{L_z}\int_0^{L_y}\int_0^{L_z} \mathbf{dr}_{||}\mathbf{dr}_{||}^{'}\rho_{ij}^*(\mathbf{r}_{||})\rho_{ij}(\mathbf{r}_{||}^{'})I(q_x,\mathbf{r}_{||},\mathbf{r}_{||}^{'})$

where $\rho_{ij}(\mathbf{r}_{||}) = \psi_i^*(\mathbf{r}_{||})\psi_j(\mathbf{r}_{||})$ (product of mode i and mode j)

and

$$I(q_x,\mathbf{r}_{||},\mathbf{r}_{||}^{'}) = \begin{cases} \left(\sqrt{q_x^2+\zeta^{-2}}\left|\mathbf{r}_{||}-\mathbf{r}_{||}^{'}\right| + \dfrac{q_x^2\left|\mathbf{r}_{||}-\mathbf{r}_{||}^{'}\right|}{\sqrt{q_x^2+\zeta^{-2}}}\right)\dfrac{K_1\left(\sqrt{q_x^2+\zeta^{-2}}\left|\mathbf{r}_{||}-\mathbf{r}_{||}^{'}\right|\right)}{2}, & \left|\mathbf{r}_{||}-\mathbf{r}_{||}^{'}\right| \neq 0 \\ \left(\dfrac{1}{2}+\dfrac{q_x^2}{2\left(q_x^2+\zeta^{-2}\right)}\right), & \left|\mathbf{r}_{||}-\mathbf{r}_{||}^{'}\right| = 0 \end{cases}$$

Total scattering is the sum of absorption and emission processes and is given by

$$\frac{1}{\tau_{ij}(E)} = \frac{1}{\tau_{ij,emi}(E)} + \frac{1}{\tau_{ij,abs}(E)}$$

The above scattering rate is between two modes i and j. Multi-modal scattering rate can be calculated by summing up contributions from different inter-mode scattering

$$\Gamma(E) = \sum_j \Gamma_{ij}(E) = \sum_j \frac{1}{\tau_{ij}(E)}$$

Electron scattering rate obtained from NEGF shows good agreement with Fermi's golden rule for 4nm GaAs ultra-thin body as seen in Fig. 6.4. Clear distinction between phonon emission and absorption processes can be observed at energy $\hbar\omega_{LO}$ above the band edge. As expected, the scattering rate, follows the 2D density of states profile but decreases with increasing energy as expected of a polar-optical phonon scattering process. NEGF scattering rate, similar to the impurity case, exhibits spikes and steps due to the numerical resolution of transverse k-space due to numerical resolution.

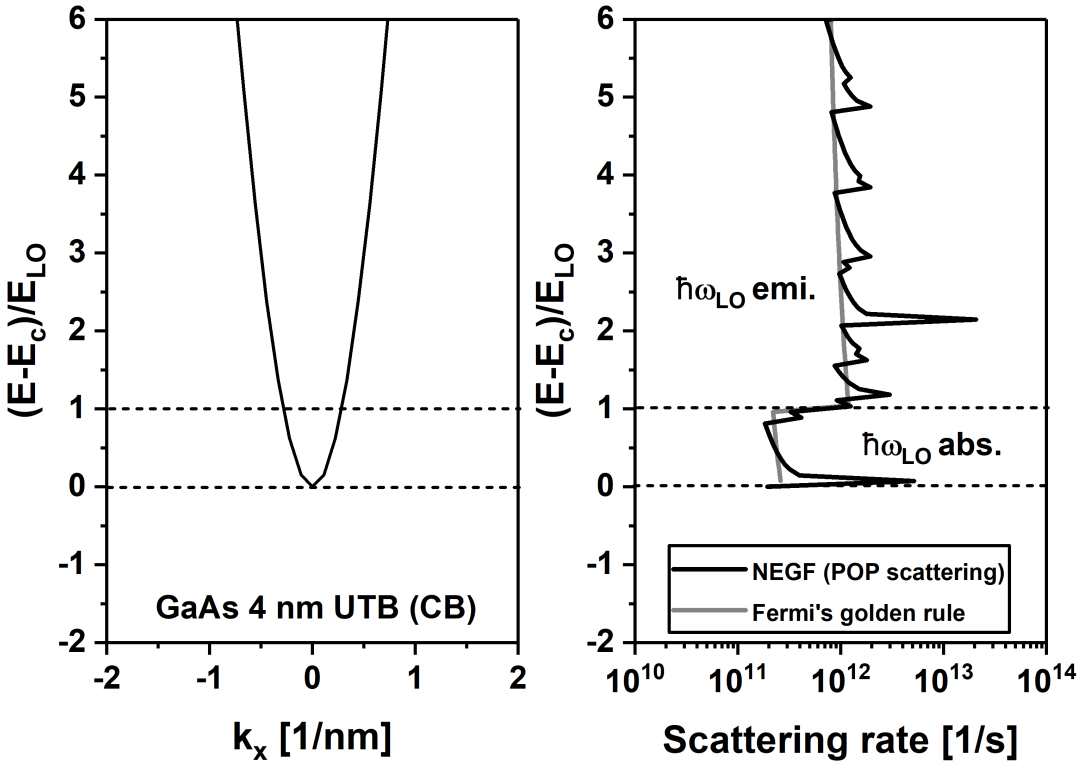

Fig. 6.4.: a) Conduction band profile of 4nm GaAs ultra-thin body. b) Comparison of conduction band scattering rates obtained from NEGF against Fermi's golden rule for polar optical phonons for 4nm GaAs ultra-thin body in 10-band sp3d5s* tight binding basis. Screening length is set at 3 nm. Good agreement is achieved between the NEGF scattering rate and Fermi's golden rule over a wide energy range. Onset of phonon emission is observed at energy 1 LO phonon above conduction bandedge.

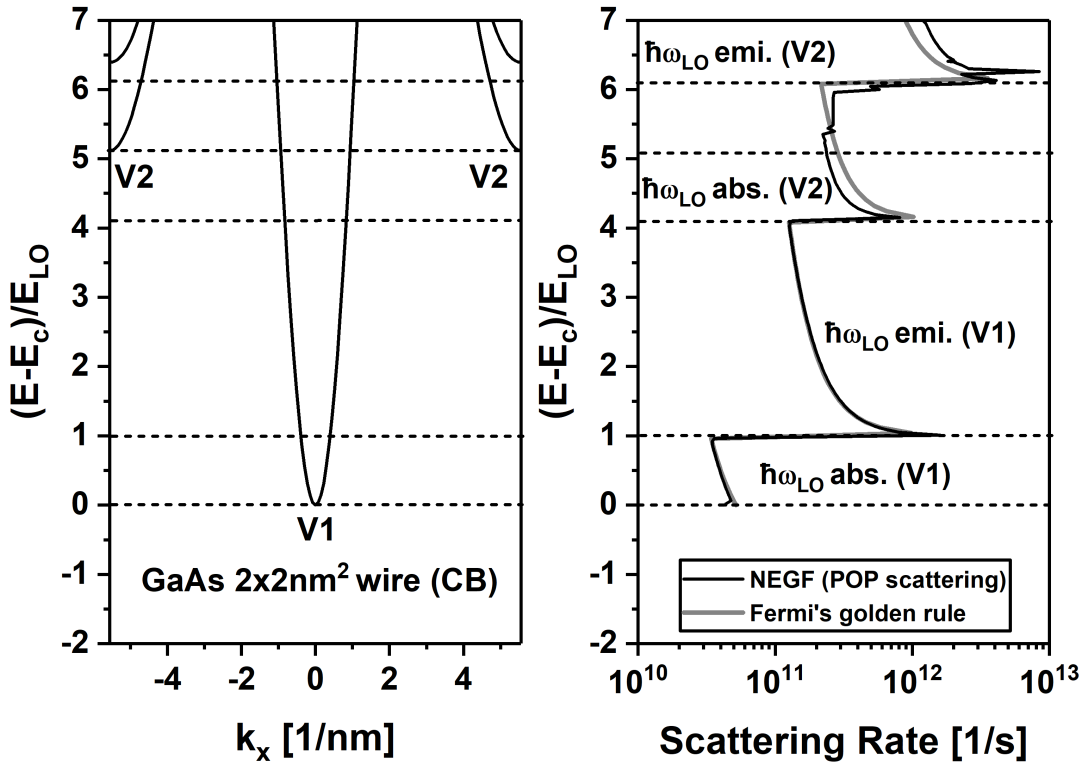

Fig. 6.5.: a) Conduction band profile of $2 \times 2nm^2$ GaAs nanowire. Valleys at Γ point and the zone boundary are labelled as V1 and V2. b) Comparison of conduction band scattering rates obtained from NEGF against Fermi's golden rule for polar optical phonons for $2 \times 2nm^2$ GaAs nanowire in 10-band sp3d5s* tight binding basis. Screening length is set at 3 nm. Fermi's golden rule shows good agreement with NEGF over a wide energy range. Onset of absorption and emission processes can be clearly observed for valleys V1 and V2.

Similarly, electron scattering rate is obtained for nanowires from NEGF and it shows good agreement with Fermi's golden rule for $2\times2nm^2$ GaAs nanowire as shown in Fig. 6.5. Scattering rate clearly shows absorption and emission processses for valleys V1 and V2. For energies near the Γ point, scattering rate is governed by phonon absorption and emission of electrons present in Valley V1. With increasing energy, we reach a point where electrons present in valley V1 can now absorb a phonon and scatter to valley V2. This results in a jump at $4\hbar\omega_{LO}$. At energy, one $\hbar\omega_{LO}$ higher than V2 electrons present at higher energies start emitting phonons. The self-energy captures both inter and intra-valley scattering processes quite nicely.

Hole scattering rate obtained from NEGF shows good agreement with Fermi's golden rule for $2 \times 2nm^2$ GaAs nanowire is as shown in Fig. 6.6. With decreasing energy from the valence band edge, hole absorption process begins and at $\hbar\omega_{LO}$, hole emission process for valley V1 begins. Soon, the hole energy is sufficient enough for the absorption of a phonon energy to scatter onto valley V2. Since valleys V1 and V2 have different effective masses, this results in a jump in the scattering rate. With further decrease in energy, holes can now scatter onto valley V3 through a phonon absorption which results in an additional bump around $-1.8\hbar\omega_{LO}$. Deviations observed from Fermi's golden rule approximation is mainly because of it's assumption of parabolic dispersion. NEGF on the other hand, employs the tight-binding bandstructure which has significant non-parabolicity away from Γ point.

Overall, comparison of sccattering rates with Fermi's golden rule show good agreement over the energy range. NEGF captures both inter and intra-valley scattering process quite nicely. This provides confidence in the scattering expressions which can now be employed to study band tails in detail.

6.3.3 Compensation factor for non-local scattering

Self-energies described above are only solved atom-blockdiagonal. In general, both polar optical phonon and impurity scattering are non-local in nature. To account for the non-locality omission, a new compensation factor is proposed based on a semi-classical

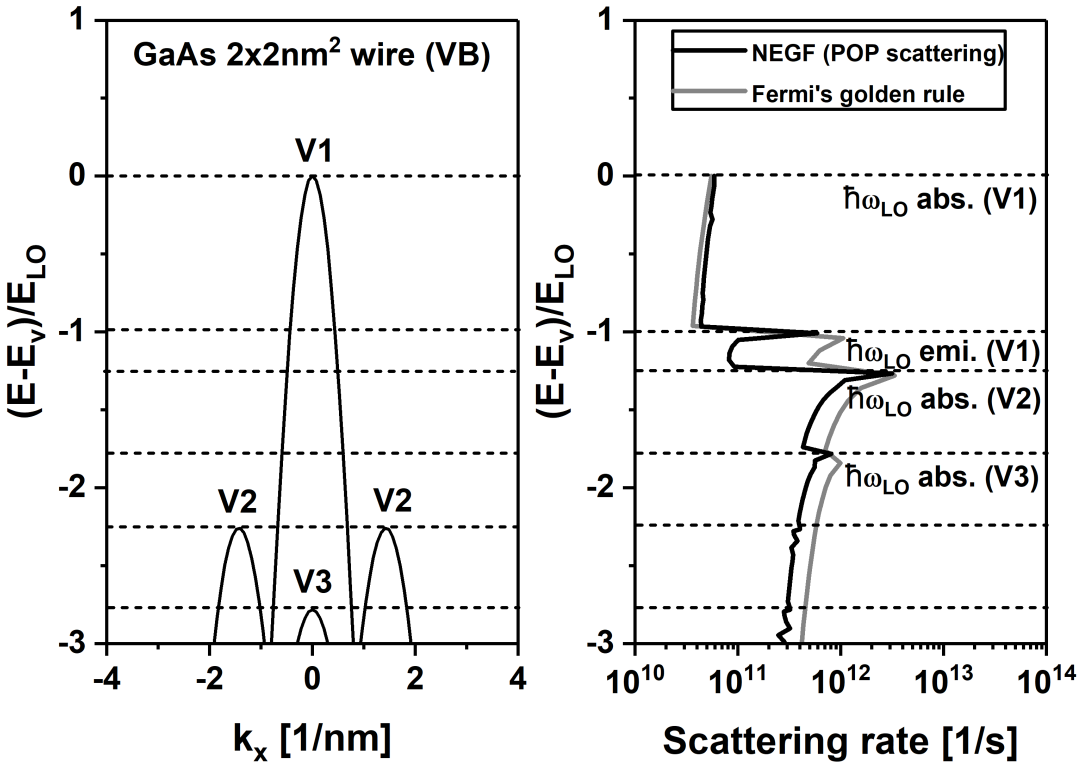

Fig. 6.6.: a) Hole band profile of $2 \times 2nm^2$ GaAs nanowire. Valley at Γ point is labeled V1 and the ones at deeper energy levels are labelled V2 and V3. b) Comparison of valence band scattering rates obtained from NEGF against Fermi's golden rule for polar optical phonons for $2 \times 2nm^2$ GaAs nanowire in 10-band tight binding basis. Screening length is set at 3 nm. Non-parabolicity of valence bands results in observed deviations from Fermi's golden rule. Onset of absorption and emission processes can be clearly observed for valleys V1, V2 and V3.

approach. The compensation factor is defined as a division of form factors of the scattering rate from Fermi's golden rule for the local case with the non-local one. The compensation factor for UTBs and nanowires can be represented as

$$S_{UTB} = \frac{\int_0^{2\pi} d\theta \int_0^{L_z}\int_0^{L_z} dz dz' \rho_{ij}(z)\rho_{ij}(z') I(|\tilde{\mathrm{k}}_{||} - \tilde{\mathrm{k}}'_{||}|, z, z')}{\int_0^{2\pi} d\theta \int_0^{L_z}\int_0^{L_z} dz dz' \rho_{ij}(z)\rho_{ij}(z') I_{Local}(|\tilde{\mathrm{k}}_{||} - \tilde{\mathrm{k}}'_{||}|, z, z')} \tag{6.32}$$

$$S_{wire} = \frac{\int_0^{L_y}\int_0^{L_z}\int_0^{L_y}\int_0^{L_z} \mathbf{dr}_{||}\mathbf{dr}'_{||}\rho^*_{ij}(\mathbf{r}_{||})\rho_{ij}(\mathbf{r}'_{||}) I(q_x, \mathbf{r}_{||}, \mathbf{r}'_{||})}{\int_0^{L_y}\int_0^{L_z}\int_0^{L_y}\int_0^{L_z} \mathbf{dr}_{||}\mathbf{dr}'_{||}\rho^*_{ij}(\mathbf{r}_{||})\rho_{ij}(\mathbf{r}'_{||}) I_{Local}(q_x, \mathbf{r}_{||}, \mathbf{r}'_{||})} \tag{6.33}$$

where

$$I_{Local}(q_{||}, z, z') = \begin{cases} \dfrac{1}{\sqrt{q_{||}^2 + \zeta^{-2}}}\left[1 - \dfrac{\zeta^{-2}}{2\left(q_{||}^2 + \zeta^{-2}\right)}\right], & |z - z'| = 0 \\ 0, & |z - z'| \neq 0 \end{cases} \tag{6.34}$$

$$I_{Local}(q_x, \mathbf{r}_{||}, \mathbf{r}'_{||}) = \begin{cases} \left(\dfrac{1}{2} + \dfrac{q_x^2}{2\left(q_x^2 + \zeta^{-2}\right)}\right), & \left|\mathbf{r}_{||} - \mathbf{r}'_{||}\right| = 0 \\ 0, & \left|\mathbf{r}_{||} - \mathbf{r}'_{||}\right| \neq 0 \end{cases} \tag{6.35}$$

For bulk, compensation factor for a thick enough UTB with 20 modes (to mimic bulk like behaviour) is calculated as an equivalent analytical expression does not exist for the bulk case due to 3D periodicity.

6.4 Urbach tail - Dependence on temperature, doping and confinement

Urbach tails are mainly observed in the context of optical measurements where the absorption spectrum decays exponentially below the band edges. Since it's representative of the available density of states, it will be used for majority of our discussions in extracting and analysing Urbach parameters. Fig 6.7 shows the density of states of bulk, ultra-thin body and nanowire GaSb in presence of scattering. Density of states along with polar optical phonon and impurity scattering is distinctly different from the ballistic case where a

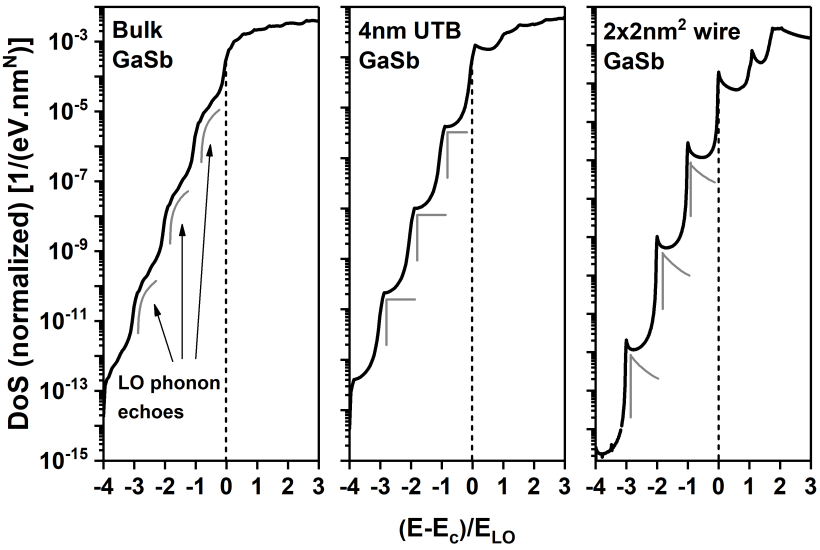

Fig. 6.7.: Density of states of bulk, 4nm ultra-thin body and $2 \times 2nm^2$ wire GaSb in the presence of polar optical phonon and charged impurity scattering. Density of states with scattering show exponentially decaying band tail with periodic pattern of LO phonon echoes mirroring the density of states profile at the bandedge. The shape of the echoes is determined by the dimensionality of the density of states as indicated by the grey illustrations. Urbach parameter is extracted by taking slope of the exponential decaying tail.

sharp drop occurs at the defined bandedge. In this case, inelastic phonon scattering processes along with impurity enhancement result in an exponential decay of the density of states. The shape of band tails has two distinct features - shape is determined by the nature of DoS at the bandedge (1D, 2D versus 3D DoS) and formation of periodic patterns determined by the LO phonon energy. Band tail is extracted by taking the slope of the exponential decay as follows

$$E_{Urbach} = \frac{(E_1 - E_2)}{log\left(\frac{DoS(E_1)}{DoS(E_2)}\right)} \tag{6.36}$$

Fig 6.8 shows the variation of Urbach parameter with doping concentration and temperature. With increasing temperature, phonon echoes are gradually washed out due to increasing contribution from the phonon bath. Phonon contribution is $\propto exp(-\hbar\omega_{LO}/k_BT)$ and results in an exponential increase in scattering strength with temperature, thereby increasing the Urbach paramater. Impurity scattering on the other hand, is an elastic process and does not contribute to formation of band tails. However, due to the elastic nature of scattering, it enhances every energy in the band tail with it's enhancement being proportional to the available density of states. Therefore, with increasing doping concentration, decay of bands get more and more gradual and this results in observed enhancement of Urbach parameter with doping. The simulation results are now compared with available experimental data.

Fig 6.9 shows the variation of Urbach parameter as a function of temperature for different doping concentrations for bulk n-type GaAs. As observed earlier with energy resolved DoS, band tails for bulk n-type GaAs increase both with temperature and doping concentration. At 300K, Urbach parameter for GaAs is around 5 meV and at $7 \times 10^{18} cm^{-3}$ increases to 12 meV. Simulation results are compared against experimental data obtained from [119]. Intrinsic data shows good agreement with experimental data as the major contributor to band tails in this regime are phonons. At $2 \times 10^{18} cm^{-3}$ doping, match is qualitative and experimental value is slightly higher than simulations. This is expected as the current model

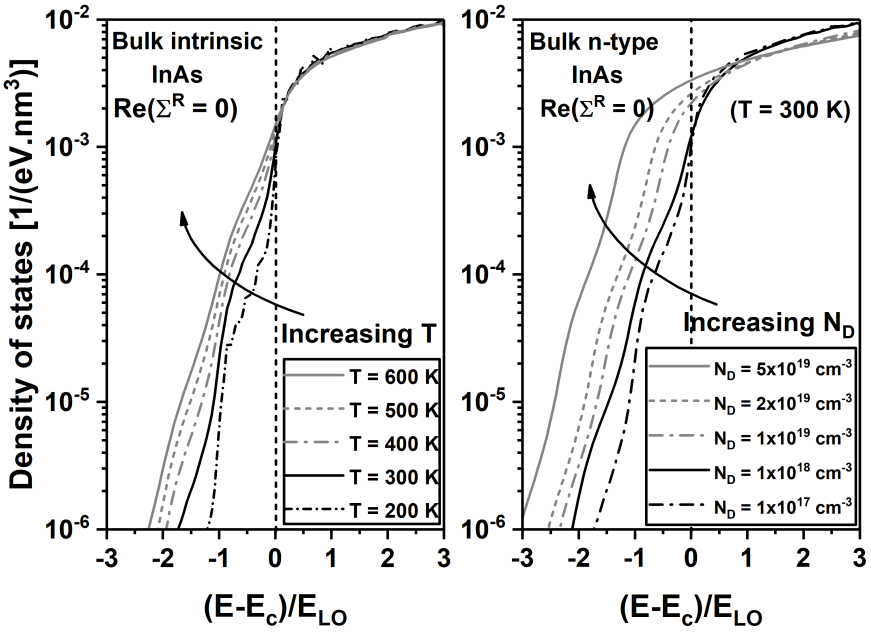

Fig. 6.8.: a) Variation of density of states of bulk InAs as a function of energy (normalized to LO phonon energy) for different temperature. Increasing temperature results in increasing contribution from phonons ($\propto exp(-\hbar\omega_{LO}/k_BT)$) blurring the individual phonon echoes. b) Variation of density of states of bulk InAs as a function of energy (normalized to LO phonon energy) for different doping concentration. Increasing the doping concentration results in increasing impurity scattering contribution resulting in a slower decay below the band edge.

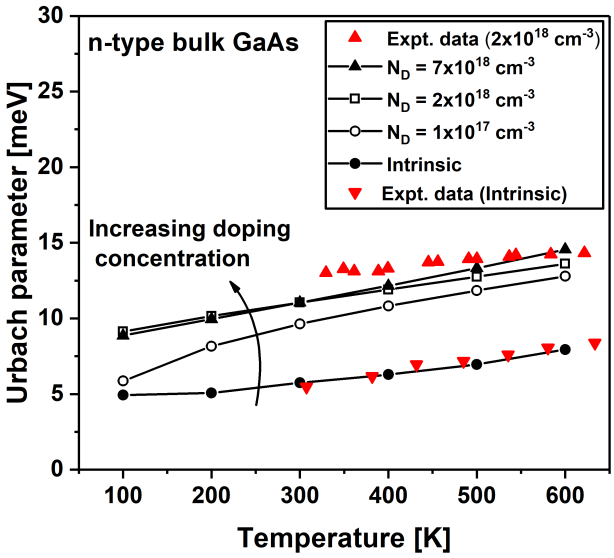

Fig. 6.9.: Variation of Urbach parameter as a function of temperature for n-type GaAs for different doping concentrations. Simulation results show good agreement with experimental data obtained from [119] for intrinsic case and for $N_D = 2 \times 10^{18} cm^{-3}$.

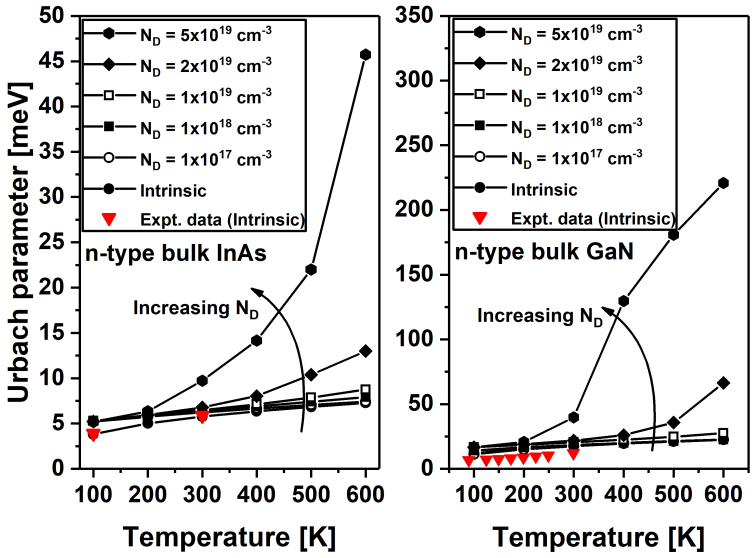

Fig. 6.10.: a) Variation of Urbach parameter as a function of temperature for n-type bulk InAs for different doping concentrations. Simulation results show good agreement with experimental data obtained from [120]. b) Variation of Urbach parameter as a function of temperature for n-type GaN for different doping concentrations. Simulation results show good agreement with experimental data obtained from [121] for GaN. With increasing doping concentration, Urbach parameter increases more rapidly with temperature due to the combined effect of higher phonon and impurity scattering.

only captures the intrinsic scattering processes from phonons and impurity potential and does not include crystal defects/disorders and neutral impurity scattering.

Urbach parameter is plotted as a function of temperature and doping concentration for bulk n-type InAs and GaN as shown in Fig 6.10 and compared against experimental data obtained from [120] for InAs and [121] for GaN. In both the cases, simulation results show good agreement with experimental results. GaN has a larger LO phonon energy (92 meV) than InAs (30 meV) and this shows up as larger Urbach parameter values which are atleast 3x higher than InAs. This results in Urbach parameter increasing much more drastically with respect to temperature for GaN when compared to InAs.

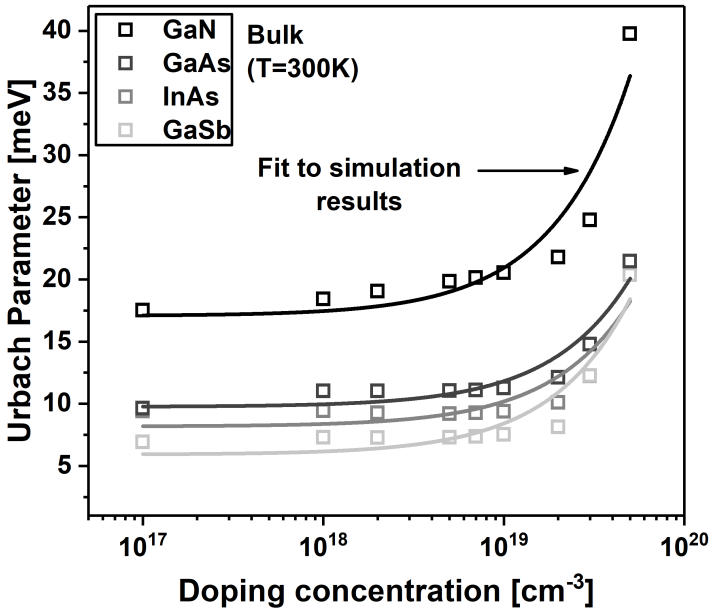

Fig. 6.11.: Variation of Urbach parameter for bulk GaN, GaAs, InAs and GaSb as a function of doping concentration. Dots correspond to the simulation results and lines correspond to the fitting curve. GaN exhibits largest Urbach parameter due to large LO phonon scattering strength.

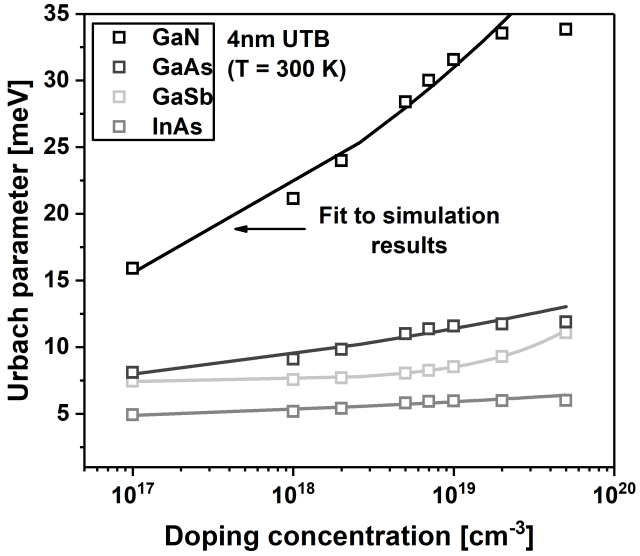

Fig. 6.12.: Variation of Urbach parameter for GaN, GaAs, InAs and GaSb ultra-thin body as a function of doping concentration. Dots correspond to the simulation results and lines correspond to the fitting curve. GaN exhibits largest Urbach parameter due to large LO phonon scattering potential.

Fig 6.11 shows the variation of Urbach parameter of GaN, GaAs, InAs and GaN with doping concentration is summarized in this plot. In general, all the materials follow similar variation with doping profile. GaN, in general has a larger Urbach parameter due to large phonon energy and is $3\times$ larger than GaAs, InAs and GaSb which have similar phonon energies (36meV, 30meV and 30meV respectively). The variation with doping is fit with a least-square fitting approach and is fit to $U_{N_D} = U_{intrinsic} + A(N_D/1E18)^u$. The curve captures the trend quite well and the corresponding parameters are summarized in Table I.

A similar dependence on doping concentration is investigated for the confined devices. Variation of Urbach parameter of GaN, GaAs, InAs and GaN with doping concentration is summarized in the plots as shown in Figs. 6.12 and 6.13 for UTB and nanowire. Though the trend is similar to that of bulk, the rate of increase with doping concentration is different from bulk. This is due to the fact that impurity scattering self-energies have different dependence on doping concentration (arising from both doping and screening length de-

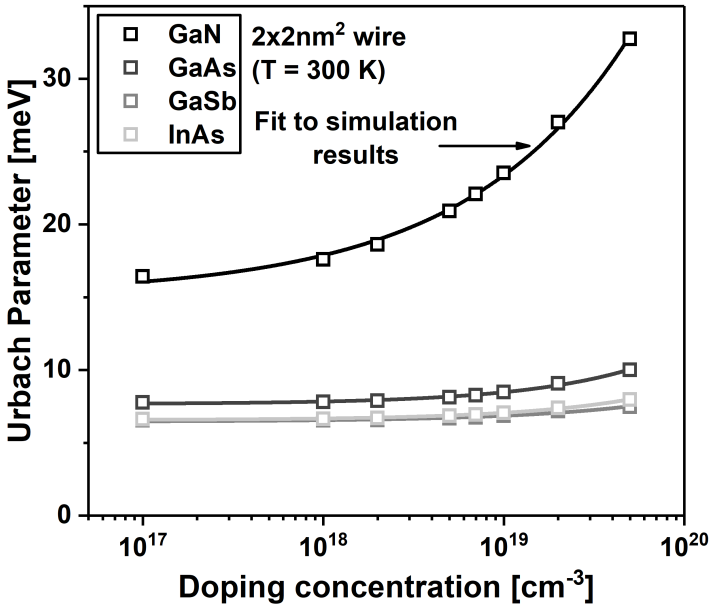

Fig. 6.13.: Variation of Urbach parameter for GaN, GaAs, InAs and GaSb nanowire as a function of doping concentration. Dots correspond to the simulation results and lines correspond to the fitting curve. GaN exhibits largest Urbach parameter due to large LO phonon scattering potential.

pendence) for UTBs and nanowires in comparison to bulk. The variation with doping is again fit with a least-square fitting approach and is fit to $U_{N_D} = U_{intrinsic} + A(N_D/1E18)^u$. The curve captures the trend quite well and the corresponding parameters are summarized in Table 6.1.

	GaN	**GaAs**	**GaSb**	**InAs**
Bulk	$A = 0.38,\ u = 1$	$A = 0.20,\ u = 1$	$A = 0.20,\ u = 1$	$A = 0.25,\ u = 1$
4nm UTB	$A = 22.21,\ u = 0.14$	$A = 2.04,\ u = 0.10$	$A = 6.92,\ u = 0.10$	$A = 0.18,\ u = 0.77$
$2{\times}2\ nm^2$ wire	$A = 2.70,\ u = 0.66$	$A = 0.17,\ u = 0.66$	$A = 0.10,\ u = 0.66$	$A = 0.11,\ u = 0.66$

Table 6.1.: Parameters for variation of Urbach parameter with doping concentration for different materials for bulk, UTB and wire. Fitting for simulation results has been performed using the expression $U(N_D) = A(N_D/1E18)^u + U_{intrinsic}$

6.5 Band gap narrowing - Dependence on temperature, doping and confinement

Self-energies carry both real and imaginary parts which provide dual information about the nature of scattering. While the imaginary part of the self-energy provides the scattering rate that is responsible for band tail creation, real part provides the appropriate shift of energies which can provide us useful information about band gap narrowing values. The real and imaginary part of the self-energy are connected through the Kramers-Krönig relation. Hence, an increase in the imaginary part (larger band tail) automatically should correspond to a larger band gap narrowing value.

As shown in Fig 6.14, bandgap narrowing is extracted by performing two sets of simulation - one with real part turned off and one with real part enabled. Difference of band shift between the two simulations provides information about the band gap narrowing.

$$E_{BGN} = E_c\left(Re\left(\Sigma^R\right) = 0\right) - E_c\left(Re\left(\Sigma^R\right) \neq 0\right) \tag{6.37}$$

To provide confidence in the values of band gap narrowing values obtained from simulations, the values are compared against corresponding experimental data.

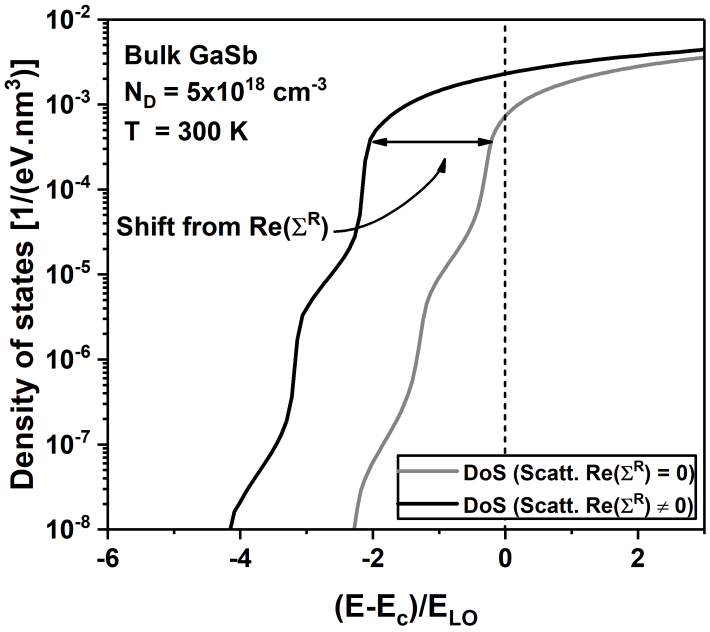

Fig. 6.14.: Density of states as a function of energy (normalized to LO phonon frequency) with and without real part of retarded scattering self-energy. Real part shifts the energy levels moving the band to lower energies. Difference between the density of states with and without the real part is used to extract band gap narrowing.

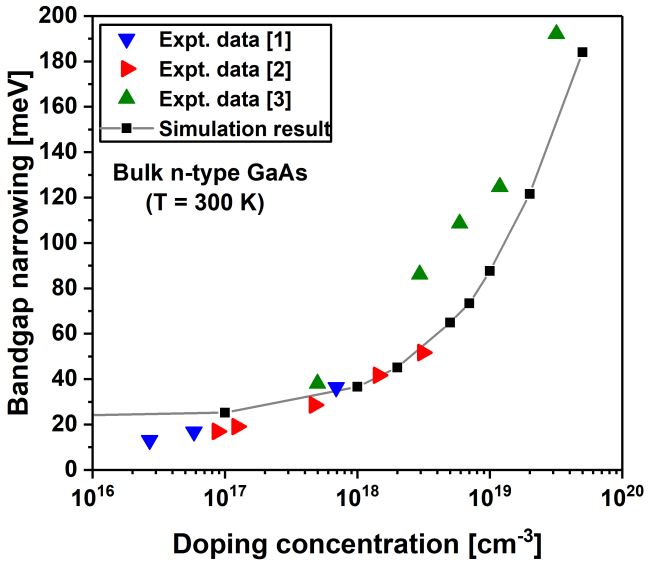

Fig. 6.15.: Variation of band gap narrowing of conduction band as a function of doping concentration for GaAs. Simulation results have been compared against a set of experimental results (Exp. data [1]) obtained from [122], (Exp .data [2]) obtained from [123] and (Exp. data [3]) obtained from [124]. Simulation results show very good agreement with available experimental data.

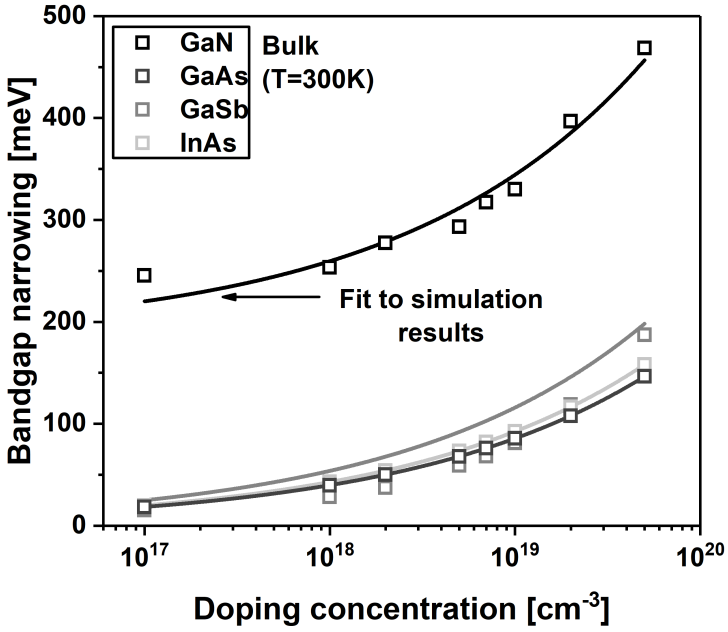

Fig. 6.16.: Variation of bandgap narrowing of conduction band as a function of doping concentration for GaN, GaAs, GaSb, InAs and GaSb. Dots correspond to the simulation results and lines correspond to the fitting curve. GaN exhibits largest band gap narrowing due to larger scattering potential.

Variation of bandgap narrowing is plotted against doping concentration for bulk n-type GaAs and compared against 3 sets of experimental data obtained from [122], [123] and [124] as shown in Fig. 6.15. As expected, band gap narrowing increases with doping concentration mainly due to increasing contribution of impurity scattering towards band shift. Simulation results show good agreement with available experimental data for bulk n-type GaAs. Note that this approach accounts only for the intrinsic effects from phonon and impurity scattering and does not take into account secondary effects such as crystal defects/disorders, exciton effects and exchange interaction of electrons. Despite the neglecting the above effects, match is quite close to experimental results highlighting the importance of intrinsic electrostatic and phononic effects towards shaping the band gap narrowing.

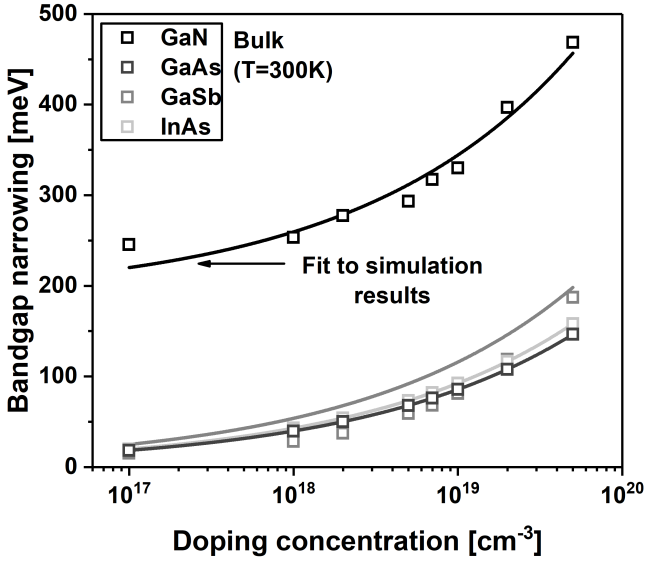

Fig. 6.17.: Variation of bandgap narrowing of conduction band as a function of doping concentration for GaN, GaAs, GaSb, InAs and GaSb. Dots correspond to the simulation results and lines correspond to the fitting curve. GaN exhibits largest band gap narrowing due to larger scattering potential.

Similar to the Urbach tail investigation, variation of band gap narrowing of GaN, GaAs, InAs and GaN with doping concentration is summarized in Fig. 6.16. In general, all the materials follow similar variation with doping profile. GaN, in general has a larger band gap parameter due to large phonon energy and is $3\times$ larger than GaAs, InAs and GaSb. Band gap narrowing values are quite large in comparison to corresponding Urbach parameter values and are of the order of few 100 meVs for high doping concentrations. The variation with doping is fit with a least-square fitting approach and is fit to $BGN_{N_D} = BGN_{intrinsic} + A(N_D/1E18)^u$. The curve captures the trend quite well and the corresponding parameters are summarized in Table 6.2.

Finally, to look at the effect of confinement on band gap narrowing, variation of band gap narrowing parameter for GaN, GaAs, InAs and GaN with doping concentration is summarized in Figs. 6.17 and 6.18 for UTB and nanowire. Though the trend is similar to that of bulk, the rate of increase with doping concentration is different from bulk. This is

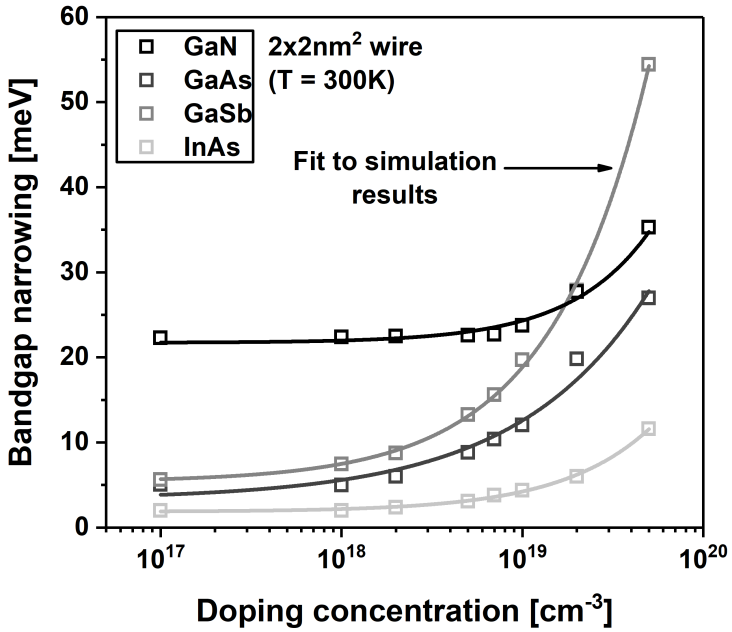

Fig. 6.18.: Variation of bandgap narrowing of conduction band as a function of doping concentration for GaN, GaAs, GaSb, InAs and GaSb. Dots correspond to the simulation results and lines correspond to the fitting curve. GaN exhibits largest band gap narrowing due to larger scattering potential.

due to the fact that impurity scattering self-energies have different dependence on doping concentration (arising from both doping and screening length dependence) for UTBs and nanowires in comparison to bulk (similar to Urbach tail dependence). The variation with doping is again fit with a least-square fitting approach and is fit to $BGN_{N_D} = BGN_{intrinsic} + A(N_D/1E18)^u$. The curve captures the trend quite well and the corresponding parameters are summarized in Table 6.2.

	GaN	**GaAs**	**GaSb**	**InAs**
Bulk	$A = 73.47,\ u = 0.33$	$A = 53.80,\ u = 0.33$	$A = 42.93,\ u = 0.33$	$A = 39.57,\ u = 0.33$
4nm UTB	$A = 22.21,\ u = 0.14$	$A = 2.04,\ u = 0.10$	$A = 6.92,\ u = 0.10$	$A = 0.18,\ u = 0.77$
2×2 nm^2 wire	$A = 0.26,\ u = 1$	$A = 2.13,\ u = 0.8$	$A = 2.32,\ u = 0.66$	$A = 0.31,\ u = 0.87$

Table 6.2.: Parameters for variation of band gap narrowing parameter with doping concentration for different materials for bulk, UTB and wire. Fitting for simulation results has been performed using the expression $BGN(N_D) = A(N_D/1E18)^u + BGN_{intrinsic}$

6.6 Conclusion

In summary, existence of band tail and band gap narrowing in polar materials is captured with NEGF + self-consistent Born approach. These values are extracted for 4 different polar materials - GaAs, InAs, GaSb and GaN for bulk, ultra-thin body and nanowire devices. Band tails are calculated based on POP and Impurity scattering, Urbach parameter is extracted and is shown to agree well with available experimental data for several materials. Increasing the doping concentration increases the Urbach parameter due to the increasing effect of impurity scattering, consistent with experimental observations. Real part of self energy is used to extract band gap narrowing parameter and the corresponding values are shown to agree well with experimental data. Finally, a fit function is used to provide fit parameters to capture variation of Urbach and band gap narrowing parameters for these materials and devices.

7. ROLE OF DIELECTRIC ENVIRONMENT ON BAND TAIL ENHANCEMENT IN 2D TRANSITION METAL DICHALCOGENIDES

7.1 Summary

In this chapter, role of dielectric environment on band tail enhancement is analyzed for 2D transition metal dichalcogenides (TMDs). 3 TMD materials, namely MoS_2, WS_2 and WSe_2 are taken up for investigation. Three important scattering mechanisms in TMDs - polar optical phonons, charged impurities and remote oxide phonons are taken into account. Variation of band tails with TMD layers, temperature and doping dependence and oxide dependence is studied in detail.

7.2 Motivation

Two dimensional materials have attracted considerable attention recently due to their unique electronic, optical and mechanical properties [27]. Unlike graphene, transition metal dichalcogenide (TMDs) have a finite band gap which provides for applications in electronics as a replacement for Si transistors [28], in optoelectronics as possible materials in light emitting diodes [29], [30] and solar cells [31] applications. TMD layers have weak van der Waals coupling which enables low cost fabrication (through mechanical cleavage) and have electronic/optical properties that show strong dependence as a function of layers. Ability to stack multiple TMD materials on top of another significantly widens the design space available resulting in a plethora of devices such as $MoS_2 - WSe_2$ p-n junctions [32], $MoS_2 - Ge$ based tunnel field-effect transistor (TFET).

Thermal and doping induced disorders lead to associated Urbach tails which are exponentially decaying density of states below band edge. Urbach tails can significantly alter

the behaviour of the device. Switching behaviour of TFET is drastically affected by such tailing states. They are known to place a fundamental limit on the lowest achievable SS in TFETs and also affect the optical behaviour such as absorption spectrum and absorption/recombination coefficient in optoelectronic devices [10, 19, 20]. 2D layered semiconductors have the ability to alleviate these problems due to their pristine surface and weak inter layer coupling. However, being an atomically thin material, their behaviour is highly dependent on the nature of the dielectric environment such as nature of oxide layer on which it is exfoliated, on the number of layers as dielectric constant of TMD materials varies sharply with layers and is anisotropic [33]. Charge scattering and mobility is shown to depend heavily on the interplay between impurity concentration and native oxides due to dielectric screening [34, 35].

This requires a rigorous treatment of both the material and associated dielectric environment to get a good understanding on the behaviour of Urbach parameters for TMD materials. Despite the immense volume of research happening in TMD area and the importance of Urbach parameters in the associated devices, there has been very little progress with regards to calculating Urbach parameters for TMD materials. Analytical work in evaluating Urbach parameters have been carried out by [113] where the Urbach parameters for TMD materials have been modeled using an analytical approach with material parameters such as deformation potentials obtained from density-functional theory. Variation of Urbach parameters have been provided against doping concentration, temperature and different dielectrics. However this work is based on bulk based analytical expressions for Urbach parameters and does not take into effect the detailed nature of TMD bandstructure and interplay between different scattering mechanisms. Experimental values for Urbach parameters of monolayer MoS_2 and WSe_2 have been characterized by [125] and [126] in the context of optical measurements.

In this work, we try to evaluate Urbach parameters for three candidate TMD materials, MoS_2, WS_2 and WSe_2 using NEGF and self-consistent Born approximation to treat scattering self-energies. Variation of Urbach parameter against several important parameters

such as temperature, doping concentration, TMD layers and oxide is presented. Wherever possible, simulation results are compared against experimental values.

7.3 Simulation approach

The atomic structures of all TMD layers are subatomically resolved with maximally localized Wannier functions (MLWFs). This treatment provides a balance between physical accuracy and computational efficiency. MLWF Hamiltonians are created by first performing electronic structure calculation in the DFT tool VASP [127] with the self-consistent electronic model and with a convergence criterion of 10^{-8} eV. A momentum mesh of $5 \times 5 \times 5$ Monkhorst-Pack grids and an energy cutoff of 520 eV are used along with van der Waals force included according to [128]. The applied DFT model is based on the generalized gradient approximation (GGA) employing the Perdew-Burke-Ernzerhof functionals. The electronic DFT Hamiltonian is transformed into an MLWF representation using the Wannier90 software [129–131] with d orbitals for the metal electrons and sp3 orbitals for the chalcogenide electrons as the initial projection. The spreading of the Wannier functions is reduced iteratively until it converges to around $2A^2$. The atom positions and their corresponding electronic Hamiltonian of finite TMD structures are then created in NEMO5 [44].

All devices are simulated using NEGF with self-consistent Born approach to account for scattering. Device is assumed to be periodic in the transverse direction and is represented by a corresponding k space. Three major scattering mechanisms are taken into account - polar optical phonons, charged impurity and remote phonon scattering. A detailed derivation of the scattering self-energies has been discussed earlier in Section 3. Only representative equations are highlighed below. Scattering self-energies with polar optical phonons take the form

$$\begin{aligned}\Sigma^{<}\left(\vec{x}_1,\vec{x}_2,k_{||},E\right) = \frac{e^2}{(2\pi)^3}\left(\frac{1}{\epsilon_\infty}-\frac{1}{\epsilon_s}\right)\frac{\hbar\omega_o}{2\epsilon_o}\int dl_{||} I(k_{||},l_{||},\vec{x}_1,\vec{x}_2) \\ \times\left[n_o G^{<}\left(\vec{x}_1,\vec{x}_2,l_{||},E-E_o\right)+\left(1+n_q\right)G^{<}\left(\vec{x}_1,\vec{x}_2,l_{||},E+E_o\right)\right]\end{aligned} \tag{7.1}$$

$$\Sigma^R\left(\vec{x}_1,\vec{x}_2,k_{||},E\right)=\frac{e^2}{(2\pi)^3}\left(\frac{1}{\epsilon_\infty}-\frac{1}{\epsilon_s}\right)\frac{\hbar\omega_o}{2\epsilon_o}\int dl_{||}I(k_{||},l_{||},\vec{x}_1,\vec{x}_2)$$
$$\times\left[(1+n_o)G^R\left(\vec{x}_1,\vec{x}_2,l_{||},E-E_o\right)+n_oG^R\left(\vec{x}_1,\vec{x}_2,l_{||},E+E_o\right)+\frac{1}{2}G^<(\vec{x}_1,\vec{x}_2,l_{||},E-E_o)\right.$$
$$\left.-\frac{1}{2}G^<(\vec{x}_1,\vec{x}_2,l_{||},E+E_o)+i\int\frac{d\tilde{E}}{2\pi}G^<\left(\vec{x}_1,\vec{x}_2,l_{||},\tilde{E}\right)\left(Pr\frac{1}{E-\tilde{E}-E_o}-Pr\frac{1}{E-\tilde{E}+E_o}\right)\right] \tag{7.2}$$

where

$$I(k_{||},l_{||},\vec{x}_1,\vec{x}_2)=$$
$$\begin{cases}\pi\left[\sqrt{\left(k_{||}-l_{||}\right)^2+\zeta^{-2}}\,|\vec{x}_1-\vec{x}_2|+\dfrac{\left(k_{||}-l_{||}\right)^2|\vec{x}_1-\vec{x}_2|}{\sqrt{\left(k_{||}-l_{||}\right)^2+\zeta^{-2}}}\right]K_1\left(\sqrt{\left(k_{||}-l_{||}\right)^2+\zeta^{-2}}\,|\vec{x}_1-\vec{x}_2|\right), \\ |\vec{x}_1-\vec{x}_2|\neq 0 \\ \pi\left[1+\dfrac{\left(k_{||}-l_{||}\right)^2}{\left(k_{||}-l_{||}\right)^2+\zeta^{-2}}\right],\ |\vec{x}_1-\vec{x}_2|=0\end{cases} \tag{7.3}$$

$\hbar\omega_o$ is the optical phonon frequency, ϵ_s and ϵ_∞ are the static and infinity frequency dielectric constants, n_o is the Bose-Einstein distribution and ζ is the screening length.

Scattering self-energies with charged impurities are given by

$$\Sigma^{<,R}\left(\vec{x}_1,\vec{x}_2,k_{||},E\right)=\frac{N_D}{(8\pi)^2}\left(\frac{e^2}{\epsilon_o\epsilon_r}\right)^2\int dl_{||}I(k_{||},l_{||},\vec{x}_1,\vec{x}_2)G^{<,R}\left(\vec{x}_1,\vec{x}_2,l_{||},E\right) \tag{7.4}$$

where

$$I(k_{||},l_{||},\vec{x}_1,\vec{x}_2)=$$
$$\begin{cases}\pi\left[\dfrac{|\vec{x}_1-\vec{x}_2|}{\left(k_{||}-l_{||}\right)^2+\zeta^{-2}}\right]K_1\left(\sqrt{\left(k_{||}-l_{||}\right)^2+\zeta^{-2}}\,|\vec{x}_1-\vec{x}_2|\right), \\ |\vec{x}_1-\vec{x}_2|\neq 0 \\ \pi\left[\dfrac{1}{\left(k_{||}-l_{||}\right)^2+\zeta^{-2}}\right],\ |\vec{x}_1-\vec{x}_2|=0\end{cases} \tag{7.5}$$

where N_D is the doping concentration, ϵ_r is the static dielectric constant and ζ is the screening length.

Scattering with remote oxide phonons is given by

$$\Sigma^{<}\left(\vec{x}_1,\vec{x}_2,k,E\right)=\frac{e^2}{(2\pi)}\frac{\hbar\omega_{SO}^{\nu}}{2\epsilon_0}\left(\frac{1}{\epsilon_{ox}^{\infty}+\epsilon_s^{\infty}}-\frac{1}{\epsilon_{ox}^{s}+\epsilon_s^{\infty}}\right)\int dlI(k,l,\vec{x}_1,\vec{x}_2,z_1,z_2)$$
$$\times\left[n_qG^{<}\left(\vec{x}_1,\vec{x}_2,l,E-E_o\right)+\left(1+n_q\right)G^{<}\left(\vec{x}_1,\vec{x}_2,l,E+E_o\right)\right] \tag{7.6}$$

$$\Sigma^{R}\left(\vec{x}_1,\vec{x}_2,k,E\right)=\frac{e^2}{(2\pi)}\frac{\hbar\omega_{SO}^{\nu}}{2\epsilon_0}\left(\frac{1}{\epsilon_{ox}^{\infty}+\epsilon_s^{\infty}}-\frac{1}{\epsilon_{ox}^{s}+\epsilon_s^{\infty}}\right)\int dlI(k,l,\vec{x}_1,\vec{x}_2,z_1,z_2)$$
$$\times\left[(1+n_o)G^{R}\left(\vec{x}_1,\vec{x}_2,l,E-E_o\right)+n_oG^{R}\left(\vec{x}_1,\vec{x}_2,l,E+E_o\right)+\frac{1}{2}G^{<}(\vec{x}_1,\vec{x}_2,l,E-E_o)\right.$$
$$\left.-\frac{1}{2}G^{<}(\vec{x}_1,\vec{x}_2,l,E+E_o)+i\int\frac{d\tilde{E}}{2\pi}G^{<}\left(\vec{x}_1,\vec{x}_2,l,\tilde{E}\right)\left(Pr\frac{1}{E-\tilde{E}-E_o}-Pr\frac{1}{E-\tilde{E}+E_o}\right)\right] \tag{7.7}$$

where

$$I(k,l,\vec{x}_1,\vec{x}_2,z_1,z_2)=\int_0^{2\pi}d\theta e^{i|k-l|\left|\vec{x}_{1,||}-\vec{x}_{2,||}\right|cos\theta}.e^{-|k-l|(z_1+z_2-2t)}$$
$$=2\pi J_o\left(|k-l|\left|\vec{x}_{1,||}-\vec{x}_{2,||}\right|\right)e^{-|k-l|(z_1+z_2-2t)} \tag{7.8}$$

$\hbar\omega_{SO}^{\nu}$ is the ν^{th} optical phonon frequency of oxide, ϵ_{ox}^{s} and ϵ_{ox}^{∞} are the static and infinite frequency dielectric constants of oxide, ϵ_s^{∞} is the infinite frequency dielectric constant of semiconductor underneath the oxide, n_q is the Bose distribution. z_1, z_2 are the spatial coordinates in the direction of interface and t is the thickness of semiconductor.

The scattering self-energies are assumed to be diagonal in both orbital and atom position. However, a simple truncation of non-local elements underestimates the scattering. This is overcome by multiplying the scattering self-energies with a compensation factor which accounts for non-locality. The compensation factor is defined as a division of form factors of the scattering rate from Fermi's golden rule for the local case with the non-local one. The compensation factor for 2D material can be represented as

$$S_{UTB}=\frac{\int_0^{2\pi}d\theta\int_0^{L_z}\int_0^{L_z}dzdz^{'}\rho_{ij}(z)\rho_{ij}(z')I(|\tilde{\mathrm{k}}_{||}-\tilde{\mathrm{k}}'_{||}|,z,z')}{\int_0^{2\pi}d\theta\int_0^{L_z}\int_0^{L_z}dzdz^{'}\rho_{ij}(z)\rho_{ij}(z')I_{Local}(|\tilde{\mathrm{k}}_{||}-\tilde{\mathrm{k}}'_{||}|,z,z')} \tag{7.9}$$

where

$$I_{Local}(q_{||},z,z') = \begin{cases} \dfrac{1}{\sqrt{q_{||}^2+\zeta^{-2}}}\left[1-\dfrac{\zeta^{-2}}{2\left(q_{||}^2+\zeta^{-2}\right)}\right],\ |z-z'|=0 \\ 0,\ |z-z'|\neq 0 \end{cases} \tag{7.10}$$

For all the discussions in the subsequent sections, device is assumed to be in equilibrium with the density corresponding to the doping concentration. Self-energies derived are solved consistently with the corresponding Green's function until particle conservation is achieved throughout the device. Following are the corresponding NEGF equations solved to achieve converged density and density of states.

$$\begin{gathered} G^R = \left(EI - H - \Sigma^R_{pop} - \Sigma^R_{imp} - \Sigma^R_{remote} - \Sigma^R_{source} - \Sigma^R_{drain}\right)^{-1} \\ G^< = G^R\left(\Sigma^<_{pop} + \Sigma^<_{imp} + \Sigma^<_{remote} + \Sigma^<_{source} + \Sigma^<_{drain}\right)G^{R\dagger} \end{gathered} \tag{7.11}$$

Urbach parameter is extracted by plotting the density of states versus energy and by taking the slope of the exponential decay as follows

$$E_{Urbach} = \frac{(E_1 - E_2)}{log\left(\dfrac{DoS(E_1)}{DoS(E_2)}\right)} \tag{7.12}$$

where E_1 and E_2 are two energy points present below E_c or above E_v. $DoS(E_1)$ and $DoS(E_2)$ correspond to the density of states at energy E_1 and E_2. Material parameters used for TMDs and oxides are tabulated below taken from [33], [132] and [35].

		ϵ_s	ϵ_∞	$\hbar\omega_{LO}$
MoS_2	1 layer	3.8	3.2	48 meV
	2 layer	5.65	4.8	
	3 layer	6.47	5.5	
	4 layer	7.3	6.2	
WS_2	1 layer	3.65	3.1	33 meV
	2 layer	5.15	4.37	
	3 layer	5.92	5.03	
	4 layer	6.7	5.69	
WSe_2	1 layer	3.7	3.145	30 meV
	2 layer	5.3	4.5	
	3 layer	6.1	5.18	
	4 layer	6.9	5.86	

Table 7.1.: Dielectric constants and phonon frequency of MoS_2, WS_2 and WSe_2 for 1-4 layers used in the simulation. Parameters have been taken from [33] and [132].

	SiO_2	BN	Al_2O_3	HfO_2
ϵ_s	3.9	5.09	12.53	23
ϵ_∞	2.5	4.1	3.2	5.03
ω^1_{SO}	55.6	93.07	48.18	12.4
ω^2_{SO}	138.1	179.1	71.41	48.35

Table 7.2.: Static and infinite dielectric constant of oxides used in the simulation along with their SO phonon frequencies. Taken from [35]

7.4 Layer dependence

Urbach parameter dependence as a function of layer is analyzed for the TMD materials. Phonon scattering potential is dependent on the product of optical phonon frequency and inverse of difference between the static and infinite frequency dielectric constant of the material. Based on the parameters used in Table 7.1, both the static and infinite dielectric constants increase from monolayer to bulk. Hence, the scattering potential is expected to be strongest for the monolayer and get weaker with increasing number of layers. Doping concentration, on the other hand, enhances the band tail through elastic scattering processes. With increasing doping concentration, the Urbach tail increases further. Fig. 7.1 shows the dependence of Urbach parameter of MoS_2 as a function of layers for different doping concentrations. As expected, Urbach parameter decreases with increasing number of layers with the value of 25 meV for monolayer and 12 meV for 4 layer device. With increasing doping concentration from $3 \times 10^{10} cm^{-2}$ to $6 \times 10^{13} cm^{-2}$, Urbach parameter increases with the rate of increase getting steeper with increasing doping. It is as high as 210 meV for monolayer for $6 \times 10^{13} cm^{-2}$ doping concentration highlighting the impact of doping. Comparison against experimental data obtained from photoluminescence measurements taken from [125] show good agreement for monolayer case.

Fig. 7.2 and 7.3 show the variation of Urbach parameter versus layers for WS_2 and WSe_2 where a similar profile is observed. In terms of the strength of phonon scattering potential, WS_2 has the weakest among the 3 TMDs and it shows up as a lower Urbach parameter in comparison to the other two materials. Comparison against experimental data shows good agreement for monolayer WS_2 providing confidence in the approach.

7.5 Temperature and doping dependence

Urbach parameter as a function of temperature is plotted for the TMD materials. With increasing temperature, phonon contribution increases exponentially. In this approach, electrons are assumed to be interacting with bulk phonons in equilibrium. Temperature dependence of phonons is given by the Bose distribution $n = 1/(exp(\hbar\omega_{LO}/k_bT) - 1)$. Due

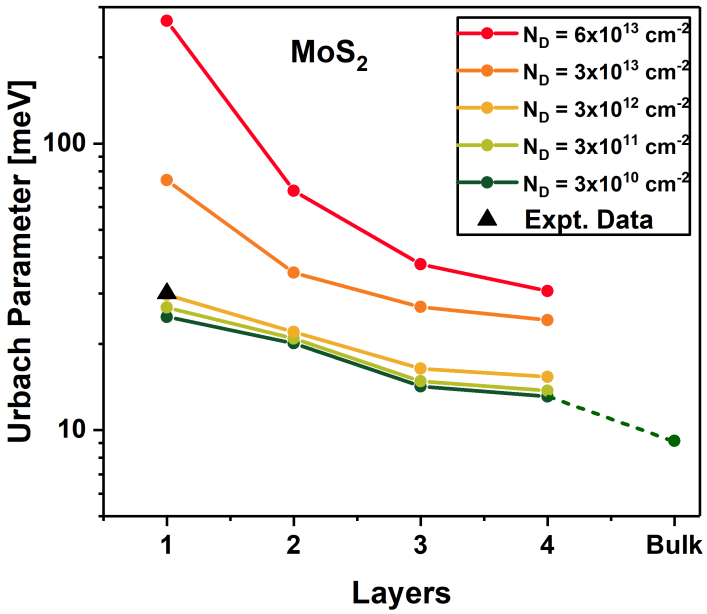

Fig. 7.1.: Variation of Urbach parameter of MoS_2 as a function of layers for doping concentration ranging from $N_D = 3 \times 10^{10} cm^{-2}$ to $N_D = 6 \times 10^{13} cm^{-2}$. Comparison against experimental data obtained from [125] shows good agreement.

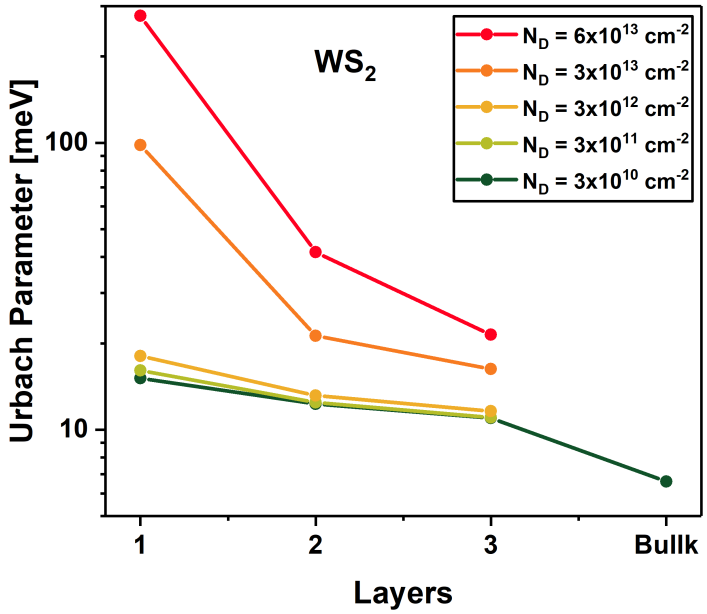

Fig. 7.2.: Variation of Urbach parameter of WS_2 as a function of layers for doping concentration ranging from $N_D = 3 \times 10^{10} cm^{-2}$ to $N_D = 6 \times 10^{13} cm^{-2}$.

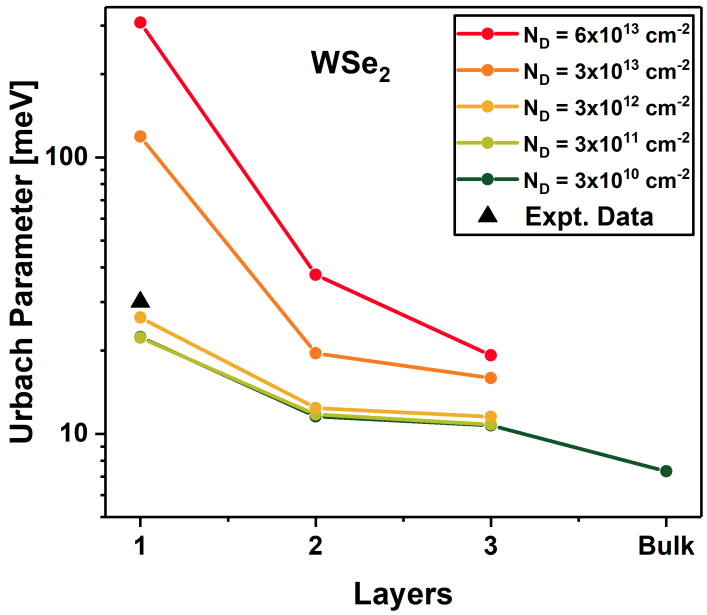

Fig. 7.3.: Variation of Urbach parameter of WSe_2 as a function of layers for doping concentration ranging from $N_D = 3 \times 10^{10} cm^{-2}$ to $N_D = 6 \times 10^{13} cm^{-2}$. Comparison against experimental data obtained from [125] shows good agreement.

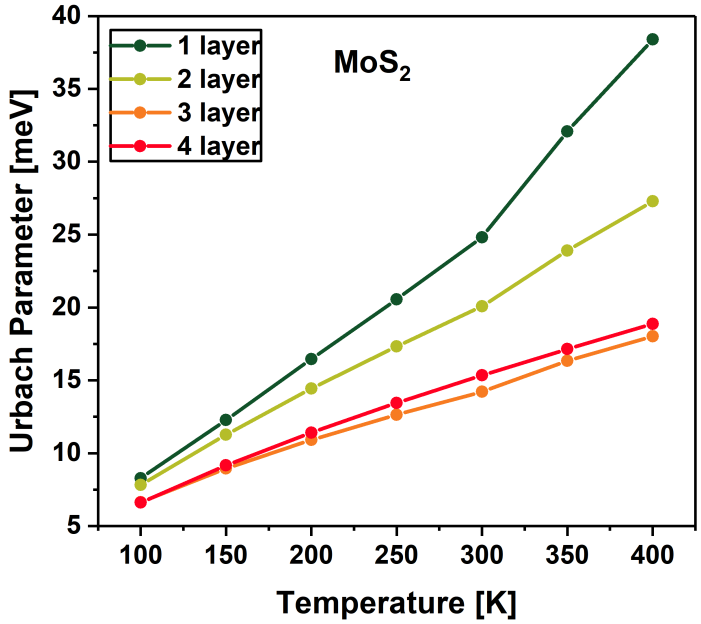

Fig. 7.4.: Variation of Urbach parameter with temperature for MoS_2 for different layers. Urbach parameter increases linearly with temperature. Monolayer MoS_2 has the largest scattering potential and has the highest rate of increase. With increasing layers, the slope decreases gradually due to decreasing scattering potential.

to exponential contribution of phonons with increasing temperature, Urbach parameter is expected to increase with temperature. Fig. 7.4 shows the variation of Urbach parameter of MoS_2 as a function of temperature for different layers. As discussed in the previous section, monolayer has the largest scattering potential and this results in both a larger value of Urbach parameter and a larger slope for dependence with temperature. With increasing number of layers, the value decreases gradually. A similar result is observed for WS_2 as shown in Fig. 7.2 but with smaller Urbach parameters due to the smaller value of scattering potentials of monolayer and multilayer WS_2 in comparison to MoS_2.

WSe_2 shows a similar profile as well (as shown in Fig. 7.6) but there is a marked difference in the slope between monolayer and multilayer cases. This can be explained by observing that Urbach parameter in general depends on the amount of scattering rate present close to the band edges. Larger the scattering rate, more gradual will be the exponentially

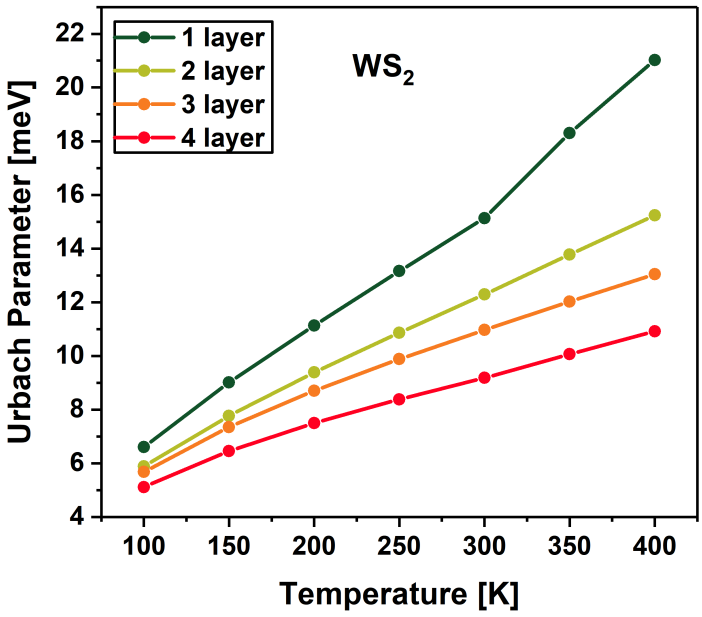

Fig. 7.5.: Variation of Urbach parameter with temperature for WS_2 for different layers. Urbach parameter increases linearly with temperature. Monolayer WS_2 has the largest scattering potential and has the highest rate of increase. With increasing layers, the slope decreases gradually due to decreasing scattering potential.

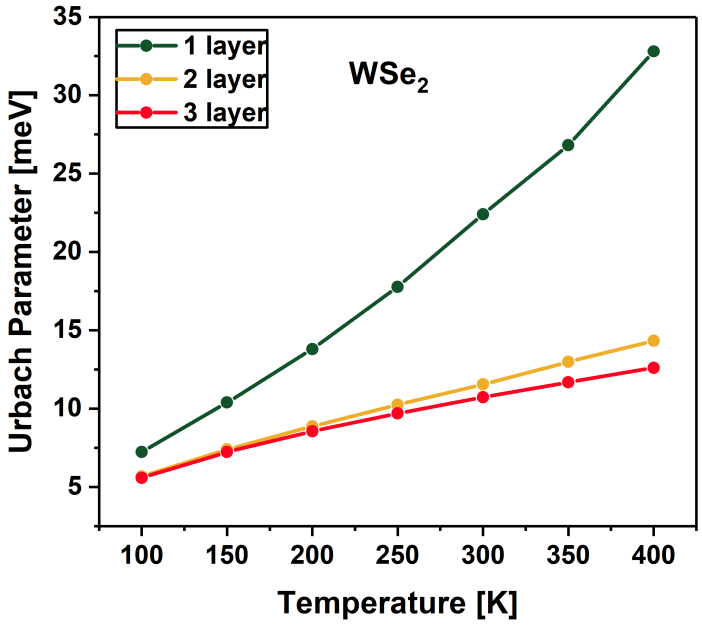

Fig. 7.6.: Variation of Urbach parameter with temperature for WSe_2 for different layers. rbach parameter increases linearly with temperature. Monolayer WSe_2 shows a stronger increase due to degenerate K and Q conduction band valleys which provides additional density of states to scatter to in comparison with 2 and 3 layers where the degeneracy is broken.

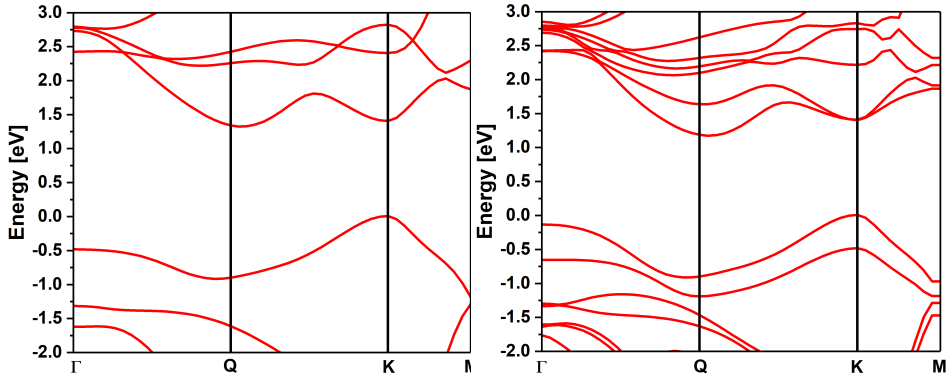

(a) (b)

Fig. 7.7.: (a) Bandstructure of 1 layer WSe_2. Conduction band has a degeneracy at K and Q valley resulting in a large conduction band density of states. (b) Bandstructure of 2 layer WSe_2. Band degeneracy at K and Q valley is lifted with only Q valley contributing to the density of states at the bandedge

decaying band tails resulting in a larger Urbach parameter. Scattering rate, depends on the product of scattering potential and available density of states. Looking at the conduction band structure of WSe_2 (Fig. 7.7) one can see that the conduction band edge has a degeneracy at K and Q valley for monolayer WSe_2. However, moving to 2-layer and higher number of layers breaks the K/Q valley degeneracy. Hence, at the bandedge, monolayer has contribution from both K and Q valleys resulting in a larger density of states whereas multilayer WSe_2 has contribution only from Q valley resulting in a reduction of the available density of states. This results in an abrupt jump in the Urbach parameter which is captured well in the temperature dependence.

7.6 Impact of remote oxide phonons

Urbach parameter is plotted against several oxides and the impact of remote phonon scattering is analyzed. Remote phonon scattering plays an important role in atomically thin semiconductors such as graphene and TMD materials. Usually, these materials are exfoli-

ated and hosted on a native oxide (such as SiO_2, Al_2O_3) and might also have a gate oxide to control charge transport in the device. These oxides, being polar in nature have strong LO phonon modes that can couple to the electrons in semiconductor. Such a electron-phonon interaction is termed remote phonon scattering, the name "remote" attributed to their origin not in the semiconductor but in oxides. Remote phonon scattering has a similar scattering formulation as polar optical phonon scattering with the phonon energy and dielectric constants now corresponding to the oxide and oxide/semiconductor respectively. Based on the values of parameters from Table 7.2, one can observe that oxides in general have two phonon modes contributing to the scattering process. Dielectrics that have a strong bond, such as SiO_2 and BN have smaller change between the static and infinite frequency dielectric constants and have phonon frequencies that are quite large. These large phonon frequencies do not contribute much to the scattering process since it's tough for electrons to emit and absorb such high frequencies as the phonon distribution decays exponentially with increasing energy. Al_2O_3 and HfO_2 on the other hand, have a large variation between the static and infinite frequency dielectric constants and have phonon frequencies that are reasonably placed in energy. Hence, the expectation, based on the parameters is that Al_2O_3 and HfO_2 will contribute strongly to the remote phonon scattering process and SiO_2 and BN will have negligible contribution to the scattering process.

Figs. 7.8, 7.9 and 7.10 show the behaviour of Urbach parameter as a function of layers for different oxide materials for doping concentration of $N_D = 3 \times 10^{12} cm^{-2}$. As expected, both Al_2O_3 and HfO_2 increase the Urbach parameter through remote phonon scattering process for monolayer TMDs. SiO_2 and BN show negligible enhancement from intrinsic values. With increasing number of layers, the Urbach parameter decreases significantly. This happens due to two reasons - decreasing polar optical phonon scattering strength with increasing number of layers and decreasing contribution of remote phonon scattering strength. Note that remote phonon scattering strength decays sharply as one moves away from the oxide-semiconductor interface due to decaying phonon modes. With increasing number of layers, the net contribution from remote phonon scattering decreases resulting in a significant decrease with increasing number of layers.

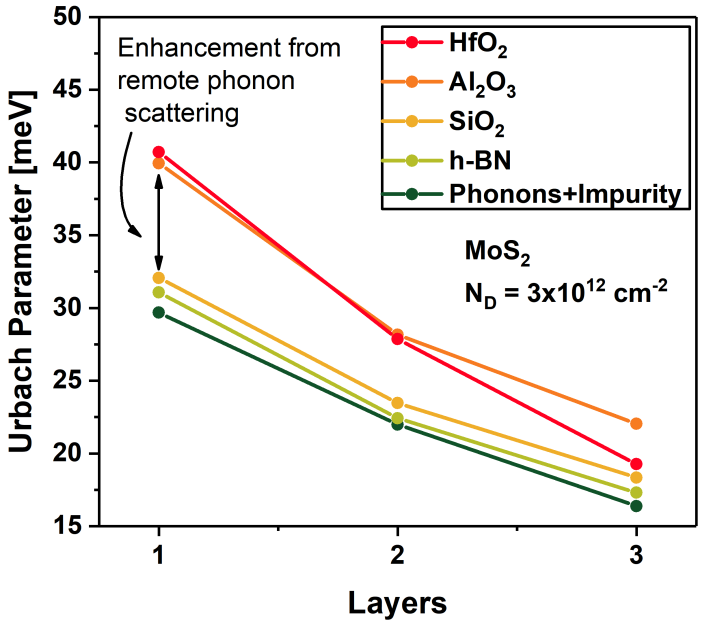

Fig. 7.8.: Variation of Urbach parameter for MoS_2 in the presence of phonons, impurity and corresponding enhancement from remote phonon scattering. Al_2O_3 and HfO_2 provide maximal enhancement raising the Urbach parameter by 10 meV. Contribution of remote phonons decreases gradually with increasing layers and Al_2O_3 is the main contributor to remote phonon process at higher layers.

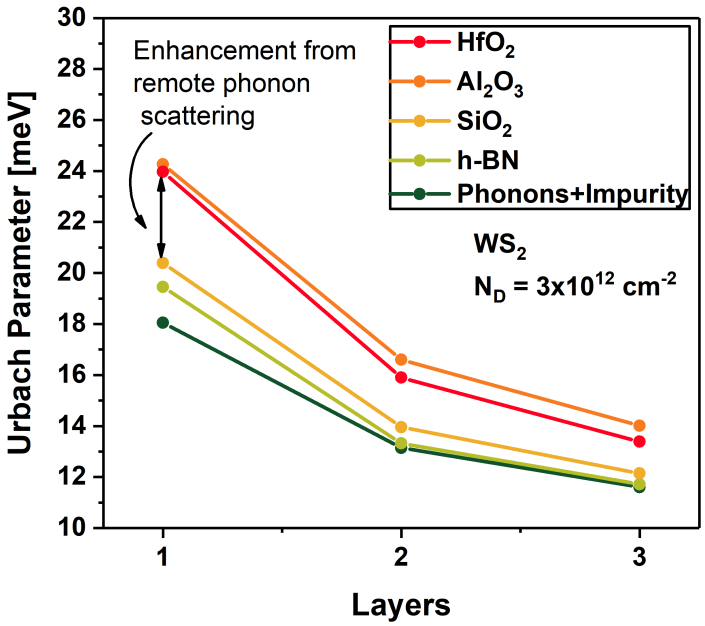

Fig. 7.9.: Variation of Urbach parameter for WS_2 in the presence of phonons, impurity and corresponding enhancement from remote phonon scattering. Al_2O_3 and HfO_2 provide only mild enhancement raising the Urbach parameter by 2 meV. Contribution of remote phonons decreases gradually with increasing layers.

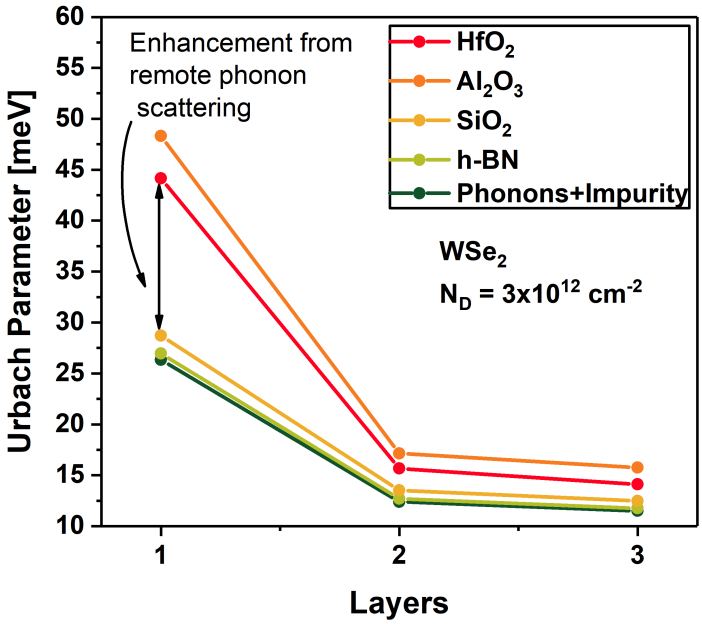

Fig. 7.10.: Variation of Urbach parameter for WSe_2 in the presence of phonons, impurity and corresponding enhancement from remote phonon scattering. Al_2O_3 and HfO_2 provide maximum enhancement raising the Urbach parameter by 20 meV. Contribution of remote phonons decreases as expected with increasing layers. WSe_2 monolayer has much higher Urbach parameter which gets further enhanced with remote phonon scattering.

7.7 Conclusion

Role of dielectric environment in enhancing band tails in transition metal dichalcogenides is discussed. Three important scattering mechanisms - polar optical phonons, charged impurity and remote phonon scattering processes are considered. Urbach parameter is shown to have strong temperature, doping and layer dependence. Strong layer dependence is shown to be dependent both on layer-dependent scattering potential and band degeneracy. Role of oxides in enhancing band tails is investigated. Among the oxide materials considered, Al_2O_3 and HfO_2 are shown to be strongest contributor to the remote phonon scattering enhancing band tails by as much as 30%.

REFERENCES

REFERENCES

[1] D. Hisamoto, W.-C. Lee, J. Kedzierski, H. Takeuchi, K. Asano, C. Kuo, E. Anderson, T.-J. King, J. Bokor, and C. Hu, "Finfet-a self-aligned double-gate mosfet scalable to 20 nm," *IEEE Transactions on Electron Devices*, vol. 47, no. 12, pp. 2320–2325, 2000.

[2] Economist. (2016) After moore's law. [Online]. Available: https://www.economist.com/technology-quarterly/2016-03-12/after-moores-law

[3] J. Xiang, W. Lu, Y. Hu, Y. Wu, H. Yan, and C. M. Lieber, "Ge/si nanowire heterostructures as high-performance field-effect transistors," *Nature*, vol. 441, no. 7092, pp. 489–493, 2006.

[4] A. I. Hochbaum, R. Fan, R. He, and P. Yang, "Controlled growth of si nanowire arrays for device integration," *Nano letters*, vol. 5, no. 3, pp. 457–460, 2005.

[5] K. Boucart and A. M. Ionescu, "Double-gate tunnel fet with high-kappa gate dielectric," *IEEE Transactions on Electron Devices*, vol. 54, no. 7, pp. 1725–1733, 2007.

[6] J. A. Del Alamo, "Nanometre-scale electronics with iii-v compound semiconductors," *Nature*, vol. 479, no. 7373, pp. 317–323, 2011.

[7] B. Radisavljevic, A. Radenovic, J. Brivio, i. V. Giacometti, and A. Kis, "Single-layer mos2 transistors," *Nature nanotechnology*, vol. 6, no. 3, pp. 147–150, 2011.

[8] S.-D. Kim, "Optimum location of silicide/si interface in ultra-thin body soi mosfets with recessed and elevated silicide source/drain contact structure," *Solid-State Electronics*, vol. 53, no. 10, pp. 1112–1115, 2009.

[9] L. Research. (2017) Tech brief: An introduction to interconnects. [Online]. Available: https://blog.lamresearch.com/tech-brief-an-introduction-to-interconnects/

[10] H. Lu and A. Seabaugh, "Tunnel field-effect transistors: State-of-the-art," *IEEE Journal of the Electron Devices Society*, vol. 2, no. 4, pp. 44–49, 2014.

[11] A. C. Seabaugh and Q. Zhang, "Low-voltage tunnel transistors for beyond cmos logic," *Proceedings of the IEEE*, vol. 98, no. 12, pp. 2095–2110, 2010.

[12] A. Alian, J. Franco, A. Vandooren, Y. Mols, A. Verhulst, S. El Kazzi, R. Rooyackers, D. Verreck, Q. Smets, A. Mocuta *et al.*, "Record performance ingaas homo-junction tfet with superior ss reliability over mosfet," in *Electron Devices Meeting (IEDM), 2015 IEEE International*. IEEE, 2015, pp. 31–7.

[13] G. Zhou, R. Li, T. Vasen, M. Qi, S. Chae, Y. Lu, Q. Zhang, H. Zhu, J.-M. Kuo, T. Kosel *et al.*, "Novel gate-recessed vertical inas/gasb tfets with record high i on of 180 μa/μm at v ds= 0.5 v," in *Electron Devices Meeting (IEDM), 2012 IEEE International*. IEEE, 2012, pp. 32–6.

[14] U. E. Avci and I. A. Young, "Heterojunction tfet scaling and resonant-tfet for steep subthreshold slope at sub-9nm gate-length," in *Electron Devices Meeting (IEDM), 2013 IEEE International*. IEEE, 2013, pp. 4–3.

[15] D. Sarkar, X. Xie, W. Liu, W. Cao, J. Kang, Y. Gong, S. Kraemer, P. M. Ajayan, and K. Banerjee, "A subthermionic tunnel field-effect transistor with an atomically thin channel," *Nature*, vol. 526, no. 7571, p. 91, 2015.

[16] J. Appenzeller, Y.-M. Lin, J. Knoch, and P. Avouris, "Band-to-band tunneling in carbon nanotube field-effect transistors," *Physical review letters*, vol. 93, no. 19, p. 196805, 2004.

[17] B. M. Borg, K. A. Dick, B. Ganjipour, M.-E. Pistol, L.-E. Wernersson, and C. Thelander, "Inas/gasb heterostructure nanowires for tunnel field-effect transistors," *Nano letters*, vol. 10, no. 10, pp. 4080–4085, 2010.

[18] P. S. University. (2011) Quantum tunneling results in record transistor performance. [Online]. Available: https://news.psu.edu/story/150641/2011/12/09/research/quantum-tunneling-results-record-transistor-performance

[19] S. Agarwal and E. Yablonovitch, "Band-edge steepness obtained from esaki/backward diode current–voltage characteristics," *IEEE Transactions on Electron Devices*, vol. 61, no. 5, pp. 1488–1493, 2014.

[20] J. Bizindavyi, A. S. Verhulst, Q. Smets, D. Verreck, B. Sorée, and G. Groeseneken, "Band-tails tunneling resolving the theory-experiment discrepancy in esaki diodes," *IEEE Journal of the Electron Devices Society*, vol. 6, pp. 633–641, 2018.

[21] J. Geng, P. Sarangapani, K.-C. Wang, E. Nelson, B. Browne, C. Wordelman, J. Charles, Y. Chu, T. Kubis, and G. Klimeck, "Quantitative multi-scale, multi-physics quantum transport modeling of gan-based light emitting diodes," *physica status solidi (a)*, vol. 215, no. 9, p. 1700662, 2018.

[22] A. Laubsch, M. Sabathil, J. Baur, M. Peter, and B. Hahn, "High-power and high-efficiency ingan-based light emitters," *IEEE transactions on electron devices*, vol. 57, no. 1, pp. 79–87, 2010.

[23] W. Guo, M. Zhang, A. Banerjee, and P. Bhattacharya, "Catalyst-free ingan/gan nanowire light emitting diodes grown on (001) silicon by molecular beam epitaxy," *Nano letters*, vol. 10, no. 9, pp. 3355–3359, 2010.

[24] P. Krogstrup, H. I. Jørgensen, M. Heiss, O. Demichel, J. V. Holm, M. Aagesen, J. Nygard, and A. F. i Morral, "Single-nanowire solar cells beyond the shockley–queisser limit," *Nature Photonics*, vol. 7, no. 4, p. 306, 2013.

[25] C. G. Bailey, D. V. Forbes, R. P. Raffaelle, and S. M. Hubbard, "Near 1 v open circuit voltage inas/gaas quantum dot solar cells," *Applied Physics Letters*, vol. 98, no. 16, p. 163105, 2011.

[26] J. Wallentin, N. Anttu, D. Asoli, M. Huffman, I. Åberg, M. H. Magnusson, G. Siefer, P. Fuss-Kailuweit, F. Dimroth, B. Witzigmann *et al.*, "Inp nanowire array solar cells achieving 13.8% efficiency by exceeding the ray optics limit," *Science*, p. 1230969, 2013.

[27] K. Novoselov, D. Jiang, F. Schedin, T. Booth, V. Khotkevich, S. Morozov, and A. Geim, "Two-dimensional atomic crystals," *Proceedings of the National Academy of Sciences*, vol. 102, no. 30, pp. 10 451–10 453, 2005.

[28] S. B. Desai, S. R. Madhvapathy, A. B. Sachid, J. P. Llinas, Q. Wang, G. H. Ahn, G. Pitner, M. J. Kim, J. Bokor, C. Hu *et al.*, "Mos2 transistors with 1-nanometer gate lengths," *Science*, vol. 354, no. 6308, pp. 99–102, 2016.

[29] R. Cheng, D. Li, H. Zhou, C. Wang, A. Yin, S. Jiang, Y. Liu, Y. Chen, Y. Huang, and X. Duan, "Electroluminescence and photocurrent generation from atomically sharp wse2/mos2 heterojunction p–n diodes," *Nano letters*, vol. 14, no. 10, pp. 5590–5597, 2014.

[30] B. W. Baugher, H. O. Churchill, Y. Yang, and P. Jarillo-Herrero, "Optoelectronic devices based on electrically tunable p–n diodes in a monolayer dichalcogenide," *Nature nanotechnology*, vol. 9, no. 4, p. 262, 2014.

[31] M.-L. Tsai, S.-H. Su, J.-K. Chang, D.-S. Tsai, C.-H. Chen, C.-I. Wu, L.-J. Li, L.-J. Chen, and J.-H. He, "Monolayer mos2 heterojunction solar cells," *ACS nano*, vol. 8, no. 8, pp. 8317–8322, 2014.

[32] C.-H. Lee, G.-H. Lee, A. M. Van Der Zande, W. Chen, Y. Li, M. Han, X. Cui, G. Arefe, C. Nuckolls, T. F. Heinz *et al.*, "Atomically thin p–n junctions with van der waals heterointerfaces," *Nature nanotechnology*, vol. 9, no. 9, p. 676, 2014.

[33] A. Kumar and P. Ahluwalia, "Tunable dielectric response of transition metals dichalcogenides mx2 (m= mo, w; x= s, se, te): Effect of quantum confinement," *Physica B: Condensed Matter*, vol. 407, no. 24, pp. 4627–4634, 2012.

[34] D. Jena and A. Konar, "Enhancement of carrier mobility in semiconductor nanostructures by dielectric engineering," *Physical review letters*, vol. 98, no. 13, p. 136805, 2007.

[35] N. Ma and D. Jena, "Charge scattering and mobility in atomically thin semiconductors," *Physical Review X*, vol. 4, no. 1, p. 011043, 2014.

[36] L. Wilson, "International technology roadmap for semiconductors (itrs)," *Semiconductor Industry Association*, 2013.

[37] D. J. Griffiths, *Introduction to quantum mechanics*. Cambridge University Press, 2016.

[38] J. Maassen, C. Jeong, A. Baraskar, M. Rodwell, and M. Lundstrom, "Full band calculations of the intrinsic lower limit of contact resistivity," *Applied Physics Letters*, vol. 102, no. 11, p. 111605, 2013.

[39] C. Weber, "The importance of metal transverse momentum for silicon contact resistivity," *Applied Physics Letters*, vol. 103, no. 19, p. 193505, 2013.

[40] Q. Gao and J. Guo, "Ab initio quantum transport simulation of silicide-silicon contacts," *Journal of Applied Physics*, vol. 111, no. 1, p. 014305, 2012.

[41] G. Hegde and R. Chris Bowen, "Effect of realistic metal electronic structure on the lower limit of contact resistivity of epitaxial metal-semiconductor contacts," *Applied Physics Letters*, vol. 105, no. 5, p. 053511, 2014.

[42] W.-W. Fang, N. Singh, L. K. Bera, H. S. Nguyen, S. C. Rustagi, G. Lo, N. Balasubramanian, and D.-L. Kwong, "Vertically stacked sige nanowire array channel cmos transistors," *IEEE electron device letters*, vol. 28, no. 3, pp. 211–213, 2007.

[43] H.-J. Cho, H. Oh, K. Nam, Y. Kim, K. Yeo, W. Kim, Y. Chung, Y. Nam, S. Kim, W. Kwon *et al.*, "Si finfet based 10nm technology with multi vt gate stack for low power and high performance applications," in *VLSI Technology, 2016 IEEE Symposium on*. IEEE, 2016, pp. 1–2.

[44] S. Steiger, M. Povolotskyi, H.-H. Park, T. Kubis, and G. Klimeck, "Nemo5: A parallel multiscale nanoelectronics modeling tool," *IEEE Transactions on Nanotechnology*, vol. 10, no. 6, pp. 1464–1474, 2011.

[45] T. B. Boykin, G. Klimeck, and F. Oyafuso, "Valence band effective-mass expressions in the sp 3 d 5 s* empirical tight-binding model applied to a si and ge parametrization," *Physical Review B*, vol. 69, no. 11, p. 115201, 2004.

[46] S.-H. Park, N. Kharche, D. Basu, Z. Jiang, S. Nayak, C. Weber, G. Hegde, K. Haume, T. Kubis, M. Povolotskyi *et al.*, "Scaling effect on specific contact resistivity in nanoscale metal-semiconductor contacts," in *Device Research Conference (DRC), 2013 71st Annual*. IEEE, 2013, pp. 125–126.

[47] I. Jarrige, N. Capron, and P. Jonnard, "Electronic structure of ni and mo silicides investigated by x-ray emission spectroscopy and density functional theory," *Physical Review B*, vol. 79, no. 3, p. 035117, 2009.

[48] J. Callaway, *Quantum theory of the solid state*. Academic Press, 2013.

[49] T. B. Boykin, G. Klimeck, R. C. Bowen, and F. Oyafuso, "Diagonal parameter shifts due to nearest-neighbor displacements in empirical tight-binding theory," *Physical Review B*, vol. 66, no. 12, p. 125207, 2002.

[50] S. Datta, *Quantum transport: atom to transistor*. Cambridge University Press, 2005.

[51] H. Kanaya, F. Hasegawa, E. Yamaka, T. Moriyama, and M. Nakajima, "Reduction of the barrier height of silicide/p-si1-xgex contact for application in an infrared image sensor," *Japanese Journal of Applied Physics*, vol. 28, no. 4A, p. L544, 1989.

[52] K. Varahramyan and E. Verret, "A model for specific contact resistance applicable for titanium silicide-silicon contacts," *Solid-State Electronics*, vol. 39, no. 11, pp. 1601–1607, 1996.

[53] N. Stavitski, M. Van Dal, A. Lauwers, C. Vrancken, A. Y. Kovalgin, and R. A. Wolters, "Systematic tlm measurements of nisi and ptsi specific contact resistance to n-and p-type si in a broad doping range," *IEEE electron device letters*, vol. 29, no. 4, pp. 378–381, 2008.

[54] D. Yu, Y. Zhang, and F. Liu, "First-principles study of electronic properties of biaxially strained silicon: Effects on charge carrier mobility," *Physical Review B*, vol. 78, no. 24, p. 245204, 2008.

[55] K. Ikeda, Y. Yamashita, A. Endoh, T. Fukano, K. Hikosaka, and T. Mimura, "50-nm gate schottky source/drain p-mosfets with a sige channel," *IEEE Electron Device Letters*, vol. 23, no. 11, pp. 670–672, 2002.

[56] S.-L. Zhang, "Nickel-based contact metallization for sige mosfets: progress and challenges," *Microelectronic Engineering*, vol. 70, no. 2, pp. 174–185, 2003.

[57] C. I. Liao, C. Y. Chen, S. Yu, C. C. Chien, C. L. Yang, J. Wu, and B. Ramachandran, "High quality sige: B of high ge layer for 14nm and beyond finfet processes," *ECS Transactions*, vol. 58, no. 7, pp. 159–162, 2013.

[58] A. Nainani, S. Gupta, V. Moroz, M. Choi, Y. Kim, Y. Cho, J. Gelatos, T. Mandekar, A. Brand, E.-X. Ping *et al.*, "Is strain engineering scalable in finfet era?: Teaching the old dog some new tricks," in *Electron Devices Meeting (IEDM), 2012 IEEE International*. IEEE, 2012, pp. 18–3.

[59] S. Datta, "Nanoscale device modeling: the greenâĂŹs function method," *Superlattices and microstructures*, vol. 28, no. 4, pp. 253–278, 2000.

[60] R. Lake, G. Klimeck, R. C. Bowen, and D. Jovanovic, "Single and multiband modeling of quantum electron transport through layered semiconductor devices," *Journal of Applied Physics*, vol. 81, no. 12, pp. 7845–7869, 1997.

[61] T. Markussen, A.-P. Jauho, and M. Brandbyge, "Electron and phonon transport in silicon nanowires: Atomistic approach to thermoelectric properties," *Physical Review B*, vol. 79, no. 3, p. 035415, 2009.

[62] S.-C. Lee and A. Wacker, "Nonequilibrium greenâĂŹs function theory for transport and gain properties of quantum cascade structures," *Physical Review B*, vol. 66, no. 24, p. 245314, 2002.

[63] S. Steiger, "Modelling nano-leds," Ph.D. dissertation, 2009.

[64] T. Kubis, C. Yeh, P. Vogl, A. Benz, G. Fasching, and C. Deutsch, "Theory of nonequilibrium quantum transport and energy dissipation in terahertz quantum cascade lasers," *Physical Review B*, vol. 79, no. 19, p. 195323, 2009.

[65] M. Luisier and G. Klimeck, "Atomistic full-band simulations of silicon nanowire transistors: Effects of electron-phonon scattering," *Physical Review B*, vol. 80, no. 15, p. 155430, 2009.

[66] A. Afzalian, T. Vasen, P. Ramvall, T. Shen, J. Wu, and M. Passlack, "Physics and performances of iii–v nanowire broken-gap heterojunction tfets using an efficient tight-binding mode-space negf model enabling million-atom nanowire simulations," *Journal of Physics: Condensed Matter*, vol. 30, no. 25, p. 254002, 2018.

[67] T. A. Ameen, H. Ilatikhameneh, J. Z. Huang, M. Povolotskyi, R. Rahman, and G. Klimeck, "Combination of equilibrium and nonequilibrium carrier statistics into an atomistic quantum transport model for tunneling heterojunctions," *IEEE Transactions on Electron Devices*, vol. 64, no. 6, pp. 2512–2518, 2017.

[68] R. C. Bowen, G. Klimeck, R. K. Lake, W. R. Frensley, and T. Moise, "Quantitative simulation of a resonant tunneling diode," *Journal of applied physics*, vol. 81, no. 7, pp. 3207–3213, 1997.

[69] P. Sarangapani, C. Weber, J. Chang, S. Cea, M. Povolotskyi, G. Klimeck, and T. Kubis, "Atomistic tight-binding study of contact resistivity in si/sige pmos schottky contacts," *IEEE Transactions on Nanotechnology*, 2018.

[70] K. Miao, S. Sadasivam, J. Charles, G. Klimeck, T. Fisher, and T. Kubis, "Büttiker probes for dissipative phonon quantum transport in semiconductor nanostructures," *Applied Physics Letters*, vol. 108, no. 11, p. 113107, 2016.

[71] R. Golizadeh-Mojarad and S. Datta, "Nonequilibrium greenâĂŹs function based models for dephasing in quantum transport," *Physical Review B*, vol. 75, no. 8, p. 081301, 2007.

[72] M. Büttiker, "Scattering theory of thermal and excess noise in open conductors," *Physical review letters*, vol. 65, no. 23, p. 2901, 1990.

[73] R. Venugopal, M. Paulsson, S. Goasguen, S. Datta, and M. Lundstrom, "A simple quantum mechanical treatment of scattering in nanoscale transistors," *Journal of Applied Physics*, vol. 93, no. 9, pp. 5613–5625, 2003.

[74] S. Sadasivam, N. Ye, J. P. Feser, J. Charles, K. Miao, T. Kubis, and T. S. Fisher, "Thermal transport across metal silicide-silicon interfaces: First-principles calculations and green's function transport simulations," *Physical Review B*, vol. 95, no. 8, p. 085310, 2017.

[75] F. Riddoch and B. Ridley, "On the scattering of electrons by polar optical phonons in quasi-2d quantum wells," *Journal of Physics C: Solid State Physics*, vol. 16, no. 36, p. 6971, 1983.

[76] B. Gelmont, M. Shur, and M. Stroscio, "Polar optical-phonon scattering in three- and two-dimensional electron gases," *Journal of applied physics*, vol. 77, no. 2, pp. 657–660, 1995.

[77] D. Vasileska, "Scattering mechanisms," 2006.

[78] A. Esposito, M. Frey, and A. Schenk, "Quantum transport including nonparabolicity and phonon scattering: application to silicon nanowires," *Journal of computational electronics*, vol. 8, no. 3, pp. 336–348, 2009.

[79] H. Brooks, "Scattering by ionized impurities in semiconductors," in *Physical Review*, vol. 83, no. 4. AMERICAN PHYSICAL SOC ONE PHYSICS ELLIPSE, COLLEGE PK, MD 20740-3844 USA, 1951, pp. 879–879.

[80] E. Conwell and V. Weisskopf, "Theory of impurity scattering in semiconductors," *Physical review*, vol. 77, no. 3, p. 388, 1950.

[81] G. D. Mahan, *Many-particle physics*. Springer Science & Business Media, 2013.

[82] B. Ridley, "Reconciliation of the conwell-weisskopf and brooks-herring formulae for charged-impurity scattering in semiconductors: Third-body interference," *Journal of Physics C: Solid State Physics*, vol. 10, no. 10, p. 1589, 1977.

[83] K. Krishnaswamy, B. Himmetoglu, Y. Kang, A. Janotti, and C. G. Van de Walle, "First-principles analysis of electron transport in basno 3," *Physical Review B*, vol. 95, no. 20, p. 205202, 2017.

[84] A. Konar, T. Fang, and D. Jena, "Effect of high-κ gate dielectrics on charge transport in graphene-based field effect transistors," *Physical Review B*, vol. 82, no. 11, p. 115452, 2010.

[85] S. Kim, A. Konar, W.-S. Hwang, J. H. Lee, J. Lee, J. Yang, C. Jung, H. Kim, J.-B. Yoo, J.-Y. Choi *et al.*, "High-mobility and low-power thin-film transistors based on multilayer mos2 crystals," *Nature communications*, vol. 3, p. 1011, 2012.

[86] H. Fang, S. Chuang, T. C. Chang, K. Takei, T. Takahashi, and A. Javey, "High-performance single layered wse2 p-fets with chemically doped contacts," *Nano letters*, vol. 12, no. 7, pp. 3788–3792, 2012.

[87] S. Wang and G. Mahan, "Electron scattering from surface excitations," *Physical Review B*, vol. 6, no. 12, p. 4517, 1972.

[88] M. V. Fischetti, D. A. Neumayer, and E. A. Cartier, "Effective electron mobility in si inversion layers in metal–oxide–semiconductor systems with a high-κ insulator: The role of remote phonon scattering," *Journal of Applied Physics*, vol. 90, no. 9, pp. 4587–4608, 2001.

[89] T. OâĂŹRegan and M. Fischetti, "Electron mobility in silicon and germanium inversion layers: The role of remote phonon scattering," *Journal of Computational Electronics*, vol. 6, no. 1, pp. 81–84, 2007.

[90] Z.-Y. Ong and M. V. Fischetti, "Theory of remote phonon scattering in top-gated single-layer graphene," *Physical Review B*, vol. 88, no. 4, p. 045405, 2013.

[91] M. Anantram, M. S. Lundstrom, and D. E. Nikonov, "Modeling of nanoscale devices," *Proceedings of the IEEE*, vol. 96, no. 9, pp. 1511–1550, 2008.

[92] J. Barker, A. Martinez, and M. Aldegunde, "Compliant energy and momentum conservation in negf simulation of electron-phonon scattering in semiconductor nanowire transistors," in *Journal of Physics: Conference Series*, vol. 367, no. 1. IOP Publishing, 2012, p. 012012.

[93] G. Klimeck, R. Lake, C. L. Fernando, R. C. Bowen, D. Blanks, M. Leng, T. Moise, Y. Kao, and W. R. Frensley, "Numerical approximations for polar optical phonon scattering in resonant tunneling diodes," *Quantum Devices and Circuits. Imperial Press, London*, 1996.

[94] *Non-local scattering with a new recursive nonequilibrium green's function method*. International Workshop on Computational Nanotechnology, 2017.

[95] H. Ilatikhameneh, Y. Tan, B. Novakovic, G. Klimeck, R. Rahman, and J. Appenzeller, "Tunnel field-effect transistors in 2-d transition metal dichalcogenide materials," *IEEE Journal on Exploratory Solid-State Computational Devices and Circuits*, vol. 1, pp. 12–18, 2015.

[96] S. Agarwal, G. Klimeck, and M. Luisier, "Leakage-reduction design concepts for low-power vertical tunneling field-effect transistors," *IEEE Electron Device Letters*, vol. 31, no. 6, pp. 621–623, 2010.

[97] Y. Lu, G. Zhou, R. Li, Q. Liu, Q. Zhang, T. Vasen, S. D. Chae, T. Kosel, M. Wistey, H. Xing *et al.*, "Performance of algasb/inas tfets with gate electric field and tunneling direction aligned," *IEEE Electron Device Letters*, vol. 33, no. 5, pp. 655–657, 2012.

[98] S. S. Sylvia, M. A. Khayer, K. Alam, and R. K. Lake, "Doping, tunnel barriers, and cold carriers in inas and insb nanowire tunnel transistors," *IEEE transactions on electron devices*, vol. 59, no. 11, pp. 2996–3001, 2012.

[99] M. A. Khayer and R. K. Lake, "Effects of band-tails on the subthreshold characteristics of nanowire band-to-band tunneling transistors," *Journal of Applied Physics*, vol. 110, no. 7, p. 074508, 2011.

[100] M. G. Pala and D. Esseni, "Interface traps in inas nanowire tunnel-fets and mosfets-sâĂŤpart i: Model description and single trap analysis in tunnel-fets," *IEEE Trans. Electron Devices*, vol. 60, no. 9, pp. 2795–2801, 2013.

[101] G. Klimeck, R. Bowen, T. Boykin, and T. Cwik, "sp3s* and sp3d5s* tight-binding parameter sets for gaas, alas, inas, gasb, alsb, insb, gap, alp, and inp for quantum dot simulations. in?, editor," in *American Physical Society, Annual March Meeting, volume*.

[102] J.-M. Jancu, R. Scholz, F. Beltram, and F. Bassani, "Empirical spds* tight-binding calculation for cubic semiconductors: General method and material parameters," *Physical Review B*, vol. 57, no. 11, p. 6493, 1998.

[103] J. Charles, P. Sarangapani, R. Golizadeh-Mojarad, R. Andrawis, D. Lemus, X. Guo, D. Mejia, J. E. Fonseca, M. Povolotskyi, T. Kubis *et al.*, "Incoherent transport in nemo5: realistic and efficient scattering on phonons," *Journal of Computational Electronics*, vol. 15, no. 4, pp. 1123–1129, 2016.

[104] J. Lindhard, "On the properties of a gas of charged particles," *Dan. Vid. Selsk Mat.-Fys. Medd.*, vol. 28, p. 8, 1954.

[105] O. Fabrichnaya, "Landolt-bornstein database," 2007.

[106] E. Lind, E. Memišević, A. W. Dey, and L.-E. Wernersson, "Iii-v heterostructure nanowire tunnel fets," *IEEE Journal of the Electron Devices Society*, vol. 3, no. 3, pp. 96–102, 2015.

[107] U. E. Avci, D. H. Morris, and I. A. Young, "Tunnel field-effect transistors: Prospects and challenges," *IEEE J. Electron Devices Soc.*, vol. 3, no. 3, pp. 88–95, 2015.

[108] M. Oehme, M. Gollhofer, D. Widmann, M. Schmid, M. Kaschel, E. Kasper, and J. Schulze, "Direct bandgap narrowing in ge ledâĂŹs on si substrates," *Optics express*, vol. 21, no. 2, pp. 2206–2211, 2013.

[109] B. Halperin and M. Lax, "Impurity-band tails in the high-density limit. i. minimum counting methods," *Physical Review*, vol. 148, no. 2, p. 722, 1966.

[110] ——, "Impurity-band tails in the high-density limit. ii. higher order corrections," *Physical Review*, vol. 153, no. 3, p. 802, 1967.

[111] S. John, C. Soukoulis, M. H. Cohen, and E. Economou, "Theory of electron band tails and the urbach optical-absorption edge," *Physical review letters*, vol. 57, no. 14, p. 1777, 1986.

[112] S. Jain and D. Roulston, "A simple expression for band gap narrowing (bgn) in heavily doped si, ge, gaas and gexsi1- x strained layers," *Solid-State Electronics*, vol. 34, no. 5, pp. 453–465, 1991.

[113] H. Zhang, W. Cao, J. Kang, and K. Banerjee, "Effect of band-tails on the subthreshold performance of 2d tunnel-fets," in *Electron Devices Meeting (IEDM), 2016 IEEE International*. IEEE, 2016, pp. 30–3.

[114] M. V. Fischetti and S. E. Laux, "Monte carlo analysis of electron transport in small semiconductor devices including band-structure and space-charge effects," *Physical Review B*, vol. 38, no. 14, p. 9721, 1988.

[115] H. Fröhlich, "Interaction of electrons with lattice vibrations," *Proc. R. Soc. Lond. A*, vol. 215, no. 1122, pp. 291–298, 1952.

[116] G. Klimeck, R. Bowen, T. Boykin, and T. Cwik, "sp3s* and sp3d5s* tight-binding parameter sets for gaas, alas, inas, gasb, alsb, insb, gap, alp, and inp for quantum dot simulations," in *APS Meeting Abstracts*, 2000.

[117] J.-M. Jancu, F. Bassani, F. D. Sala, and R. Scholz, "Transferable tight-binding parametrization for the group-iii nitrides," *Applied physics letters*, vol. 81, no. 25, pp. 4838–4840, 2002.

[118] S. Goodnick and P. Lugli, "Effect of electron-electron scattering on nonequilibrium transport in quantum-well systems," *Physical Review B*, vol. 37, no. 5, p. 2578, 1988.

[119] S. Johnson and T. Tiedje, "Temperature dependence of the urbach edge in gaas," *Journal of applied physics*, vol. 78, no. 9, pp. 5609–5613, 1995.

[120] G. Antonioli, D. Bianchi, and P. Franzosi, "Intrinsic urbach rule and electronâĂŤphonon interaction in gaas and related iii-v compounds," *physica status solidi (b)*, vol. 106, no. 1, pp. 79–84, 1981.

[121] S. Chichibu, T. Mizutani, T. Shioda, H. Nakanishi, T. Deguchi, T. Azuhata, T. Sota, and S. Nakamura, "Urbach–martienssen tails in a wurtzite gan epilayer," *Applied physics letters*, vol. 70, no. 25, pp. 3440–3442, 1997.

[122] H. Yao and A. Compaan, "Plasmons, photoluminescence, and band-gap narrowing in very heavily doped n-gaas," *Applied Physics Letters*, vol. 57, no. 2, pp. 147–149, 1990.

[123] H. Luo, W. Shen, Y. Zhang, and H. Yang, "Study of band gap narrowing effect in n-gaas for the application of far-infrared detection," *Physica B: Condensed Matter*, vol. 324, no. 1-4, pp. 379–386, 2002.

[124] E. Harmon, M. Melloch, and M. Lundstrom, "Effective band-gap shrinkage in gaas," *Applied physics letters*, vol. 64, no. 4, pp. 502–504, 1994.

[125] M. Amani, D.-H. Lien, D. Kiriya, J. Xiao, A. Azcatl, J. Noh, S. R. Madhvapathy, R. Addou, K. Santosh, M. Dubey *et al.*, "Near-unity photoluminescence quantum yield in mos2," *Science*, vol. 350, no. 6264, pp. 1065–1068, 2015.

[126] H. Fang, C. Battaglia, C. Carraro, S. Nemsak, B. Ozdol, J. S. Kang, H. A. Bechtel, S. B. Desai, F. Kronast, A. A. Unal *et al.*, "Strong interlayer coupling in van der waals heterostructures built from single-layer chalcogenides," *Proceedings of the National Academy of Sciences*, vol. 111, no. 17, pp. 6198–6202, 2014.

[127] J. Hafner, "Ab-initio simulations of materials using vasp: Density-functional theory and beyond," *Journal of computational chemistry*, vol. 29, no. 13, pp. 2044–2078, 2008.

[128] T. Bucko, J. Hafner, S. Lebegue, and J. G. Angyán, "Improved description of the structure of molecular and layered crystals: ab initio dft calculations with van der waals corrections," *The Journal of Physical Chemistry A*, vol. 114, no. 43, pp. 11 814–11 824, 2010.

[129] N. Marzari and D. Vanderbilt, "Maximally localized generalized wannier functions for composite energy bands," *Physical review B*, vol. 56, no. 20, p. 12847, 1997.

[130] K. S. Thygesen, L. B. Hansen, and K. W. Jacobsen, "Partly occupied wannier functions: Construction and applications," *Physical Review B*, vol. 72, no. 12, p. 125119, 2005.

[131] R. Das, S. K. Pandey, and P. Mahadevan, "Layer dependent electronic structure changes in transition metal dichalcogenides-the role of geometric confinement," *arXiv preprint arXiv:1702.04535*, 2017.

[132] Z. Jin, X. Li, J. T. Mullen, and K. W. Kim, "Intrinsic transport properties of electrons and holes in monolayer transition-metal dichalcogenides," *Physical Review B*, vol. 90, no. 4, p. 045422, 2014.

APPENDIX

A. FERMI'S GOLDEN RULE FOR POLAR OPTICAL PHONON SCATTERING

Subsequent derivation of Fermi's golden rule for polar optical phonons assumes Frohlich coupling with bulk optical phonons. Optical phonon energy is taken to be at a single average LO phonon energy and is assumed to have flat dispersion. Screening is taken into account through a constant screening length (following either the Debye approximation or Lindhard formalism). Calculated rate accounts for multiple modes and takes both inter and intra mode scattering into account.

A.1 Bulk/quasi1D device

According to Fermi's golden rule, scattering rate for an electron with an optical phonon in an initial momentum state $\vec{k}$ to a final momentum state $\vec{k}'$ is given by

$$P\left(\mathbf{k},\mathbf{k}+\mathbf{q}\right)=\frac{2\pi}{\hbar}\left|\left\langle \mathbf{k}+\mathbf{q}\right|H_{imp}\left|\mathbf{k}\right\rangle \right|^{2}\delta\left(E(\mathbf{k}+\mathbf{q})-E(\mathbf{k})\pm\hbar\omega_{LO}\right) \tag{A.1}$$

Polar optical LO phonon scattering potential is of the form

$$H_{ph}(q)=\frac{q}{q^{2}+\zeta^{-2}}\left[e^{2}\hbar\omega_{LO}\left(\frac{1}{\epsilon_{\infty}}-\frac{1}{\epsilon_{s}}\right)\right]^{1/2}\left(a_{q}e^{i\mathbf{q}.\mathbf{r}}-a_{q}^{\dagger}e^{-i\mathbf{q}.\mathbf{r}}\right)$$

where $a_q^\dagger$ and a_q are the creation and annihilation operators, $\hbar\omega_{LO}$ is the LO optical phonon frequency, ζ is the screening length, ϵ_s is the static dielectric constant and ϵ_∞ is the high frequency dielectric constant. Scattering rate for emission process can be written as

$$\frac{1}{\tau_{em}(\mathbf{k})}=\frac{2\pi}{\hbar}\frac{e^{2}\hbar\omega_{LO}}{2}\left(\frac{1}{\epsilon_{\infty}}-\frac{1}{\epsilon_{s}}\right)\left(1+N_{ph}\right)\int\frac{\mathbf{dq}}{\left(2\pi\right)^{3}}\frac{q^{2}}{\left(q^{2}+\zeta^{-2}\right)^{2}}\delta\left(E(\mathbf{k})-E(\mathbf{k}+\mathbf{q})-\hbar\omega_{LO}\right)$$

Converting the momentum integral to polar coordinates and by using the parabolic dispersion relation, we get

$$E(\mathbf{k}) - E(\mathbf{k}+\mathbf{q}) = -\frac{\hbar^2 q^2}{2m^*} - \frac{\hbar^2 kq}{m^*} cos\theta$$

$$\frac{1}{\tau_{em}(\mathbf{k})} = \frac{e^2\hbar\omega_{LO}(1+N_{ph})}{4\pi\hbar}\left(\frac{1}{\epsilon_\infty} - \frac{1}{\epsilon_s}\right)\int_0^\infty dq \frac{q^4}{\left(q^2+\zeta^{-2}\right)^2}\int_0^\pi d\theta\delta\left(\frac{\hbar^2q^2}{2m^*} + \frac{\hbar^2 kqcos\theta}{m^*} + \hbar\omega_{LO}\right) \tag{A.2}$$

Performing a change of variables for the polar integral, the integral becomes

$$\int_0^\pi d\theta\delta\left[\frac{\hbar^2q^2}{2m^*} + \frac{\hbar^2 kqcos\theta}{m^*} + \hbar\omega_{LO}\right] = \frac{1}{a}\int_{-a}^{a} dx\delta(x+b)$$

where $a = \dfrac{\hbar^2 kq}{m^*}$ and $b = \dfrac{\hbar^2q^2}{2m^*} + \hbar\omega_{LO}$. For the delta function to have a non-vanishing value within the integration range, $|a| > |b|$ which gives us limits for range of q

$$\left(\frac{2m^*}{\hbar^2}\right)^{1/2}\left[\sqrt{E} - \sqrt{E-\hbar\omega_{LO}}\right] \leq q \leq \left(\frac{2m^*}{\hbar^2}\right)^{1/2}\left[\sqrt{E} + \sqrt{E-\hbar\omega_{LO}}\right]$$

Hence, the emission scattering rate can be written as

$$\frac{1}{\tau_{em}(\mathbf{k})} = \theta\left(E-\hbar\omega_{LO}\right)\frac{e^2m^*\hbar\omega_{LO}\left(1+N_{ph}\right)}{4\pi\hbar^3k}\left(\frac{1}{\epsilon_\infty} - \frac{1}{\epsilon_s}\right)\int_{q_-}^{q+} dq\frac{q^3}{\left(q^2+\zeta^{-2}\right)^2} \tag{A.3}$$

A similar procedure for the absorption rate gives us

$$\frac{1}{\tau_{ab}(\mathbf{k})} = \frac{e^2m^*\hbar\omega_{LO}N_{ph}}{4\pi\hbar^3k}\left(\frac{1}{\epsilon_\infty} - \frac{1}{\epsilon_s}\right)\int_{q_-}^{q+} dq\frac{q^3}{\left(q^2+\zeta^{-2}\right)^2} \tag{A.4}$$

where the integration limits of q are

$$\left(\frac{2m^*}{\hbar^2}\right)^{1/2}\left[\sqrt{E+\hbar\omega_{LO}} - \sqrt{E}\right] \leq q \leq \left(\frac{2m^*}{\hbar^2}\right)^{1/2}\left[\sqrt{E+\hbar\omega_{LO}} + \sqrt{E}\right]$$

Total scattering rate is the sum of emission and absorption scattering rates.

$$\frac{1}{\tau(\mathbf{k})} = \frac{1}{\tau_{em}(\mathbf{k})} + \frac{1}{\tau_{ab}(\mathbf{k})}$$

Dimension check

$$\frac{1}{\tau(E)} = \frac{C^2.kg.kg.m^2.s^{-2}}{\left(kg.m^2.s^{-1}\right)^3 m^{-1}.\left(C^2.kg^{-1}.m^{-3}.s^2\right)} = \frac{1}{s}$$

A.2 Ultra-thin body (UTB) device

For discussion below, x and y directions will be assumed periodic and z will be the confinement direction. According to Fermi's golden rule, scattering rate for an electron with an optical phonon in an initial momentum state $\mathbf{k}$ to a final momentum state $\mathbf{k}'$ is given by

$$P\left(\mathbf{k},\mathbf{k}'\right)=\frac{2\pi}{\hbar}\left|\left\langle\mathbf{k}\right|H_{imp}\left|\mathbf{k}'\right\rangle\right|^{2}\delta\left(E(\mathbf{k})-E(\mathbf{k}')\pm\hbar\omega_{LO}\right) \tag{A.5}$$

Electron-phonon coupling Hamiltonian is given by

$$H_{e-ph}=\frac{Cq}{q^{2}+\zeta^{-2}}\left(a_{q}e^{i\mathbf{q}.\mathbf{r}}-a_{q}^{\dagger}e^{-i\mathbf{q}.\mathbf{r}}\right) \tag{A.6}$$

where q is the phonon momentum, ζ is the screening length, a_q and $a_q^{\dagger}$ are particle annihilation and creation operators and coupling constant C is described by Frohlich interaction

$$C=i\left[\frac{2\pi}{V}e^{2}\hbar\omega_{LO}\left(\frac{1}{\epsilon_{\infty}}-\frac{1}{\epsilon_{s}}\right)\right]^{1/2} \tag{A.7}$$

where $\hbar\omega_{LO}$ is the LO optical phonon frequency, ϵ_s is the static dielectric constant and ϵ_∞ is the high frequency dielectric constant. The electronic wavefunction is of the form

$$\left|\mathbf{k}\right\rangle=\frac{1}{\sqrt{A}}e^{ik_{x}x}\psi_{i}(\mathbf{r}_{||}) \tag{A.8}$$

where $\psi_i(\mathbf{r}_{||})$ corresponds to the i^{th} mode wavefunction in the confinement direction.

$$\left\langle\mathbf{k}\right|H_{imp}\left|\mathbf{k}'\right\rangle=\sum_{q}\left\langle\mathbf{k}\right|\frac{Cq}{q^{2}+\zeta^{-2}}\left(a_{q}e^{i\mathbf{q}.\mathbf{r}}-a_{q}^{\dagger}e^{-i\mathbf{q}.\mathbf{r}}\right)\left|\mathbf{k}'\right\rangle$$

$$=\sum_{q}\pm\sqrt{N_{ph}+\frac{1}{2}\mp\frac{1}{2}}\frac{Cq}{q^{2}+\zeta^{-2}}\left\langle\mathbf{k}\right|e^{\pm i\mathbf{q}.\mathbf{r}}\left|\mathbf{k}'\right\rangle$$

where the first sign corresponds to phonon absorption process and the second sign corresponds to phonon emission process. Converting the summation over phonon momentum to an integral, we get

$$\left\langle\mathbf{k}\right|H_{imp}\left|\mathbf{k}'\right\rangle=\pm\sqrt{N_{ph}+\frac{1}{2}\mp\frac{1}{2}}\frac{C}{(2\pi)^{3}A}\int_{-\infty}^{\infty}\mathbf{dq}$$
$$\int_{-\infty}^{\infty}\mathbf{dr}_{||}\int_{0}^{L_{z}}dz.e^{-i\mathbf{k}_{||}^{'}.\mathbf{r}_{||}}\psi_{i}^{*}(z)H(q)e^{\pm i\mathbf{q}_{||}\mathbf{r}_{||}}e^{iq_{z}z}e^{i\mathbf{k}_{||}\mathbf{r}_{||}}\psi_{j}(z)$$

$$= \pm\sqrt{N_{ph} + \frac{1}{2} \mp \frac{1}{2}} \frac{C}{(2\pi)^3} \int_{-\infty}^{\infty} \mathbf{dq} \int_{-\infty}^{\infty} \mathbf{dr}_{||} e^{i\left(\mathbf{k}_{||} - \mathbf{k}'_{||} \pm \mathbf{q}_{||}\right).\mathbf{r}_{||}} \int_0^{L_z} dz \psi_i^*(z) \psi_j(z) H(q) e^{\pm i q_z z}$$

$$= \pm\sqrt{N_{ph} + \frac{1}{2} \mp \frac{1}{2}} \frac{C}{(2\pi)\sqrt{A}} \int_{-\infty}^{\infty} \mathbf{dq} \delta\left(\mathbf{k}_{||} - \mathbf{k}'_{||} \pm \mathbf{q}_{||}\right) \int_0^{L_z} dz \rho_{ij}(z) H(q) e^{\pm i q_z z}$$

$$= \pm\sqrt{N_{ph} + \frac{1}{2} \mp \frac{1}{2}} \frac{C}{(2\pi)\sqrt{A}} \int_{-\infty}^{\infty} \mathbf{dq}_{||} \delta\left(\mathbf{k}_{||} - \mathbf{k}'_{||} \pm \mathbf{q}_{||}\right) \int_{-\infty}^{\infty} dq_z \int_0^{L_z} dz \rho_{ij}(z) H(q) e^{\pm i q_z z} \tag{A.9}$$

$$\left|\langle \mathbf{k}| H_{imp} |\mathbf{k}'\rangle\right|^2 = \left(N_{ph} + \frac{1}{2} \mp \frac{1}{2}\right) \frac{C^2 V}{(2\pi)^2 A} \int_{-\infty}^{\infty} d\vec{q}_{||} \delta\left(\mathbf{k}_{||} - \mathbf{k}'_{||} \pm \mathbf{q}_{||}\right) \int_{-\infty}^{\infty} dq_z \int_0^{L_Z} \int_0^{L_z} dz dz' \rho_{ij}(z) \rho_{ij}(z') H(q)^2 e^{\pm i q_z (z - z')} \tag{A.10}$$

The above expression can be simplified by interchanging the integration order between q_z and $z,\ z'$ and integrating $H(q)^2 e^{iq_z(z-z')}$ with respect to q_z

$$\int_{-\infty}^{\infty} dq_z H(q)^2 e^{\pm i q_z (z - z')} = \int_{-\infty}^{\infty} dq_z \frac{\left(q_{||}^2 + q_z^2\right)}{\left(q_{||}^2 + q_z^2 + \zeta^{-2}\right)^2} e^{i q_z (z - z')}$$

Scattering kernel integral that needs to be solved

$$\int_{-\infty}^{\infty} dq_z \frac{\left(q_{||}^2 + q_z^2\right)}{\left(q_{||}^2 + q_z^2 + \zeta^{-2}\right)^2} e^{\pm i q_z (z - z')}$$

Let $a = z - z'$, $b = \sqrt{q_{||}^2 + \zeta^{-2}}$ and $c = q_{||}$. Converting the above integral into a complex function integral, we get

$$\int_{-\infty}^{\infty} dz \frac{e^{\pm iaz} \left(c^2 + z^2\right)}{(z^2 + b^2)^2}$$

The function has residues at $z = \pm ib$. Since we are performing a real integral, only the residues in upper half-plane matter. Using Cauchy's residue theorem, we get

$$I(q_{||}, z, z') = \frac{e^{-\sqrt{q_{||}^2 + \zeta^{-2}} |z - z'|}}{\sqrt{q_{||}^2 + \zeta^{-2}}} \left[1 - \frac{|z - z'| \zeta^{-2}}{2\sqrt{q_{||}^2 + \zeta^{-2}}} - \frac{\zeta^{-2}}{2\left(q_{||}^2 + \zeta^{-2}\right)}\right]$$

The above integrand carries information about the non-locality of scattering and is referred to as the scattering kernel.

$$|\langle \mathbf{k}| H_{imp} |\mathbf{k}'\rangle|^2 = \left(N_{ph} + \frac{1}{2} \mp \frac{1}{2}\right) \frac{C^2 V}{(2\pi)^2 A} \int_{-\infty}^{\infty} \mathbf{dq}_{||} \delta\left(\mathbf{k}_{||} - \mathbf{k}_{||}^{'} \pm \mathbf{q}_{||}\right) \int_0^{L_z} \int_0^{L_z} dz dz^{'} \rho_{ij}(z) \rho_{ij}(z') I(q_{||}, z, z')$$

$$= \left(N_{ph} + \frac{1}{2} \mp \frac{1}{2}\right) \frac{C^2 V}{(2\pi)^2 A} \int_{-\infty}^{\infty} \mathbf{dq}_{||} \delta\left(\mathbf{k}_{||} - \mathbf{k}_{||}^{'} \pm \mathbf{q}\right) F(q_{||})$$

where $F(q_{||}) = \int_0^{L_z} \int_0^{L_z} dz dz^{'} \rho_{ij}(z) \rho_{ij}(z') I(q_{||}, z, z')$ is the form factor. Scattering rate can now be derived by summing over all possible final momentum states.

$$\frac{1}{\tau(\mathbf{k}_{||})} = \sum_{k'} P(\mathbf{k}_{||}, \mathbf{k}_{||}^{'}) = \sum_{k'} \frac{2\pi}{\hbar} \left(N_{ph} + \frac{1}{2} \mp \frac{1}{2}\right) \frac{C^2 V}{(2\pi)^2 A} \int_{-\infty}^{\infty} \mathbf{dq}_{||} \delta\left(\mathbf{k}_{||} - \mathbf{k}_{||}^{'} \pm \mathbf{q}_{||}\right) F(q_{||}) \delta\left(E(\mathbf{k}) - E(\mathbf{k}') \pm \hbar\omega_{LO}\right) \tag{A.11}$$

Converting the summation to integration and multiplying by 2 for spin degeneracy, we get

$$\frac{1}{\tau(k_{||})} = \frac{2}{\hbar} \left(N_{ph} + \frac{1}{2} \mp \frac{1}{2}\right) \frac{C^2 V}{(2\pi)^3} \int \mathbf{dk}_{||}^{'} \delta\left(E(\mathbf{k}) - E(\mathbf{k}') \pm \hbar\omega_{LO}\right) \int_{-\infty}^{\infty} \mathbf{dq}_{||} \delta\left(\mathbf{k}_{||} - \mathbf{k}_{||}^{'} \pm \mathbf{q}_{||}\right) F(q_{||})$$

$$\int \mathbf{dk}_{||}^{'} \int_{-\infty}^{\infty} \mathbf{dq}_{||} \delta\left(E(\mathbf{k}) - E(\mathbf{k}') \pm \hbar\omega_{LO}\right) \delta\left(\mathbf{k}_{||} - \mathbf{k}_{||}^{'} \pm \mathbf{q}_{||}\right) F(q_{||}) = \int \int k' dk' d\theta \delta\left(E(\mathbf{k}) - E(\mathbf{k}') \pm \hbar\omega_{LO}\right) F(|\mathbf{k}_{||} - \mathbf{k}_{||}^{'}|)$$

$$\int \int k' dk' d\theta \delta\left(E(\mathbf{k}) - E(\mathbf{k}') \pm \hbar\omega_{LO}\right) F(|\mathbf{k}_{||} - \mathbf{k}_{||}^{'}|) = \frac{m^*}{\hbar^2} \int \int dE(k') d\theta \delta\left(E(\mathbf{k}) - E(\mathbf{k}') \pm \hbar\omega_{LO}\right) F(|\tilde{\mathbf{k}}_{||} - \tilde{\mathbf{k}}_{||}'|)$$

$$= \frac{m^*}{\hbar^2} \int_0^{2\pi} d\theta F(E(\mathbf{k}_{||}), \theta)$$

where

$$|\tilde{\mathbf{k}}_{||} - \tilde{\mathbf{k}}_{||}'| = \left[2k^2 \pm \frac{2\left(\hbar\omega_{LO} \pm (E_i - E_j)\right)}{\hbar^2} - 2k \left[k^2 \pm \frac{2\left(\hbar\omega_{LO} \pm (E_i - E_j)\right)}{\hbar^2}\right]^{1/2} cos\theta\right]^{1/2} \tag{A.12}$$

where $k = \dfrac{2m^*E}{\hbar^2}$, E_i and E_j are the energies corresponding to modes i and j and $+$symbol refers to the absorption process and $-$ symbol refers to the emission process. Finally, the scattering rate can be expressed as

$$\frac{1}{\tau_{ij}(E)} = \frac{4\pi e^2 m^* \hbar\omega_{LO}}{\hbar^3}\left(\frac{1}{\epsilon_\infty} - \frac{1}{\epsilon_s}\right)\left[N_{ph}\int_0^{2\pi} d\theta F_a(E,\theta) + (N_{ph}+1)\int_0^{2\pi} d\theta F_e(E,\theta)\right]$$

Dimension check

$$\frac{1}{\tau_{ij}(E)} = \frac{C^2.kg.kg.m^2.s^{-2}}{(kg.m^2.s^{-1})^3.(C^2.kg^{-1}.m^{-3}.s^2)}.m = \frac{1}{s}$$

The above scattering rate is between two modes i and j. Multi-modal scattering rate can be calculated by summing up contributions from different inter-mode scattering

$$\Gamma(E) = \sum_j \Gamma_{ij}(E) = \sum_j \frac{1}{\tau_{ij}(E)}$$

A.3 Nanowire device

For discussion below, x will be the periodic direction along the length of wire and $y,\ z$ will be the periodic directions.

According to Fermi's golden rule, scattering rate for an electron with an optical phonon in an initial momentum state $\mathbf{k}$ to a final momentum state $\mathbf{k}'$ is given by

$$P(\mathbf{k},\mathbf{k}') = \frac{2\pi}{\hbar}\left|\langle\mathbf{k}|\, H_{imp}\,|\mathbf{k}'\rangle\right|^2 \delta\left(E(\mathbf{k}) - E(\mathbf{k}') \pm \hbar\omega_{LO}\right) \tag{A.13}$$

Electron-phonon coupling Hamiltonian is given by

$$H_{e-ph} = \frac{Cq}{q^2+\zeta^{-2}}\left(a_q e^{i\mathbf{q}.\mathbf{r}} - a_q^\dagger e^{-i\mathbf{q}.\mathbf{r}}\right) \tag{A.14}$$

where q is the phonon momentum, ζ is the screening length, a_q and $a_q^\dagger$ are particle annihilation and creation operators and coupling constant C is described by Frohlich interaction

$$C = i\left[\frac{2\pi}{V}e^2\hbar\omega_{LO}\left(\frac{1}{\epsilon_\infty} - \frac{1}{\epsilon_s}\right)\right]^{1/2} \tag{A.15}$$

where $\hbar\omega_{LO}$ is the LO optical phonon frequency, ϵ_s is the static dielectric constant and ϵ_∞ is the high frequency dielectric constant. The electronic wavefunction is of the form

$$|\mathbf{k}\rangle = \frac{1}{\sqrt{L}} e^{ik_x x}\psi_i(\mathbf{r}_{||}) \tag{A.16}$$

where $\psi_i(\mathbf{r}_{||})$ corresponds to the i^{th} mode wavefunction in the confinement direction.

$$\langle \mathbf{k}| H_{imp} |\mathbf{k}'\rangle = \sum_q \langle \mathbf{k}| \frac{Cq}{q^2+\zeta^{-2}} \left(a_q e^{i\mathbf{q}.\mathbf{r}} - a_q^\dagger e^{-i\mathbf{q}.\mathbf{r}}\right) |\mathbf{k}'\rangle$$

$$= \sum_q \pm \sqrt{N_{ph} + \frac{1}{2} \mp \frac{1}{2}} \frac{Cq}{q^2+\zeta^{-2}} \langle \mathbf{k}| e^{\pm i\mathbf{q}.\mathbf{r}} |\mathbf{k}'\rangle$$

where the first sign corresponds to phonon absorption process and the second sign corresponds to phonon emission process. Converting the summation over phonon momentum to an integral, we get

$$\langle \mathbf{k}| H_{imp} |\mathbf{k}'\rangle = \pm\sqrt{N_{ph} + \frac{1}{2} \mp \frac{1}{2}} \frac{C}{(2\pi)^3 L} \int_{-\infty}^{\infty} \mathbf{dq} \int_{-\infty}^{\infty} dx \int_0^{L_y}\int_0^{L_z} \mathbf{dr}_{||}.e^{-ik_x' x} \psi_i^*(\mathbf{r}_{||}) \frac{q}{q^2+\zeta^{-2}} e^{\pm i\mathbf{q}_{||}\mathbf{r}_{||}} e^{\pm iq_x x} e^{ik_x x} \psi_j(\mathbf{r}_{||})$$

$$= \pm\sqrt{N_{ph} + \frac{1}{2} \mp \frac{1}{2}} \frac{C}{(2\pi)^3 L} \int_{-\infty}^{\infty} \mathbf{dq} \int_{-\infty}^{\infty} dx.e^{i(k_x - k_x' \pm q_x)} \int_0^{L_y}\int_0^{L_z} \mathbf{dr}_{||}.\psi_i^*(\mathbf{r}_{||}) \frac{q}{q^2+\zeta^{-2}} e^{\pm i\mathbf{q}_{||}\mathbf{r}_{||}} \psi_j(\mathbf{r}_{||})$$

$$= \pm\sqrt{N_{ph} + \frac{1}{2} \mp \frac{1}{2}} \frac{C}{(2\pi)^2 \sqrt{L}} \int_{-\infty}^{\infty} \mathbf{dq} \delta\left(k_x - k_x^{'} \pm q_x\right) \int_0^{L_y}\int_0^{L_z} \mathbf{dr}_{||} \psi_i^*(\mathbf{r}_{||}) \psi_j(\mathbf{r}_{||}) \frac{q}{q^2+\zeta^{-2}} e^{\pm i\mathbf{q}_{||}\mathbf{r}_{||}}$$

$$= \pm\sqrt{N_{ph} + \frac{1}{2} \mp \frac{1}{2}} \frac{C}{(2\pi)^2 \sqrt{L}} \int_{-\infty}^{\infty} dq_x \delta\left(k_x - k_x^{'} \pm q_x\right) \int_{-\infty}^{\infty} \mathbf{dq}_{||} \int_0^{L_y}\int_0^{L_z} \mathbf{dr}_{||} \rho_{ij}(\mathbf{r}_{||}) \frac{q}{q^2+\zeta^{-2}} e^{\pm i\mathbf{q}_{||}\mathbf{r}_{||}} \tag{A.17}$$

$$|\langle \mathbf{k}| H_{imp} |\mathbf{k}'\rangle|^2 = \left(N_{ph} + \frac{1}{2} \mp \frac{1}{2}\right) \frac{C^2 V}{(2\pi)^4 L} \int_{-\infty}^{\infty} dq_x \delta\left(k_x - k_x^{'} \pm q_x\right) \int_{-\infty}^{\infty} \mathbf{dq}_{||} \int_0^{L_y}\int_0^{L_z}\int_0^{L_y}\int_0^{L_z} \mathbf{dr}_{||}\mathbf{dr}_{||}^{'} \rho_{ij}^*(\mathbf{r}_{||}) \rho_{ij}(\mathbf{r}_{||}^{'}) \frac{q^2}{\left(q^2+\zeta^{-2}\right)^2} e^{\pm i\mathbf{q}_{||}(\mathbf{r}_{||} - \mathbf{r}_{||}^{'})} \tag{A.18}$$

The above expression can be simplified by interchanging the integration order between $\mathbf{q}_{||}$ and $\mathbf{r}_{||},\ \mathbf{r}_{||}^{'}$ and integrating $\frac{q^2}{\left(q^2+\zeta^{-2}\right)^2} e^{\pm i\mathbf{q}_{||}(\mathbf{r}_{||} - \mathbf{r}_{||}^{'})}$ with respect to $\mathbf{q}_{||}$

$$\int_{-\infty}^{\infty} \mathbf{dq}_{||} \frac{q^2}{\left(q^2+\zeta^{-2}\right)^2} e^{\pm i\mathbf{q}_{||}(\mathbf{r}_{||} - \mathbf{r}_{||}^{'})} = \int_0^{\infty} q_{||} dq_{||} \int_0^{2\pi} d\theta \frac{\left(q_{||}^2 + q_x^2\right)}{\left(q_{||}^2 + q_x^2 + \zeta^{-2}\right)^2} e^{\pm i\mathbf{q}_{||}(\mathbf{r}_{||} - \mathbf{r}_{||}^{'})}$$

$$= \int_0^\infty \frac{q_{||} dq_{||}.\left(q_{||}^2 + q_x^2\right) 2\pi J_0\left(q_{||}\left|r_{||} - r_{||}^{'}\right|\right)}{\left(q_{||}^2 + q_x^2 + \zeta^{-2}\right)^2}$$

where $J_0(x)$ is the Bessel-J function of 0th order. The above function integral can be solved by using the relation

$$\int_0^\infty dx \frac{J_\nu(bx) x^{\nu+1}}{(x^2+a^2)^{\mu+1}} = \frac{a^{\nu-\mu} b^\mu}{2^\mu \Gamma(\mu+1)} K_{\nu-\mu}(ab)$$
$$for \quad -1 < Re(\nu) < Re\left(2\mu + \frac{3}{2}\right),\ a > 0,\ b > 0$$

where $K_{\nu-\mu}(x)$ is the Bessel-K function. Using the relation and by transfering 2π in the integral to prefactor, we get

$$I(q_x, \mathbf{r}_{||}, \mathbf{r}_{||}^{'}) = \int_{-\infty}^{\infty} \mathbf{dq}_{||} H(q)^2 e^{i\mathbf{q}_{||}(\mathbf{r}_{||} - \mathbf{r}_{||}^{'})}$$

$$= \begin{cases} \left(\sqrt{q_x^2 + \zeta^{-2}}\left|\mathbf{r}_{||} - \mathbf{r}_{||}^{'}\right| + \dfrac{q_x^2\left|\mathbf{r}_{||} - \mathbf{r}_{||}^{'}\right|}{\sqrt{q_x^2 + \zeta^{-2}}}\right) \dfrac{K_1\left(\sqrt{q_x^2 + \zeta^{-2}}\left|\mathbf{r}_{||} - \mathbf{r}_{||}^{'}\right|\right)}{2}, & \left|\mathbf{r}_{||} - \mathbf{r}_{||}^{'}\right| \neq 0 \\ \left(\dfrac{1}{2} + \dfrac{q_x^2}{2\left(q_x^2 + \zeta^{-2}\right)}\right), & \left|\mathbf{r}_{||} - \mathbf{r}_{||}^{'}\right| = 0 \end{cases}$$

The above integrand carries information about the non-locality of scattering and is referred to as the scattering kernel.

$$\begin{aligned} \left|\langle \mathbf{k}| H_{imp} |\mathbf{k}'\rangle\right|^2 &= \left(N_{ph} + \frac{1}{2} \mp \frac{1}{2}\right) \frac{C^2 V}{(2\pi)^3 L} \int_{-\infty}^{\infty} dq_x \delta\left(k_x - k_x^{'} \pm q_x\right) \\ &\int_0^{L_y}\int_0^{L_z}\int_0^{L_y}\int_0^{L_z} \mathbf{dr}_{||}\mathbf{dr}_{||}^{'} \rho_{ij}^*(\mathbf{r}_{||}) \rho_{ij}(\mathbf{r}_{||}^{'}) I(q_x, \mathbf{r}_{||}, \mathbf{r}_{||}^{'}) \\ &= \left(N_{ph} + \frac{1}{2} \mp \frac{1}{2}\right) \frac{C^2 V}{(2\pi)^3 L} \int_{-\infty}^{\infty} dq_x \delta\left(k_x - k_x^{'} \pm q_x\right) F(q_x) \end{aligned} \tag{A.19}$$

where $F(q_x) = \int_0^{L_y}\int_0^{L_z}\int_0^{L_y}\int_0^{L_z} \mathbf{dr}_{||}\mathbf{dr}_{||}^{'} \rho_{ij}^*(\mathbf{r}_{||}) \rho_{ij}(\mathbf{r}_{||}^{'}) I(q_x, \mathbf{r}_{||}, \mathbf{r}_{||}^{'})$ is the form factor. Scattering rate can now be derived by summing over all possible final momentum states.

$$\frac{1}{\tau(k_x)} = \sum_{k'} P(k_x, k_x^{'}) = \sum_{k'} \frac{2\pi}{\hbar}\left(N_{ph} + \frac{1}{2} \mp \frac{1}{2}\right)\frac{C^2V}{(2\pi)^3L} \\ \int_{-\infty}^{\infty} dq_x \delta\left(k_x - k_x^{'} \pm q_x\right) F(q_x) \delta\left(E(\mathbf{k}) - E(\mathbf{k}') \pm \hbar\omega_{LO}\right) \tag{A.20}$$

Converting the summation to integration and multiplying by 2 for spin degeneracy, we get

$$\frac{1}{\tau(k_x)} = \frac{2}{\hbar}\left(N_{ph} + \frac{1}{2} \mp \frac{1}{2}\right)\frac{C^2V}{(2\pi)^2}\int dk_x \delta\left(E(\mathbf{k}) - E(\mathbf{k}') \pm \hbar\omega_{LO}\right)\int_{-\infty}^{\infty} dq_x \delta\left(k_x - k_x^{'} + q_x\right) F(q_x) \tag{A.21}$$

Assuming a parabolic dispersion relation, we have

$$k_x = \sqrt{\frac{2m^*\left(E - E_i\right)}{\hbar^2}} \quad k_x^{'} = \sqrt{\frac{2m^*\left(E - E_j + \hbar\omega_{LO}\right)}{\hbar^2}}$$

for absorption process and

$$k_x = \sqrt{\frac{2m^*\left(E - E_i\right)}{\hbar^2}} \quad k_x^{'} = \sqrt{\frac{2m^*\left(E - E_j - \hbar\omega_{LO}\right)}{\hbar^2}}$$

for emission process. E_i and E_j are the energies corresponding the modes i and j. This gives two choices for scattering from k_x state to k_x^i state with $q_x = \pm(k_x \pm k_x^{'})$. This gives us

$$\frac{1}{\tau_{a/e}(k_x)} = \frac{2}{\hbar}\left(N_{ph} + \frac{1}{2} \mp \frac{1}{2}\right)\frac{C^2V}{(2\pi)^2} \\ \int dk_x \delta\left(E(\mathbf{k}) - E(\mathbf{k}') \mp \hbar\omega_{LO}\right)\left[F_{a/e}(k_x - k_x^{'}) + F_{a/e}(k_x + k_x^{'})\right]$$

By changing the coordinates from k_x to E, we get

$$\frac{1}{\tau_{ij,a}(E)} = \frac{e^2\hbar\omega_{LO}N_{ph}}{\hbar^2}\left(\frac{1}{\epsilon_\infty} - \frac{1}{\epsilon_s}\right)\cdot\frac{2}{(2\pi)^2}\cdot\sqrt{2m^*}\left(\frac{F_a(k_x - k_x^{'}) + F_a(k_x + k_x^{'})}{\sqrt{E - E_j + \hbar\omega_{LO}}}\right)$$

for the absorption process (expression changes to $\frac{1}{\sqrt{E - E_j}}$ for the lowest subband) and

$$\frac{1}{\tau_{ij,e}(E)} = \frac{e^2\hbar\omega_{LO}\left(N_{ph} + 1\right)}{\hbar^2}\left(\frac{1}{\epsilon_\infty} - \frac{1}{\epsilon_s}\right)\cdot\frac{2}{(2\pi)^2}\cdot\sqrt{2m^*}\left(\frac{F_e(k_x - k_x^{'}) + F_e(k_x + k_x^{'})}{\sqrt{E - E_j - \hbar\omega_{LO}}}\right)$$

for the emission process ($E > E_j + \hbar\omega_{LO}$). Total scattering rate is a sum of both the absorption and emission processes.

Dimension check

$$\frac{1}{\tau_{ij}(E)} = \frac{C^2.kg.m^2.s^{-2}kg^{1/2}}{(kg.m^2.s^{-1})^2.(C^2.kg^{-1}.m^{-3}.s^2)}.\frac{1}{kg^{1/2}ms^{-1}} = \frac{1}{s}$$

The above scattering rate is between two modes i and j. Multi-modal scattering rate can be calculated by summing up contributions from different inter-mode scattering

$$\Gamma(E) = \sum_j \Gamma_{ij}(E) = \sum_j \frac{1}{\tau_{ij}(E)}$$

B. FERMI'S GOLDEN RULE FOR CHARGED IMPURITY SCATTERING

Subsequent Fermi's Golden rule derivation for charged impurity scattering follows the Brooks-Herring scattering approach where the charged impurity centers are screened by electrons (other approaches include Conwell-Weisskopf formalism [82] and Ridley formalism [80]). Screening is taken into account through a density dependent screening length (following either the Debye approximation of the Lindhard formalism).

B.1 Bulk/quasi1D device

According to Fermi's golden rule, scattering rate for an electron in an initial momentum state $\mathbf{k}$ to a final momentum state $\mathbf{k}+\mathbf{q}$ is given by

$$P\left(\mathbf{k},\mathbf{k}+\mathbf{q}\right)=\frac{2\pi}{\hbar}\left|\left\langle \mathbf{k}+\mathbf{q}\right|H_{imp}\left|\mathbf{k}\right\rangle \right|^{2}\delta\left(E(\mathbf{k}+\mathbf{q})-E(\mathbf{k})\right) \tag{B.1}$$

Impurity potential is given by

$$H_{imp}(r)=\frac{Ze^{2}}{4\pi\epsilon r}exp\left(-r/\zeta\right)$$

where ζ is the screening length. Ze corresponds to the charge density present on the impurity atom. Since most of the impurity atoms under consideration of this study have $Z=1$, Z will be set to 1 in further discussions. For mathematical convenience, the Hamiltonian will be represented in the momentum space

$$H_{imp}(\mathbf{q})=\frac{Ze^{2}}{\epsilon}\frac{1}{q^{2}+\zeta^{-2}}$$

Scattering rate can now be written as

$$\frac{1}{\tau(\mathbf{k})}=\frac{Ze^{2}n_{D}}{\epsilon}\frac{2\pi}{\hbar}\sum_{q}\left|\left\langle \mathbf{k}+\mathbf{q}\right|\left|H_{imp}\right|\left|\mathbf{k}\right\rangle \right|^{2}\delta\left(E(\mathbf{k}+\mathbf{q})-E(\mathbf{k})\right) \tag{B.2}$$

where n_D is the average doping density per unit volume.

$$\frac{1}{\tau(\mathbf{k})} = \frac{e^4 n_D}{4\pi^2 \epsilon^2 \hbar} \int \mathbf{dq} \frac{q^2}{\left(q^2 + \zeta^{-2}\right)^2} \delta\left(E(\mathbf{k}+\mathbf{q}) - E(\mathbf{k})\right) \tag{B.3}$$

Assuming a parabolic dispersion relation $E(k) = \dfrac{\hbar^2 k^2}{2m^*}$ and by converting the momentum integral to spherical coordinates, we get

$$\frac{1}{\tau(\mathbf{k})} = \frac{e^4 n_D}{2\pi\epsilon^2 \hbar} \int_0^\infty dq \frac{q^2}{\left(q^2 + \zeta^{-2}\right)^2} \int_0^\pi d\theta sin\theta \delta\left(\frac{\hbar^2 q^2}{2m^*} + \frac{\hbar^2 k q cos\theta}{m^*}\right)$$

With change of variables $x = \dfrac{\hbar^2 k q cos\theta}{m^*}$, the scattering rate turns out to be (integration limit is upto $2k$ due to constraint on $cos\theta \leq 1$ inside the delta function)

$$\frac{1}{\tau(\mathbf{k})} = \frac{e^4 n_D}{2\pi\epsilon^2} \frac{m^*}{\hbar^2 k} \int_0^{2k} dq \frac{q}{\left(q^2 + \zeta^{-2}\right)^2} = \frac{2e^4 m^* n_D}{\pi \hbar^3 \epsilon_o^2} \frac{k}{\zeta^{-2}\left(\zeta^{-2} + 4k^2\right)} \tag{B.4}$$

Representing the scattering rate in energy space, we get

$$\frac{1}{\tau(E)} = \frac{2e^4 m^* n_D}{\pi \hbar^3 \epsilon^2} \frac{\sqrt{\dfrac{2m^* E}{\hbar^2}}}{\zeta^{-2}\left(\zeta^{-2} + \dfrac{8m^* E}{\hbar^2}\right)}$$

Dimension check

$$\frac{1}{\tau(E)} = \frac{C^4.kg.}{(kg.m^2.s^{-1})^3.(C^2.kg^{-1}m^{-3}.s^2)^2.nm^3} . \frac{nm^{-1}}{nm^{-2}.nm^{-2}} = \frac{1}{s}$$

B.2 Ultra-thin body (UTB) device

For discussion below, x and y directions will be assumed periodic and z will be the confinement direction.

According to Fermi's golden rule, scattering rate for an electron scattering with a LO phonon in an initial momentum state $\mathbf{k}$ to a final momentum state $\mathbf{k}'$ is given by

$$P\left(\mathbf{k},\mathbf{k}'\right)=\frac{2\pi}{\hbar}\left|\left\langle\mathbf{k}\right|H_{imp}\left|\mathbf{k}'\right\rangle\right|^{2}\delta\left(E(\mathbf{k})-E(\mathbf{k}')\pm\hbar\omega_{LO}\right) \tag{B.5}$$

Impurity potential is given by

$$H_{imp}(r)=\frac{Ze^{2}}{4\pi\epsilon r}exp\left(-r/\zeta\right)$$

where ζ is the screening length. Ze corresponds to the charge present on the impurity atom. Since most of the impurity atoms have $Z=1$, Z will be neglected in further discussions. For mathematical convenience (which shall become clear later), the Hamiltonian will be represented in terms of it's Fourier transform. Hence $H_{imp}(r)$ will be represented as

$$H_{imp}(r)=\frac{1}{\left(2\pi\right)^{3}}\int_{-\infty}^{\infty}H(\mathbf{q})e^{i\mathbf{q}.\mathbf{r}}\mathbf{dq}$$

where

$$H(\mathbf{q})=\frac{e^{2}}{\epsilon}\frac{1}{q^{2}+\zeta^{-2}}$$

The electronic wavefunctions correspond to the Bloch wavefunctions

$$\left|\mathbf{k}\right\rangle=\frac{1}{\sqrt{A}}e^{i\vec{k_{||}}.\vec{r}_{||}}\psi_{i}(z) \tag{B.6}$$

where $\psi_i(z)$ corresponds to the i^{th} mode wavefunction in the confinement direction.

$$\left\langle\mathbf{k}\right|H_{imp}\left|\mathbf{k}'\right\rangle=\frac{e^{2}}{\epsilon\left(2\pi\right)^{3}A}\int_{-\infty}^{\infty}\mathbf{dq}\int_{-\infty}^{\infty}\mathbf{dr}_{||}\int_{0}^{L_{z}}dz.e^{-i\mathbf{k}_{||}^{'}.\mathbf{r}_{||}}\psi_{i}^{*}(z)H(q)e^{i\mathbf{q}_{||}\mathbf{r}_{||}}e^{iq_{z}z}e^{i\mathbf{k}_{||}\mathbf{r}_{||}}\psi_{j}(z)$$

$$=\frac{e^{2}}{\epsilon\left(2\pi\right)^{3}A}\int_{-\infty}^{\infty}\mathbf{dq}\int_{-\infty}^{\infty}\mathbf{dr}_{||}e^{i\left(\mathbf{k}_{||}-\mathbf{k}_{||}^{'}+\mathbf{q}_{||}\right).\mathbf{r}_{||}}\int_{0}^{L_{z}}dz\psi_{i}^{*}(z)\psi_{j}(z)H(q)e^{iq_{z}z}$$

$$=\frac{e^{2}}{\epsilon\left(2\pi\right)\sqrt{A}}\int_{-\infty}^{\infty}\mathbf{dq}\delta\left(\mathbf{k}_{||}-\mathbf{k}_{||}^{'}+\mathbf{q}_{||}\right)\int_{0}^{L_{z}}dz\rho_{ij}(z)H(q)e^{iq_{z}z}$$

$$= \frac{e^2}{\epsilon\,(2\pi)\,\sqrt{A}} \int_{-\infty}^{\infty} \mathbf{dq}_{||} \delta\left(\mathbf{k}_{||} - \mathbf{k}_{||}^{'} + \mathbf{q}_{||}\right) \int_{-\infty}^{\infty} dq_z \int_0^{L_z} dz \rho_{ij}(z) H(q) e^{iq_z z} \tag{B.7}$$

$$\begin{aligned} \left|\langle \mathbf{k}| \, H_{imp} \, |\mathbf{k}'\rangle\right|^2 = \frac{e^4}{\epsilon^2 (2\pi)^2 A} \int_{-\infty}^{\infty} d\vec{q}_{||} \delta\left(\mathbf{k}_{||} - \mathbf{k}_{||}^{'} + \mathbf{q}_{||}\right) \int_{-\infty}^{\infty} dq_z \\ \int_0^{L_Z} \int_0^{L_z} dz dz^{'} \rho_{ij}(z) \rho_{ij}(z') H(q)^2 e^{iq_z (z - z')} \end{aligned} \tag{B.8}$$

The above expression can be simplified by interchanging the integration order between q_z and $z,\ z'$ and integrating $H(q)^2 e^{iq_z(z-z')}$ with respect to q_z

$$\int_{-\infty}^{\infty} dq_z H(q)^2 e^{iq_z(z-z')} = \int_{-\infty}^{\infty} dq_z \frac{1}{\left(q_{||}^2 + q_z^2 + \zeta^{-2}\right)^2} e^{iq_z(z-z')}$$

Scattering kernel integral that needs to be solved

$$\int_{-\infty}^{\infty} dq_z \frac{1}{\left(q_{||}^2 + q_z^2 + \zeta^{-2}\right)^2} e^{iq_z(z-z')}$$

Let $a = z - z'$ and $b = \sqrt{q_{||}^2 + \zeta^{-2}}$. Converting the above integral into a complex function integral, we get

$$\int_{-\infty}^{\infty} dz \frac{e^{iaz}}{(z^2 + b^2)^2}$$

The function has residues at $z = \pm ib$. Since we are performing a real integral, only the residues in upper half-plane matter. Using Cauchy's residue theorem, we get

$$\begin{aligned} I = 2\pi i \left[\frac{d}{dz}\left(z - ib\right)^2 f(z)\right]_{z=ib} = 2\pi i \left[\frac{iae^{iaz}(z+ib)^2 - 2e^{iaz}(z+ib)}{(z+ib)^4}\right]_{z=ib} \\ = \frac{\pi e^{-ab}}{2b^2}\left[a + \frac{1}{b}\right] = \frac{\pi e^{-|z-z'|\sqrt{q_{||}^2+\zeta^{-2}}}}{2\left(q_{||}^2 + \zeta^{-2}\right)} \left[\frac{1}{\sqrt{q_{||}^2 + \zeta^{-2}}} + |z - z'|\right] \end{aligned} \tag{B.9}$$

The above integrand carries information about the non-locality of scattering and is referred to as the scattering kernel.

$$\left|\langle \mathbf{k}| \, H_{imp} \, |\mathbf{k}'\rangle\right|^2 = \frac{e^4}{\epsilon^2 (2\pi)^2 A} \int_{-\infty}^{\infty} \mathbf{dq}_{||} \delta\left(\mathbf{k}_{||} - \mathbf{k}_{||}^{'} + \mathbf{q}_{||}\right) \int_0^{L_z} \int_0^{L_z} dz dz^{'} \rho_{ij}(z) \rho_{ij}(z') I(q_{||}, z, z')$$

$$= \frac{e^4}{\epsilon^2 (2\pi)^2 A} \int_{-\infty}^{\infty} \mathbf{dq}_{||} \delta\left(\mathbf{k}_{||} - \mathbf{k}_{||}^{'} + \mathbf{q}_{||}\right) F(q_{||})$$

where $F(q_{||}) = \int_0^{L_z}\int_0^{L_z} dzdz^{'}\rho_{ij}(z)\rho_{ij}(z')I(q_{||},z,z')$ is the form factor. Scattering rate can now be derived by summing over all possible final momentum states.

$$\frac{1}{\tau_m(\mathbf{k}_{||})} = \sum_{k'} P(\mathbf{k}_{||},\mathbf{k}_{||}^{'}) = \sum_{k'}\frac{2\pi}{\hbar}\frac{e^4 N_D}{\epsilon^2(2\pi)^2 A}\int_{-\infty}^{\infty}\mathbf{dq}_{||}\delta\left(\mathbf{k}_{||}-\mathbf{k}_{||}^{'}+\mathbf{q}_{||}\right)F(q_{||})\delta\left(E(\mathbf{k})-E(\mathbf{k}')\right) \tag{B.10}$$

Note the prefactor N_D in the expression above. The above derivation holds good for each of the scattering centers. If there are N_D such scattering centers per unit length along confinement direction, then the prefactor gets multiplied by N_D. Converting the summation to integration and multiplying by 2 for spin degeneracy, we get

$$\frac{1}{\tau_m(k_{||})} = 2.\frac{e^4 N_D}{\hbar\epsilon^2}\frac{1}{(2\pi)^3}\int \mathbf{dk}_{||}^{'}\delta\left(E(\mathbf{k})-E(\mathbf{k}')\right)\int_{-\infty}^{\infty}\mathbf{dq}_{||}\delta\left(\mathbf{k}_{||}-\mathbf{k}_{||}^{'}+\mathbf{q}_{||}\right)F(q_{||})$$

$$\int \mathbf{dk}_{||}^{'}\int_{-\infty}^{\infty}\mathbf{dq}_{||}\delta\left(E(\mathbf{k})-E(\mathbf{k}')\right)\delta\left(\mathbf{k}_{||}-\mathbf{k}_{||}^{'}+\mathbf{q}_{||}\right)F(q_{||}) =$$

$$\int\int k'dk'd\theta\delta\left(E(\mathbf{k})-E(\mathbf{k}')\right)F(|\mathbf{k}_{||}-\mathbf{k}_{||}^{'}|)$$

$$\int\int k'dk'd\theta\delta\left(E(\mathbf{k})-E(\mathbf{k}')\right)F(|\mathbf{k}_{||}-\mathbf{k}_{||}^{'}|) = \frac{m^*}{\hbar^2}\int\int dE(k')d\theta\delta\left(E(\mathbf{k})-E(\mathbf{k}')\right)F(|\tilde{\mathbf{k}}_{||}-\tilde{\mathbf{k}}_{||}^{'}|)$$

$$= \frac{m^*}{\hbar^2}\int_0^{2\pi} d\theta F(E(\mathbf{k}_{||}),\theta)$$

where

$$|\tilde{\mathbf{k}}_{||}-\tilde{\mathbf{k}}_{||}^{'}| = \left[\frac{2m^*}{\hbar^2}\left(2E-E_i-E_j\right)-2.\frac{2m^*}{\hbar^2}\sqrt{E-E_i}.\sqrt{E-E_j}cos\theta\right]^{1/2} \tag{B.11}$$

E_i and E_j are the energies corresponding the modes i and j. Finally, the scattering rate can be expressed as

$$\frac{1}{\tau_{ij}(E)} = \frac{2e^4 N_D m^*}{\hbar^3\epsilon^2(2\pi)^3}\int_0^{2\pi} d\theta F(E,\theta)$$

Dimension check

$$\frac{1}{\tau_{ij}(E)} = \frac{C^4.nm^{-3}.kg}{(kg.m^2.s^{-1})^3.(C^2.kg^{-1}.m^{-3}.s^2)^2}.nm^3 = \frac{1}{s}$$

The above scattering rate is between two modes i and j. Multi-modal scattering rate can be calculated by summing up contributions from different inter-mode scattering

$$\Gamma(E) = \sum_j \Gamma_{ij}(E) = \sum_j \frac{1}{\tau_{ij}(E)}$$

B.3 Nanowire device

For discussion below, x will be the periodic direction along the length of wire and $y,\ z$ will be the periodic directions.

According to Fermi's golden rule, scattering rate for an electron in an initial momentum state $\mathbf{k}$ to a final momentum state $\mathbf{k}'$ is given by

$$P\left(\mathbf{k},\mathbf{k}'\right)=\frac{2\pi}{\hbar}\left|\left\langle\mathbf{k}\right|H_{imp}\left|\mathbf{k}'\right\rangle\right|^{2}\delta\left(E(\mathbf{k})-E(\mathbf{k}')\right) \tag{B.12}$$

Impurity potential is given by

$$H_{imp}(r)=\frac{Ze^{2}}{4\pi\epsilon r}exp\left(-r/\zeta\right)$$

where ζ is the screening length. Ze corresponds to the charge present on the impurity atom. Since most of the impurity atoms have $Z=1$, Z will be neglected in further discussions. For mathematical convenience (which shall become clear later), the Hamiltonian will be represented in terms of it's Fourier transform. Hence $H_{imp}(r)$ will be represented as

$$H_{imp}(r)=\frac{1}{\left(2\pi\right)^{3}}\int_{-\infty}^{\infty}H(\mathbf{q})e^{i\mathbf{q}.\mathbf{r}}\mathbf{dq}$$

where

$$H(\mathbf{q})=\frac{e^{2}}{\epsilon}\frac{1}{q^{2}+\zeta^{-2}}$$

The electronic wavefunctions correspond to the Bloch wavefunctions

$$\left|\mathbf{k}\right\rangle=\frac{1}{\sqrt{L}}e^{ik_{x}x}\psi_{i}(\mathbf{r}_{||}) \tag{B.13}$$

where $\psi_{i}(\mathbf{r}_{||})$ corresponds to the i^{th} mode wavefunction in the confinement direction.

$$\left\langle\mathbf{k}\right|H_{imp}\left|\mathbf{k}'\right\rangle=\frac{e^{2}}{\epsilon\left(2\pi\right)^{3}L}\int_{-\infty}^{\infty}\mathbf{dq}\int_{-\infty}^{\infty}dx\int_{0}^{L_{y}}\int_{0}^{L_{z}}\mathbf{dr}_{||}.e^{-ik_{x}^{\prime}x}\psi_{i}^{*}(\mathbf{r}_{||})H(q)e^{i\mathbf{q}_{||}\mathbf{r}_{||}}e^{iq_{x}x}e^{ik_{x}x}\psi_{j}(\mathbf{r}_{||})$$

$$=\frac{e^{2}}{\epsilon\left(2\pi\right)^{3}L}\int_{-\infty}^{\infty}\mathbf{dq}\int_{-\infty}^{\infty}dx.e^{i(k_{x}-k_{x}^{\prime}+q_{x})}\int_{0}^{L_{y}}\int_{0}^{L_{z}}\mathbf{dr}_{||}.\psi_{i}^{*}(\mathbf{r}_{||})H(q)e^{i\mathbf{q}_{||}\mathbf{r}_{||}}\psi_{j}(\mathbf{r}_{||})$$

$$=\frac{e^{2}}{\epsilon\left(2\pi\right)^{2}\sqrt{L}}\int_{-\infty}^{\infty}\mathbf{dq}\delta\left(k_{x}-k_{x}^{'}+q_{x}\right)\int_{0}^{L_{y}}\int_{0}^{L_{z}}\mathbf{dr}_{||}\psi_{i}^{*}(\mathbf{r}_{||})\psi_{j}(\mathbf{r}_{||})H(q)e^{i\mathbf{q}_{||}\mathbf{r}_{||}}$$

$$= \frac{e^2}{\epsilon (2\pi)^2 \sqrt{L}} \int_{-\infty}^{\infty} dq_x \delta \left(k_x - k_x^{'} + q_x \right) \int_{-\infty}^{\infty} \mathbf{dq}_{||} \int_0^{L_y} \int_0^{L_z} \mathbf{dr}_{||} \rho_{ij}(\mathbf{r}_{||}) H(q) e^{i\mathbf{q}_{||}\mathbf{r}_{||}} \tag{B.14}$$

$$\begin{aligned} |\langle \mathbf{k}| \, H_{imp} \, |\mathbf{k}'\rangle|^2 = \frac{e^4}{\epsilon^2 (2\pi)^4 L} \int_{-\infty}^{\infty} dq_x \delta \left(k_x - k_x^{'} + q_x \right) \int_{-\infty}^{\infty} \mathbf{dq}_{||} \\ \int_0^{L_y} \int_0^{L_z} \int_0^{L_y} \int_0^{L_z} \mathbf{dr}_{||} \mathbf{dr}_{||}^{'} \rho_{ij}^{*}(\mathbf{r}_{||}) \rho_{ij}(\mathbf{r}_{||}^{'}) H(q)^2 e^{i\mathbf{q}_{||}(\mathbf{r}_{||} - \mathbf{r}_{||}^{'})} \end{aligned} \tag{B.15}$$

The above expression can be simplified by interchanging the integration order between $\mathbf{q}_{||}$ and $\mathbf{r}_{||},\ \mathbf{r}_{||}^{'}$ and integrating $H(q)^2 e^{i\mathbf{q}_{||}(\mathbf{r}_{||} - \mathbf{r}_{||}^{'})}$ with respect to $\mathbf{q}_{||}$

$$\int_{-\infty}^{\infty} \mathbf{dq}_{||} H(q)^2 e^{i\mathbf{q}_{||}(\mathbf{r}_{||} - \mathbf{r}_{||}^{'})} = \int_0^{\infty} q_{||} dq_{||} \int_0^{2\pi} d\theta \frac{1}{\left(q_{||}^2 + q_x^2 + \zeta^{-2} \right)^2} e^{i\mathbf{q}_{||}(\mathbf{r}_{||} - \mathbf{r}_{||}^{'})}$$

$$= \int_0^{\infty} \frac{q_{||} dq_{||} . 2\pi J_0 \left(q_{||} \left| r_{||} - r_{||}^{'} \right| \right)}{\left(q_{||}^2 + q_x^2 + \zeta^{-2} \right)^2}$$

where $J_0(x)$ is the Bessel-J function of 0th order. The above function integral can be solved by using the relation

$$\int_0^{\infty} dx \frac{J_\nu(bx) x^{\nu+1}}{(x^2 + a^2)^{\mu+1}} = \frac{a^{\nu-\mu} b^\mu}{2^\mu \Gamma(\mu+1)} K_{\nu-\mu}(ab)$$
$$for \quad -1 < Re(\nu) < Re\left(2\mu + \frac{3}{2} \right),\ a > 0,\ b > 0$$

where $K_{\nu-\mu}(x)$ is the Bessel-K function. Using the relation and by transfering 2π in the integral to prefactor, we get

$$I(q_x, \mathbf{r}_{||}, \mathbf{r}_{||}^{'}) = \int_{-\infty}^{\infty} \mathbf{dq}_{||} H(q)^2 e^{i\mathbf{q}_{||}(\mathbf{r}_{||} - \mathbf{r}_{||}^{'})}$$

$$= \begin{cases} \dfrac{\left| \mathbf{r}_{||} - \mathbf{r}_{||}^{'} \right|}{2\sqrt{q_x^2 + \zeta^{-2}}} K_1 \left(\sqrt{q_x^2 + \zeta^{-2}} \left| \mathbf{r}_{||} - \mathbf{r}_{||}^{'} \right| \right), & \left| \mathbf{r}_{||} - \mathbf{r}_{||}^{'} \right| \neq 0 \\ \dfrac{1}{2\left(q_x^2 + \zeta^{-2} \right)}, & \left| \mathbf{r}_{||} - \mathbf{r}_{||}^{'} \right| = 0 \end{cases}$$

The above integrand carries information about the non-locality of scattering and is referred to as the scattering kernel.

$$\begin{aligned}|\langle \mathbf{k}| H_{imp} |\mathbf{k}'\rangle|^2 &= \frac{e^4}{\epsilon^2(2\pi)^3 L}\int_{-\infty}^{\infty} dq_x \delta\left(k_x - k_x^{'} + q_x\right) \\ &\int_0^{L_y}\int_0^{L_z}\int_0^{L_y}\int_0^{L_z} \mathbf{dr}_{||}\mathbf{dr}_{||}^{'}\rho_{ij}^{*}(\mathbf{r}_{||})\rho_{ij}(\mathbf{r}_{||}^{'})I(q_x, \mathbf{r}_{||}, \mathbf{r}_{||}^{'}) \\ &= \frac{e^4}{\epsilon^2(2\pi)^3 L}\int_{-\infty}^{\infty} dq_x \delta\left(k_x - k_x^{'} + q_x\right) F(q_x)\end{aligned} \tag{B.16}$$

where $F(q_x) = \int_0^{L_y}\int_0^{L_z}\int_0^{L_y}\int_0^{L_z} \mathbf{dr}_{||}\mathbf{dr}_{||}^{'}\rho_{ij}^{*}(\mathbf{r}_{||})\rho_{ij}(\mathbf{r}_{||}^{'})I(q_x, \mathbf{r}_{||}, \mathbf{r}_{||}^{'})$ is the form factor. Scattering rate can now be derived by summing over all possible final momentum states.

$$\frac{1}{\tau_m(k_x)} = \sum_{k'} P(k_x, k_x^{'}) = \sum_{k'} \frac{2\pi}{\hbar}\frac{e^4 N_D}{\epsilon^2(2\pi)^3 L}\int_{-\infty}^{\infty} dq_x \delta\left(k_x - k_x^{'} + q_x\right) F(q_x)F(q_{||})\delta\left(E(\mathbf{k}) - E(\mathbf{k}')\right) \tag{B.17}$$

N_D is the number of scattering centers present per unit area along the confinement direction. Converting the summation to integration and multiplying by 2 for spin degeneracy, we get

$$\frac{1}{\tau_m(k_x)} = 2.\frac{e^4 N_D}{\hbar\epsilon^2 L^2}\frac{1}{(2\pi)^3}\int dk_x \delta\left(E(\mathbf{k}) - E(\mathbf{k}')\right)\int_{-\infty}^{\infty} dq_x \delta\left(k_x - k_x^{'} + q_x\right) F(q_x) \tag{B.18}$$

Assuming a parabolic dispersion relation, we have

$$k_x = \sqrt{\frac{2m^*\left(E - E_i\right)}{\hbar^2}} \quad k_x^{'} = \sqrt{\frac{2m^*\left(E - E_j\right)}{\hbar^2}}$$

where E_i and E_j are the energies corresponding the modes i and j. This gives two choices for scattering from k_x state to $k_x^{'}$ state with $q_x = k_x \pm k_x^{'}$. This gives us

$$\frac{1}{\tau_m(k_x)} = 2.\frac{e^4 N_D}{\hbar\epsilon^2}\frac{1}{(2\pi)^3}\int dk_x \delta\left(E(\mathbf{k}) - E(\mathbf{k}')\right)\left[F(k_x - k_x^{'}) + F(k_x + k_x^{'})\right]$$

By changing the coordinates from k_x to E, we get

$$\frac{1}{\tau_{ij}(E)} = \frac{e^4 N_D\sqrt{2m^*}}{\hbar^2\epsilon^2(2\pi)^3}\left(\frac{F(k_x - k_x^{'}) + F(k_x + k_x^{'})}{\sqrt{E - E_i}}\right)$$

Dimension check

$$\frac{1}{\tau_{ij}(E)} = \frac{C^4.nm^{-3}.kg^{1/2}nm^2}{(kg.m^2.s^{-1})^2.(C^2.kg^{-1}.m^{-3}.s^2)^2}.\frac{1}{kg^{1/2}ms^{-1}} = \frac{1}{s}$$

The above scattering rate is between two modes i and j. Multi-modal scattering rate can be calculated by summing up contributions from different inter-mode scattering

$$\Gamma(E) = \sum_j \Gamma_{ij}(E) = \sum_j \frac{1}{\tau_{ij}(E)}$$

C. FERMI'S GOLDEN RULE FOR REMOTE PHONON SCATTERING

C.1 Ultra-thin body (UTB) device

Remote phonon scattering is mediated by surface oxide (SO) phonons which interact with electrons right under the oxide. Oxides have multiple SO modes that contribute to scattering. Calculated rate accounts for multiple modes and takes both inter and intra mode scattering into account. For discussion below, x and y directions will be assumed periodic and z will be the confinement direction.

According to Fermi's golden rule, scattering rate for an electron in an initial momentum state $\mathbf{k}$ to a final momentum state $\mathbf{k}'$ is given by

$$P\left(\mathbf{k},\mathbf{k}'\right)=\frac{2\pi}{\hbar}\left|\langle\mathbf{k}|\,H_{imp}\,|\mathbf{k}'\rangle\right|^{2}\delta\left(E(\mathbf{k})-E(\mathbf{k}')\pm\hbar\omega_{SO}\right) \tag{C.1}$$

According to Fermi's golden rule, scattering rate for an electron with an optical phonon in an initial momentum state $\mathbf{k}$ to a final momentum state $\mathbf{k}'$ is given by

$$P\left(\mathbf{k},\mathbf{k}'\right)=\frac{2\pi}{\hbar}\left|\langle\mathbf{k}|\,H_{imp}\,|\mathbf{k}'\rangle\right|^{2}\delta\left(E(\mathbf{k})-E(\mathbf{k}')\pm\hbar\omega_{SO}\right) \tag{C.2}$$

Electron-phonon coupling Hamiltonian is given by

$$H_{e-ph}=F_{\nu}\sum_{q}\frac{e^{-q_{||}z}}{\sqrt{q_{||}}}\left(a_{q}e^{i\mathbf{q}_{||}\cdot\mathbf{r}_{||}}+a_{q}^{\dagger}e^{-i\mathbf{q}_{||}\cdot\mathbf{r}_{||}}\right) \tag{C.3}$$

where q is the surface 2D phonon momentum, a_q and $a_q^{\dagger}$ are particle annihilation and creation operators and coupling constant F_ν is described as

$$F_{\nu}=\left[\frac{e\hbar\omega_{SO}^{\nu}}{2S\epsilon_{o}}\left(\frac{1}{\epsilon_{ox}^{\infty}+\epsilon_{s}^{\infty}}-\frac{1}{\epsilon_{ox}^{o}+\epsilon_{s}^{\infty}}\right)\right]^{1/2} \tag{C.4}$$

where $\hbar\omega_{SO}^{\nu}$ is νth oxide SO optical phonon frequency, ϵ_{ox}^{o} is static oxide dielectric constant,ϵ_{ox}^{∞} is oxide high frequency dielectric constant and ϵ_{s}^{∞} is semiconducotor high frequency dielectric constant. The electronic wavefunction is of the form

$$|\mathbf{k}\rangle = \frac{1}{\sqrt{A}} e^{ik_x x} \psi_i(\mathbf{r}_{||}) \tag{C.5}$$

where $\psi_i(\mathbf{r}_{||})$ corresponds to the i^{th} mode wavefunction in the confinement direction.

$$\langle \mathbf{k}| H_{imp} |\mathbf{k}'\rangle = \sum_q \langle \mathbf{k}| \frac{e^{-q_{||}z}}{\sqrt{q_{||}}} F_\nu \left(a_q e^{i\mathbf{q}_{||}\cdot\mathbf{r}_{||}} + a_q^\dagger e^{-i\mathbf{q}_{||}\cdot\mathbf{r}_{||}} \right) |\mathbf{k}'\rangle$$

$$= \sum_{q_{||}} \sqrt{N_{ph} + \frac{1}{2} \mp \frac{1}{2}} \frac{e^{-q_{||}z}}{\sqrt{q_{||}}} F_\nu \langle \mathbf{k}| e^{\pm i\mathbf{q}_{||}\cdot\mathbf{r}_{||}} |\mathbf{k}'\rangle$$

where the first sign corresponds to phonon absorption process and the second sign corresponds to phonon emission process. Converting the summation over phonon momentum to an integral, we get

$$\langle \mathbf{k}| H_{imp} |\mathbf{k}'\rangle = \sqrt{N_{ph} + \frac{1}{2} \mp \frac{1}{2}} \frac{F_\nu}{A(2\pi)^2} \int_{-\infty}^{\infty} \mathbf{dq}_{||}$$
$$\int_{-\infty}^{\infty} \mathbf{dr}_{||} \int_0^{L_z} dz . e^{-i\mathbf{k}_{||}^{'}\cdot\mathbf{r}_{||}} \psi_i^*(z) H(q_{||}, z) e^{\pm i\mathbf{q}_{||}\mathbf{r}_{||}} e^{iq_z z} e^{i\mathbf{k}_{||}\mathbf{r}_{||}} \psi_j(z)$$

$$= \sqrt{N_{ph} + \frac{1}{2} \mp \frac{1}{2}} \frac{F_\nu}{A(2\pi)^2} \int_{-\infty}^{\infty} \mathbf{dq}_{||} \int_{-\infty}^{\infty} \mathbf{dr}_{||} e^{i\left(\mathbf{k}_{||} - \mathbf{k}_{||}^{'} \pm \mathbf{q}_{||}\right)\cdot\mathbf{r}_{||}} \int_0^{L_z} dz \psi_i^*(z) \psi_j(z) H(q_{||}, z)$$

$$= \sqrt{N_{ph} + \frac{1}{2} \mp \frac{1}{2}} \frac{F_\nu}{\sqrt{A}} \int_{-\infty}^{\infty} \mathbf{dq}_{||} \delta\left(\mathbf{k}_{||} - \mathbf{k}_{||}^{'} \pm \mathbf{q}_{||}\right) \int_0^{L_z} dz \rho_{ij}(z) H(q_{||}, z)$$

$$= \sqrt{N_{ph} + \frac{1}{2} \mp \frac{1}{2}} \frac{F_\nu}{\sqrt{A}} \int_{-\infty}^{\infty} \mathbf{dq}_{||} \delta\left(\mathbf{k}_{||} - \mathbf{k}_{||}^{'} \pm \mathbf{q}_{||}\right) \int dz \rho_{ij}(z) H(q_{||}, z) \tag{C.6}$$

$$|\langle \mathbf{k}| H_{imp} |\mathbf{k}'\rangle|^2 = \left(N_{ph} + \frac{1}{2} \pm \frac{1}{2} \right) F_\nu^2 \int_{-\infty}^{\infty} d\vec{q}_{||} \delta\left(\mathbf{k}_{||} - \mathbf{k}_{||}^{'} \pm \mathbf{q}_{||}\right)$$
$$\int_0^{L_Z} \int_0^{L_z} dz dz^{'} \rho_{ij}(z) \rho_{ij}(z') H(q_{||}, z) H(q_{||}, z') \tag{C.7}$$

Scattering kernel of this system can be defined as

$$I(q_{||}, z, z') = H(q_{||}, z) H(q_{||}, z') = \frac{e^{-q_{||}(z+z')}}{\sqrt{q_{||}}}$$

The above integrand carries information about the non-locality of scattering and is referred to as the scattering kernel.

$$|\langle \mathbf{k}| H_{imp} |\mathbf{k}'\rangle|^2 = \left(N_{ph} + \frac{1}{2} \pm \frac{1}{2}\right) F_\nu^2 \int_{-\infty}^{\infty} \mathbf{dq}_{||} \delta\left(\mathbf{k}_{||} - \mathbf{k}_{||}^{'} \pm \mathbf{q}_{||}\right)$$
$$\int_0^{L_z}\int_0^{L_z} dz dz^{'} \rho_{ij}(z)\rho_{ij}(z') I(q_{||}, z, z')$$
$$= \left(N_{ph} + \frac{1}{2} \pm \frac{1}{2}\right) F_\nu^2 \int_{-\infty}^{\infty} \mathbf{dq}_{||} \delta\left(\mathbf{k}_{||} - \mathbf{k}_{||}^{'} \pm \mathbf{q}\right) F(q_{||})$$

where $F(q_{||}) = \int_0^{L_z}\int_0^{L_z} dz dz^{'} \rho_{ij}(z)\rho_{ij}(z') I(q_{||}, z, z')$ is the form factor. Scattering rate can now be derived by summing over all possible final momentum states.

$$\frac{1}{\tau(\mathbf{k}_{||})} = \sum_{k'} P(\mathbf{k}_{||}, \mathbf{k}_{||}^{'}) = \sum_{k'} \frac{2\pi}{\hbar} \left(N_{ph} + \frac{1}{2} \pm \frac{1}{2}\right) F_\nu^2$$
$$\int_{-\infty}^{\infty} \mathbf{dq}_{||} \delta\left(\mathbf{k}_{||} - \mathbf{k}_{||}^{'} \pm \mathbf{q}_{||}\right) F(q_{||}) \delta\left(E(\mathbf{k}) - E(\mathbf{k}') \pm \hbar\omega_{SO}^{\nu}\right) \tag{C.8}$$

Converting the summation to integration and multiplying by 2 for spin degeneracy, we get

$$\frac{1}{\tau(k_{||})} = \frac{2}{\hbar} \left(N_{ph} + \frac{1}{2} \mp \frac{1}{2}\right) \frac{F_\nu^2 A}{(2\pi)} \int \mathbf{dk}_{||}^{'} \delta\left(E(\mathbf{k}) - E(\mathbf{k}') \pm \hbar\omega_{SO}^{\nu}\right)$$
$$\int_{-\infty}^{\infty} \mathbf{dq}_{||} \delta\left(\mathbf{k}_{||} - \mathbf{k}_{||}^{'} \pm \mathbf{q}_{||}\right) F(q_{||})$$

$$\int \mathbf{dk}_{||}^{'} \int_{-\infty}^{\infty} \mathbf{dq}_{||} \delta\left(E(\mathbf{k}) - E(\mathbf{k}') \pm \hbar\omega_{SO}^{\nu}\right) \delta\left(\mathbf{k}_{||} - \mathbf{k}_{||}^{'} \pm \mathbf{q}_{||}\right) F(q_{||}) =$$
$$\int\int k' dk' d\theta \delta\left(E(\mathbf{k}) - E(\mathbf{k}') \pm \hbar\omega_{SO}^{\nu}\right) F(|\mathbf{k}_{||} - \mathbf{k}_{||}^{'}|)$$

$$\int\int k' dk' d\theta \delta\left(E(\mathbf{k}) - E(\mathbf{k}') \pm \hbar\omega_{SO}^{\nu}\right) F(|\mathbf{k}_{||} - \mathbf{k}_{||}^{'}|) =$$
$$\frac{m^*}{\hbar^2} \int\int dE(k') d\theta \delta\left(E(\mathbf{k}) - E(\mathbf{k}') \pm \hbar\omega_{SO}^{\nu}\right) F(|\tilde{\mathbf{k}}_{||} - \tilde{\mathbf{k}}_{||}'|)$$

$$= \frac{m^*}{\hbar^2} \int_0^{2\pi} d\theta F(E(\mathbf{k}_{||}), \theta)$$

where

$$|\tilde{\mathbf{k}}_{||} - \tilde{\mathbf{k}}_{||}'| = \left[2k^2 \pm \frac{2\left(\hbar\omega_{SO}^{\nu} \pm (E_i - E_j)\right)}{\hbar^2} - 2k\left[k^2 \pm \frac{2\left(\hbar\omega_{SO}^{\nu} \pm (E_i - E_j)\right)}{\hbar^2}\right]^{1/2} cos\theta\right]^{1/2} \tag{C.9}$$

where $k = \frac{2m^*E}{\hbar^2}$, E_i and E_j are the energies corresponding to modes i and j and $+$symbol refers to the absorption process and $-$ symbol refers to the emission process. Finally, the scattering rate can be expressed as

$$\frac{1}{\tau_{ij}(E)} = \frac{2e^2m^*}{(2\pi)\hbar^3}\frac{\hbar\omega_{SO}^{\nu}}{2\epsilon_o}\left(\frac{1}{\epsilon_{ox}^{\infty}+\epsilon_s^{\infty}} - \frac{1}{\epsilon_{ox}^{o}+\epsilon_s^{\infty}}\right)$$
$$\left[N_{ph}\int_0^{2\pi} d\theta F_a(E,\theta) + (N_{ph}+1)\int_0^{2\pi} d\theta F_e(E,\theta)\right]$$

Dimension check

$$\frac{1}{\tau_{ij}(E)} = \frac{C^2.kg.kg.m^2.s^{-2}}{(kg.m^2.s^{-1})^3.(C^2.kg^{-1}.m^{-3}.s^2)}.m = \frac{1}{s}$$

The above scattering rate is between two modes i and j. Multi-modal scattering rate can be calculated by summing up contributions from different inter-mode scattering

$$\Gamma(E) = \sum_j \Gamma_{ij}(E) = \sum_j \frac{1}{\tau_{ij}(E)}$$

For multiple oxide SO phonon modes, scattering rate is summed up over all possible modes.

$$\Gamma_{total}(E) = \sum_{\nu} \Gamma_{\nu}(E)$$